UNIVERSITAT POLITÈCNICA DE VALÈNCIA

Experimental and theoretical study of B_2X_3 sesquichalcogenides under extreme conditions

Doctoral Thesis

Author:

Samuel Gallego Parra

Supervisors:

Oscar Gomis Hilario

Rosario Isabel Vilaplana Cerda

Tutor:

Francisco Javier Manjón Herrera

December, 2022

“Heroes are heroes because they are heroic in behavior, not because they won or lost.”

Nassim Nicholas Taleb

Resumen

Los sesquicalcogenuros con estequiometria B_2X_3, con A = Al, Ga e In y X = S, Se y Te, han recibido gran atención a lo largo de los últimos años, en particular en como modificarlos para obtener nuevas estructuras con propiedades inéditas, permitiendo su uso en una amplia variedad de aplicaciones. Si bien vías como el uso de altas/bajas temperaturas o modificar la composición química han sido bastante explotadas para modificar y obtener nuevas estructuras, las altas presiones están ganando auge como una tercera vía para obtener nuevos materiales. El uso de altas presiones implica emplear celdas de yunques de diamantes, preparadas para alcanzar altas presiones, además de altas temperaturas. A estos dispositivos se acoplan multitud de técnicas experimentales, como espectroscópicas (Raman e IR), difracción y absorción de rayos X, medidas de absorción óptica, de resistividad, etc., con el fin de estudiar como la materia evoluciona en dichas condiciones extremas. Adicionalmente, los cálculos teóricos son empleados como apoyo a los resultados experimentales.

Dentro de los trabajos existentes a altas presiones de esta familia de compuestos, estos han llegado a conclusiones incluso contradictorias, arrojando más dudas acerca su comportamiento bajo presión. De todos los integrantes de estos sesquicalcogenuros, Ga_2S_3, In_2S_3 y In_2Se_3, han sido los más estudiados bajo presión. En esta tesis se han evaluado los efectos de la alta presión en estos tres sesquicalcogenuros, haciendo uso de espectroscopia Raman y difracción de rayos X, siempre con el soporte de los cálculos teóricos, con el fin de aclarar los resultados publicados anteriormente.

Fruto de estos trabajos, la presente tesis recoge los cuatro artículos publicados en revistas indexadas. Dichos artículos han dado luz al comportamiento bajo presión de estos compuestos, como caracterización de propiedades vibracionales y estructurales bajo presión, mecanismos de transición, transiciones de fase inducidas bajo presión, así como caracterizar dichas fases de alta presión. Con todo ello, estos trabajos pretenden no solo conocer fehacientemente el comportamiento bajo presión de estos tres sesquicalcogenuros, sino impulsar futuros trabajos en el resto de los compuestos de esta familia y en otros similares, como en compuestos ternario AB_2X_4 con estructura tipo espinela y vacantes ordenadas.

Abstract

B_2X_3 sesquichalcogenides (A = Al, Ga and In, X = S, Se y Te) have received special attention along last years, with great emphasis in tailor them to attain new structures to novel properties, driving them in a huge number of applications. Although high/low temperature or varying chemical composition have been extensively used to modify and obtain new structures, high pressure is gaining relevance as an alternative way to synthetised new materials. To reach such pressures and additionally high/low temperatures, diamond anvil cells are used. Many experimental techniques can be coupled to these tools to study matter under extreme conditions (Raman and IR spectroscopy, X-ray diffraction and absorption, optical absorption, and resistivity measurements, among others). Additionally, computational simulations are used to give further support to the experimental results.

Despite the several existing works devoted to the behaviour under pressure of this family, controversial results have been reported. The most studied of these sesquichalcogenides have been Ga_2S_3, In_2S_3 and In_2Se_3. The aim of this thesis is to revisit the pressure effects by means of Raman spectroscopy and X-ray diffraction, with the help of computational simulations, for the purpose of clarify the results published earlier.

The current thesis contains the four articles published in indexed journals, resulting from the study of these three sesquichalcogenides. Such articles shed light to the pressure behavior of these compounds, their vibrational and structural properties under pressure, pressure-induced phase transitions and the mechanisms behind them and characterize such high-pressure phases. With these works, we pursue not only a depth understanding of the pressure behavior of these sesquichalcogenides, but boost future high-pressure works on the rest of the family and other similar compounds, as AB_2X_4 with spinel structure and ordered vacancies.

Resum

Els sesquicalcogenurs amb estequiometria B_2X_3, amb B = Al, Ga, i In i X = S, Se, i Te, han rebut una gran atenció al llarg dels darrers anys, en particular sobre com modificar-los per tal d'obtindre noves estructures amb propietats inédites, permetent el seu ús en una àmplia varietat d'aplicacions. Si bé l'ùs d'altes/baixes temperatures o modificar la composició química han segut prou explotades per a modificar i obtindre noves estructures, les altes pressions estan guanyant importància com una tercera via per a obtindrer nous materials. L'ús d'altes presions implica emprar cel·les d'encluses de diamants, preparades per a assolir altes presions, a més a més d'altes temperatures. A aquestos dispositius s'acoblen multitud de tècniques experimentals, com ara espectroscòpiques (Raman i IR), difracció i absorció de raigs X, mesures òptiques, de resistivitat, etc, amb la finalitat d'estudiar com la matèria evoluciona en aquestes condicions extremes. Adicionalment, els càlculs teòrics son emprats com a recolçament dels resultats experimentals.

Dins dels treballs existents a altes presions a aquesta familia de compostos s'ha arribat a determinades conclusions algunes de les quals son contradictòries, el que ha sembrat moltes dubtes al voltant del seu comportament sota pressió. De tots els integrants d'aquestos sesquicalcogenurs, Ga_2S_3, In_2S_3 i In_2Se_3 han sigut els més estudiats sota pressió. En aquesta tesi doctoral s'han evaluat els efectes de les altes pressions a aquestos tres sesquicalcogenurs, fent ús de l'espectroscopia Raman i la difracció de raigs X, sempre amb el suport dels càlculs teòrics, amb el fi d'aclarir els resultats previament publicats.

Fruit d'aquestos treballs, la present tesi doctoral recull els quatre articles publicats a revistes indexades. Aquestos articles han vessat llum sobre el comportament sota pressió d'aquestos compostos, com ara la caracterització de les seues propietats vibracionals i estructurals sota pressió, les transicions de fase induides sota pressió i els mecanismes d'eixes transicions, així com la caracterització de les seues fases d'alta pressió. Amb tot, aquestos treballs pretenen no només conèixer el comportament sota pressió d'aquestos tres sesquicalcogenurs, sino també impulsar futurs treballs a la resta de compostos d'aquesta familia i altres compostos rel·lacionats, com ara els compostos ternaris AB_2X_4 de tipus espinela i de vacants ordenades.

INDEX

Acknowledgements

I would never imagine this day to write my acknowledgements, which can be trickier than the dissertation itself. Indeed, I would require many dissertations to thank all the people supporting me since I started this path in my life. Nevertheless, I will be brief because I used to thank all of them for their great daily support every day. It is because of them I am about to conclude this part of my life. More than four years of investing my time, highly motivated, encouraged and doing my best, even facing this last year which has been very hard but, at the same time, full of learnings and new opportunities.

First, I am indebted to my supervisors, Sari, Oscar and Javi, who believed in me and gave me their valuable time to help me in my scientific career and personal growth. I would also like to thank Juan Ángel for all his valuable pieces of advice and for being here, for better or worse. Moreover, I wish also to thank their continuous support and patience during my PhD. Without a doubt whatsoever, they were the beginning of this outcoming dissertation and what I will become.

Second, my gratitude extends to all high-pressure community and Universtitat Politècnica of València, where I have found not only collaborators but also friends. In particular, I would like to express my thanks to Estelina, for her kindness and lovely smile and Catalin, for his excellent support and supervision during my short stay in ALBA synchrotron in July 2022. Regarding scientific stays, I would like to thank Jaime Segura Ruiz for his supervision during my four-month stay at The European Synchrotron Radiation Facility (ESRF) in 2021.

Words cannot express my gratitude to my friends, who are always there for everything. I would mention, specially, Shafi, Hussein, Adrián, Paco, Isabel, Silvia, Bea, Aitana, Raquel, Jose Carlos, Zicri, Cristina, Sandra, Eduardo, Erick, Ivan, Julia, Leila, Meryem, Adrián, Alfredo, Sofia, Laura, Mariola...the list is endless! Finally, I am extremely grateful to family, in especial my mother and sister.

Sincerely, thank you all very much.

Chapter 1
Introduction

The purpose of this first chapter is fivefold. First, I aim to give a general view of the compounds studied under extreme conditions. In this sense, the nine compounds that constitute these B_2X_3 sesquichalcogenides are briefly seen. Second, I intend to comment on what we understand by extreme conditions, specifically high pressures (HP). In particular, I will introduce the designed devices to reach such conditions and the main findings that HP allows to observe. The third and fourth sections display the experimental and theoretical methods used to undertake this present thesis. Finally, in the last section, I will comment on the objectives pursued in this thesis.

Albeit the main scope of this thesis is the changes and phase transitions (PT) occurring in In_2Se_3, Ga_2S_3 and In_2S_3 compounds at HP, the first and second sections will display to the reader relevant aspects of the B_2X_3 family (*B*=Al, Ga, In; *X*=S, Se, Te), as well as a veritable tour of the extreme conditions.

1. OVERVIEW OF GROUP-III B_2X_3 SESQUICHALCOGENIDES

Group-III B_2X_3 sesquichalcogenides (*B*=Al, Ga, In; *X*=S, Se, Te) are compounds that have drawn considerable attention for many years in an attempt to tailor their properties for several applications. The unequal number of cations and anions within this stoichiometry results in the mismatch between valence electrons, leading to vacancies. Although *B* cations can be coordinated only tetrahedrally (*B* = Ga), or both tetrahedrally and octahedrally (*B* = Al, In), vacancies are always located in tetrahedral sites.

These vacancies are necessary to hold the Grimm-Sommerfeld rule,[1, 2], therefore, maintaining the charge neutrality. These vacancies represent one-third of the cation sites and can be arranged along the structures in an orderly fashion (helices, lines, and planes[3]), or can be totally disordered in cation sites. Such vacancies allow building materials with anisotropic properties, tuning the bandgap, adding other elements, and even promoting PTs in a way to reaccommodate the intrinsic vacancies. In case ordered vacancies are present in their crystalline structures, these compounds are considered ordered vacancy compounds (OVCs). However, the intrinsic vacancies can be disordered at room conditions (RC), at high temperature (HT), or HP. In general, most of the structures found in this family come from the original spinel, zincblende, or wurtzite-like structures, yielding disordered spinels (DS), defective or disordered zincblende (DZ), or defective or disordered wurtzite (DW) structures, respectively.

Among the Al-based B_2X_3 sesquichalcogenides, Al_2S_3 is the most studied. We have witnessed an abrupt interest in secondary aluminium-sulfur (Al-S) batteries in recent years. For instance, the theoretical capacity of Al_2S_3 as a cathode, if it fully lithiated, is 1874 mAh/g. Experimentally, it was observed at about 62% of such theoretical capacity,[4] mainly due to the irreversible formation of LiAl and Li_2S in the core of the cathode at the initial discharge. However, the lithiation of Al_2S_3 occurs at low potential, thus clearly recommending this sesquicalchogenide as an anode material. To avoid these irreversible reactions and adequate it as anode material, AlS_x films deposited on nitrogen-doped nanosheets have been investigated.[5] As a result, they exhibited a reliable cyclability with a sustainable capacity of 640 mAh/g in the range of 0.6-3.5 V. More recent research points out the use of pure Al and S as anode and

cathode material, respectively.[6-10] These Al-S batteries, with a theoretical capacity of 1072 mAh/g, offer an excellent substitute for Li batteries, in addition to the abundance of both Al and S in the earth's crust. Al_2S_3 plays a key role in these Al-S batteries because it is deposited on the S cathode in the discharge process, so many strategies have emerged to facilitate its oxidation. In this sense, many works have focused on Al_2S_3 and how to oxide it back to S[7, 11] to enhance the performance of these promising Al-S batteries.

Regarding other Al_2X_3 compounds, they have been the subject of many studies, but not as extensively as Al_2S_3. Al_2Se_3 deposited on Si(111) has shown relevant properties, as HT stability, high order degree and lack of dangling bonds. All of these properties are crucial for the next-generation of silicon-based self-assembled nanostructures.[12] Luminescence in the near UV spectral region has been observed on Al_2Se_3 nanocrystals, which makes it suitable for optoelectronic blue light emitters.[13] As for Al_2Te_3, there is no relevant works to remark, just its use for its good thermally stability to improve the stability of Al_2Te_3-Sb_2Te_3 materials to build phase change random access memories.[14]

Table 1 summarizes the different phases of all Al_2X_3 found in the literature. For Al_2S_3, the phase diagram shows that α-Al_2S_3 transforms into γ-Al_2S_3 at 990 ºC, which melts congruently at around 1083 ºC.[15] Other phases, such as δ- and α'-Al_2S_3 with β-In_2S_3 and DZ-like structure, respectively, have been synthesized at both HT and HP.[16, 17] On the other hand, α-Al_2Se_3 melts congruently at around 940 ºC.[15] In contrast, β-Al_2Se_3 has been observed at RC but has not been studied under HT.[13] As occurred in Al_2S_3, phase with β-In_2S_3-like structure, the α'-Al_2S_3, can be synthesized at both HT and HP.[17] Finally, α-Al_2Te_3 transforms into β-Al_2Te_3 at around 720 ºC, melting congruently at around 865 ºC.[15] However, further information about the structure of β-Al_2Te_3 has been reported.[15, 18] Finally, it must be stressed that other phases that are quasi-stoichiometric can be obtained with DW structure, as β-Al_2S_3, β-Al_2Se_3 and β'-Al_2Te_3.[19-21]

To date, there are just a few experimental works devoted to the synthesis at HT and HP of Al_2X_3 compounds, such as δ-Al_2S_3, α'-Al_2S_3 and α'-Al_2Se_3.[16, 17] In this context, many pressure-induced PTs have been theoretically predicted for stoichiometric Al_2S_3, following the sequence (transition pressure values in brackets): δ-Al_2S_3 → γ-Al_2S_3 (≈10 GPa) → *Pbcn* (≈25 GPa) → β-Al_2S_3 (≈75 GPa) → $P6_3/mmc$ (≈100 GPa) → *P*-1 (≈175 GPa) (see **Fig. S1** of **Ref. 22**). In summary, it can be said that these Al_2X_3 sesquichalcogenides are the least studied. They constitute, without a doubt whatsoever, a landscape to be explored, especially in HP.

Table 1. Phases found in literature of Al_2X_3 (X = S, Se, Te) sesquichalcogenides. Vac. indicates if vacancies are ordered (O) or disordered (D). The P,T column refers to conditions under which the phases have been observed. More information is given in the footnote.

	Phase (Vac.)	**P,T**	**S.G. (nº)**	**Struc. type**	**Crystal system**	**Lattice parameters**	**Ref.**
Al_2S_3	α-Al_2S_3 (O)	RC	$P6_1$ (169)	α-Al_2S_3	Hexagonal	$a = b =$ 6.49 Å, c = 17.17 Å	[23, 24]
	γ-Al_2S_3 (O)	1000 ºC	R-3c (167)	α-Al_2O_3	Trigonal	$a = b$ = 6.47 Å, c = 17.27 Å	[15, 19, 25]
	δ-Al_2S_3 (O)	6.5 GPa, 1200 ºC	$I4_1/amd$ (141)	β-In_2S_3	Tetragonal	$a = b =$ 7.03 Å, c = 29.81 Å	[16]
	α'-Al_2S_3 (D)	4.0 GPa, 400 ºC	Fd-3m (227)	DS	Cubic	a = 9.94 Å	[17]
	β-Al_2S_3[a,b] (D)	HT	$P6_3/mc$ (186)	DW	Hexagonal	$a = b =$ 3.58 Å, c = 5.83 Å	[19]
Al_2Se_3	α-Al_2Se_3 (O)	RC	Cc (9)	α'-Ga_2S_3	Monoclinic	a = 11.68 Å, b = 6.73 Å, c = 7.32 Å, β = 121.1 º	[15, 26]
	α'-Al_2Se_3 (D)	6.0 GPa, 600 ºC	Fd-3m (227)	DS	Cubic	a = 10.45 Å	[17]
	β-Al_2Se_3[b] (D)	RC	$P6_3/mc$ (186)	DW	Hexagonal	$a = b =$ 3.89 Å, c = 6.30 Å	[20]
Al_2Te_3	α-Al_2Te_3 (O)	RC	$P12_1/c1$ (14)	Al_2Te_3	Monoclinic	a = 7.18 Å, b = 12.85 Å, c = 14.17 Å, β = 90.04 º	[15, 21, 27]
	β-Al_2Te_3[c] (?)	720 ºC	?	?	?	?	[15, 18]
	β'-Al_2Te_3[b,d] (D)	RC	$P6_3/mc$ (186)	DW	Hexagonal	$a = b =$ 4.08 Å, c = 6.94 Å	[21]

[*] RC = room conditions, S.G. = space group, DS = defective spinel, DZ = defective wurtzite.
[a] Temperature reached is not indicated.
[b] Almost stoichiometric.
[c] No more information about this phase is given in the references mentioned.
[d] Obtained via thermal decomposition of AlTeX compounds (X = Cl, Br, I).

When it comes to Ga-based B_2X_3 sesquichalcogenides, several studies have made efforts to explore them for many applications. In this sense, α'-Ga_2S_3, the stable phase at RC (see **Table 2**) exhibits interesting properties. Good transparency in the infrared (IR) region, large second-harmonic generation (SHG) effects and high laser-induced damage threshold (LIDT) properties in α'-Ga_2S_3 have been demonstrated. These features make this material competitive with other IR nonlinear optical (NLO) compounds, such as $AgGaGeS_4$, $LiGaS_2$, $Li_2Ga_2GeS_6$ and $BaGa_4S_7$ for second-order nonlinear optical devices.[28] Absence of strong phonon absorption peaks in α'-Ga_2S_3 for wavelengths above 100 μm has been measured, which entails promising

applications in the THz range.[29] On the other hand, α'-Ga_2S_3 meets suited properties for blue to UV photodetectors,[30, 31] gas sensors,[32] light emitters,[33, 34] sodium ion batteries,[35] micro-tunable laser,[36] and silicon-based optical switches,[37] among other applications.

Table 2. Phases found in literature of Ga_2X_3 (*X* = S, Se, Te) sesquichalcogenides. Vac. indicates if vacancies are ordered (O) or disordered (D). The P,T column refers to conditions under which the phases have been observed. More information is given in the footnote.

	Phase	**P,T**	**S.G. (nº)**	**Struc. type**	**Crystal system**	**Lattice parameters**	**Ref.**
Ga_2S_3	α'-Ga_2S_3 (O)	RC	*Cc* (9)	α'-Ga_2S_3	Monoclinic	*a* = 11.11 Å, *b* = 6.40 Å, *c* = 7.02 Å, β = 121.73 º	38, 39
	α-Ga_2S_3[a,b] (D)	920-1080 ºC, RC	$P6_1$ (169)	α-Al_2S_3	Hexagonal	*a* = *b* = 6.39 Å, *c* = 18.04 Å	40, 41
	β-Ga_2S_3[a,b] (D)	920-1080 ºC, RC	$P6_3/mc$ (186)	DW	Hexagonal	*a* = *b* = 3.68 Å, c = 6.03 Å	40-43
	γ-Ga_2S_3[a,b] (D)	858-911 ºC, RC	*F*-43*m* (216)	DZ	Cubic	*a* = *b* = 3.68 Å, c = 6.03 Å	41, 43-45
Ga_2Se_3	Mono-β-Ga_2Se_3[c] (O)	RC	*Cc* (9)	β-Ga_2Se_3	Monoclinic	*a* = *b* = 6.60 Å, *c* = 11.65 Å, β = 108.84 º	46-49
	Ortho-β-Ga_2Se_3[c] (O)	RC	*Imm*2 (44)	α-II-In_2Te_3	Tetragonal	*a* = 3.90 Å, *b* = 11.83Å, *c* = 5.79 Å	47-50
	α(γ)-Ga_2Se_3[b,d] (D)	730 ºC (RC)	*F*-43*m* (216)	DZ	Cubic	*a* = 5.42 (5.63) Å	51, 52
Ga_2Te_3	β-Ga_2Te_3 (D)	RC	*F*-43*m* (216)	DZ	Cubic	*a* = 5.89 Å	44, 53, 54
	Ortho α-Ga_2Te_3[e] (O)	RC	*Imm*2 (44)	α-II-In_2Te_3	Tetragonal	*a* = 4.10 Å, *b* = 23.6 Å *c* = 12.5 Å	55, 56

*RC = room conditions, S.G. = space group, DZ = defective wurtzite, DZ = defective zincblende.
[a] Almost stequiometric.
[b] It can be synthetised at RC depending on temperature, Ga/*X* (*X* = S, Se, Te) ratios or adding other cations/anions.
[c] Monoclicnic (mono) and orthorhombic (ortho) differ in how the vacancy arrays are displayed along the structure. In the former vacancies lie on helices along [001], in the latter are placed in straight lines.
[d] Both zincblende-type structures quite similar have been reported in literature, depending on the temperature and Ga/Se ratio.
[e] Synthetised from a mixture of pure Ga and Te at 450ºC.[56]

α'-Ga_2S_3 melts congruently at about 1100 ºC. Sub-stoichiometric (sulphur defective) phases close to 2:3 relation can be obtained according to the Ga-S phase diagram,[41,

[43, 57, 58] which are displayed in **Table 2**. A few works have explored these sub-stoichiometric phases and their properties for several applications in optoelectronics,[59, 60] photoelectronics,[61] sensing,[62] and nonlinear optics.[28] The earlier works focused on the HP behavior of α'-Ga_2S_3 as well as in the different phases observed under increasing and decreasing pressure. They will be discussed in sections **2.2.** and **2.4.** of **Chapter 2**. Additionally, other phases of Ga_2S_3 (α, β, γ) have been synthesized at HT and quenched at RC.

β-Ga_2Se_3 (see **Table 2**) is the stable phase of Ga_2Se_3 at RC and has been extensively studied as a matrix for dopants, such as $Cr^{+2/+3}$,[63] Fe^{+2},[64] Co^{+2},[65] and Mn^{+2},[66] among others. These cations can occupy the vacancies in the structure. These vacancies in order to release highly anisotropic materials, mono-β-Ga_2Se_3 has been growth on several substrates.[67-69] The control of vacancies allows not only tuning anisotropic properties, such as optical transmission and photoluminescence,[48] but also passivating the interfaces.[70] In this sense, it is interesting to note that the different properties are quite dependent on how vacancies are ordered through the structure. In fact, there are two β-Ga_2Se_3 phases: monoclinic (mono)-β-Ga_2Se_3 and orthorhombic (ortho)-β-Ga_2Se_3 with α-II-In_2Te_3-like structure (more details in **Table 2**). Unlike α'-Ga_2S_3, β-Ga_2Se_3 transforms into α-Ga_2Se_3 at about 1000 ºC. This α-Ga_2Se_3 not only observed at HT, but can also quench at RC. Due to the presence of disordered vacancies, α-Ga_2Se_3 has been considerably studied for absorbing and buffer layers in solar cells,[71, 72] optoelectronic applications,[73, 74] luminescence devices,[75] and thermoelectric materials,[76] among others. Moreover, it has shown ferroelectricity in nanoflakes, removing the requirement of a polar point group, thus expanding ferroelectric materials to defective compounds with a non-polar point group.[77, 78] Another DZ structure, γ-Ga_2Se_3, has been observed experimentally, whose lattice parameter differs a bit somewhat compared to α-Ga_2Se_3. However, this latter γ-Ga_2Se_3 and the conditions to obtain it remains unclear.[52]

Regarding the heaviest sesquichalcogenide in this group, β-Ga_2Te_3 (see **Table 2**), the DZ structure is the only stable phase at RC, which melts congruently at about 810 ºC.[54, 79] Similarly to α-Ga_2Se_3, β-Ga_2Te_3 has been in the spotlight of multiple works due to the disordered vacancies in cation sites. More specifically, it has been studied mainly for selector devices and cross-point arrays for emerging memories,[80, 81] anodes for lithium-ion batteries,[82] and thermoelectric and highly efficient phase-change materials.[76, 83-85]

Again, the α-II-In_2Te_3-like structure is observed in ortho-α-Ga_2Te_3 (see **Table 2**). However, there are no evidences of the mono-β-Ga_2Se_3-like structure in Ga_2Te_3. Despite of that, properties of mono and ortho structures in both Ga_2Se_3 and Ga_2Te_3 have been explored via theoretical calculations, in an attempt to highlight how the ordering of vacancies tailors the band gap energy, even in intermediate compounds with stoichiometry $Ga_2(Se_{1-x}Te_x)_3$.[86] As a result, band gaps ranging from 0.6 to 2.4 eV have been predicted as a function of the exchanged-correlation functional employed. The different works focused on the HP behaviour of Ga_2Se_3 and Ga_2Te_3 will be shown and discussed in section **2.4.** of **Chapter 2**.

The last members of these sesquichalcogenides concern those with In cations. Among all the phases observed within the chemical formula In_2S_3, the β and α phases (see **Table 3**) are the most promising. The former, which is stable at RC, has been intensively studied as a thermoelectric material,[87, 88] gas sensor,[30, 89] photocatalyst,[90, 91] solar cell absorber,[92] optoelectronic devices,[93] and water splitting, *inter alia*. Due to the presence of vacancies, β-In_2S_3 has attracted enormous attention for the inclusion of other cations in the empty spaces of its structure. Sm^{+3}, Dy^{+3}, and Tb^{+3} cations can induce ferromagnetism effects demanded for spintronic, magnetic, and memory storage devices;[94, 95] Tm^{+3} cations can improve photoelectric and luminescent properties for photovoltaic, photoelectric, and sensors applications;[96] finally, Cu^{+2}/Mn^{+2} cations allow tailoring the electrical conductivity and making this material suitable for photocatalytic applications.[97] Other phases of In_2S_3 can be obtained at HT (γ) or at HP and HT (ε).

According to its phase diagram, β-In_2S_3 undergoes a PT to α-In_2S_3 at about 420ºC,[87, 88, 98] and this HT phase can be obtained at RC via varying In/S ratio or cation/anion substitution.[87, 99, 100] This result has stimulated the tailoring of its high anisotropic properties due to the intrinsic mixture of In atoms and vacancies in cation sites, being observed that α-In_2S_3 offers excellent features for photovoltaics applications,[101] thermoelectric devices,[88, 100] and solar cells.[99, 102, 103] In relation to the phases observed at HP in In_2S_3, they will be shown and discussed in section **2.3.** of **Chapter 2**.

Table 3. Phases found in literature of In_2X_3 (X = S, Se, Te) sesquichalcogenides. Vac. indicates if vacancies are ordered (O) or disordered (D). The P,T column refers to conditions under which the phases have been observed. More information is given in the footnote.

	Phase	P,T	S.G. (nº)	Struc. type	Crystal system	Lattice parameters	Ref.
In_2S_3	β-In_2S_3 (O)	RC	$I4_1/amd$ (141)	β-In_2S_3	Tetragonal	$a = b =$ 7.61 Å, c = 32.24 Å	98, 104-106
	α-In_2S_3[a] (D)	420 ºC, RC	Fd-3m (227)	DS	Cubic	a = 10.72 Å	87, 88, 98
	γ-In_2S_3[a] (D)	1090 ºC, RC	P-3m1 (164)	γ-In_2S_3	Trigonal	$a = b =$ 3.87 Å, c = 9.16 Å	98, 107, 108
	ε-In_2S_3[a] (O)	3.5 GPa, 500 ºC	R-3c (167)	α-Al_2O_3	Trigonal	$a = b =$ 6.56 Å, c = 17.57 Å	109
In_2Se_3	α-In_2Se_3 (3R) (O)	RC	$R3m$ (160)	α-In_2Se_3 (3R)	Rhombohedral	$a = b =$ 4.05 Å, c = 28.77 Å	110, 111
	α-In_2Se_3[b] (2H) (O)	RC	$P6_3/mmc$ (194)	α-In_2Se_3 (2H)	Hexagonal	$a = b =$ 4.03 Å, c = 19.24 Å	112, 113
	β-In_2Se_3[a] (3R) (O)	200 ºC, RC	$R3m$ (166)	α-Bi_2Te_3	Rhombohedral	$a = b =$ 4.00 Å, c = 28.40Å	110, 114
	β-In_2Se_3[a,b] (2H) (O)	200 ºC, RC	$P6_3/mmc$ (194)	β-In_2Se_3 (2H)	Hexagonal	$a = b =$ 4.02 Å, c = 19.22 Å	110, 114

	β'-In_2Se_3[a,c] (O)	-196 ºC, RC	*C*2/*m* (12)	β'-In_2Se_3	Monoclinic	*a* = 6.94Å, *b* = 4.02 Å, *c* = 10.21 Å, β = 103.30 º	[115-117]
	γ-In_2Se_3 (O)	520 ºC, RC	$P6_1$ (169)	α-Al_2S_3	Hexagonal	*a* = *b* = 7.13 Å, *c* = 19.38 Å	[118, 119]
	δ-In_2Se_3 (O)	730 ºC, RC	*P*-3*m*1 (164)	Ta_2S_2C	Trigonal	*a* = *b* = 4.02 Å, *c* = 9.65 Å	[114, 120]
	α'-In_2Se_3[d] (?)	-125 ºC	?	?	?	?	[121, 122]
In_2Te_3	α-I-In_2Te_3[e] (O)	RC	*F*-43*m* (216)	Defective anti fluorite	Cubic	*a* = 18.50 Å	[123, 124]
	α-II-In_2Te_3[e] (O)	RC	*Imm*2 (44)	α-II-In_2Te_3	Tetragonal	*a* = 4.36 Å, *b* = 13.02 Å, *c* = 6.17 Å	[125, 126]
	β-In_2Te_3 (D)	625 ºC	*F*-43*m* (216)	DZ	Cubic	*a* = 6.16 Å	[123, 127]

[*]RC= room conditions, S.G.= space group, DS = defective spinel, DZ = defective zincblende.
[a] It can be synthetised at RC depending on temperature, In/*X* (*X* = S, Se, Te) ratios or adding other cations/anions.
[b] (3R) and (2H) polymorphs differ in the stacking sequence of *B* and *X* layers, in rhombohedral and hexagonal crystal structure, respectively. Only α(3R) and β(3R)-In_2Se_3 will be discussed in the text.
[c] β'-In_2Se_3 can be obtained at RC or cooling thin samples or very few layers of β-In_2Se_3.
[d] No more information about this phase is given in the references mentioned.
[e] There are two α phase mainly influenced by a non-exact stoichiometric In_2Te_3 chemical formula. The most common is the α-I-In_2Te_3.

Among all the sesquichalcogenides considered in this section, it can be said that In_2Se_3 is the most fascinating compound, in terms of how many publications have been published over the last decades, according to the promising applications in which this material can be used. In_2Se_3 offers several phases in which vacancies are displayed in layers, giving rise to 2D layered structures. Except for the 2D layered α-Al_2Te_3 structure, all 2D layered phases found in this family of sesquichacogenides are exclusively found in In_2Se_3. For the sake of brevity, we will focus on the α(3R)- and β(3R)-In_2Se_3 phases, the most explored in literature (for now, we will refer them as α and β-In_2Se_3, respectively; further information in **Table 3**). More details concerning the other phases of In_2Se_3 can be found in earlier works.[111, 121, 128, 129] While α-In_2Se_3 is the stable phase at RC, β-In_2Se_3 is obtained at HT (see **Table 3**). However, as stressed in other sesquichalcogenides, HT phases can be obtained at RC by several synthesis methods. Both phases of In_2Se_3 have attracted attention in modulating between them and enhancing their inherent properties. The α- and β-In_2Se_3 encompass a broad range of applications: phase change memories,[130-132] gas sensor,[133] neuromorphic systems,[134] photosensitive devices,[135] catalysis,[136] polarization-dependent optical properties,[137] photodetectors,[131, 138] *inter alia*. The former, a 2D ferroelectric phase, and the latter, a 2D paraelectric phase, stand out for their different properties because of their polar (α-In_2Se_3) and non-polar (β-In_2Se_3) point groups.

Piezoelectricity and ferroelectricity have been extensively examined in α-In_2Se_3,[139, 140] meanwhile β-In_2Se_3 has been proposed as a topological insulator for sharing the same tetradymite-like structure with well-known topological insulators, as Bi_2Te_3,

Sb_2Te_3 and Bi_2Se_3.[141, 142] Other phases of In_2Se_3 are obtained at LT (α' and β') or at HT (γ and δ).[126-129] Again, all earlier articles related to the HP behaviour of In_2Se_3 will be shown and discussed in section **2.1.** of **Chapter 2**.

The heaviest sesquichalcogenide of the In_2X_3 family, In_2Te_3, has not received as much attention as In_2Se_3. The high number of citations devoted to In_2Te_3 mainly propose it for applications, such as phase-change random access memory,[143] photodetector,[144] and gas sensor.[145] Very recently, relevant magnetoresistance properties have been measured in α-I-In_2Te_3 that also shows a high stability in ambient air at RC.[146] Above 625 ºC, α-I-In_2Te_3 changes to β-In_2Te_3, which melts congruently at about 670 ºC.[147, 148]

To guide the reader, I have plotted in **Fig. 1** the different structures observed in this above commented family. As mentioned in **Tables 1**, **2**, and **3**, vacancies can be found either ordered o disordered in the different structures. Such ordering can be in many forms. For instance, vacancies can form a helix (see **Figs. 1a)**, **1b)**, and **1c)**). With tetrahedrally-coordinated cations, α-Al_2S_3 adopts a structure with S.G. $P6_1$ (**Fig. 1a)**) at RC, while γ-In_2Se_3 does so at HT. With octahedrally-coordinated cations, the structure with S.G. *R*-3*c* (**Fig. 1b)**) is found at HT in both γ-Al_2S_3 and ε-In_2S_3, at RC and at HP, respectively. With both tetrahedrally- and octahedrally-coordinated cations, β-In_2S_3 crystallizes in a structure with S.G. $I4_1/amd$ (**Fig. 1c)**) at RC. This structure is also obtained in δ-Al_2S_3 at HT and HP. On the other hand, vacancies can form straight lines (see **Figs. 1d)** and **1e)**). This feature has only been observed at RC. The structure with S.G. *Cc* (**Fig. 1d)**) has been found in α-Al_2Se_3, α'-Ga_2S_3, and mono-β-Ga_2Se_3, while the structure with S.G. *Imm*2 (**Figure 1e)**), has been observed in ortho-β-Ga_2Se_3, mono-α-Ga_2Te_3, and α-II-In_2Te_3, respectively.

The vacancies can also be in layers, thus giving rise to 2D layered structures (see **Figs. 1f)**, **1g)**, **1h)**, **1i)** and 1**j)**). **Figures 1f)**, **1g)** and **1h)** display the structures of α-In_2Se_3 (S.G. *R*3*m*), β-In_2Se_3 (S.G. *R*-3*m*) and β'-In_2Se_3 (S.G. *C*2/*m*), respectively. The former shows both tetrahedrally- and octahedrally-coordinated cations, while the β and β' phases show only octahedrally-coordinated cations. On the other hand, **Figures 1i)** and **1j)** show the layered structures only found in α-Al_2Te_3 (S.G. $P2_1/c$), at RC, and δ-In_2Se_3 (S.G. *P*-3*m*1), at HT, with tetrahedrally- and octahedrally-coordinated cations, respectively. Finally, vacancies can be disordered in cation sites (see **Figs. 1k)**, **1l)**, **1m)**, **1n)**, and **1o)**). The vacancy fraction occupation of 1/3 can be found in all cation sites, as shown in the DZ (S.G. *Fd*-3*m*) and DW (S.G. $P6_3/mc$) structures (**Figs. 1k)** and **1l)**, respectively) with tetrahedrally-coordinated cations. As can be seen in **Table 1**, **2** and **3**, DZ structures are mainly found in Ga_2X_3 sesquichalcogenides at HT (X = S, Se) and at RC (X = Te), as well as in β-In_2Te_3 at HT. Meanwhile, DW structures are seen in Al_2X_3 sesquichalcogenides at HT (X = S, Se) and at RC (X = Te) as well as in β-Ga_2S_3 at HT. Tetrahedrally and octahedrally-coordinated cations are found in the DS structure (S.G. *Fd*-3*m,* **Fig. 1m)**) observed in Al_2X_3 sesquichalcogenides at HT and HP (X = S, Se) as well as in α'-In_2S_3 at HT. In all these structures (DZ, DW, and DS), cation-vacancy disorder occurs only in tetrahedral cation sites. However, there are less common structures in which the vacancies are distributed among cation sites with different coordination numbers. As an example, this can be found in γ-In_2S_3 (s.g.

P-3*m*1, **Fig. 1n)**) and in α-Ga_2S_3 (s.g. $P6_1$, **Fig. 1o)**), both at HT, the former with both tetrahedral and octahedral cations, the later with just tetrahedral cations.

In short, this B_2X_3 sesquichalcogenides, that are OVCs because of the presence of intrinsic vacancies in their crystallographic structures, can be synthesized in several structures. The structures observed at RC and at HT have been shown schematically, standing out how vacancies can be best positioned to tailor their properties. At this moment, several questions arise: how can these structures and their properties be changed at HP? Could we obtain completely different phases at HP? How relevant are the PTs observed at HP? In the next we are going to explore this magnificent field of the solid-state physics.

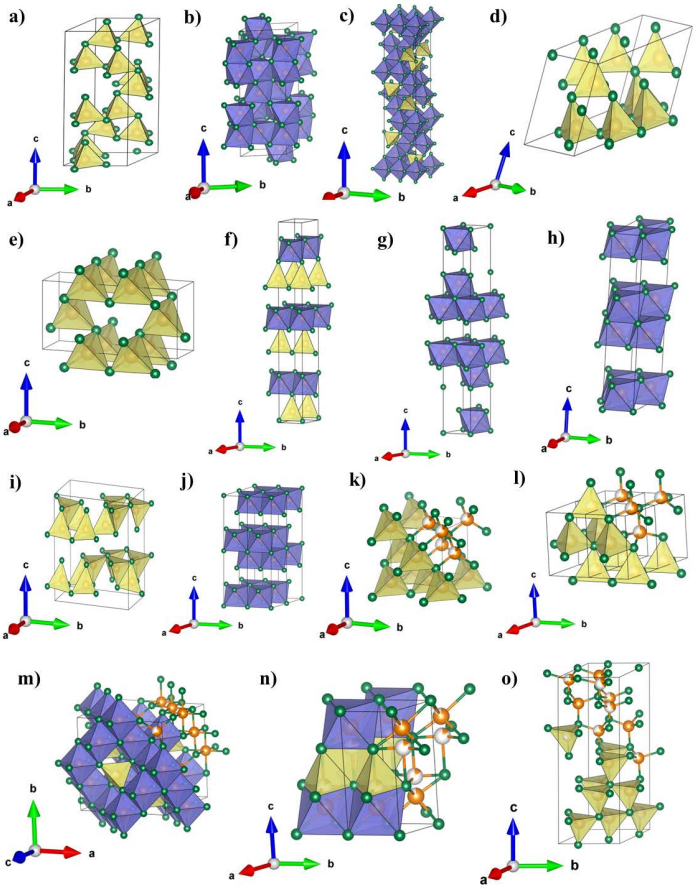

Figure 1. Structures found at RC or HT in B_2X_3 sesquichalcogenides: a) S.G. $P6_1$; b) S.G. *R*-3*c*; c) S.G. $I4_1/amd$; d) S.G. *Cc*; e) S.G. *Imm*2; f) S.G. *R*3*m*; g) S.G. *R*-3*m*; h) S.G. *C*2*m*; i) S.G. $P2_1/c$; j) S.G. *P*-3*m*1; k) S.G. *F*-43*m*; l) S.G. $P6_3/mc$; m) S.G. *Fd*-3*m*; n) S.G. *P*-3*m*1; o) S.G. $P6_1$. As can be seen, vacancies are arranged in many ways: **a)-c)** helixes, **d)-e)** straight lines, **f)-j)** layers and **k)-o)** disordered in cation sites. Personal compilation.

2. HIGH PRESSURE STUDIES: WHY IS RELEVANT TO STUDY THE MATTER UNDER EXTREME CONDITIONS?

How much pressure can be considered as HP? Several definitions can be obtained by reading some sources. Here I give just a few:

"…it is worthwhile to think for a moment about the definition of the term "high" pressure…from superhard materials like diamond and boron nitride, through metals, molecular solids, to living organisms…" **Ref. 149**.

""high" implies conditions that produce some extraordinary (not found at "normal", ambient conditions) effects or behavior for the given object of study." **Ref. 149**.

"If one asks for a definition of high pressure (HP), the answer will certainly depend on the scientific environment… physics, chemistry, materials science, geophysics, biology, or food technology…" **Ref. 150**.

"Among our scientific community, there is a certain agreement in that HP refer to the study of those phenomena occurring above 1000 bar (1 kbar). Other terms like "ultra high pressure" were coined to refer to phenomena involving pressures above 1000000 bar (1 Mbar)." **Ref. 150**.

We can conclude that the term "HP" depends on which materials and science fields are involved or how high the pressures achieved. To get an idea about what pressures we can handle, **Fig. 2** depicts the pressure ranges that can be found in our universe, from the almost vacuum in the Milky Way galaxy (≈10^{-24} GPa, 10^{-20} atm) to the highest pressure calculated in the proton center (≈10^{26} GPa, 10^{30} atm).[151]

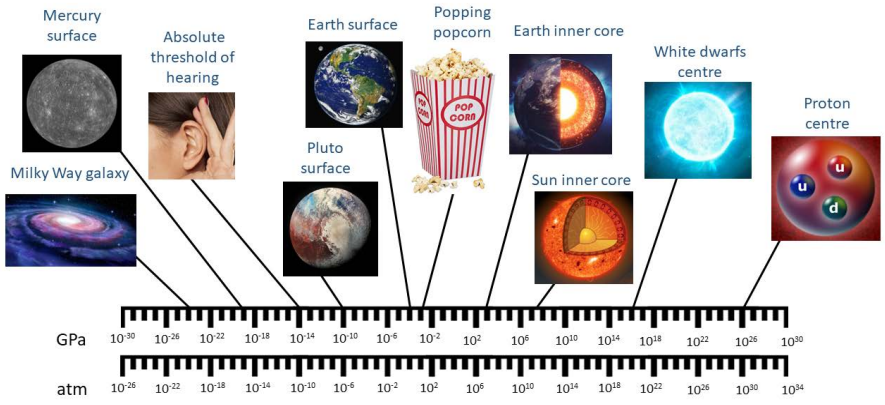

Figure 2. Pressure ranges existing in our universe. Personal compilation.

Pressure, P, is a thermodynamic parameter that measures how much force, F, is exerted upon an area, A, P = F/A. The higher the force or lesser the area, the higher the resulting pressure. When pressure is applied at every point of the volume sample (solid, liquid, or gas), we talk about hydrostatic pressure since it is exerted equally in all points of the sample. Pressure and temperature can be compared in the way that

both alter the sample volume, the former decreasing it (via merely decreasing lattice parameters) and the latter increasing it (via thermal expansion and phonon population effects). As Weistein genuinely exemplifies in **Ref. 152**, 100 kbar of pressure (very easily attainable) in Si yields a volume decrease of 5%. In contrast, only a volume increase of 1.8% is induced from 0 K up to the melting point (at 1687 K).

Tools for exerting HP on a sample have evolved since the first designs released by P. W. Bridgman, considered the father of HP, who was awarded the Nobel Prize Physics in 1946. In total, Bridgman published about 200 papers between 1906 and 1961 on the properties of materials under compression. These publications involved resistivity and compressibility measurements at HP, and covered many phenomena from the pressure dependence of the resistance of a number of metals[153] to the study of the phase diagram of water,[154] up to 4.4 and 9.8 GPa, respectively. **Figure 3a)** shows the opposed anvil used for resistivity measurements at HP employed by Bridgman,[153] commonly known as Bridgman anvil. After Bridgman, H. G. Drickamer can also be considered a pioneer in the field of HP, mostly in the study of molecular, atomic, and electronic properties of materials under compression. Drickamer first received the Bridgman Award by the International Association for the Advancement of High Pressure Science and Technology (AIRAPT) in 1977 for his improved HP instrumentation in many spectroscopic and non-spectroscopic techniques. We can visualize in **Figs. 3b)** and **3c)** a piston-cylinder cell designed for X-ray diffraction (XRD) measurements[155] and an adapted Bridgman anvil for Mössbauer measurements,[156] respectively, both conceived by Drickamer.

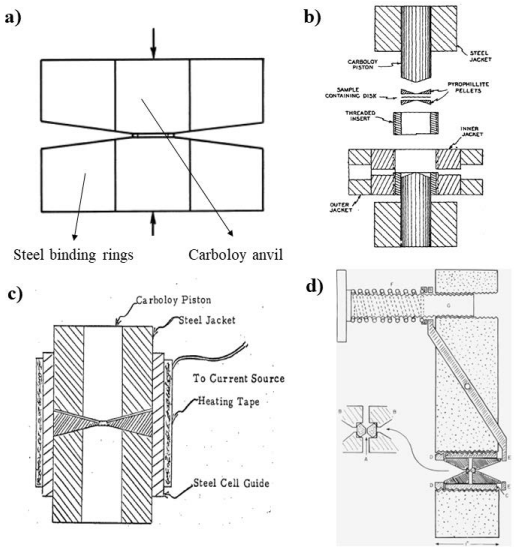

Figure 3. HP devices with **a), c)** carboloy anvils and **b)** pistons. **d)** Design of the first DAC. Personal compilation.

These first designs of opposing anvils, amid others, have in common the use of carboloy or tungsten carbide as anvil material, not hard enough to reach HP.

Moreover, such anvils did not allow an *in-situ* observation of the pressure effects on the sample. At that time, H. T. Hall produced, for the first time, synthetic diamonds using iron sulfide and graphite at 1200ºC and 10 GPa in his own-designed pressure chamber.[157] This yielded to the first HP tool with diamonds as anvils, the diamond anvil cell (DAC) (**Fig. 3d)**), designed by C.E. Weir, E. R. Lippincott, A.V. Valkenburg and E.N. Bunting at the National Bureau of Standards in 1959.[158] The introduction of a metallic gasket allowed the sample to be held in a hole, where a pressure sensor was also placed, both surrounded with different pressure transmitting media (PTM). Since then, many types of DACs have been released, raising several advantages in comparison to the first designs (**Fig. 3**). First, the feasibility to access to the sample by means of optical and spectroscopic techniques. Second, an optical microscope that allows *in-situ* observation and photography. Third, the use of metallic gaskets that reduce the stress gradient in the sample. Fourth, solid, liquid and gas samples can be studied due to these metallic gaskets. Finally, small quantities of samples are enough to run any HP experiment.[149, 150]

Commercial and home-made DACs are adapted to pressure ranges up to 3 Mbar (even higher). They can cover low temperatures (down to 4 K) or HT (with resistive heating up to 1000 K or laser heating from 1000 K to 5000 K) and are accessible with many optic and spectroscopic techniques. DACs can be tailored to different techniques and environments with the materials used to build the DAC, the types and sizes of diamonds used, and the dimensions of the DAC. Brands as BETSA and Almax-easyLab offer an extensive catalogue of DACs according to the experiment requirements (the reader is referred to the official webs of these brands). **Figure 4** displays a few DACs commonly employed in ALBA synchrotron.

Figure 4. Types of DACs commonly used in HP-XRD experiments: a) MDAC-XRD, b) MDAC-TBT, c) screw-driven Boehler-Almax DAC. Photons taken in high-pressure lab of ALBA synchrotron.

Figure 4a) shows a membrane DAC (MDAC) for HP-XRD measurements (MDAC-XRD). Depending on the culet of the diamonds, up to 100 GPa can be achieved. It offers a full and radial angle aperture of 76º and 20º, respectively, and can be accessible via visible electromagnetic spectrum and X-rays above 10 keV. For HP experiments to be conducted at temperatures from room temperature (RT) to 10 K, a MDAC-TBT (showed in **Fig. 4b)**) is most suitable, which is built with super alloys and tungsten carbide seats. Depending on the diamonds, XRD, Raman scattering (RS) and infrared (IR) absorption techniques can be coupled. Finally, **Fig. 4c)** shows a Boehler-Almax screw-driven DAC with a large aperture (up to 85º), required for HP-XRD measurements with large 2θ ranges.

The DAC and other cells, such as large volume and piston-cylinder cells, are used to generate static pressures. In **Fig. 5** we can observe the ranges of pressure and temperature covered by these static pressure devices. Dynamic pressures are generated by shock waves (via explosives, a gun or pulsed lasers) and are employed to chance not only pressure, but also temperature, density and particle velocity, in a very short time period. Under such conditions, dynamic material properties can be evaluated: stress-strain, elastic constants, and dynamic fracture, amid others.[149, 150]

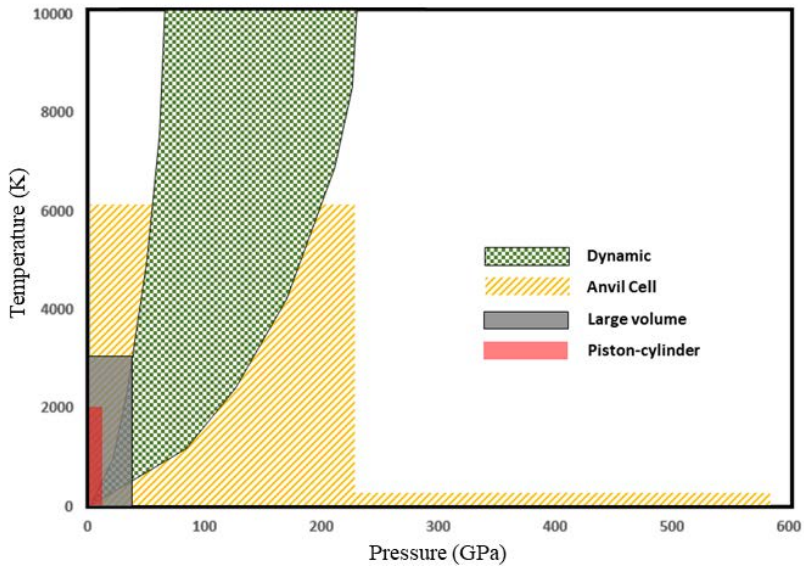

Figure 5. Types of DACs commonly used in HP experiments. Photons taken in high-pressure lab of ALBA synchrotron. Personal compilation.

Numerous intriguing materials have been discovered thanks to the release of new HP devices. This is possible because HP leads to structural changes in bond lengths and bond angles. In this way, changes in coordination number, electron density, cationic and anionic radius, bond breaking/formation and bond strength can be induced, which may also result in the occurrence of PTs. Relevant findings in HP field can be enumerated almost indefinitely. For the sake of brevity, **Table 4** gathers the main

findings, which serve as a brief overview of what HP can offer us, as an exploitable landscape to seek materials with tailored and novel properties.

Table 4. Relevant findings in HP field.

Topic	Description	Ref.
Chemical bonding	Stabilization under HP of a new chemical bonding, known as metavalent bonding, recently proposed at RC.	159-163
Low-Z compounds	Exploration of water phase diagram, up to 15 polymorphs.	164
	Discovering of superionic water ice phase by laser-driven shock waves between 100-400 GPa and 1700-2700 ºC.	165
	Single-bonded cubic form of nitrogen, above 100 GPa and 1700 ºC using a laser-heated diamond cell.	166
	Metallization of H_2 above 400 GPa and -190 ºC	167, 168
Electrides	Synthesis of electride phase of Na at about 200 GPa.	169
	Synthesis of electride phase of Li at about 80 GPa	170
Noble gas compounds	Synthesis of $Xe(N_2)_2$-I and II-phases at HP and HT.	171
	Syntheis of NiAr at 140 GPa assisted by laser heating.	172
	Synthesis of As_4O_6:2He at HP, above 3 GPa.	173
Superconductivity	Superconductivity in H_3S at 155 GPa and -70 ºC	174
	Superconductivity in H_3S at 182 GPa and -10 ºC	175
Super hard materials	Synthesis of the hardest and strongest amorphous material, which can scratch diamond, at 25 GPa and 1200 ºC.	176
Unexpected stoichiometries	Stabilization of $NaCl_3$ and Na_3Cl stoichiometries at 60 GPa.	177
2D materials	Discovering of van der Waals $(PH_3)_2H_2$ compound at 1.2 GPa and 1000 K.	178

3. EXPERIMENTAL METHODS

In this section, I will present the experimental techniques coupled to the DACs that are mainly employed in this thesis: XRD and RS. As other techniques used at extreme conditions, both have extensively probed their relevant performance to follow *in-situ* the structural and vibrational changes induced at HP, respectively. After that, I will show more details about the methodology followed to use DACs.

3.1. Diamond anvil cell (DAC)

The use of DACs requires a specific methodology, which can vary depending on the experimental technique. A schematic view of a DAC is depicted in **Fig. 6** (taken from **Ref. 179**).

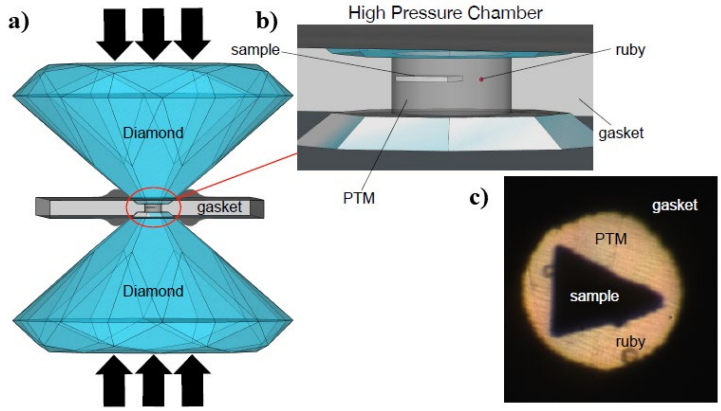

Figure 6. a) Design of the DAC. A gasket with a perforated hole is squeezed between the two diamonds. b) View of the chamber containing the sample, the pressure transmitting medium (PTM) and the pressure sensor (usually ruby and a metal, like copper, were used for HP-RS and HP-XRD measurements, respectively). c) Example of a loaded DAC. Figure taken from **Ref. 179**.

To keep hydrostatic pressure, a centered hole is made in the gasket, which acts as a chamber, typically with 40-30 μm and 100 μm of pre-indentation thickness and diameter, respectively, for a 300 μm of diamond culet. Once the gasket is perforated, it is placed in the bottom diamond and loaded with the sample, the PTM and the pressure sensor. Depending on the technique, the pressure sensor can be different. After that, the piston with the upper diamond is closed with a screwed tap. Pistons with membranes (membrane-type DACs, showed in **Fig. 4a)** and 4**b)**) allows the DAC to be pressed via filling it with He. For further information regarding the parameters to be considered for preparing gaskets and DACs, the reader is referred to **Ref. 180**.

3.2. Raman spectroscopy (RS)

RS is an optical technique that exploits the inelastic scattering of light by matter that is perturbed by radiation. In this technique, an incident light ray of monochromatic frequency υ_o encounters matter, scattering the incident light. The major of this scattered light propagates at the same frequency of the incident light, υ_o, named Mie or Rayleigh scattering. In contrast, what is known as Raman scattering is inelastically emitted and is at least 6 orders of magnitude weaker than elastic scattering. There are two types of inelastic light scattering: scattering of optical phonons (RS) and scattering of acoustic phonons (Brillouin scattering). In both cases, scattered light can be observed with downshifted ($\upsilon_s=\upsilon_o-\upsilon_{vib}$) and upshifted ($\upsilon_s=\upsilon_o+\upsilon_{vib}$) frequencies, where υ_{vib} corresponds to the frequency of the materials phonon or vibration. The downshifted value is named as Stokes scattering and the upshifted value as anti-Stokes scattering. **Fig. 7** shows the characteristic types of scattering mentioned.

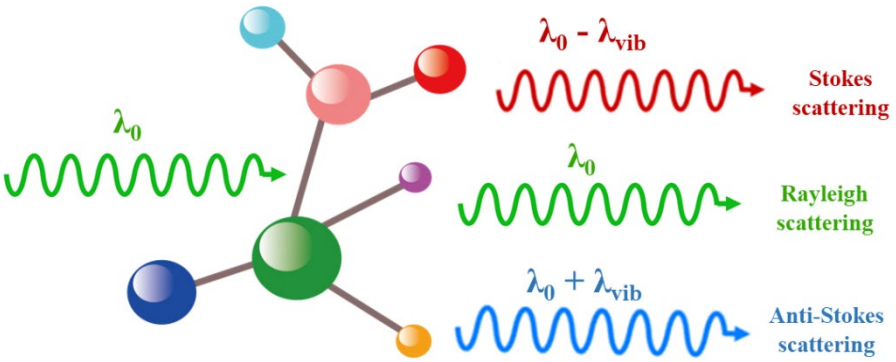

Figure 7. Incident and scattered lights in RS process. Personal compilation.

What we observe by means of RS corresponds to the transitions between vibrational levels. Let's look to **Fig. 8**. Before being irradiated, the electron in the sample is in the electronic ground state (S_0). After being irradiated, the photon is absorbed and can promote the electron to a real (S_1) state (resonant RS) or virtual excited state (non-resonant RS). Each energy state is divided in several vibrational states. Now, let's assume that after being irradiated the electron promotes to a virtual state (between S_0 and S_1 for a short time), as a result from the distortion of the electron cloud around the nuclei. After that, the electron can relax back to the ground state by emitting a photon (scattered light that is measured in RS). This scattered light can be downshifted in frequency, giving rise to Stokes scattering, if the electron that comes back to the ground state has a higher vibrational energy than before being irradiated (**Fig. 8a)**). By contrast, the scattered light can be upshifted in frequency, anti-Stokes scattering, if the electron that comes back to the ground state has a smaller vibrational energy than before being irradiated (**Fig. 8b)**). Unlike both inelastic scattering, in Rayleigh scattering the electron relaxes to the ground state, at the same vibrational state as was before, after promoting to the virtual state (**Fig. 8c)**).

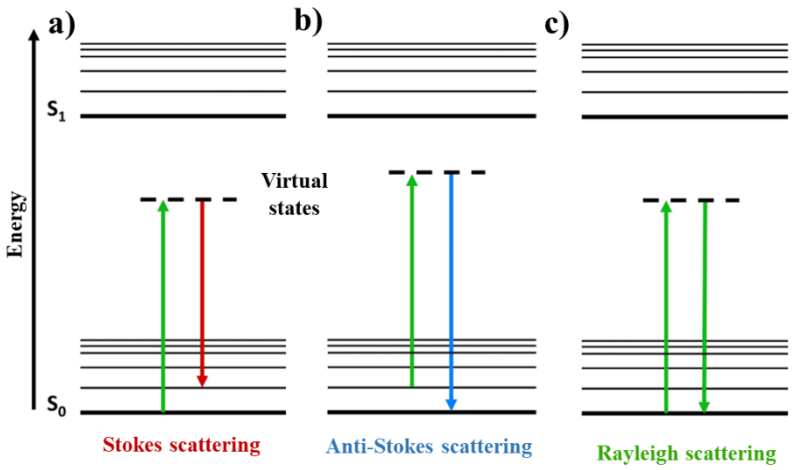

Figure 8. Electronic (S_0 and S_1) energy levels and their corresponding vibrational energy levels involved in a) Stokes, b) anti-Stokes and c) Rayleigh scattering. Personal compilation.

With inelastic scattering we can determine in solids the energy of the mechanical waves, which propagate along the lattice. In quantum mechanics, these waves are referred as phonons. They are responsible for many phenomena as the speed of sound, heat transfer within solids, anharmonicity, thermodynamic properties, electron-phonon coupling, and for exotic properties as superconductivity. Within periodic solids, phonons not only have energy (or equivalently frequency or wavenumber) but also have momentum, given by the wavevector (q) which depends on its location in the Brillouin zone (BZ). Therefore, all the combinations of energy levels and momenta give rise to the phonon dispersion curves in solids. Considering N atoms per primitive cell, 3N branches depending on q are defined in the first BZ. Three of them are acoustical, with $\omega=0$ at the zone center ($k=0$), one of them longitudinal (vibration and displacement of the atoms in the same direction) and two transverse (vibration and displacement of the atoms in perpendicular directions). The rest of the 3N-3 branches are optical, with nonzero frequencies throughout the BZ, discerning again between longitudinal and transverse branches.

As an example, phonon dispersion curves of Si is shown in **Fig. 9**.[181] Because in RS the wavevector of incident, k_o, and scattered light, k_s, are in opposite direction with equal module, optical phonons measured with RS are limited to the zone center (Γ point) of the BZ. For the case of Si, only one optical phonon at the Γ point above 15 THz (more precisely at 520 cm^{-1}) can be measured via RS (see **Fig. 9**). Acoustic phonons at the Γ point have zero frequency. Far from the Γ point, acoustic phonons do not have nonzero frequencies anymore and become nondegenerate, splitting in longitudinal and transverse branches (TA and LA modes) that can be measured by Brillouin spectroscopy. In the same way, the optical phonons split in longitudinal and transverse branches (TO and LO modes). To explore the rest of the phonon dispersion curves, inelastic neutron scattering (INS) or inelastic X-ray scattering (IXS)

techniques are required, where k_o and k_s have considerable different directions or modules. Further information about RS can be found elsewhere.[181-184]

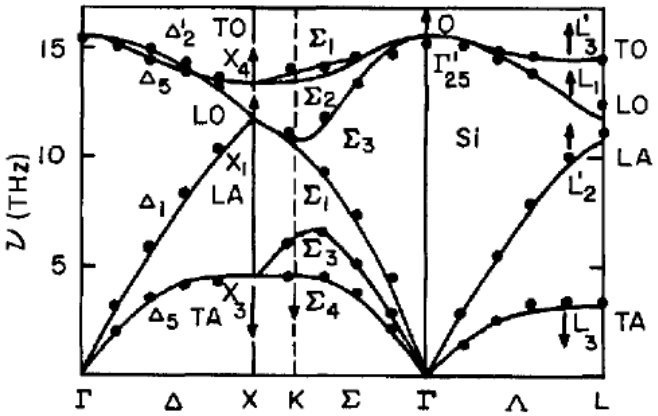

Figure 9. Phonon dispersion for Si at RC. Black circles refer to experimental measurements from neutron scattering. Black lines show a fitted model. Arrows show the frequency shift as a function of pressure. Figure taken from **Ref. 181**.

The effects of pressure in phonons and the details of HP-RS measurements can be found in **Ref. 185**. They can be exemplified with the phonon dispersion curves of Si. The frequency phonons upshift (downshift) as pressure increases because of the shortening (lengthening) of the bond lengths. Both cases can be observed at any high symmetry point throughout the BZ. Frequency upshift of phonons are the most common feature,[186] while frequency downshift reflects incipient PTs to other crystal system.[187] It can be said that RS offers a fingerprint of the phase under study, where not only vibrational properties are present, but also structural and chemical properties are involved.

The major of unpolarized RC-RS and HP-RS measurements have been performed at the Universitat Politècnica de València (UPV). The experimental setup employed is depicted in **Fig. 10**.

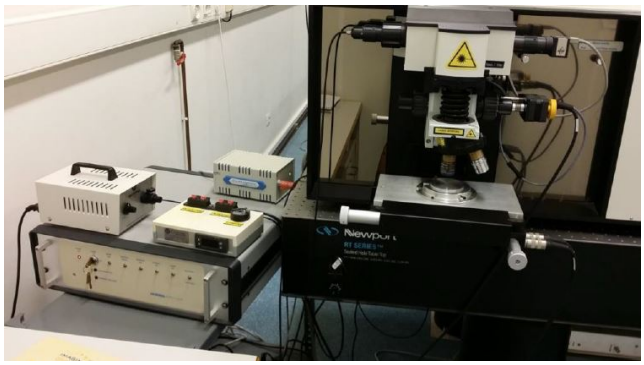

Figure 10. RS equipment used at UPV.

This equipment is composed of a 800 mm focal length LabRAM HR UV Raman microspectrometer (from HORIBA JobinYvon company) that has a coupled Olympus BX41 confocal microscope to focus the light onto the sample, located inside the chamber, through the diamonds, and collect the scattered light in backscattering geometry. The system has two thermoelectrically-cooled multichannel CCD detectors (a normal and a EM-CCD) allowing a resolution better than 2 cm^{-1}. To get a good signal-to-noise ratio in RS measurements, a high intensity, highly monochromatic light source is required, as gas lasers and current solid-state lasers offer. The system has several coupled lasers with five laser lines: i) a gas He:Ne laser (632.8 nm); ii) a gas He:Cd laser (325.0 and 442.0 nm); and iii) two solid-state lasers (532.1 nm and 785.0 nm). Edge filters and ULF filters (632.8 nm) are used to block the laser line by adjusting the angle between the filter and the laser, allowing RS spectra (usually Raman Stokes) above 10 to 30 cm^{-1}. Frequencies, intensities, and linewidths of Raman phonons are obtained by fitting Raman modes with Voigt profiles that have a fixed Gaussian linewidth to the experimental setup resolution (typically around 1.6 cm^{-1}).[188, 189] Ruby fluorescence scale is typically used to determine the pressure inside the chamber.[190]

3.3. X-ray diffraction (XRD)

XRD is a technique based on the constructive and destructive interference between the X-ray waves scattered by the atomic lattice planes in matter. Let's look to **Fig. 11** (figure taken from **Ref. 191**). The incident X-ray beam is elastically scattered for the different *hkl* planes, which could be seen as mirrors. While the waves of the incident beam are emitted in phase, those from the diffracted beam interact between them, yielding constructive or destructive interference. Whether it is constructive or destructive will depend on the angle (θ) of the incident X-rays. In real space, Bragg's law corresponds to $2d_{hkl}\sin(\theta) = n\lambda$, which stablishes θ, the Bragg angle, that yields a constructive interference at a given wavelength (λ) of the incident X-ray beam for an interplanar space between a set of *hkl* planes (d_{hkl}) and an integer (n). Interference will be observed if the dimensions of λ and d_{hkl} are comparable.

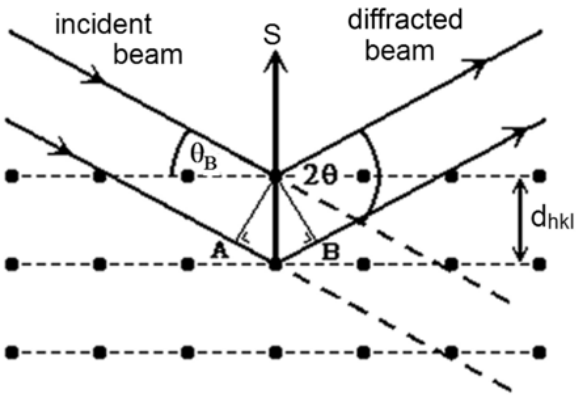

Figure 11. Bragg's law in real space. Figure taken from **Ref. 191**.

Another way to see the X-ray diffraction phenomenon can be seen in the reciprocal space via Ewald's sphere (**Figure 12**).

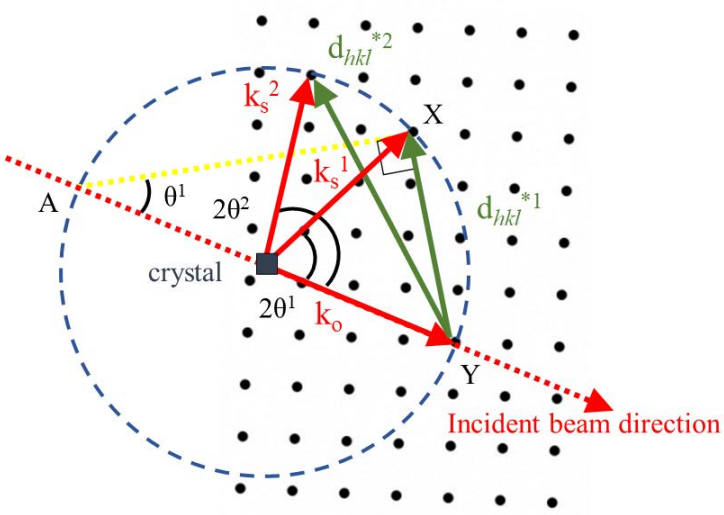

Figure 12. Ewald sphere in reciprocal space. Personal compilation.

Let's consider the wavevectors of the incident and diffracted beams, k_o and k_s. Since the diffracted beams are scattered elastically, $|k_o| = |k_s| = 1/\lambda$, thus incident and diffracted beams form a sphere, the Ewald's sphere. Centered in the crystal position, diffraction occurs in those points where the Ewald's sphere touches a point of the reciprocal lattice. By definition, each d_{hkl}^* vector has as module $1/d_{hkl}$, from the relation between reciprocal and real spaces. Geometry stablishes that, if we take the triangle delimited by the points A, X, and Y, $\sin(\theta^1) = (1/d_{hkl})(2/\lambda)$. Rearranged, the Bragg's law is recovered. With this construction it is easy to find at which 2θ refracted beams are located (in our Ewald's sphere in **Fig. 12**, two diffracted beams are found at $2\theta^1$ and $2\theta^2$ angles). To access to more points in the reciprocal lattice, crystal orientation or λ should be modified.

The Ewald's sphere, as is shown in **Fig. 12**, assumes a perfect crystal. This view totally changes with powder samples. In such situation, an ideal powder should contain crystallites in all possible orientations. Each set of *hkl* planes will give rise to a cone of diffraction, a Debye ring (**Fig. 13a)**, taken from **Ref. 192**). In this way, many Debye rings for each set of *hkl* planes in the reciprocal space ((**Figure 13b)**, taken from **Ref. 193**) are observed, instead of points. At this point, we will be referring to powder X-ray diffraction (PXRD), because it is the diffraction technique used in this thesis. Further information about PXRD can be found elsewhere.[192, 194-196]

X-rays can be generated by two methods. The most common way to generate X-rays is done in laboratory diffractometers, by ionization of inner shell electrons of certain metals, followed by their relaxation from upper shells, releasing X-rays of specific wavelengths. On the other hand, the method used for HP-XRD experiments, carried

out in synchrotrons, is that X-rays are obtained from the Bremsstrahlung radiation of accelerated electrons travelling at relativistic velocities in storage rings.

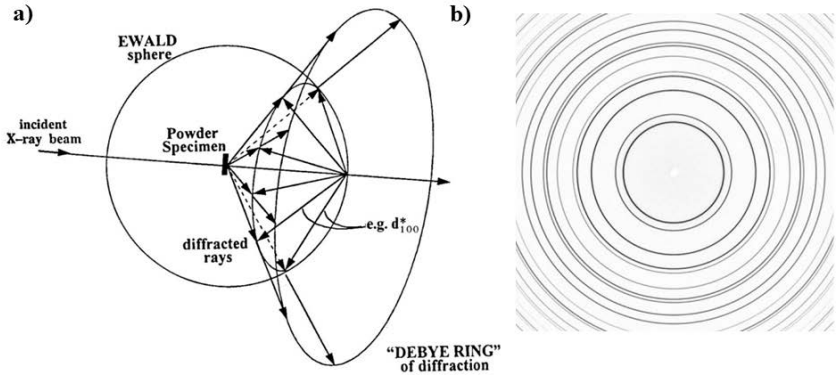

Figure 13. a) Scheme of a Debye ring from a powder sample. b) Diffraction image of CeO_2 standard powder measured at APS 11-ID-C. Figures taken from **Ref. 192** and **193**, respectively.

DACs employed in HP-XRD measurements are of the same kind as those used in optical measurements at HP, but the high absorption of diamond below 10 keV constraints HP-XRD to energies not typically available in laboratory diffractometers but easily obtained in synchrotron facilities. This can be tailored by the reduction of diamond thickness, as is exemplified in **Fig. 14**, taken from **Ref. 197**. The smaller is the diamond thickness, the lesser is the X-ray absorption.

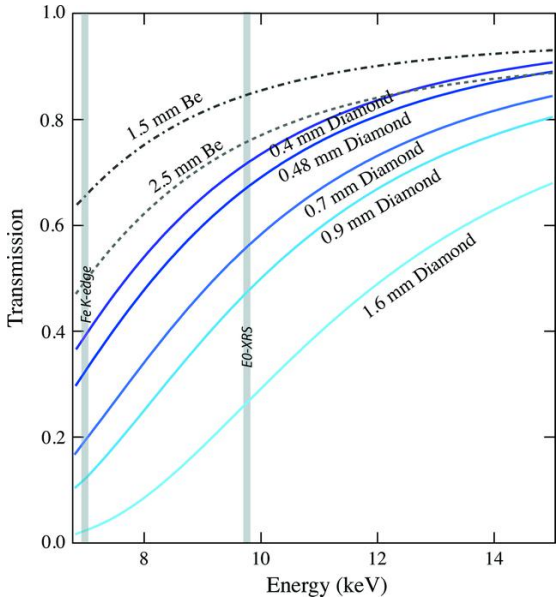

Figure 14. Comparative of X-ray transmission simulated for several diamond and Be thickness at different X-ray energies. Figure taken from **Ref. 197**.

The unique features that synchrotron radiation (SR) offers are: a high intensity, a highly narrow collimation, a continuous and very broad spectral range (from IR up to hard X-ray radiation), a high degree of polarization, a high brightness (large flux within a small solid angle), a pulse time structure and a high beam stability. Extensive information about the bounties of SR can be found in many updated books.[198-201]

All the HP-XRD measurements of this thesis were carried out in ALBA Synchrotron (schematic view in **Fig. 15**, taken from ALBA Synchrotron website[202]). As other synchrotrons spread worldwide, ALBA Synchrotron has an electron gun (1) of tungsten impregnated of BaO that is heated to produce electrons a high energy (90000 eV). These electrons are accelerated in the linear accelerator, LINAC, (2), reaching energies up to 100 MeV. Then, they are transferred to the Booster synchrotron, where again are accelerated up to 3.0 GeV (3), reaching the 99.9999985% of the speed of light. Finally, these accelerated electrons pass to the storage ring (4). Thanks to the sequence of basic cells, based on two bending magnets and quadrupoles, their speed and energy is maintained. More details concerning the abovementioned accelerators can be consulted in the ALBA Synchrotron website.[203]

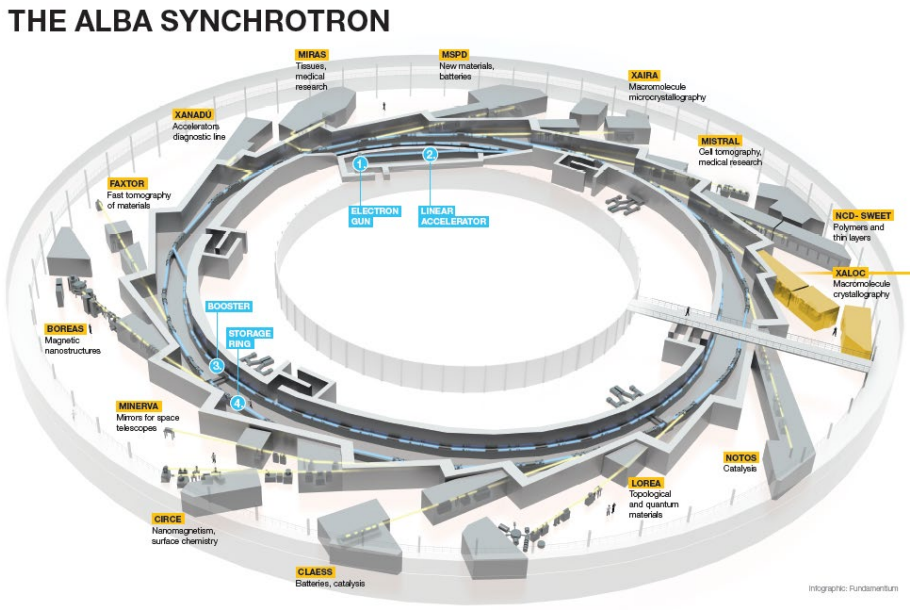

Figure 15. Schematic view of ALBA Synchrotron. Figure taken from ALBA Synchrotron website.[202]

When the trajectory of these relativistic electrons is bent, SR is emitted and conducted to the different beamlines via insertion devices (undulators or wigglers) and then modulated in their respective optical hutchs with a double crystal monochromator. In each beamline, SR is tailored according to the requirements of the experiments to be carried out. In total, we can find in ALBA synchrotron (**Fig. 15**) up to 14 beamlines,

10 operating and 4 in the construction stages. In particular, the HP-XRD measurements are accomplished at the HP endstation, located in the experimental hutch of the BL04 MSPD beamline (**Fig. 16**).

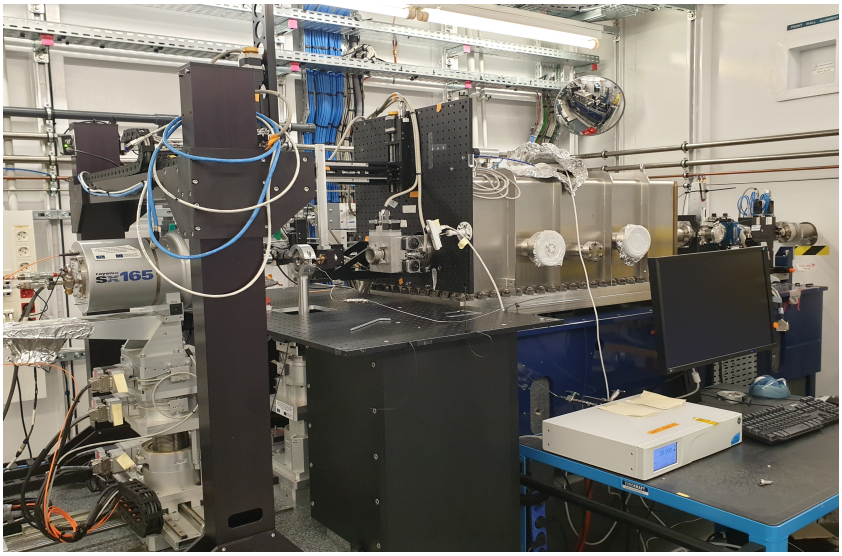

Figure 16. View of HP endstation of the experimental hutch in the BL04 MSPD beamline of ALBA Synchrotron.

A more detailed view is depicted in **Figure 17**. Two beryllium windows (**Fig. 17a)**) act as a barrier, separating the optical instruments of the optical hutch (under ultra-high vacuum) from the ambient pressure. In this part, beryllium windows are employed to protect the optical instruments of the optical hutch from the room light of the experimental hutch. The X-ray beam for MSPD beamline can be modulated from 8 to 50 keV. To adapt this energy, a few stripes are used. Considering the uncoated Si substrate, other two stripes of Rh and Pt are placed, which work as energy cut off at about 15 keV, 33 keV, and 41 keV, respectively. The fast shutter is open and closed to allow the beam to pass and slits define its size and remove spurious beam scattered from the optical instruments. After this section, Kirkpatrick-Baez (KB) mirrors (**Fig. 17b)**) are placed, which focus the beam down to a dozen micron spot (20 x 20 μm^2). KB mirrors are optimized for 30 keV, but ensure a small spot in the 20-50 keV energy range. The smaller the X-ray spots, the higher the pressures that can be monitored inside DACs.

Figure 17c) shows the DAC environment. Between the DAC and the KB mirrors, a collimator with a pin-hole that cleans the beam from spurious scattering is placed. The sample tower (**Fig. 15d)**), based on rotation/tilt/translation stages, allows alignment of very small samples (< 50 μm), determine the rotation axis, and place the sample along the beam. The determination of the rotation axis of the sample is crucial because the measurements are performed while rotating the DAC between 5-30º, to ensure good statistics. A CCD X-ray detector, SX165 (Rayonix), is employed to collect the Debye diffraction ring patterns.

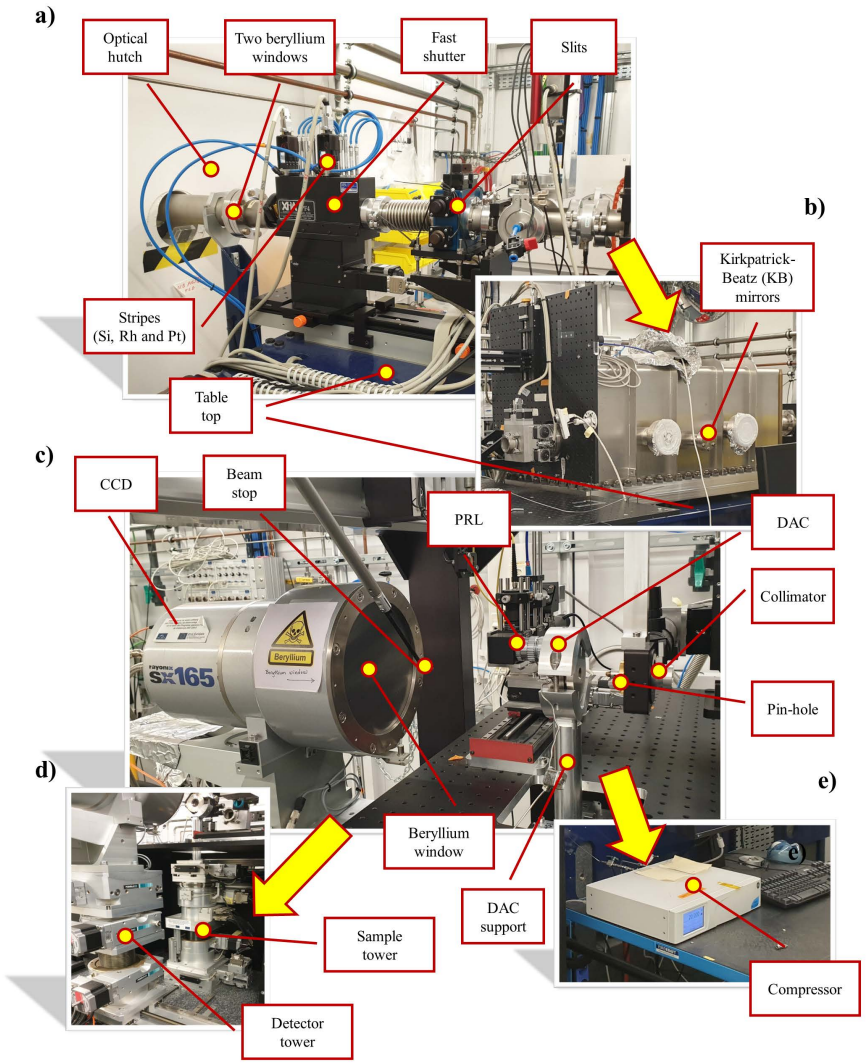

Figure 17. Detailed view of HP endstation of the experimental hutch in the BL04 MSPD beamline, in ALBA Synchrotron. Main components are marked.

As the DAC support, a detector tower allows to move and rotate the CCD (**Fig. 17d)**). To prevent damage on the CCD, a beam stop is located after the DAC. The CCD has a beryllium window to protect it from the room light and the scattered beam. For HP-XRD, we can employ several pressure gauges: i) the equation of state (EoS) of metal powders, such as Cu or Au; or ii) the luminescence of rubies, as in RS measurements. For the last method, a PRL (pressure ruby by luminescence) spectrometer can be focused on the chamber (**Fig. 15c)**). Finally, to increase/decrease the pressure in the DAC, a compressor with He (**Fig. 17e)**) is

connected through a capillary to fill the membrane. Further information about the MSPD beamline are gathered in **Ref. 204** and from ALBA Synchrotron website.[205]

4. COMPUTATIONAL SIMULATIONS

Any work devoted to HP field is usually supported by computation simulations. This support not only reinforce the experimental results, but also allow us to simulate the pressure behavior of any compound at very HP (sometimes unattainable for technical reasons), study compounds whose synthesis at RC is not easy, to evaluate certain properties under HP which cannot be studied experimentally, or to predict PTs induced by HP. On the other hand, these computational simulations are performed under certain approximations to tackle with many-body interacting systems. Even with these approximations, computational simulations based on quantum mechanics have become a trustworthy for their results very close to experimental ones.

Such calculations involve three steps: a mathematical model for the interaction between nuclei and electrons in our material, an algorithm to resolve the equations concerning to this model, and a collection of tools to analyze the outputs obtained. In quantum mechanics, the time-independent Schrödinger equation stablishes the relation between the Hamiltonian (H), the wave function (Ψ), which describes the state of system, and its energy (E). This complex equation can be solved given only the nuclei position and the electron number without any experimental input. These methods are well-known as *ab initio* (or first principles) methods. In this way, we can minimize the energy and forces on the atoms inside our system by optimizing the nuclei position and lattice parameters, allowing us not only to optimize the geometry, but also to evaluate energy-depending properties such as EoS, phonon spectra, chemical properties, etc.

Within the *ab initio* methods, density functional theory (DFT) has gained popularity because of its balance between computational cost and accuracy. This method employs the Kohn-Sham equation, which simplifies calculations, from interacting to non-interacting electrons. In return, the unknown exchange-correlation energy must be approximated. DFT allows properties of any system to be determine by using functionals of the electron density (n). Further explanations about DFT basis and its use in HP filed can be found in **Ref. 206**.

Since every simulation compel many specific parameters for each system studied in this thesis, these parameters will be properly described in each section of **Chapter 2**. The main simulations have been performed by Alfonso Muñoz González and Plácida Rodríguez Hernández.

5. OBJETIVES

The aim of this thesis is to study the pressure behavior of vibrational and structural properties, with the help of computational simulations, of Ga_2S_3, In_2S_3 and In_2Se_3, as was mentioned in the section **1.1**. The results from these studies have been published in indexed journals, whose author's versions are included in this thesis, as sections of **Chapter 2**. More specially:

i. Section **2.1**: Vilaplana, R., et al., "***Experimental and theoretical studies on α-In2Se3 at high pressure***. Inorganic chemistry, 2018. 57(14): p. 8241-8252. Citations: 35. Before its publication, I conducted my Final Master Project based on the results of this study, with the name *Vibrational and structural characterization of In_2Se_3 and its applications* (UPV, Alcoy campus, Spain. July 24, 2017). For this work, I was awarded with the best Final Master Project in the academic year 2016-2017, by the company Flejes Industriales SA. (UPV, Campus Alcoy, Spain. June 29, 2018). The results were presented in the 55th European High Pressure Research Group International Meeting (55th EHPRG, Poznan, Poland. September 3–8, 2017), names *Vibrational study of In_2Se_3 under high pressure* (Poster).

ii. Section **2.2**: Gallego-Parra, S., et al., ***Structural, vibrational and electronic properties of α'-Ga_2S_3 under compression***. Physical Chemistry Chemical Physics, 2021. 23(11): p. 6841-6862. Citations: 5. The results were presented in the 56th EHPRG (Aveiro, Portugal. September 2–7, 2018), names *High-pressure Raman study of ordered-vacancy Ga_2S_3* (Poster) and the Conference on Science at Extreme Conditions (CSEC. Edinburg, United Kingdom. July 25-30, 2021), names *Structural, vibrational and electronic properties of α'-Ga_2S_3 under compression* (Online oral presentation).

iii. Section **2.3**: Gallego-Parra, S., et al., ***Pressure-induced order–disorder transitions in β-In_2S_3: an experimental and theoretical study of structural and vibrational properties***. Physical Chemistry Chemical Physics, 2021. 23(41): p. 23625-23642. Citations: 1. As was extremely well received on the part of the readers of the journal, the editors select this article to be part of the 2021 PCCP HOT articles. The results were presented in the 57th EHPRG (Prague, Czech Republic. September 1–6, 2019), names *Experimental and theoretical analyses of β-In_2S_3 under compression* (Poster), the Higher European Research Course for Users of Large Experimental Systems (HERCULES, Grenoble, France. March 2-April 3, 2020), names *Study of high-pressure structural behaviour of the β-In_2S_3* (Poster), the European Materials Research Society Fall Meeting (EMRS. Strasbourg, France. September 20-23, 2021), names *Pressure-induced order-disorder transitions in β-In_2S_3: and experimental and theoretical study of structural and vibrational properties* (Online oral presentation), and 56th Course: Crystallography under extreme conditions (Erice, Italy. June 3-11, 2022), names *Pressure-induced order–disorder transitions in β-In_2S_3: an experimental and theoretical study of structural and vibrational properties* (Poster). For this last contribution, I was awarded a poster prize with the best scientific content.

iv. Section **2.4**: Gallego-Parra, S., et al., **High-Pressure Synthesis of β- and α-In2Se3-Like Structures in Ga_2S_3**. Citations: 0. Chemistry of Materials, 2022. 34(13): p. 6068-6086. The results were presented in the 29th Condense Matter Division (29th CMD. Manchester, United Kingdom. August 21-26. 2022), names *High-Pressure Synthesis of β- and α-In_2Se_3-Like Structures in Ga_2S_3* (Oral presentation), the X AUSE Conference and V ALBA User's Meeting (Cerdaynola del Vallés, Spain. September 5-8. 2022), names *High pressure structural and vibrational studies of β- and α-In_2Se_3-like Ga_2S_3* (Oral presentation), and 59th EHPRG (Uppsala, Sweden. September 5-8. 2022), names *Synthesis of van der Waals Ga_2S_3 structures under high pressure* (Online oral presentation).

After the different published works are presented in **Chapter 2**, I will discuss the main results obtained in each of them in **Chapter 3**, in individually sections. Then, I will summarize the main remarks of these works in **Chapter 4**, considering possible future studies to further investigate the pressure behaviour of these sesquichalcogenides B_2X_3 under extreme conditions.

6. BIBLIOGRAPHY

1. H. Ehrenreich, F. Seitz and D. Turnbull, *Solid State Physics*, Elsevier Science, 1982.
2. E. Parthé, *Crystal Chemistry of Tetrahedral Structures*, Gordon and Breach, 1964.
3. C.-Y. Lu, J. A. Adams, Q. Yu, T. Ohta, M. A. Olmstead and F. S. Ohuchi, *Phys. Rev. B*, 2008, **78**, 075321.
4. H. Senoh, T. Takeuchi, H. Kageyama, H. Sakaebe, M. Yao, K. Nakanishi, T. Ohta, T. Sakai and K. Yasuda, *J. Power Sources*, 2010, **195**, 8327-8330.
5. X. Meng, Y. Cao, J. A. Libera and J. W. Elam, *Chem. Mater.*, 2017, **29**, 9043-9052.
6. W. Chu, X. Zhang, J. Wang, S. Zhao, S. Liu and H. Yu, *Energy Storage Mater.*, 2019, **22**, 418-423.
7. S. Lysgaard and J. M. a. García Lastra, *J. Phys. Chem. C*, 2021, **125**, 16444-16450.
8. J. Tu, W.-L. Song, H. Lei, Z. Yu, L.-L. Chen, M. Wang and S. Jiao, *Chem. Rev.*, 2021, **121**, 4903-4961.
9. G. A. Elia, K. V. Kravchyk, M. V. Kovalenko, J. Chacón, A. Holland and R. G. Wills, *J. Power Sources*, 2021, **481**, 228870.
10. G. Cohn, L. Ma and L. A. Archer, *J. Power Sources*, 2015, **283**, 416-422.
11. T. Gao, X. Li, X. Wang, J. Hu, F. Han, X. Fan, L. Suo, A. J. Pearse, S. B. Lee and G. W. Rubloff, *Angew. Chem.*, 2016, **128**, 10052-10055.
12. J. Adams, A. Bostwick, T. Ohta, F. S. Ohuchi and M. A. Olmstead, *Phys. Rev. B*, 2005, **71**, 195308.
13. O. Balitskii, P. Y. Demchenko, E. Mijowska and K. Cendrowski, *Mater. Res. Bull.*, 2013, **48**, 916-919.
14. K. Ren, F. Rao, Z. Song, S. Lv, Y. Cheng, L. Wu, C. Peng, X. Zhou, M. Xia and B. Liu, *Appl. Phys. Lett.*, 2012, **100**, 052105.
15. C. Shi, B. Yang, B. Hu, Y. Du and S. Yao, *J. Phase Equilib. Diffus.*, 2019, **40**, 392-402.
16. P. Donohue, *J. Solid State Chem.*, 1970, **2**, 6-8.
17. K.-J. Range and H.-J. Hübner, *Z. Naturforsch., B*, 1973, **28**, 353-355.
18. H. Okamoto, *J. Phase Equilib. Diffus.*, 2000, **21**, 106-107.
19. J. Flahaut, Contribution à l'étude du sulfure d'aluminium et des thioaluminates, University of Mason, 1952.
20. A. Schneider and G. Gattow, *Z. anorg. allg. Chem.*, 1954, **277**, 49-59.
21. R. Kniep and P. Blees, *Z. Naturforsch., B*, 1988, **43**, 182-188.
22. S. Shao, W. Zhu, J. Lv, Y. Wang, Y. Chen and Y. Ma, *npj Comput. Mater.*, 2020, **6**, 1-6.
23. B. Krebs, A. Schiemann and M. Läge, *Z. anorg. allg. Chem.*, 1993, **619**, 983-988.
24. B. Eisenmann, *Z. Kristallogr. Cryst. Mater.*, 1992, **198**, 307-308.
25. J. Flahaut, *C. R. Hebd. Seances Acad. Sci.*, 1951, **232**, 334-336.
26. G. Steigmann and J. Goodyear, *Acta Crystallogr.*, 1966, **20**, 617-619.
27. O. Conrad, A. Schiemann and B. Krebs, *Z. anorg. allg. Chem.*, 1997, **623**, 1006-1010.

28. M.-J. Zhang, X.-M. Jiang, L.-J. Zhou and G.-C. Guo, *J. Mater. Chem. C*, 2013, **1**, 4754-4760.
29. Z. Huang, J.-G. Huang, K. Kokh, V. Svetlichnyi, A. Shabalina, Y. M. Andreev and G. Lanskii, *Ga_2S_3: Optical properties and perspectives for THz applications*,in *2015 40th International Conference on Infrared, Millimeter, and Terahertz waves (IRMMW-THz)*, 2015.
30. C.-H. Ho, M.-H. Lin, Y.-P. Wang and Y.-S. Huang, *Sens. Actuators, A*, 2016, **245**, 119-126.
31. K. Park, D. Kim, T. T. Debela, M. Boujnah, G. M. Zewdie, J. Seo, I. S. Kwon, I. H. Kwak, M. Jung and J. J. N. A. Park, *Nanoscale Adv.*, 2022.
32. M. M. Alsaif, N. Pillai, S. Kuriakose, S. Walia, A. Jannat, K. Xu, T. Alkathiri, M. Mohiuddin, T. Daeneke and K. Kalantar-Zadeh, *ACS Appl. Nano Mater.*, 2019, **2**, 4665-4672.
33. C.-H. Ho, X.-R. Lai, C.-A. Chuang, W.-L. Kuo and K.-K. Tiong, *Adv. Photonics Res.*, 2021, **2**, 2000110.
34. Z. M. Hu, G. T. Fei and L. De Zhang, *Mater. Lett.*, 2019, **239**, 17-20.
35. P. Wang, M. Liu, F. Mo, Z. Long, F. Fang, D. Sun, Y.-N. Zhou and Y. Song, *Nanoscale*, 2019.
36. L. Wang and C. Tu, *Nanotechnol.*, 2020, **31**, 165603.
37. K. Xu, B. Y. Zhang, Y. Hu, M. W. Khan, R. Ou, Q. Ma, C. Shangguan, B. J. Murdoch, W. Chen and X. Wen, *J. Mater. Chem. C*, 2021, **9**, 3115-3121.
38. C. Jones, J. Bryan, K. Kirschbaum and J. Edwards, *Z. fur Krist. - New Cryst. Struct.*, 2001, **216**, 349-350.
39. J. Goodyear and G. Steigmann, *Acta Crystallogr.*, 1963, **16**, 946-949.
40. A. Tomas, M. Guymont, M. Pardo, M. Guittard and J. Flahaut, *phys. status solidi (a)*, 1988, **107**, 775-784.
41. M. Pardo, M. Guittard, A. Chilouet and A. Tomas, *J. Solid State Chem.*, 1993, **102**, 423-433.
42. G. Collin, J. Flahaut, M. Guittard and A.-M. Loireau-Lozach, *Mater. Res. Bull.*, 1976, **11**, 285-292.
43. M. Pardo, A. Tomas and M. Guittard, *Mater. Res. Bull.*, 1987, **22**, 1677-1684.
44. H. Hahn and W. Klingler, *Z. anorg. Chem.*, 1949, **259**, 135-142.
45. M. Guymont, A. Tomas, M. Pardo and M. Guittard, *phys. status solidi (a)*, 1989, **113**, K5-K7.
46. D. Lübbers and V. Leute, *J. Solid State Chem.*, 1982, **43**, 339-345.
47. T. Nakayama and M. Ishikawa, *J. Phys. Soc. Jpn.*, 1997, **66**, 3887-3892.
48. M. Peressi and A. Baldereschi, *J. Appl. Phys.*, 1998, **83**, 3092-3095.
49. G.-Y. Huang, N. Abdul-Jabbar and B. Wirth, *J. Phys.: Condens. Matter*, 2013, **25**, 225503.
50. A. Jain, S. P. Ong, G. Hautier, W. Chen, W. D. Richards, S. Dacek, S. Cholia, D. Gunter, D. Skinner and G. Ceder, *Apl Materials*, 2013, **1**, 011002.
51. Z. Dai and F. Ohuchi, *Appl. Phys. Lett.*, 1998, **73**, 966-968.
52. R. Ollitrault-Fichet, J. Rivet and J. Flahaut, *J. Solid State Chem.*, 1980, **33**, 49-61.
53. N. Serebryanaya, *Powder Diffr.*, 1992, **7**, 99-102.

54. M. Guymont, A. Tomas and M. Guittard, *Philos. Mag. A*, 1992, **66**, 133-139.
55. C. Chou, J. Hutchison, D. Cherns, M. J. Casanove, J. Steeds, R. Vincent, B. Lunn and D. Ashenford, *J. Appl. Phys.*, 1993, **74**, 6566-6570.
56. P. Newman and J. Cundall, *Nature*, 1963, **200**, 876-876.
57. R. Lieth, H. Heijligers and C. vd Heijden, *J. Electrochem. Soc.*, 1966, **113**, 798-801.
58. A. Zavrazhnov, S. Berezin, A. Kosykov, A. Naumov, M. Berezina and N. Brezhnev, *J. Therm. Anal. Calorim.*, 2018, 1-10.
59. Y. Zheng, X. Tang, W. Wang, L. Jin and G. Li, *Adv. Funct. Mater.*, 2021, **31**, 2008307.
60. M. Isik and N. Gasanly, *Vacuum*, 2020, **179**, 109501.
61. N. Zhou, L. Gan, R. Yang, F. Wang, L. Li, Y. Chen, D. Li and T. Zhai, *ACS Nano*, 2019, **13**, 6297-6307.
62. E. Sutter, J. S. French, A. Balgarkashi, N. Tappy, A. Fontcuberta i Morral, J. C. Idrobo and P. Sutter, *Nano Lett.*, 2019, **19**, 8903-8910.
63. E. Yitamben, T. Lovejoy, A. Pakhomov, S. Heald, E. Negusse, D. Arena, F. Ohuchi and M. Olmstead, *Phys. Rev. B*, 2011, **83**, 045203.
64. C.-S. Yoon, F. Medina, L. Martinez, T.-Y. Park, M.-S. Jin and W.-T. Kim, *Appl. Phys. Lett.*, 2003, **83**, 1947-1949.
65. C.-S. Yoon, K.-H. Park, D.-T. Kim, T.-Y. Park, M.-S. Jin, S.-K. Oh and W.-T. Kim, *J. Phys. Chem. Solids*, 2001, **62**, 1131-1137.
66. T. Lovejoy, E. Yitamben, S. Heald, F. Ohuchi and M. Olmstead, *Phys. Rev. B*, 2011, **83**, 155312.
67. T. Ohta, D. Schmidt, S. Meng, A. Klust, A. Bostwick, Q. Yu, M. A. Olmstead and F. Ohuchi, *Phys. Rev. Lett.*, 2005, **94**, 116102.
68. T. Lovejoy, E. Yitamben, T. Ohta, S. Fain Jr, F. Ohuchi and M. Olmstead, *Phys. Rev. B*, 2010, **81**, 245313.
69. N. Teraguchi, M. Konagai, F. Kato and K. Takahashi, *J. Cryst. Growth*, 1991, **115**, 798-801.
70. S. Takatani, A. Nakano, K. Ogata and T. K. T. J. J. j. o. a. p. Kikawa, *Jpn. J. Appl. Phys.*, 1992, **31**, L458.
71. R. Valeev, V. Kriventsov and N. Mezentsev, *Bull. Russ. Acad. Sci.: Phys.*, 2013, **77**, 1154-1156.
72. N. Kojima, C. Morales, Y. Ohshita and M. Yamaguchi, *Ga_2Se_3 and $(InGa)_2Se_3$ as novel buffer layers in the GaAs on Si system* in *9th Int. Conf. on Concentrator Photovoltaic Systems. AIP Conference Proceedings*, 2013.
73. T. Okamoto, N. Kojima, A. Yamada, M. Konagai, K. Takahashi, Y. Nakamura and O. Nittono, *Jpn. J. Appl. Phys.*, 1992, **31**, L143.
74. M. Afifi, A. Bekheet, H. El-Shair and I. Zedan, *Phys. B*, 2003, **325**, 308-318.
75. C.-H. Ho, *ACS Omega*, 2020, **5**, 18527-18534.
76. C.-e. Kim, K. Kurosaki, M. Ishimaru, H. Muta and S. Yamanaka, *J. Electron. Mater.*, 2011, **40**, 999-1004.
77. W. Xue, Q. Jiang, F. Wang, R. He, R. Pang, H. Yang, P. Wang, R. Yang, Z. Zhong and T. Zhai, *Small*, 2022, **18**, 2105599.
78. M. Kerkhoff and V. Leute, *J. Alloys Compd.*, 2004, **381**, 124-129.

79. J. Antonopoulos, T. Karakostas, G. Bleris and N. Economou, *J. Mater. Sci.*, 1981, **16**, 733-738.
80. D. Lee, T. Kim, J. Kim and H. Sohn, *Phys. Status Solidi*, 2020, **217**, 2000478.
81. J. Kim, J. Lee, M. Kang and H. Sohn, *Nanoscale Res. Lett.*, 2021, **16**, 1-7.
82. Y.-H. Lee, Y. Hwa and C.-M. Park, *J. Mater. Chem. A*, 2021, **9**, 20553-20564.
83. A. Kolobov, P. Fons, M. Krbal, K. Mitrofanov, J. Tominaga and T. Uruga, *Phys. Rev. B*, 2017, **95**, 054114.
84. R. Al-Orainy, A. Nagat, S. Hussein and A. Ebnalwaled, *Int. Res. J. Eng. Technol.*, 2015, **2**, 816.
85. H. Zhu, J. Yin, Y. Xia and Z. Liu, *Appl. Phys. Lett.*, 2010, **97**, 083504.
86. G.-Y. Huang, N. Abdul-Jabbar and B. Wirth, *Acta Mater.*, 2014, **71**, 349-369.
87. P. Wyżga, W. Carrillo-Cabrera, L. Akselrud, I. Veremchuk, J. Wagler, C. Hennig, A. A. Tsirlin, A. Leithe-Jasper, E. Kroke and R. Gumeniuk, *Dalton Trans.*, 2020, **49**, 15903-15913.
88. P. Wyżga, I. Veremchuk, C. Himcinschi, U. Burkhardt, W. Carrillo-Cabrera, M. Bobnar, C. Hennig, A. Leithe-Jasper, J. Kortus and R. Gumeniuk, *Dalton Trans.*, 2019, **48**, 8350-8360.
89. R. Souissi, N. Bouguila, M. Bendahan, T. Fiorido, K. Aguir, M. Kraini, C. Vázquez-Vázquez and A. Labidi, *Sens. Actuators, B*, 2020, **319**, 128280.
90. Y. C. Zhang, N. Afzal, L. Pan, X. Zhang and J. J. Zou, *Adv. Sci.*, 2019, 1900053.
91. A. Stoliaroff, N. Barreau, S. Jobic and C. Latouche, *Theor. Chem. Acc.*, 2018, **137**, 102.
92. L. A. Wägele, D. Rata, G. Gurieva and R. Scheer, *Phys. Status Solidi C*, 2017, **14**, 1600204.
93. W. Huang, L. Gan, H. Yang, N. Zhou, R. Wang, W. Wu, H. Li, Y. Ma, H. Zeng and T. Zhai, *Adv. Funct. Mater.*, 2017, **27**, 1702448.
94. Y. Liu, C. Zhai, K. Zhang, L. Du, M. Zhu and M. Zhang, *J. Magn. Magn. Mater.*, 2020, **503**, 166618.
95. Z. Li, T. Yang, Q. Zhao and M. Zhang, *Phys. Chem. Chem. Phys.*, 2017, **19**, 16758-16764.
96. Y. Liu, L. Du, K. Gu and M. Zhang, *J. Lumin.*, 2019, 116775.
97. A. Kennedy, H. Ganesan, R. Marnadu, S. K. Kannan, S. I. Arockiam, M. Ubaidullah, M. Shkir, S. AlFaify and S. Gedi, *Opt. Mater.*, 2022, **124**, 111769.
98. P. Pistor, J. M. Merino Álvarez, M. León, M. Di Michiel, S. Schorr, R. Klenk and S. Lehmann, *Acta Crystallogr., Sect. B: Struct. Sci., Cryst. Eng. Mater.*, 2016, **72**, 410-415.
99. A. Lafond, X. Rocquefelte, M. Paris, C. Guillot-Deudon and V. Jouenne, *Chem. Mater.*, 2011, **23**, 5168-5176.
100. P. Wyżga, S. Grimm, V. Garbe, E. Zuñiga-Puelles, C. Himcinschi, I. Veremchuk, A. Leithe-Jasper and R. Gumeniuk, *J. Mater. Chem. C*, 2021, **9**, 4008-4019.

101. K. Benchouk, J. Ouerfelli, M. Saadoun and A. Siyoucef, *Phys. Procedia*, 2009, **2**, 971-974.
102. R. Demir, F. Göde, E. Güneri and F. M. Emen, *J. Mol. Struct.*, 2021, **1227**, 129565.
103. Y. Sim, J. Kim and M.-J. Seong, *J. Alloys Compd.*, 2016, **685**, 518-522.
104. G. King, *Acta Crystallogr.*, 1962, **15**, 512-512.
105. G. Steigmann, H. Sutherland and J. Goodyear, *Acta Crystallogr.*, 1965, **19**, 967-971.
106. N. S. Rampersadh, A. M. Venter and D. G. Billing, *Phys. B*, 2004, **350**, E383-E385.
107. R. Diehl and R. Nitsche, *J. Cryst. Growth*, 1975, **28**, 306-310.
108. R. Diehl, C. D. Carpentier and R. Nitsche, *Acta Crystallogr., Sect. B: Struct. Crystallogr. Cryst. Chem.*, 1976, **32**, 1257-1260.
109. K. J. Range and M. Zabel, *Z. Naturforsch., B*, 1978, **33**, 463-464.
110. K. Osamura, Y. Murakami and Y. Tomiie, *J. Phys. Soc. Jpn.*, 1966, **21**, 1848-1848.
111. G. Han, Z. G. Chen, J. Drennan and J. Zou, *Small*, 2014, **10**, 2747-2765.
112. S. Popović, B. Čelustka and D. Bidjin, *phys. status solidi (a)*, 1976, **33**, K23-K24.
113. S. Popović, B. Čelustka, Ž. Ružic‐Toroš and D. Broz, *phys. status solidi (a)*, 1977, **41**, 255-262.
114. H. Lutz, M. Fischer, H.-P. Baldus and R. Blachnik, *J. Less-Common Met.*, 1988, **143**, 83-92.
115. J. L. Collins, C. Wang, A. Tadich, Y. Yin, C. Zheng, J. Hellerstedt, A. Grubisic-Cabo, S. Tang, S.-K. Mo and J. Riley, *ACS Applied Electronic Materials*, 2020, **2**, 213-219.
116. C. Xu, J. Mao, X. Guo, S. Yan, Y. Chen, T. W. Lo, C. Chen, D. Lei, X. Luo and J. Hao, *Nat. Commun.*, 2021, **12**, 1-9.
117. F. Zhang, Z. Wang, J. Dong, A. Nie, J. Xiang, W. Zhu, Z. Liu and C. Tao, *ACS nano*, 2019, **13**, 8004-8011.
118. A. Pfitzner and H. Lutz, *J. Solid State Chem.*, 1996, **124**, 305-308.
119. A. Likforman, D. Carré and R. Hillel, *Acta Crystallogr., Sect. B: Struct. Crystallogr. Cryst. Chem.*, 1978, **34**, 1-5.
120. S. Popović, A. Tonejc, B. Gržeta-Plenković, B. Čelustka and R. Trojko, *J. Appl. Crystallogr.*, 1979, **12**, 416-420.
121. J. Van Landuyt, G. Van Tendeloo and S. Amelinckx, *phys. status solidi (a)*, 1975, **30**, 299-314.
122. C. Manolikas, *J. Solid State Chem.*, 1988, **74**, 319-328.
123. R. Desai, D. Lakshminarayana, P. Patel, P. Patel and C. Panchal, *Mater. Chem.*, 2005, **94**, 308-314.
124. H. Hahn and W. Klingler, *Z. anorg. Chem.*, 1949, **260**, 97-109.
125. J. Woolley, B. Pamplin and P. Holmes, *J. Less-Common Met.*, 1959, **1**, 362-376.
126. T. Karakostas and N. Economou, *Phys. Status Solidi*, 1975, **31**, 89-99.
127. A. Kunjomana and E. Mathai, *Mater. Res. Bull.*, 1991, **26**, 1347-1353.

128. J. Ye, S. Soeda, Y. Nakamura and O. Nittono, *Jpn. J. Appl. Phys.*, 1998, **37**, 4264-4271.
129. L. Liu, J. Dong, J. Huang, A. Nie, K. Zhai, J. Xiang, B. Wang, F. Wen, C. Mu and Z. Zhao, *Chem. Mater.*, 2019, **31**, 10143-10149.
130. S. Wan, Y. Li, W. Li, X. Mao, C. Wang, C. Chen, J. Dong, A. Nie, J. Xiang and Z. Liu, *Adv. Funct. Mater.*, 2019, **29**, 1808606.
131. M. Lin, D. Wu, Y. Zhou, W. Huang, W. Jiang, W. Zheng, S. Zhao, C. Jin, Y. Guo and H. Peng, *J. Am. Chem. Soc.*, 2013, **135**, 13274-13277.
132. X. Tao and Y. Gu, *Nano Lett.*, 2013, **13**, 3501-3505.
133. Z. Xie, F. Yang, X. Xu, R. Lin and L. Chen, *Front. Chem.*, 2018, **6**, 430.
134. J. Gao, Y. Zheng, W. Yu, Y. Wang, T. Jin, X. Pan, K. P. Loh and W. Chen, *SmartMat*, 2021, **2**, 88-98.
135. J. Zhou, Q. Zeng, D. Lv, L. Sun, L. Niu, W. Fu, F. Liu, Z. Shen, C. Jin and Z. Liu, *Nano Lett.*, 2015, **15**, 6400-6405.
136. Y. Yan, Z. Zeng, M. Huang and P. Chen, *Mater. Today Adv.*, 2020, **6**, 100059.
137. C. Zheng, L. Yu, L. Zhu, J. L. Collins, D. Kim, Y. Lou, C. Xu, M. Li, Z. Wei and Y. Zhang, *Sci. Adv.*, 2018, **4**, eaar7720.
138. J. O. Island, S. I. Blanter, M. Buscema, H. S. van der Zant and A. Castellanos-Gomez, *Nano Lett.*, 2015, **15**, 7853-7858.
139. F. Xue, J. Zhang, W. Hu, W.-T. Hsu, A. Han, S.-F. Leung, J.-K. Huang, Y. Wan, S. Liu and J. Zhang, *ACS Nano*, 2018, **12**, 4976-4983.
140. Y. Zhou, D. Wu, Y. Zhu, Y. Cho, Q. He, X. Yang, K. Herrera, Z. Chu, Y. Han and M. C. Downer, *Nano Lett.*, 2017, **17**, 5508-5513.
141. H. Zhang, C.-X. Liu, X.-L. Qi, X. Dai, Z. Fang and S.-C. Zhang, *Nat. Phys.*, 2009, **5**, 438.
142. Y. Chen, J. G. Analytis, J.-H. Chu, Z. Liu, S.-K. Mo, X.-L. Qi, H. Zhang, D. Lu, X. Dai and Z. Fang, *Science*, 2009, **325**, 178-181.
143. H. Zhu, K. Chen, Z. Ge, H. Xu, Y. Su, J. Yin, Y. Xia and Z. Liu, *J. Mater. Sci.*, 2010, **45**, 3569-3574.
144. J. Yao, Z. Deng, Z. Zheng and G. Yang, *ACS Appl. Mater. Interfaces*, 2016, **8**, 20872-20879.
145. R. Desai, D. Lakshminarayana, P. Patel and C. Panchal, *Sens. Actuators, B*, 2005, **107**, 523-527.
146. S. Zhang, J. Zhang, B. Liu, X. Jia, G. Wang and H. J. S. r. Chang, 2019, **9**, 1-7.
147. E. Kadykalo, L. Marushko, I. Ivashchenko, O. Zmiy and I. Olekseyuk, *J. Phase Equilib. Diffus.*, 2013, **34**, 221-228.
148. E. G. Grochowski, D. R. Mason, G. A. Schmitt and P. Smith, *J. Phys. Chem. Solids*, 1964, **25**, 551-558.
149. P. Dera and E. Boldyreva, *High-Pressure Crystallography: From Fundamental Phenomena to Technological Applications*, Springer Netherlands, 2010.
150. J. M. Recio, J. M. Menendez and A. O. de la Roza, *An Introduction to High-Pressure Science and Technology*, CRC Press, 2016.
151. P. Shanahan and W. Detmold, *Phys. Rev. Lett.*, 2019, **122**, 072003.

152. B. A. Weinstein and R. Zallen, in *Light Scattering in Solids IV*, Springer, 1984, pp. 463-527.
153. P. W. Bridgman, in *Volume VII Collected Experimental Papers, Volume VII*, Harvard University Press, 2013, pp. 4113-4197.
154. P. Bridgman, in *Volume V Collected Experimental Papers, Volume V*, Harvard University Press, 2013, pp. 3200-3202.
155. E. Perez—Albuerne, K. Forsgren and H. Drickamer, *Rev. Sci. Instrum.*, 1964, **35**, 29-33.
156. P. Debrunner, R. Vaughan, A. Champion, J. Cohen, J. Moyzis and H. Drickamer, *Rev. Sci. Instrum.*, 1966, **37**, 1310-1315.
157. H. T. Hall, *Science*, 1970, **169**, 868-869.
158. C. Weir, E. Lippincott, A. Van Valkenburg and E. Bunting, *J. Res. Natl. Bur. Stand. A Phys. Chem.*, 1959, **63**, 55.
159. M. Xu, S. Jakobs, R. Mazzarello, J.-Y. Cho, Z. Yang, H. Hollermann, D. Shang, X. Miao, Z. Yu and L. Wang, *J. Phys. Chem. C*, 2017, **121**, 25447-25454.
160. J. A. Sans, R. Vilaplana, E. L. da Silva, C. Popescu, V. P. Cuenca-Gotor, A. n. Andrada-Chacón, J. Sánchez-Benitez, O. Gomis, A. L. Pereira and P. Rodríguez-Hernández, *Inorg. Mater.*, 2020.
161. V. P. Cuenca-Gotor, J. Á. Sans, O. Gomis, A. Mújica, S. Radescu, A. Munoj, P. Rodriguez-Hernadez, E. L. Da Silva, C. Popescu, J. Ibañez, R. Vilaplana and F. J. Manjon, *Phys. Chem. Chem. Phys.*, 2020.
162. M. Wuttig, V. L. Deringer, X. Gonze, C. Bichara and J. Y. Raty, *Adv. Mater.*, 2018, **30**, 1803777.
163. M. Wuttig, *phys. status solidi (b)*, 2009, **246**, 1820-1825.
164. C. G. Salzmann, *J. Chem. Phys.*, 2019, **150**, 060901.
165. M. Millot, F. Coppari, J. R. Rygg, A. Correa Barrios, S. Hamel, D. C. Swift and J. H. Eggert, *Nature*, 2019, **569**, 251-255.
166. M. I. Eremets, A. G. Gavriliuk, I. A. Trojan, D. A. Dzivenko and R. Boehler, *Nat. Mater.*, 2004, **3**, 558-563.
167. R. P. Dias and I. F. Silvera, *Science*, 2017, eaal1579.
168. P. Loubeyre, F. Occelli and P. Dumas, *Nature*, 2020, **577**, 631-635.
169. Y. Ma, M. Eremets, A. R. Oganov, Y. Xie, I. Trojan, S. Medvedev, A. O. Lyakhov, M. Valle and V. Prakapenka, *Nature*, 2009, **458**, 182.
170. T. Matsuoka and K. Shimizu, *Nature*, 2009, **458**, 186-189.
171. R. T. Howie, R. Turnbull, J. Binns, M. Frost, P. Dalladay-Simpson and E. Gregoryanz, *Sci. Rep.*, 2016, **6**, 34896.
172. A. A. Adeleke, M. Kunz, E. Greenberg, V. B. Prakapenka, Y. Yao and E. Stavrou, *ACS Earth Space Chem.*, 2019, **3**, 2517-2524.
173. J. A. Sans, F. J. Manjón, C. Popescu, V. P. Cuenca-Gotor, O. Gomis, A. Muñoz, P. Rodríguez-Hernández, J. Contreras-García, J. Pellicer-Porres and A. L. Pereira, *Phys. Rev. B*, 2016, **93**, 054102.
174. A. Drozdov, M. Eremets, I. Troyan, V. Ksenofontov and S. I. Shylin, *Nature*, 2015, **525**, 73-76.

175. E. Snider, N. Dasenbrock-Gammon, R. McBride, X. Wang, N. Meyers, K. V. Lawler, E. Zurek, A. Salamat and R. P. Dias, *Phys. Rev. Lett.*, 2021, **126**, 117003.
176. S. Zhang, Z. Li, K. Luo, J. He, Y. Gao, A. V. Soldatov, V. Benavides, K. Shi, A. Nie and B. Zhang, *Natl. Sci. Rev.*, 2022, **9**, nwab140.
177. W. Zhang, A. R. Oganov, A. F. Goncharov, Q. Zhu, S. E. Boulfelfel, A. O. Lyakhov, E. Stavrou, M. Somayazulu, V. B. Prakapenka and Z. Konôpková, *Science*, 2013, **342**, 1502-1505.
178. M. Ceppatelli, D. Scelta, M. Serrano-Ruiz, K. Dziubek, G. Garbarino, J. Jacobs, M. Mezouar, R. Bini and M. Peruzzini, *Nat. Commun.*, 2020, **11**, 1-11.
179. S. Anzellini and S. Boccato, *Crystals*, 2020, **10**, 459.
180. E. Soignard and P. McMillan, in *High-Pressure Crystallography*, Springer, 2004, pp. 81-100.
181. M. Cardona and G. Güntherodt, *Light Scattering in Solids IV: Electronic Scattering, Spin Effects, SERS, and Morphic Effects*, Springer Berlin Heidelberg, 2014.
182. W. H. Weber and R. Merlin, *Raman Scattering in Materials Science*, Springer Berlin Heidelberg, 2013.
183. E. Smith and G. Dent, *Modern Raman Spectroscopy: A Practical Approach*, Wiley, 2019.
184. J. R. Ferraro and K. Nakamoto, *Introductory Raman Spectroscopy*, Elsevier Science, 2012.
185. J. González and F. J. Manjón, in *An Introduction to High Pressure Science and Technology*, CRC Press, Boca Raton, 2016, pp. 265-300.
186. B. A. Weinstein and G. Piermarini, *Phys. Rev. B*, 1975, **12**, 1172.
187. B. Weinstein, *Phys. Rev. B*, 2021, **104**, 054105.
188. A. Debernardi, C. Ulrich, M. Cardona and K. Syassen, *phys. status solidi (b)*, 2001, **223**, 213-223.
189. B. Garcia-Domene, H. Ortiz, O. Gomis, J. Sans, F. Manjón, A. Muñoz, P. Rodríguez-Hernández, S. Achary, D. Errandonea and D. Martínez-García, *J. Appl. Phys.*, 2012, **112**, 123511.
190. H. K. Mao, J. A. Xu and P. M. Bell, *J. Geophys. Res.: Solid Earth*, 1986, **91**, 4673-4676.
191. A. Pandey, S. Dalal, S. Dutta and A. Dixit, *J. Mater. Sci.: Mater. Electron.*, 2021, **32**, 1341-1368.
192. R. Jenkins and R. Snyder, *Introduction to X-Ray Powder Diffractometry*, Wiley, 2012.
193. L. Lutterotti, R. Vasin and H.-R. Wenk, *Powder Diffr.*, 2014, **29**, 76-84.
194. M. Ladd and R. Palmer, *Structure Determination by X-ray Crystallography: Analysis by X-rays and Neutrons*, Springer US, 2014.
195. R. E. Dinnebier and S. J. L. Billinge, *Powder Diffraction: Theory and Practice*, Royal Society of Chemistry, 2015.
196. V. Pecharsky and P. Zavalij, *Fundamentals of powder diffraction and structural characterization of materials*, Springer Science & Business Media, 2008.

197. S. Petitgirard, G. Spiekermann, C. Weis, C. Sahle, C. Sternemann and M. Wilke, *J. Synchrotron Radiat.*, 2017, **24**, 276-282.
198. S. Mobilio, F. Boscherini and C. Meneghini, *Synchrotron Radiation*, Springer, 2016.
199. S. P. Cramer, in *X-Ray Spectroscopy with Synchrotron Radiation*, Springer, 2020, pp. 39-68.
200. D. Attwood, A. Sakdinawat and L. Geniesse, *X-Rays and Extreme Ultraviolet Radiation: Principles and Applications*, Cambridge University Press, 2017.
201. P. Willmott, *An Introduction to Synchrotron Radiation: Techniques and Applications*, Wiley, 2019.
202. ALBA Synchrotron, The ALBA Synchrotron (infographic), https://www.cells.es/en/outreach/educational-materials, (accessed 16/09/2022, 2022).
203. ALBA Synchrotron, Accelerators, https://www.cells.es/en/accelerators, (accessed 16/09/22, 2022).
204. F. Fauth, I. Peral, C. Popescu and M. Knapp, *Powder Diffr.*, 2013, **28**, S360-S370.
205. ALBA Synchrotron BL04-MSPD information, https://www.cells.es/en/beamlines/bl04-mspd/information, (accessed 16/09/2022, 2022).
206. A. Muñoz González and P. Rodríguez Hernández, in *An Introduction to High Pressure Science and Technology*, CRC PRess, Boca Raton, 2016, pp. 75-104.

Chapter 2
Publications

Inorganic Chemistry

Article

Cite This: Inorg. Chem. 2018, 57, 8241−8252

pubs.acs.org/IC

Experimental and Theoretical Studies on α-In_2Se_3 at High Pressure

Rosario Vilaplana,*[,†] Samuel Gallego Parra,[‡] Alejandro Jorge-Montero,[§] Plácida Rodríguez-Hernández,[§] Alfonso Munoz,[§] Daniel Errandonea,[∥] Alfredo Segura,[∥] and Francisco Javier Manjón[‡]

[†]Centro de Tecnologías Físicas, Universitat Politècnica de València, 46022 Valencia, Spain

[‡]Instituto de Diseño para la Fabricación y Producción Automatizada, Universitat Politècnica de València, 46022 Valencia, Spain

[§]Departamento de Física, Instituto de Materiales y Nanotecnología, MALTA Consolider Team, Universidad de La Laguna, 38207 San Cristóbal de La Laguna, Spain

[∥]Departamento de Física Aplicada-ICMUV, MALTA Consolider Team, Universidad de Valencia, Edificio de Investigación, C/Dr. Moliner 50, 46100 Burjassot, Spain

Supporting Information

ABSTRACT: α(R)-In_2Se_3 has been experimentally and theoretically studied under compression at room temperature by means of X-ray diffraction and Raman scattering measurements as well as by *ab initio* total-energy and lattice-dynamics calculations. Our study has confirmed the α ($R3m$) → β' ($C2/m$) → β ($R\bar{3}m$) sequence of pressure-induced phase transitions and has allowed us to understand the mechanism of the monoclinic $C2/m$ to rhombohedral $R\bar{3}m$ phase transition. The monoclinic $C2/m$ phase enhances its symmetry gradually until a complete transformation to the rhombohedral $R\bar{3}m$ structure is attained above 10−12 GPa. The second-order character of this transition is the reason for the discordance in previous measurements. The comparison of Raman measurements and lattice-dynamics calculations has allowed us to tentatively assign most of the Raman-active modes of the three phases. The comparison of experimental results and simulations has helped to distinguish between the different phases of In_2Se_3 and resolve current controversies.

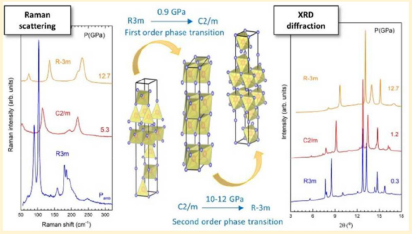

1. INTRODUCTION

Indium selenide (In_2Se_3), a semiconductor with a direct bandgap of 1.45 eV,[1] has led to plenty of studies for decades mainly focused on its multiple applications as thermoelectric material,[2,3] phase random access memories,[4−6] photodetectors,[7,8] solar cells,[9] ferroelectricity,[10,11] and anisotropic photoconductivity.[12,13] Furthermore, it has been studied in the context of 2D materials, like graphene, and promising novel materials, like topological insulators (TIs).[14,15] In this regard, A_2B_3-type chalcogenides have recently attracted scientific interest since some of them are 3D TIs, like α-Sb_2Te_3, α-Bi_2Se_3, α-Bi_2Te_3, and $SnBi_2Te_4$ whose vibrational properties have been studied at high pressure.[16−19]

In_2Se_3 is a polymorphic compound with at least five known stable and three metastable phases. Like many $A^{III}{}_2B^{VI}{}_3$ compounds, some of these phases contain cation vacancies and can be classified depending on how vacancies are arranged in the unit cell. In particular, vacancies occur in structures where cations only have 4-fold coordination because the sp^3 hybridization of cation atoms imposes that the octet rule is satisfied only if 1/3 of cation positions remain unoccupied.[20] In this way, In_2Se_3 has layered phases without vacancies (α, β', and β) and other phases with vacancies (γ, δ, κ, α', and γ').[21−39] The α-In_2Se_3 phase is the stable phase at room conditions;[23−25] however, it has been reported that there are two α phases at ambient conditions: a rhombohedral α(R) phase and an hexagonal α(H) phase. Moreover, it has been discussed at length whether the α(R) phase belongs to the noncentrosymmetric rhombohedral space group (S.G.) $R3m$ or to the centrosymmetric rhombohedral S.G. $R\bar{3}m$. On the other hand, the hexagonal α(H) phase was mainly suggested to correspond to S.G. $P63/mmc$, but the atomic parameters of this structure have not been solved yet.[24,26,27]

The reason for the discrepancy in the α(R) phase between the S.G. $R3m$ and $R\bar{3}m$ resides in the difficulty of powder X-ray diffraction (XRD) measurements to distinguish between both S.G.s. To resolve this controversy, Raman scattering (RS) measurements were carried out; however, it is not easy to perform RS measurements because of the extraordinary high sensitivity of In_2Se_3, like many other chalcogenides that are good for phase change memories, to laser light. In this regard,

Received: March 23, 2018
Published: June 26, 2018

DOI: 10.1021/acs.inorgchem.8b00778
Inorg. Chem. 2018, 57, 8241−8252

Experimental and theoretical studies on α-In_2Se_3 at high pressure

Rosario Vilaplana[1*], Samuel Gallego Parra[2], Alejandro Jorge-Montero [3], Plácida Rodríguez-Hernández[3], Alfonso Munoz[3], Daniel Errandonea[4], Alfredo Segura[4] and Francisco Javier Manjón[2]

[1]*Centro de Tecnologías Físicas, Universitat Politècnica de València, 46022 Valencia (Spain)*
[2] *Instituto de Diseño para la Fabricación y Producción Automatizada, Universitat Politècnica de València, 46022 Valencia (Spain)*
[3]*Departamento de Física, Instituto de Materiales y Nanotecnología, MALTA Consolider Team, Universidad de La Laguna, 38207 San Cristóbal de La Laguna, Spain*
[4]*Departamento de Física Aplicada-ICMUV, MALTA Consolider Team, Universidad de Valencia, Edificio de Investigación, C/Dr. Moliner 50, 46100 Burjassot, Spain*
*Corresponding author: R. Vilaplana (rovilap@fis.upv.es)

ABSTRACT

α(R)-In_2Se_3 has been experimentally and theoretically studied under compression at room temperature by means of X-ray diffraction and Raman scattering measurements as well as by *ab initio* total-energy and lattice-dynamics calculations. Our study has confirmed the α ($R3m$) → β′ ($C2/m$) → β (R-$3m$) sequence of pressure-induced phase transitions and has allowed us to understand the mechanism of the monoclinic C2/m to rhombohedral R-3m phase transition. The monoclinic C2/m phase enhances its symmetry gradually until a complete transformation to the rhombohedral R-3m structure is attained above 10-12 GPa. The second-order character of this transition is the reason for the discordance in previous measurements. The comparison of Raman measurements and lattice-dynamics calculations has allowed us tentatively assigning most of the Raman-active modes of the three phases. The comparison of experimental results and simulations has helped to distinguish between the different phases of In_2Se_3 and resolve current controversies.

Keywords: Indium selenide, high-pressure, Raman, *ab initio*, x-ray diffraction, phase transition

PACS: 31.15.A-, 61.05.cp, 62.50.-p, 64.30.Jk, 71.15.Mb

1. INTRODUCTION

Indium selenide (In_2Se_3), a semiconductor with a direct bandgap of 1.45 eV,[1] has led to plenty of studies for decades mainly focused on its multiple applications as thermoelectric material,[2, 3] phase random access memories,[4-6] photodetectors,[7, 8] solar cells,[9] ferroelectricity[10, 11] and anisotropic photoconductivity.[12, 13] Furthermore, it has been studied in the context of 2D materials, like graphene, and promising novel materials, like topological insulators (TIs).[14, 15] In this regard, A_2B_3-type chalcogenides have recently attracted scientific interest since some of them are 3D TIs, like α-Sb_2Te_3, α-Bi_2Se_3, α-Bi_2Te_3 and $SnBi_2Te_4$ whose vibrational properties have been studied at high pressure.[16-19]

In_2Se_3 is a polymorphic compound with at least five known stable and three metastable phases. Like many $A^{III}{}_2B^{VI}{}_3$ compounds, some of these phases contain cation vacancies and can be classified depending on how vacancies are arranged in the unit cell. In particular, vacancies occur in structures where cations only have fourfold coordination because the sp^3 hybridization of cations atoms imposes that the octet rule is satisfied only if 1/3 of cation positions remain unoccupied.[20] In this way, In_2Se_3 has layered phases without vacancies (α, β′ and β) and other phases with vacancies (γ, δ, κ, α′ and γ′).[21-39] The α-In_2Se_3 phase is the stable phase at room conditions;[23-25] however, it has been reported that there are two α phases at ambient conditions: a rhombohedral α(R) phase and an hexagonal α(H) phase. Moreover, it has been lengthy discussed whether the α(R) phase belongs to the non-centrosymmetric rhombohedral space group (S.G.) *R*3*m* or to the centrosymmetric rhombohedral S.G. *R*-3*m*. On the other hand, the hexagonal α(H) phase was mainly suggested to correspond to S.G. *P*63/*mmc,* but the atomic parameters of this structure have not been solved yet.[24, 26, 27]

The reason for the discrepancy in the α(R) phase between the S.G. *R*3*m* and *R*-3*m* resides in the difficulty of powder X-ray diffraction (XRD) measurements to distinguish between both S.G.s. To resolve this controversy, Raman scattering (RS) measurements were carried out; however, it is not easy to perform RS measurements because of the extraordinary high sensitivity of In_2Se_3, like many other chalcogenides that are good for phase change memories, to laser light. In this regard, several papers reporting RS measurements at room conditions have been published,[30-33, 35, 36] but there are no clear conclusions about the nature of the α(R) phase since there is a lack of theoretical calculations to compare with experimental data.

It is important to know the different arrangements of In and Se atoms in the different In_2Se_3 polytypes and to understand their different properties and their behavior at high temperatures and pressures in order to optimize the multiple applications of this interesting material. Noteworthy, the layered tetradymite (S.G. *R*-3*m*) structure of the β-phase of In_2Se_3 has been found at room conditions in many compounds showing 3D TI properties, like α-Sb_2Te_3, α-Bi_2Se_3, α-Bi_2Te_3 and $SnBi_2Te_4$. In fact, in all these layered compounds, where layers are formed by quintuple (α-Sb_2Te_3, α-Bi_2Se_3, α-Bi_2Te_3) or septuple ($SnBi_2Te_4$) atomic layers, the *R*-3*m* phase is composed of regular octahedral units around the cation in the binary compounds and around the Sn cation in the ternary compound.[40, 41]

In the last years, the high-pressure (HP) behavior of α-In_2Se_3 has attracted considerable interest. A sequence of pressure-induced phase transitions: α → β′ → β → defective cubic Th_3P_4 at 0.8, 5.0, and 32 GPa, respectively, was reported on the basis of powder HP-XRD measurements.[39] Additionally, HP-RS measurements found a phonon with a negative pressure coefficient in the β (*R*-3*m*) phase.[39] Curiously, this soft phonon was not observed in two previous HP-RS studies that, in turn, did not identify the intermediate β′ phase between the α and β phases.[42, 43] In this context, it is worthy to note that HP-RS studies of vibrational properties of the tetradymite phase of α-Sb_2Te_3, α-Bi_2Se_3 and α-Bi_2Te_3 have not reported any experimental or theoretical soft mode in the *R*-3*m* phase.[40] More recently, a HP study has revealed a superconductivity enhancement in α-In_2Se_3 under compression when it undergoes the transition to the defective cubic Th_3P_4 structure.[44] Finally, a recent HP study has also reported the transition from γ-In_2Se_3 to β-In_2Se_3 under compression.[45]

In order to shed light into: i) the nature of the α(R) phase; ii) the existence of an intermediate β′ phase between α and β phases; and iii) the presence of a soft phonon in the β phase, we performed *ab initio* calculations of In_2Se_3 with *R*3*m*, *C*2/*m* and *R*-3*m* structures. We found that our calculations did not support the existence of a soft phonon in the β(*R*-3*m*) phase. This result made us suspect that laser heating could be locally damaging the sample used in **Ref. 39**, thus generating nanoclusters of selenium, which exhibit soft phonons, as previously reported in other selenide.[46] Therefore, we have revisited in this work the behavior of α-In_2Se_3 at HP by conducting HP-XRD and HP-RS measurements at room temperature and *ab initio* total-energy and lattice-dynamics calculations up to 20 GPa. **Table 1** presents the main details of the α, β′ and β phases of In_2Se_3 involved in this work.[21, 23, 24, 31, 37-39] In sections 2 and 3, we show the experimental and theoretical details. In section 4, we show the HP results of XRD and RS measurements and of *ab initio* calculations. In section 5, we discuss the mechanism involved in the *C*2/*m* to *R*-3*m* phase transition and comment on the previous difficulties in observing the intermediate β′ phase. Finally, in section 6 we summarize our results and provide some conclusions. We also show that our RS measurements provide clear evidence that the α(R) phase is the non-centrosymmetric *R*3*m* phase. Furthermore, our experimental and theoretical results provide clear evidence that there is an intermediate β′ phase with monoclinic *C*2/*m* symmetry between the α(*R*3*m*) and β(*R*-3*m*) phases. Moreover, the β'-to-β phase transition is of second-order and takes place above 10 GPa. Finally, we show that upon hydrostatic compression the sample likely reverts to the original phase on decompression, but with considerable disorder likely due to the strong first-order character of the α-to- β' phase transition.

Table 1. Crystal structure, S.G., number of α, β′ and β phases

Phase	Crystal structure	S.G.	Number	Refs.
α	Rhombohedral	*R*3*m*	160	23, 24, 31
β′	Monoclinic	*C2/m*	12	37-39
β	Rhombohedral	*R-3m*	166	21, 23, 24

2. EXPERIMENTAL DETAILS

α-In_2Se_3 powders used in this work are commercial In_2Se_3 powders purchased from Alfa Aesar Company (99.99%). In XRD and RS experiments, the samples were loaded in a DAC with a 4:1 methanol-ethanol mixture as a pressure-transmitting medium. The culet-size of the diamond anvils was 500 μm. We used an Inconel gasket, pre-indented to 50 μm, in which we drilled a 250 μm diameter hole. The 4:1 methanol-ethanol mixture is hydrostatic up to 10 GPa and quasi-hydrostatic up to the maximum pressure reached in our experiments.[47] In addition, we took precautions to minimize the deviatoric stresses induced in the experiments during the DAC loading.[48] HP-XRD measurements at room temperature up to 25 GPa were conducted at the BL04-MSPD beamline of ALBA synchrotron using the equation of state of copper powder mixed with the sample to determine the pressure inside the DAC. Incident monochromatic beam with wavelength of 0.4638 Å was focused to 20 x 20 μm.[49] Images covering a 2θ range up to 20° were collected using a Rayonix SX165 CCD located at 240 mm from sample. One-dimensional diffraction profiles of intensity as a function of 2θ were obtained by integration of the observed intensities with the Fit2D software.[50] Rietveld refinements were carried out with GSAS package software.[51] The equation of state (EOS) of copper was used for pressure calibration.[52]

HP-RS measurements were performed with a LabRAM HR UV microspectrometer coupled to a Peltier cooled CCD camera, using a 532 nm solid state laser excitation line with a power smaller than 1 mW and a spectral resolution better than 2 cm^{-1}. In order to be sure that no heating effects occur during the measurements the sample were checked during all Raman experiment. Concerning the analysis of Raman spectra under pressure, Raman peaks have been fitted to Voigt profiles (Lorentzian profile convoluted by a Gaussian profile) where the spectrometer resolution is taken as the fixed Gaussian width. As already commented, two HP runs were performed in In_2Se_3 in order to obtain the spectra of the first phase since the transition is about 0.8 GPa. The pressure was determined by the ruby luminescence method;[53] the shape and separation of the R1 and R2 ruby lines were checked at each pressure and neither a significant increase in width nor an overlapping of both peaks were detected.

3. SIMULATION DETAILS

Structural and vibrational data were obtained by means of *ab initio* total-energy and lattice-dynamics calculations in the framework of the density functional theory (DFT).[54] This method allows an accurate description of the physical properties of semiconductors at HP.[55] The simulations were conducted with the *Vienna Ab Initio Simulation Package* (VASP).[56] The projector-augmented wave scheme (PAW)[57] was employed to take into account the full nodal character of the all-electron charge density in the core region. The plane waves basis set was extended to a cut off of 320 eV in order to have accurate results. The exchange-correlation energy was described in the generalized-gradient approximation (GGA) with the Perdew-Burke-Ernzenhof prescription.[58] For each of the studied phases, integrations within the Brillouin zone (BZ) were performed with dense meshes of Monkhorst-Pack k-special points. In this way, a high convergence of 1 meV per formula unit was accomplished. At a set of selected volumes, the lattices parameters and atomics positions were fully optimized

by calculating the forces on the atoms and the stress tensor. In the optimized resulting structures, the forces on the atoms were lower than 0.002 eV/Å and the deviation of the stress tensor components from the diagonal hydrostatic form less than 0.1 GPa. In our simulations, after the relaxation process of the considered structure, we obtain a set of energies and volumes at different pressures.[59]

Lattice-dynamic calculations were carried out at the center of the Brillouin zone (Γ point). The direct force-constant approach (or supercell method) [60] was employed. This method requires highly converged results on forces. The diagonalization of the dynamical matrix determines the frequencies of Raman- and infrared-active modes. From the calculations, the symmetries of the eigenvectors of the different vibrational modes are also identified at the Γ point.

4. RESULTS

4.1. HP-XRD measurements

The α (*R*3*m*) structure of In_2Se_3 can be visualized as a layered structure composed of quintuple layers (Se-In-Se-In-Se) that are linked by weak van der Waals forces (see **Fig. 1**). In this structure, there are five inequivalent atoms occupying *3a* Wyckoff sites (In1, In2, Se1, Se2 and Se3). The two inequivalent In1 and In2 atoms have sixfold and fourfold coordination, respectively. The three inequivalent Se atoms also have different coordinations. The Se atom in the center of the layer (Se2) is fourfold coordinated to three In1 and one In2 atoms, forming a distorted tetrahedron; while Se atoms at the layer surface (Se1 and Se3) have a threefold coordination. However, Se1 atoms linked to In1 atoms show bond distances above 2.7 Å at room pressure, while Se3 atoms linked to In2 atoms show smaller bond distances below 2.7 Å at room pressure.

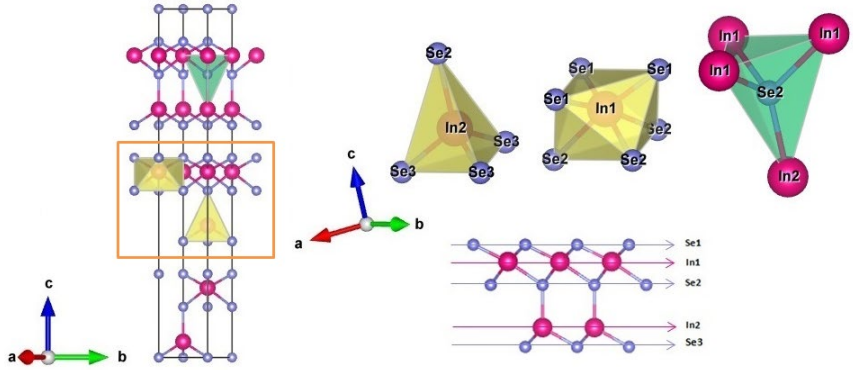

Figure 1: Detail of the structure of the α In_2Se_3 phase. Right bottom corner: quintuple layer. Right top corner: three polyhedra centered in In2, In1 and Se2 atoms.

HP-XRD measurements on powder samples were performed up to 20.2 GPa as shown in **Fig. 2**. XRD patterns below 0.5 GPa can be indexed with the α(*R*3*m*) phase, while those above 1.2 GPa can be indexed with the β′ phase. At 11.9 GPa, the XRD pattern

can still be properly assigned to the β′ phase; however, patterns above 12.7 GPa can only be indexed with the β-phase. Our results are in good agreement with those of **Ref. 39**, thus confirming the existence of the intermediate the β′ phase between α and β phases. The only difference with respect to **Ref. 39** is the pressure at which we locate the β′→ β transition. One of the main characteristics of this transition is the merging of several Bragg peaks near 2θ = 15º (they correspond to a d-spacing in the range 1.68 - 1.52 Å as shown in **Fig. S1** of the Supporting Information). Zhao *et al.,* pointed at this merging as the indication of the β′ → β transition at 5 GPa.[39] However, the merging of the two peaks into a single one is smooth and keeps on up to higher pressures, making it difficult to accurately determine the transition pressure. In addition, to the peak merging, there are additional changes in the XRD pattern that help to determine more accurately the transition pressure. In particular, a weak peak present at 11.9 GPa (see inset of **Fig. 2**), but disappearing at 12.7 GPa, can be indexed with the β′ phase and not with the β phase. In addition, the R-values of the Rietveld refinements are smaller for the β′ phase than for the β phase at all pressures from 1.2 to 11.9 GPa, as it was also found in previous examples of two phases linked by a group-subgroup relationship.[61-63] We consider that this evidence supports that the transition pressure is around 12.7 GPa and not around 5.0 GPa as previously assigned.[39] The gradual transformation of β′ phase into β phase and the fact that there is no volume discontinuity suggests that the β′→ β phase transition is a second-order transformation,[64] as the one observed under compression in the related compound InSe.[65] We will show below that these conclusions are supported by our HP-RS measurements and *ab initio* calculations.

For the sake of completeness, we show in **Fig. 3** the pressure evolution of the experimental and theoretical lattice parameters and unit cell volume in the different phases (see numerical data in **Table S1** of the Supporting Information). As observed, the change in volume from the α phase at 0.5 GPa (399 $Å^3$ → V/Z = 133 $Å^3$) to the β' phase at 1.2 GPa (248.7 $Å^3$ → V/Z = 124.35 $Å^3$) implies a relative change ΔV/V = 6%. Note that a extrapolation of the α phase up to 1.2 GPa would yield a ΔV/V = 4% which is in good agreement with **Ref. 39**. On the other hand, the change in volume from the β' phase at 11.9 GPa $Å^3$ (216.3 → V/Z = 108.15 $Å^3$) to the β phase at 12.7 GPa (319.9 $Å^3$ → V/Z = 106.63 $Å^3$) results in a ΔV/V = 1%. If we extrapolate the β' phase up to 12.7 GPa then we obtain a ΔV/V = 0%, what agrees with the second-order character of the β'-β phase transition, as suggested in **Ref. 39**. As regards the α phase, it can be observed that there is a slightly larger compression of the experimental c lattice parameter and the volume than of the theoretical one. We think that this small difference is due to the fact that DFT calculations tend to overestimate compression for the van der Waals interaction between the layers. In any case, there is a rather good agreement between our experimental and theoretical values.

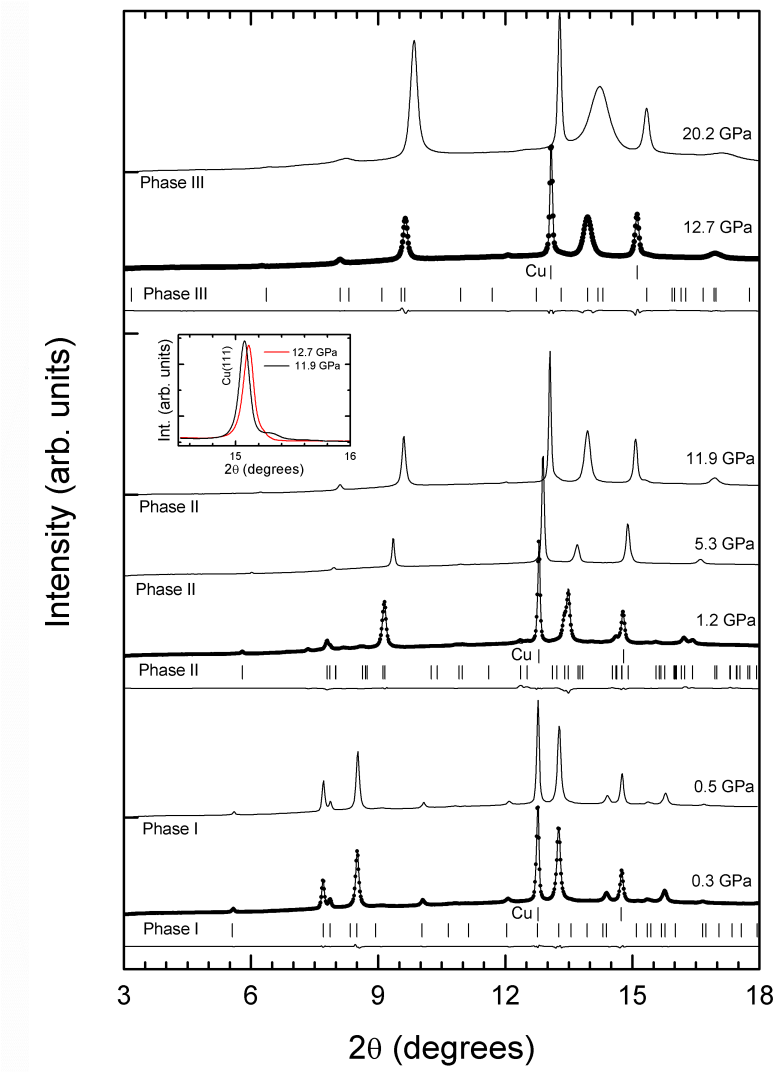

Figure 2: HP-XRD patterns at selected pressures. Rietveld refinements are shown for: i) the phase I (rhombohedral structure, S.G. R3m) at 0.3 GPa; ii) the phase II (monoclinic structure, S.G. *C*2/*m*) at 1.2 GPa and iii) the phase III (rhombohedral structure, S.G. *R*-3*m*) at 12.7 GPa. Experimental data are plotted as solid lines, calculated profiles as circles and residuals are also shown by solid lines in the bottom part of the refined patterns. The background has been removed from all XRD patterns. Vertical ticks indicate the position of Bragg reflections as well as the vertical ticks up indicate the position of cupper reflections. The inset shows the small changes associated to the conclusion of the second-order phase transition.

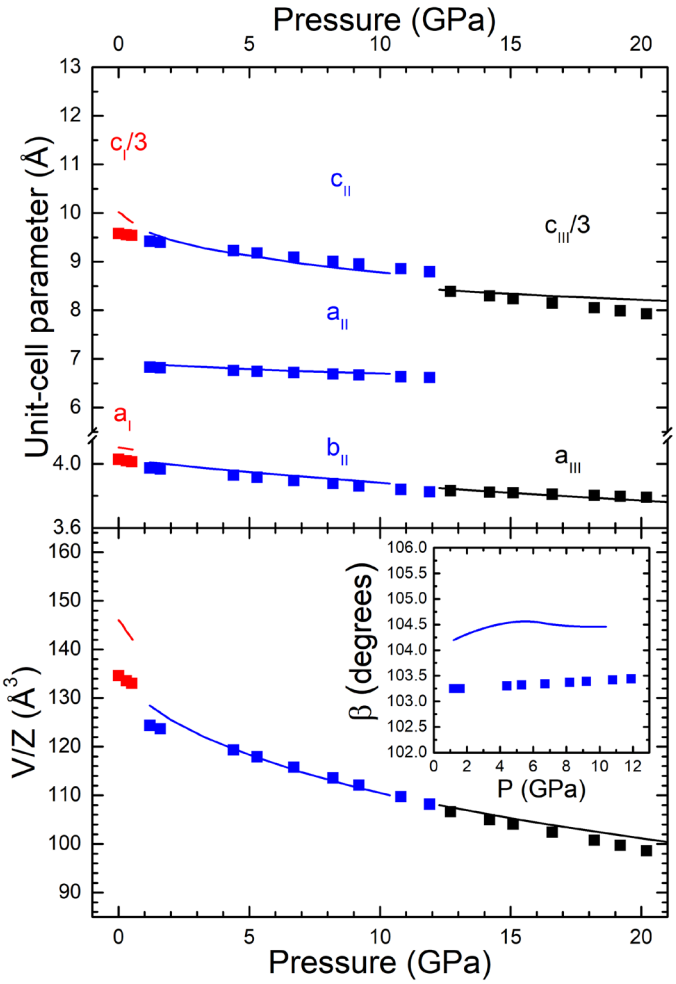

Figure 3: Pressure dependence of the experimental (symbols) and theoretical (line) lattice parameters and unit cell volume of the α, β' and β phases in In_2Se_3. The inset shows the pressure dependence of the monoclinic β' angle.

We have used a Birch-Murnaghan state equation of 2nd order in order to obtain the state equation parameters at room pressure for α, β′ and β phases of In_2Se_3 and to compare them with those reported in **Ref. 39** (see **Table 2**). As can be seen in **Table 2**, the bulk modulus of the phase I and II are underestimated in **Ref. 39**. The underestimation of the bulk modulus in **Ref. 39** can be caused by the fact that data points for the pressure region where phase coexistence is observed have been included in the EOS determination. In our case, we have carefully selected only data points for phase I where either phase I or phase II were detected as single phases, which make as confident in the EOS parameters determined in the present work.

Table 2: Birch-Murnaghan 2nd order state equation parameters at ambient pressure obtained for α, β′ and β phases of In_2Se_3 and its comparison with a previous study.

	Phase I	**Phase II**	**Phase III**	
V_0 (Å^3)	403.8(5)	256(1)	375(2)	This work
B_0 (GPa)	40(2)	48(4)	60(6)	
V_0 (Å^3)	407.9	260.1	369.8	**Ref. 39**
B_0 (GPa)	31	35	66	

It must be stressed that the β (*R*-3*m*) phase can be transformed by group-subgroup relationships into the β′ (*C*2/*m*) phase. In fact, *C*2/*m* is a translationengleiche subgroup of *R*-3*m*. This means that if some geometrical relations are satisfied by the unit-cell parameters in the β′ phase, the β′ phase can be reduced to the higher symmetry β phase. The relations are: $a_m = 2\ b_m \sin 120°$ and $\beta = \sin^{-1}\left(\frac{1}{4}\right) + 90° = 104.4775°$, where a_m, b_m, and β are unit-cell parameters of β′. Under these conditions, the monoclinic β′ structure becomes the rhombohedral β structure. The unit-cell of both structures are related by $a_r = b_m$ and $c_r = 3\ c_m \sin\beta$, where subindexes *r* and *m* refer to the rhombohedral and monoclinic structures. From the analysis of the pressure dependence determined for the β′ phase, we confirmed that the "magic" relation between the unit-cell parameters that transform β′ into β in In_2Se_3 is achieved only at 12.7 GPa.

4.2. HP-RS measurements

As already mentioned, a Raman mode with a negative pressure coefficient was observed in previous HP-RS measurements on α-In_2Se_3,[30] which was not observed in other HP studies.[31, 32] In this context, we want to stress that we observed the appearance of soft phonons that were attributed to the formation of nanocluster of Se atoms because of the local decomposition of the sample.[33] Therefore, we assumed that the observation of a soft phonon in previous HP-RS measurements of In_2Se_3 could evidence thermal degradation of the sample by laser heating and could provide a distorted understanding of the pressure effects on α-In_2Se_3. Consequently, we decided to repeat HP-RS measurements in α-In_2Se_3 by taking into account the strong sensitivity of this material to laser light. In this way, we could compare RS measurements with lattice dynamics calculations as a check to verify the goodness of our HP-RS measurements and calculations and also in order to understand why in previous HP-RS experiments[42, 43] the β′ phase was not identified.

The irreducible representations of the Raman active phonons at Γ for the three phases α(*R*3*m*), β′ (*C*2/*m*), and β (*R*-3*m*) phases (see **Table 3**) show that there are eight, six and four Raman-active modes corresponding to the α, β′ and β phases, respectively. However, since the α phase is non-centrosymmetric, all Raman-active modes are also infrared-active and a TO-LO splitting could be observed.[27]

Table 3. The irreducible representations of the Raman active phonons in Γ for the α, β′ and β phases.

Phase	Raman-active modes in the centre zone Γ
α	$\Gamma = 4A_1 + 4E$
β′	$\Gamma = 4A_g + 2B_g$
β	$\Gamma = 2A_{1g} + 2E_g$

Figure 4 shows the RS spectra of In_2Se_3 compressed up to 20 GPa. As observed, there is no phonon mode that softens under pressure in the whole range of pressures studied. This result is in agreement with **Refs. 42, 43** and in contrast to **Ref. 39**. In the RS spectrum at room pressure, all modes of the initial phase are indicated with arrows, with the exception of the E^1 mode whose frequency is below our spectrometer range. Unfortunately, most of the modes are overlapped, so we show in **Fig. S2** a detailed view with all resolved modes of α phase. A comparison of the pressure dependence of the experimental and theoretical Raman-active mode frequencies of α-In_2Se_3 is shown in **Fig. 5**. A good agreement is found between experimental and theoretical frequencies and pressure coefficients for this phase, with no soft phonon either in RS measurements or in calculations.

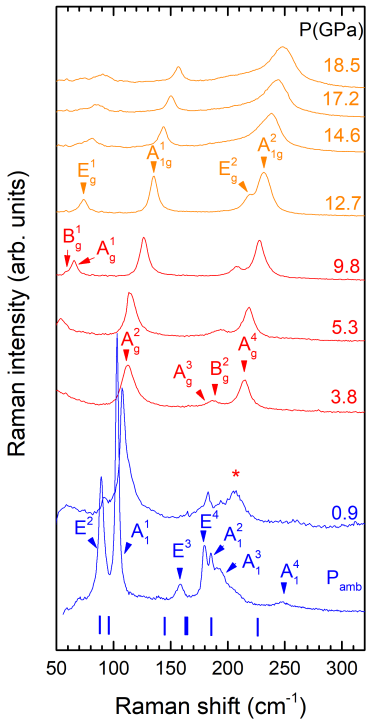

Figure 4: HP-RS spectra at different pressures. Spectra corresponding to α, β′ and β phases are shown in blue, red and orange colours, respectively.

Our HP-RS measurements show that the transition to β′ phase occurs about 0.9 GPa because the RS spectrum at that pressure shows clearly the modes of the α phase with a new peak which corresponds to the next phase (see the asterisk symbol in **Fig. 4**). This indicates the onset of the transition to the new phase. We have adjusted the shape of the Raman peaks with pseudo-Voigt functions and in this way we have been able to resolve the two peaks that we have tentatively assigned to the A_g^3 and B_g^2 modes (see RS spectrum at 3.8 GPa); and later, those assigned to the A_g^1 and B_g^1 (see RS spectrum at 9.8 GPa) of the β′ phase. For more information, resolved A_g^3 and B_g^2 modes at 3.8, 5.3 and 9.8 GPa are displayed in **Fig. S3**. A comparison of the pressure dependence of the experimental and theoretical Raman-active mode frequencies of β′-In_2Se_3 is shown in **Fig. 5**.

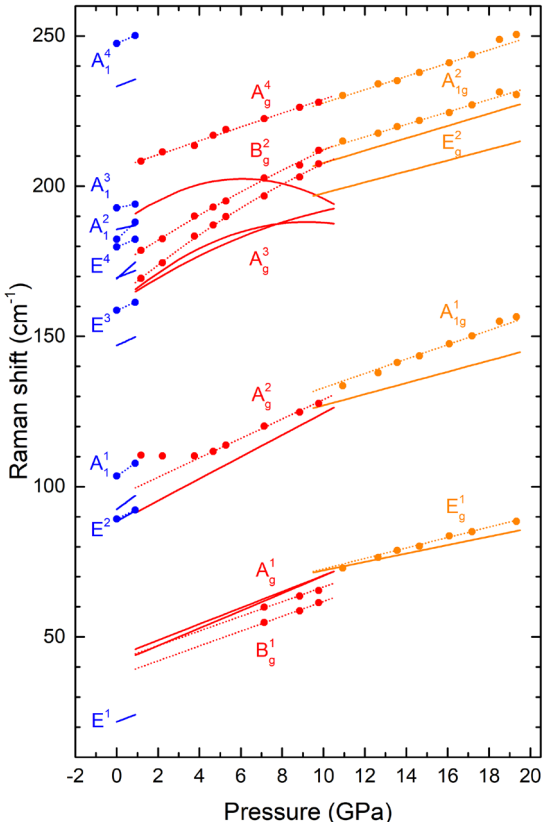

Figure 5: Pressure dependence of the experimental (symbols) and theoretical (lines) Raman-active mode frequencies of the α, β′ and β phases in blue, red and orange colours, respectively. Short dotted lines represent fitted experimental Raman modes.

The first thing to point out is the strong similarity of the calculated modes in the β′ and β phases. A_g^1 and B_g^1 modes of β′ phase are almost overlapped and difficult to distinguish of E_g^1 mode of β phase. The same happens with A_g^3 and B_g^2 modes of β′

phase and E_g^2 mode of β phase. On the other hand, A_g^2 modes of β′phase and A_{1g}^1 of β phase are indistinguishable, as well as the A_g^4 of β′ phase and A_{1g}^2 mode of β phase. Therefore, our calculations show that both phases are very similar and provide a valuable help to understand why previous HP-RS measurements have not been able to identify the intermediate β′ phase transition. Between 5 and 10 GPa calculations show an abrupt decrease of the highest frequency A_g^3 mode (see **Fig. 5**).

According to our RS measurements and calculations, the β′-to-β phase transition takes place around 10-12 GPa and not around 5.0 GPa as suggested by previous HP-XRD measurements.[39] In order to corroborate experimentally the pressure at which the transition to the β phase is completed, we have plotted the full width at half maximum (FWHM) of the phonon A_g^2 in the β′ phase (see **Fig. 6**). The FWHM decreases with increasing pressure and stabilizes about 10-12 GPa. Therefore, this result reinforces the fact that the transition is completed around 10-12 GPa. In other words, it seems that this process is gradual and it takes a range of pressures to be completed.

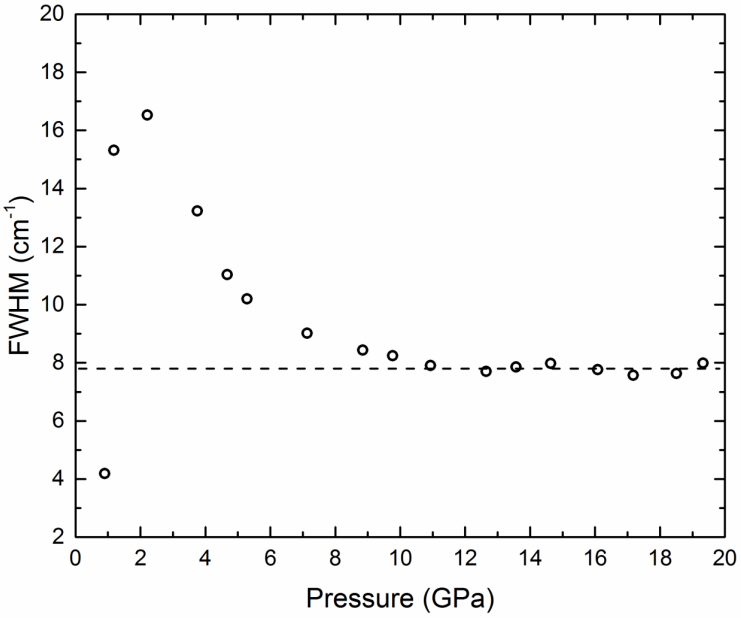

Figure 6: Pressure dependence of the FWHM of the A_g^2 mode in the β′ phase, which changes to the A_{1g}^1 mode in the β phase above 10-12 GPa.

Summing up, HP-RS results and its comparison to *ab initio* calculations have allowed us to assign most of the modes of the different phases. In **Tables 4, 5** and **6** we have summarized experimental and theoretical Raman mode frequencies together with their pressure coefficients for the three phases. It should be noted that the E^1 (α phase) mode is not observed in our setup owing to their low frequency. The same happens with the Bg^1 and A_g^1 (β′ phase) which can be observed at about 7.0 GPa. Note that the A_g^4 (β′ phase) mode is the only one whose pressure dependence is different in

experiment and calculations. At present, we have no explanation for this fact as well as for the rather large difference between some experimental and theoretical absolute frequencies. In **Fig. S4** of the Supporting Information, we show the RS data on downstroke. Despite the difficulty on the discrimination between β′ and β phases due to the second-order character of this phase transition, we can appreciate by looking at the $A_{1g}{}^1$ mode of the β phase a sign of the back transformation to the $A_g{}^2$ mode of β′ phase. Note that this mode becomes more intense and defined below 10 GPa.

Table 4. Experimental and theoretical Raman-active mode frequencies and their pressure coefficients as derived from a fit to $\omega(P) = \omega_0 + a(P - P_o)$ of the α phase (P_o = 0 GPa).

Mode	ω_o (exp) (cm^{-1})	a (exp) (cm^{-1} GPa^{-1})	ω_o (th) (cm^{-1})	a (th) (cm^{-1} GPa^{-1})
E^1	27[a]		21.7	2.68
E^2	89.2	3.28	88.5	3.85
A_1^1	103.5	4.77	92.5	5.09
E^3	158.7	2.98	147.0	3.19
E^4	179.8	2.80	169.5	2.69
A_1^2	182.3	6.36	169.2	6.16
A_1^3	192.8	1.33	185.6	1.42
A_1^4	247.5	2.98	233.2	2.71

[a] This E-type mode was observed in **Ref. 26** in good agreement with our theoretical data.

Table 5. Experimental and theoretical Raman-active mode frequencies of the β′ phase and their pressure coefficients derived from a primer order fit $\omega(P) = \omega_0 + a(P - P_o)$ or to $\omega(P) = \omega_0 + a(P - P_o) + b(P - P_o)^2$ (P_o = 0.9 GPa).

Mode	ω_o (exp) (cm^{-1})	a (exp) (cm^{-1} GPa^{-1})	b (exp) x 100 (cm^{-1} GPa^{-1})	ω_o (th) (cm^{-1})	a (th) (cm^{-1} GPa^{-1})	b (th) x 100 (cm^{-1} GPa^{-1})
B_g^1	39.3	2.47		43.9	2.90	
A_g^1	44.4	2.44		45.9	2.69	
A_g^2	99.9	3.23		91.3	3.65	
B_g^2	177.3	4.43	-6.8	164.9	4.31	-14.9
A_g^3	167.9	5.54	-13.1	165.6	5.41	-32.6
A_g^4	207.9	2.3		190	4.46	-43

Table 6. Experimental and theoretical Raman-active mode frequencies of the β phase and their pressure coefficients as derived from a fit to $\omega(P) = \omega_0 + a(P - P_o)$ or to $\omega(P) = \omega_0 + a(P - P_0) + b(P - P_0)^2$ (P_0 = 10 GPa).

Mode	ω_o (exp) (cm^{-1})	a (exp) (cm^{-1} GPa^{-1})	ω_o (th) (cm^{-1})	a (th) (cm^{-1} GPa^{-1})
E_g^1	72.6	1.74	72.1	1.41
A_{1g}^1	132.9	2.39	127.1	1.86
E_g^2	212.3	2.07	197.7	1.81
A_{1g}^2	227.7	2.20	207.7	2.05

Finally, we must comment that the RS spectrum of the released sample appears to be that of an amorphous or disordered-like α phase since the position of the broad bands is similar to the frequencies of the Raman-active phonons in the α phase (see **Fig. S5**). However, our RS spectrum of the released sample does not look similar to that of previous amorphous In_2Se_3.[66] Our RS spectrum clearly reflects a similarity with the RS spectrum of the α phase while that of Weszka et al. shows much close similarity to those of Se clusters, as already commented by Weszka *et al.*, likely due to thermal heating of their nm-size samples with the green and blue lasers.[66] Besides, we have to stress that our result shows the irreversibility of the compression process in α-In_2Se_3. This makes sense if we consider that there is a considerable rearrangement of cations, especially at the α → β′transition (7% volume reduction and "average" fivefold to sixfold coordination change for In atoms), and that the β′ phase cannot be recovered at ambient conditions in equilibrium conditions. Note the two infrared modes (A_u^1 and B_u^1) with imaginary frequency at ambient pressure in **Fig S6** of the Supporting Information. For the sake of completeness, **Fig. S6** shows the IR active modes obtained by our *ab initio* calculations. Interestingly, it shows a monotone progression from β′ to β IR modes around 10 GPa; we even see how the two lowest β′ soft IR modes coincide with the lowest IR mode of the β phase at 10 GPa. Concluding, we can say that the Raman modes of all these phases are not easy to discern, especially those of the β′ and β phases; however, we have been able to discern the phonons associated with both β′ and β phases and show that the β′→ β transition is completed around 10 GPa.

5. DISCUSSION

In order to shed light on the mechanisms of pressure-induced phase transitions in α-In_2Se_3, we have plotted two images of three phases involved by using the VESTA software (see **Fig. 7**).[67] In the images at the top, we highlight the polyhedra associated with In atoms, while in the image at the bottom the polyhedra associated with Se atoms. From these theoretical structures, we have obtained the bond distances associated with these polyhedra as a function of pressure. **Figures 8 a)** and **b)** show the evolution of the bond distances versus pressure of the polyhedra associated with the In and Se atoms of α, β' and β phases in **Fig. 7**.

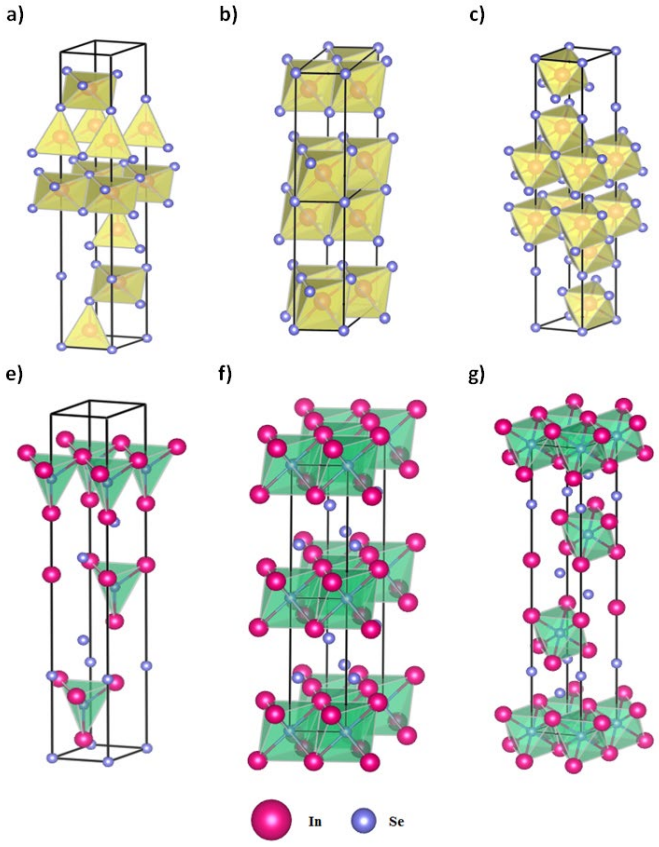

Figure 7: Schematic view of the phases of In_2Se_3 as a function of pressure. a), b), and c) images show the different polyhedra associated with In atoms in the α, β′, and β phases, respectively; while d), e), and f) images show the polyhedra associated with Se atoms at the centre of the quintuple layers in each phase.

As can be seen in **Fig. 8a)** and **8b)**, the α → β′ phase transition implies a discontinuity in the bond distances of the polyhedra associated with In and Se atoms which highlights the change in coordination for In and Se atoms already commented. On the other hand, **Fig. 9** shows two units of β′ phase highlighting the polyhedra associated with In and Se atoms. The quintuple block is showed at the bottom right corner. The β′ phase is characterized by one irregular octahedron associated with Se atoms, in the middle of the quintuple block, and another irregular octahedron associated with In atoms. These two irregular octahedra are plotted separately at the right top corner. Polyhedra associated with the In atoms has four different bond distances whereas that related to the Se atoms has only two different bond distances (see **Fig. 8a)** and **8b)**). It is noted that in β′ phase, the two polyhedra associated with In1 and In2 atoms (a

tetrahedron and an octahedron) of the α phase become equivalent since the effective coordination number of In1 atom increased. The polyhedron associated with the Se atom also increased its coordination. In other words, these two polyhedra become sixfold coordinated.

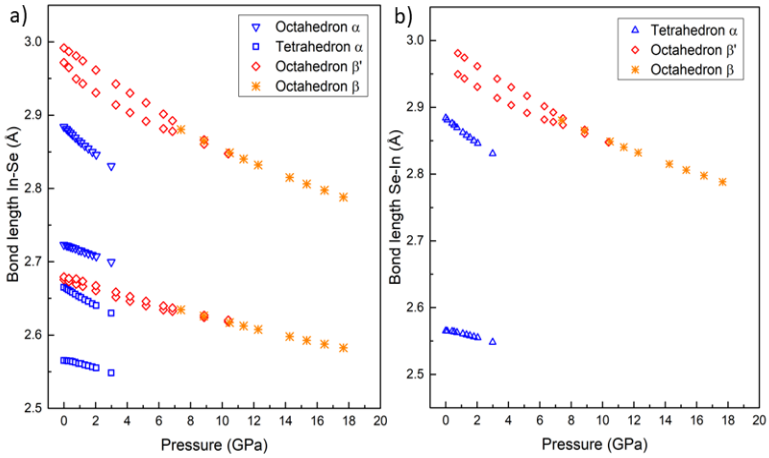

Figure 8: Pressure dependence of the In-Se bond distances for the different phases α, β' and β. a) In-Se distances associated with the polyhedral units around In atoms of Fig. 7: α phase: octahedron (empty triangle symbol) and tetrahedron (empty square symbol); β′ phase: irregular octahedron (empty rhombus symbol); β phase: regular octahedron (asterisk symbol). b) In-Se distances associated with the polyhedral units around Se atoms of Fig. 7: α phase: irregular tetrahedron (empty triangle symbol); β′ phase: irregular octahedron (empty rhombus symbol); β phase: regular octahedron (asterisk symbol).

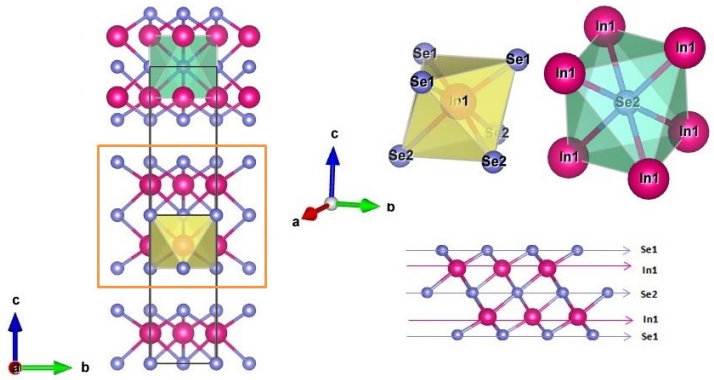

Figure 9: Detail of two unit cells of β′-In_2Se_3. Right bottom corner: the quintuple layer. Right top corner: the two irregular octahedra associated with In and Se atoms.

In turn, the β′→ β phase transition proceeds with a progressive regularization of the octahedral units associated with the In and Se atoms as pressure increases. When the transition is completed, the octahedron associated with In atoms continues being irregular but only with two different bond distances. Contrary, the octahedron associated with Se atom becomes regular (see the **Figs. 8a)** and **8b)**). It is worthy to note that values of bond distances from about 6.0 to 9.0 GPa are very close but the transition is not completed up to approximately 10 GPa according to the calculation. This pressure again is slightly higher than reported in XRD experiment of Zhao in **Ref. 39** and in accordance with our results of HP- XRD and RS.

We can conclude that the progressive regularization of the octahedra of both In and Se atoms without any discontinuity in the bond distance is an indication of the second-order character of the β'-β phase transition. The full regularization of the octahedron of the Se atom indicates the end of the transition to the *R*-3*m* phase. Both β'and β phases are energetically competitive, as it can be seen from the enthalpy difference versus pressure at a temperature 0 K of the three phases (**Fig. 10**). Despite these enthalpies are calculated at 0 K, the pressure values of the α-β′ and β′-β transitions are quite close to values obtained experimentally.

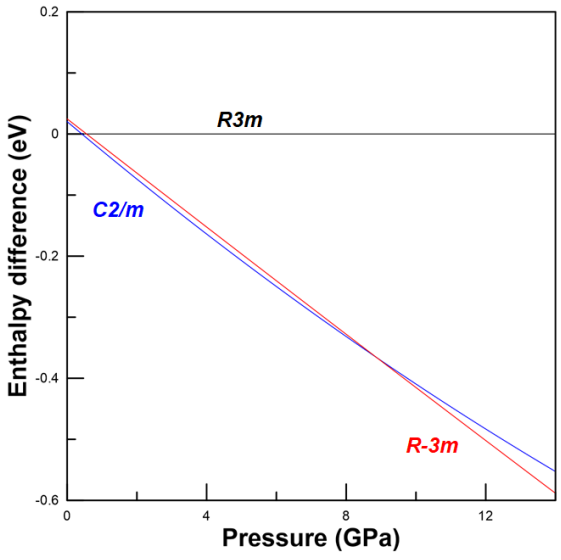

Figure 10: The enthalpy difference versus pressure at 0 K for the α, β′ and β phases of In_2Se_3.

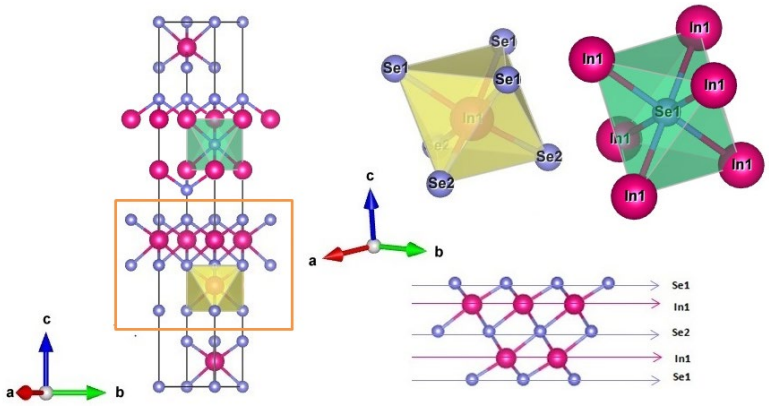

Figure 11. Detail of the hexagonal unit cell of β-In_2Se_3. Right bottom corner: quintuple layer. Right top corner: two polyhedra centered in In and Se atoms.

In **Figure 11** is shown the hexagonal unit cell of β-In_2Se_3. In addition, **Figs. 12a)** and **12b)** show the pressure dependence of the mean or "effective" coordination number (ECoN) of the octahedra of In and Se atoms in the β′ and β phases. Several proposals have been made for the calculation of ECoN by adding all surrounding atoms with number between 0 and 1. We have used that adopted in the VESTA software[68-70] whose definition is given at the Supporting Information. These two figures support that the transition from β′ to β phase is gradual and completed around 10 GPa. It is worthy to note that the effective coordination number of the octahedron associated with Se atoms reaches a constant value equal to 6, indicating the regularization of these octahedra and supporting that phase transition to the β phase is completed about 10 GPa.

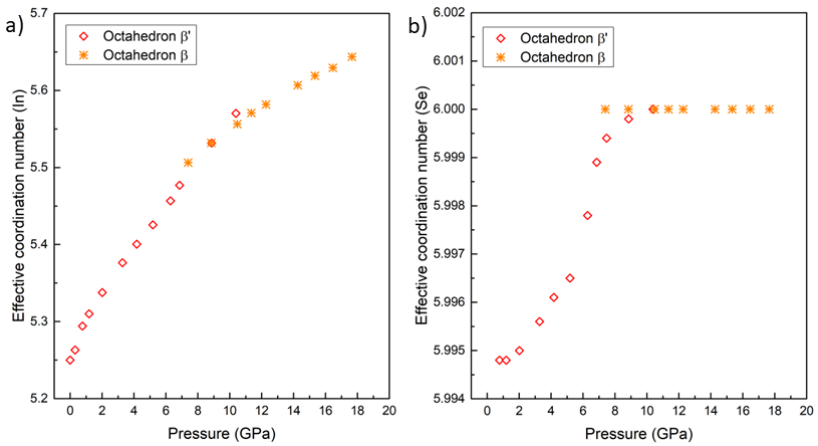

Figure 12. Pressure dependence of the effective coordination index of the octahedron associated with a) In atom and b) Se atom in β′ (empty rhombus symbol) and β (asterisk symbol) phases.

We have visualized in **Fig. 13** the atomic vibrations which are responsible for the A_g^2 (β′ phase) and A_{1g}^1 (β phase) modes with the program Jmol.[71] As observed, the central Se layer of quintuple layers keeps fixed in them and Se and In symmetric layers compress out-plane in the Ag^2 mode of the β′ phase (**Fig. 13a)**) ; however, in the A_{1g}^1 mode of the β phase, they stretch the quintuple layers (**Fig. 13b)**).

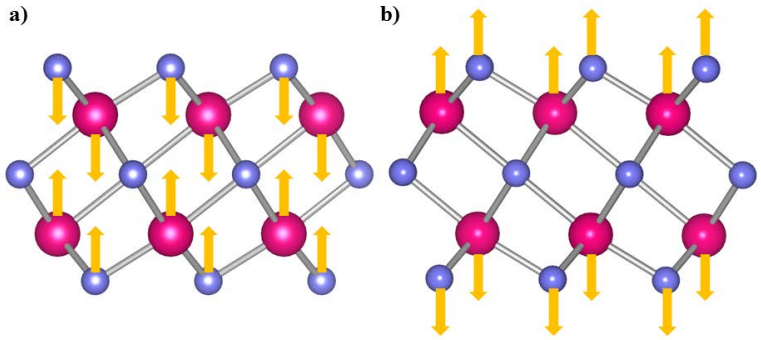

Figure 13. a) Schematic atomic displacement of A_g^2 mode of the β´phase. b) Schematic atomic displacement of A_{1g}^1 mode of the β phase.

We can conclude that the monoclinic β′ phase symmetrizes gradually until it reaches a relationship of network parameters that makes the structure rhombohedral. Once reached the high symmetry, the structure remains stable up to the highest pressure covered by our studies. A consequence of the transition mechanism is that the nature of the transition is second-order (no volume discontinuity). The fact that the β´→ β phase transition is very subtle might be the reason why Zhao *et al.* gave a transition pressure lower than us, and why Rasmussen *et al.* conclude from their RS experiment that the α → β phase transition occurs directly at about 0.7 GPa,[42] despite XRD measurements were properly conducted. Similar conclusion was reached by Ke *et al.* [43] arguing that there is a shear shift of planes in an attempt to explain the mechanism that leads directly from α to β phase. Such a claim is not plausible, given that, as we have seen above in the descriptions of the different phases, the α phase is formed by sheets of octahedra and tetrahedra centred at the In1 and In2 atoms while β phase only contains octahedra associated with In atoms. Therefore, a shift of planes cannot lead from α to β. Besides, the lack of full reversibility to the α phase clearly indicates the reconstructive character of the α → β´phase transition.

6. CONCLUSIONS

We have performed a joint experimental and theoretical study of the structural and vibrational properties of α(R)-In_2Se_3 under compression by means of X-ray diffraction and Raman scattering measurements as well as by *ab initio* total-energy and lattice-dynamics calculations. Our study has confirmed the *R*3*m* nature of the α(R) phase and the α → β′ → β sequence of pressure-induced phase transitions. Moreover, our study has allowed us to understand that the reason for the discordance in previous measurements is the second-order character of the β'-β phase transition (both phases are energetically very close in a narrow pressure region) and the

difficulty to discern between both phases from the experimental point of view. In fact, both our experimental and theoretical techniques clearly indicate that the β'-β phase transition occurs about 10-12 GPa by a gradual symmetrization of the monoclinic β' phase until it reaches a relationship of network parameters that makes the structure rhombohedral (β phase). The changes in the X-ray diffraction patterns and Raman-active modes during the β'-β phase transition are very subtle and consequently difficult to detect experimentally. That is the reason for the discordance between previous measurements. Furthermore, our Raman results and its comparison to *ab initio* calculations have allowed us to assign most of the modes of the three different phases. We hope the present work will stimulate further experiments at both high pressure and high temperature in order to clarify the thermodynamic equilibrium between β' and β phases.

7. ACKNOWLEDGMENTS

The authors acknowledge financial support from Spanish government MINECO, the Spanish Agencia Estatal de Investigacion (AEI), and Fondo Europeo de Desarrollo Regional (FEDER) under Grants No. MAT2016-75586-C4-1/2/3-P and MAT2015-710

8. REFERENCES

1. C.-H. Ho, C.-H. Lin, Y.-P. Wang, Y.-C. Chen, S.-H. Chen and Y.-S. Huang, *ACS Appl. Mater. Interfaces*, 2013, **5**, 2269-2277.
2. J. Cui, X. Liu, X. Zhang, Y. Li and Y. Deng, *J. Appl. Phys.*, 2011, **110**, 023708.
3. J. Cui, X. Zhang, Y. Deng, H. Fu, Y. Yan, Y. Gao and Y. Li, *Scr. Mater.*, 2011, **64**, 510-512.
4. H. Lee, D.-H. Kang and L. Tran, *Mater. Sci. Eng., B*, 2005, **119**, 196-201.
5. B. Yu, S. Ju, X. Sun, G. Ng, T. D. Nguyen, M. Meyyappan and D. B. Janes, *Appl. Phys. Lett.*, 2007, **91**, 133119.
6. Y.-T. Huang, C.-W. Huang, J.-Y. Chen, Y.-H. Ting, K.-C. Lu, Y.-L. Chueh and W.-W. Wu, *ACS Nano*, 2014, **8**, 9457-9462.
7. Q. Li, Y. Li, J. Gao, S. Wang and X. Sun, *Appl. Phys. Lett.*, 2011, **99**, 243105.
8. T. Zhai, X. Fang, M. Liao, X. Xu, L. Li, B. Liu, Y. Koide, Y. Ma, J. Yao and Y. Bando, *ACS Nano*, 2010, **4**, 1596-1602.
9. S. H. Kwon, B. T. Ahn, S. K. Kim, K. H. Yoon and J. Song, *Thin Solid Films*, 1998, **323**, 265-269.
10. H. Peng, D. T. Schoen, S. Meister, X. F. Zhang and Y. Cui, *J. Am. Chem. Soc.*, 2007, **129**, 34-35.
11. W. Ding, J. Zhu, Z. Wang, Y. Gao, D. Xiao, Y. Gu, Z. Zhang and W. Zhu, *Nat. Commun.*, 2017, **8**.
12. H. Peng, C. Xie, D. T. Schoen and Y. Cui, *Nano Lett.*, 2008, **8**, 1511-1516.
13. R. Sreekumar, R. Jayakrishnan, C. Sudha Kartha, K. Vijayakumar, S. Khan and D. Avasthi, *J. Appl. Phys.*, 2008, **103**, 023709.
14. M. Lin, D. Wu, Y. Zhou, W. Huang, W. Jiang, W. Zheng, S. Zhao, C. Jin, Y. Guo and H. Peng, *J. Am. Chem. Soc.*, 2013, **135**, 13274-13277.

15. Z. Wang, X. Guo, H. Li, T. Wong, N. Wang and M. Xie, *Appl. Phys. Lett.*, 2011, **99**, 023112.
16. Y. Xia, D. Qian, D. Hsieh, L. Wray, A. Pal, H. Lin, A. Bansil, D. Grauer, Y. S. Hor and R. J. Cava, *Nat. Phys.*, 2009, **5**, 398.
17. H. Zhang, C.-X. Liu, X.-L. Qi, X. Dai, Z. Fang and S.-C. Zhang, *Nat. Phys.*, 2009, **5**, 438.
18. Y. Chen, J. G. Analytis, J.-H. Chu, Z. Liu, S.-K. Mo, X.-L. Qi, H. Zhang, D. Lu, X. Dai and Z. Fang, *Science*, 2009, **325**, 178-181.
19. D. Hsieh, Y. Xia, D. Qian, L. Wray, F. Meier, J. Dil, J. Osterwalder, L. Patthey, A. Fedorov and H. Lin, *Phys. Rev. Lett.*, 2009, **103**, 146401.
20. P. Newman, *J. Phys. Chem. Solids*, 1962, **23**, 19-23.
21. H. Lutz, M. Fischer, H.-P. Baldus and R. Blachnik, *J. Less-Common Met.*, 1988, **143**, 83-92.
22. A. Pfitzner and H. Lutz, *J. Solid State Chem.*, 1996, **124**, 305-308.
23. K. Osamura, Y. Murakami and Y. Tomiie, *J. Phys. Soc. Jpn.*, 1966, **21**, 1848-1848.
24. S. Popović, A. Tonejc, B. Gržeta-Plenković, B. Čelustka and R. Trojko, *J. Appl. Crystallogr.*, 1979, **12**, 416-420.
25. G. Han, Z. G. Chen, J. Drennan and J. Zou, *Small*, 2014, **10**, 2747-2765.
26. J. Cui, L. Wang, Z. Du, P. Ying and Y. Deng, *J. Mater. Chem. C*, 2015, **3**, 9069-9075.
27. Z. Song, H. Liu, Z. Du, X. Liu and J. Cui, *phys. status solidi (a)*, 2016, **213**, 986-993.
28. G. P. Vassilev, B. Daouchi, M.-C. Record and J.-C. Tedenac, *J. Alloys Compd.*, 1998, **269**, 107-115.
29. A. Likforman, D. Carré and R. Hillel, *Acta Crystallogr., Sect. B: Struct. Crystallogr. Cryst. Chem.*, 1978, **34**, 1-5.
30. K. Kambas, C. Julien, M. Jouanne, A. Likforman and M. Guittard, *phys. status solidi (b)*, 1984, **124**.
31. R. Lewandowska, R. Bacewicz, J. Filipowicz and W. Paszkowicz, *Mater. Res. Bull.*, 2001, **36**, 2577-2583.
32. X. Tao and Y. Gu, *Nano Lett.*, 2013, **13**, 3501-3505.
33. E. Mafi, A. Soudi and Y. Gu, *J. Phys. Chem. C*, 2012, **116**, 22539-22544.
34. J. O. Island, S. I. Blanter, M. Buscema, H. S. J. van der Zant and A. Castellanos-Gomez, *Nano Letters*, 2015, **15**, 7853-7858.
35. D. Wu, A. J. Pak, Y. Liu, Y. Zhou, X. Wu, Y. Zhu, M. Lin, Y. Han, Y. Ren and H. Peng, *Nano Lett.*, 2015, **15**, 8136-8140.
36. Y. Zhou, D. Wu, Y. Zhu, Y. Cho, Q. He, X. Yang, K. Herrera, Z. Chu, Y. Han and M. C. Downer, *Nano Lett.*, 2017, **17**, 5508-5513.
37. J. Van Landuyt, G. Van Tendeloo and S. Amelinckx, *phys. status solidi (a)*, 1975, **30**, 299-314.
38. C. Manolikas, *J. Solid State Chem.*, 1988, **74**, 319-328.
39. J. Zhao and L. Yang, *J. Phys. Chem. C*, 2014, **118**, 5445-5452.
40. F. J. Manjon, R. Vilaplana, O. Gomis, E. Pérez‐González, D. Santamaría‐Pérez, V. Marín‐Borrás, A. Segura, J. González, P. Rodríguez‐Hernández and A. Munoz, *Phys. Status Solidi B*, 2013, **250**, 669-676.

41. R. Vilaplana, J. A. Sans, F. J. Manjón, A. Andrada-Chacón, J. Sánchez-Benítez, C. Popescu, O. Gomis, A. Pereira, B. García-Domene and P. Rodríguez-Hernández, *J. Alloys Compd.*, 2016, **685**, 962-970.
42. A. M. Rasmussen, S. T. Teklemichael, E. Mafi, Y. Gu and M. D. McCluskey, *Appl. Phys. Lett.*, 2013, **102**, 062105.
43. F. Ke, C. Liu, Y. Gao, J. Zhang, D. Tan, Y. Han, Y. Ma, J. Shu, W. Yang and B. Chen, *Appl. Phys. Lett.*, 2014, **104**, 212102.
44. F. Ke, H. Dong, Y. Chen, J. Zhang, C. Liu, J. Zhang, Y. Gan, Y. Han, Z. Chen and C. Gao, *Adv. Mater.*, 2017, **29**.
45. A. M. Rasmussen, E. Mafi, W. Zhu, Y. Gu and M. D. McCluskey, *High Pressure Res.*, 2016, **36**, 549-556.
46. R. Vilaplana, O. Gomis, F. J. Manjón, H. Ortiz, E. Pérez-González, J. López-Solano, P. Rodríguez-Hernández, A. Múñoz, D. Errandonea and V. Ursaki, *J. Phys. Chem. C*, 2013, **117**, 15773-15781.
47. G. Piermarini, S. Block and J. Barnett, *J. Appl. Phys.*, 1973, **44**, 5377-5382.
48. S. Klotz, J. C. Chervin, P. Munsch and G. L. Marchand, *J. Phys. D: Appl. Phys.*, 2009, **42**, 075413.
49. F. Fauth, I. Peral, C. Popescu and M. Knapp, *Powder Diffr.*, 2013, **28**, S360-S370.
50. A. Hammersley, S. Svensson, M. Hanfland, A. Fitch and D. Hausermann, *High Pressure Res.*, 1996, **14**, 235-248.
51. B. H. Toby, *J. Appl. Crystallogr.*, 2001, **34**, 210-213.
52. A. Dewaele, P. Loubeyre and M. Mezouar, *Phys. Rev. B*, 2004, **70**, 094112.
53. K. Syassen, *High Pressure Res.*, 2008, **28**, 75-126.
54. P. Hohenberg and W. Kohn, *Phys. Rev.*, 1964, **136**, B864.
55. A. Mujica, A. Rubio, A. Munoz and R. Needs, *Rev. Mod. Phys.*, 2003, **75**, 863.
56. G. Kresse and J. Furthmüller, *Phys. Rev. B*, 1996, **54**, 11169.
57. P. E. Blöchl, *Phys. Rev. B*, 1994, **50**, 17953-17979.
58. J. P. Perdew, K. Burke and M. Ernzerhof, *Phys. Rev. Lett*, 1996, **77**, 1.
59. O. Nielsen and R. M. Martin, *Phys. Rev. B*, 1985, **32**, 3780.
60. Computer Code Phonon, http://wolf.ifj.edu.pl/phonon/).
61. D. Errandonea, R. Kumar, O. Gomis, F. J. Manjón, V. Ursaki and I. Tiginyanu, *J. Appl. Phys.*, 2013, **114**, 233507.
62. J. Gleissner, D. Errandonea, A. Segura, J. Pellicer-Porres, M. Hakeem, J. Proctor, S. Raju, R. Kumar, P. Rodríguez-Hernández and A. Muñoz, *Phys. Rev. B*, 2016, **94**, 134108.
63. D. Errandonea, R. Kumar, S. Achary, O. Gomis, F. J. Manjón, R. Shukla and A. Tyagi, *J. Appl. Phys.*, 2012, **111**, 053519.
64. D. Errandonea, *Europhys. Lett.*, 2007, **77**, 56001.
65. D. Errandonea, D. Martínez-García, A. Segura, J. Haines, E. Machado-Charry, E. Canadell, J. Chervin and A. Chevy, *Phys. Rev. B*, 2008, **77**, 045208.
66. J. Weszka, P. Daniel, A. Burian, A. Burian and A. Nguyen, *J. Non-Cryst. Solids*, 2000, **265**, 98-104.
67. K. Momma and F. Izumi, *J. Appl. Crystallogr.*, 2011, **44**, 1272-1276.

68. K. Robinson, G. Gibbs and P. Ribbe, *Science*, 1971, **172**, 567-570.
69. R. Hoppe, *Z. Kristallogr. Cryst. Mater.*, 1979, **150**, 23-52.
70. R. Hoppe, S. Voigt, H. Glaum, J. Kissel, H. P. Müller and K. Bernet, *J. Less-Common Met.*, 1989, **156**, 105-122.
71. Jmol: an open-source Java viewer for chemical structures, http://jmol.sourceforge.net).

Supporting Information

Experimental and theoretical studies on α-In_2Se_3 at high pressure

Rosario Vilaplana[1*], Samuel Gallego Parra[2], Alejandro Jorge-Montero [3], Plácida Rodríguez-Hernández[3], Alfonso Munoz[3], Daniel Errandonea[4], Alfredo Segura[4] and Francisco Javier Manjón[2]

[1]Centro de Tecnologías Físicas, Universitat Politècnica de València, 46022 Valencia (Spain)
[2] Instituto de Diseño para la Fabricación y Producción Automatizada, Universitat Politècnica de València, 46022 Valencia (Spain)
[3]Departamento de Física, Instituto de Materiales y Nanotecnología, MALTA Consolider Team, Universidad de La Laguna, 38207 San Cristóbal de La Laguna, Spain
[4]Departamento de Física Aplicada-ICMUV, MALTA Consolider Team, Universidad de Valencia, Edificio de Investigación, C/Dr. Moliner 50, 46100 Burjassot, Spain
*Corresponding author: R. Vilaplana (rovilap@fis.upv.es)

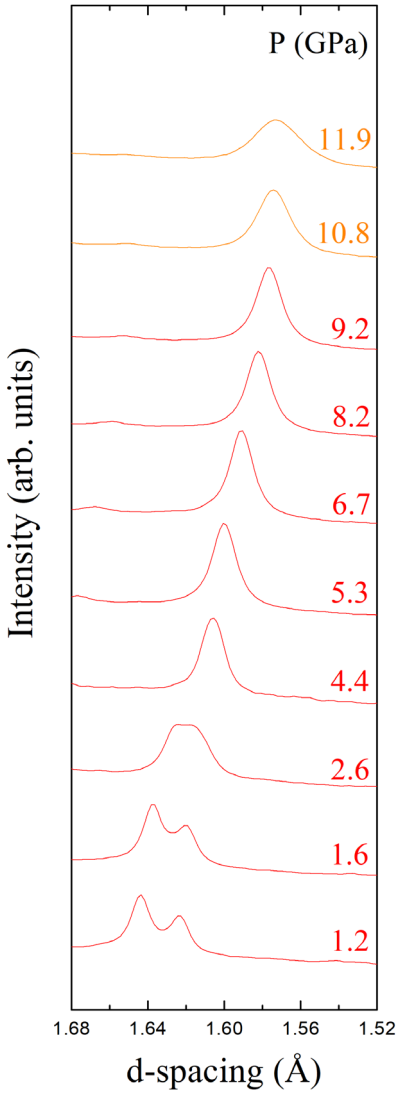

Figure S1. Selected x-ray powder diffraction patterns of β'- and β-In_2Se_3 under compression. Red and orange lines indicate some reflections between 1.68 and 1.52 of the d-spacing of the β' and β phases, respectively.

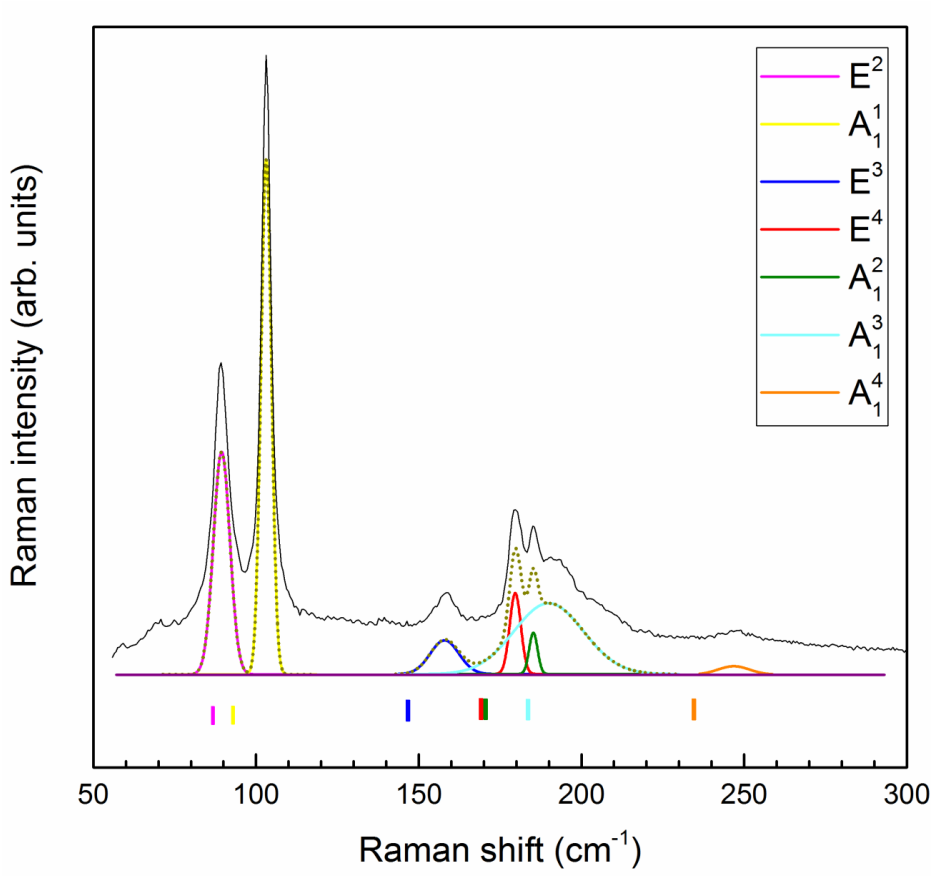

Figure S2. Raman spectrum of α-In_2Se_3 at room pressure. Bottom marks represent the theoretical frequencies at 0 GPa for identification of the Raman-active modes of the α phase. Due to its low frequency, E^1 mode has not been observed experimentally.

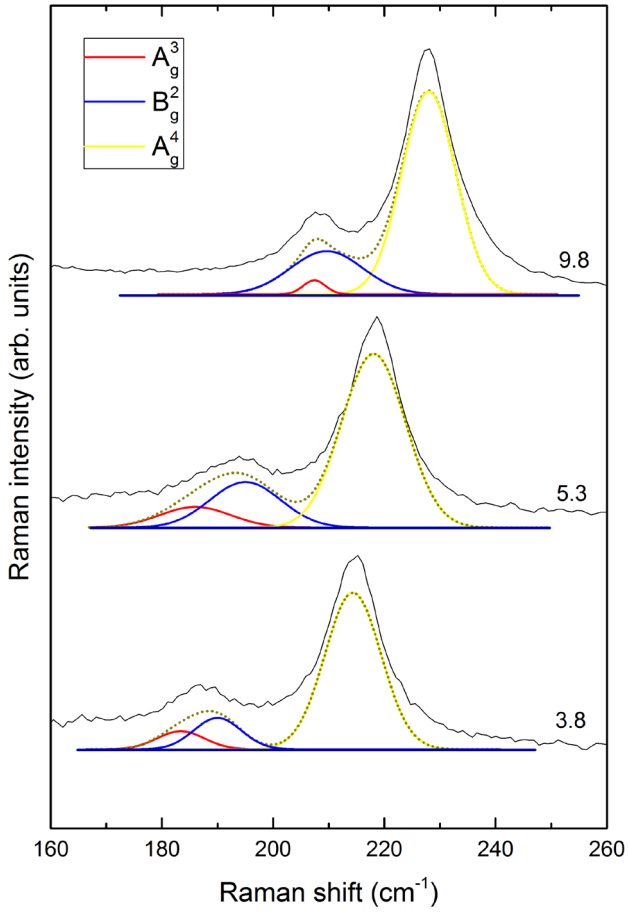

Figure S3. Detail of the RS spectra of the β´ phase at different pressures, where A_g^3 and B_g^2 modes are resolved, providing evidence of the stability of this phase up to 10 GPa. The A_g^4 mode is resolved for its proximity to the previous coupled modes as well.

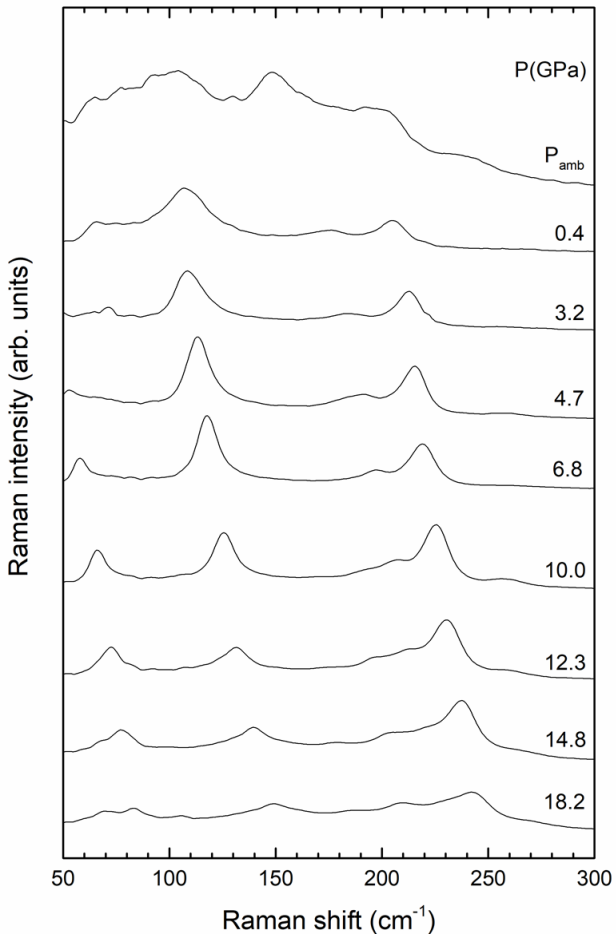

Figure S4. Raman spectra of In_2Se_3 at different pressures on downstroke from 20 GPa.

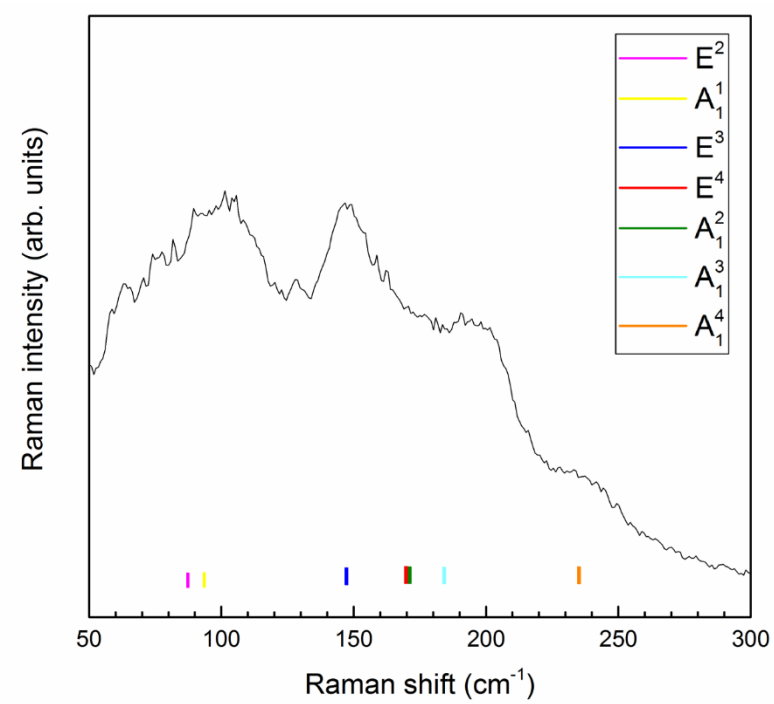

Figure S5. Detail of the Raman spectrum of In_2Se_3 at room pressure after decreasing pressure. Marks represent the theoretical frequencies of Raman-active modes of the α phase at 0 GPa.

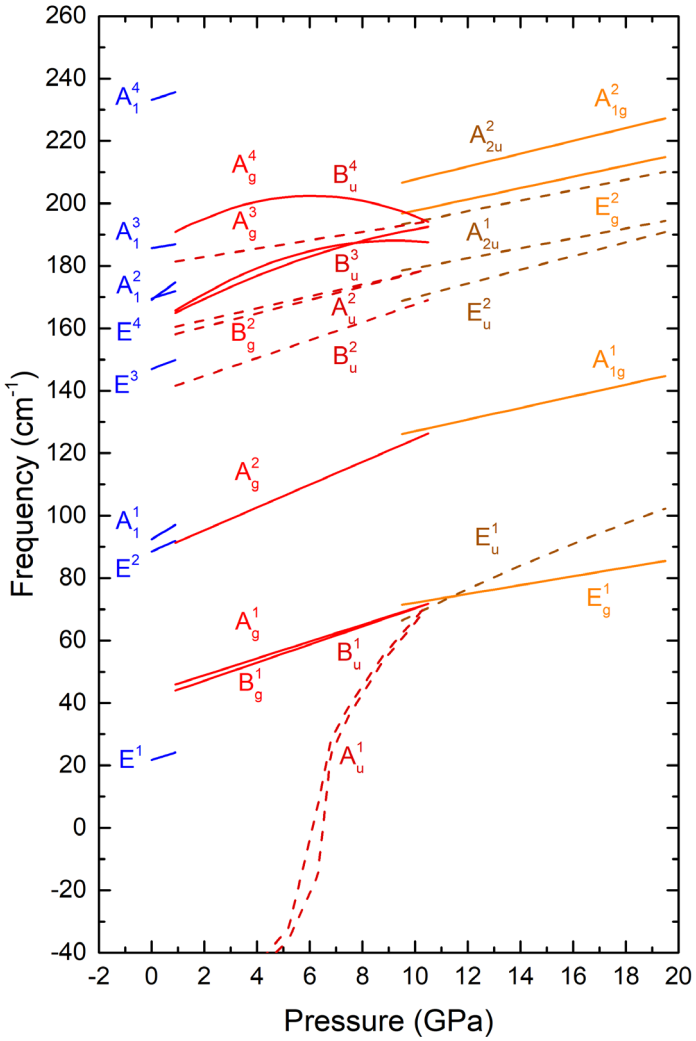

Figure S6. Pressure dependence of the theoretical frequencies of Raman-active (continuous lines) and IR-active (dash lines) modes of the α, β' and β phases in blue, red and orange, respectively. Modes of α phase are both Raman and IR.

Table S1: Experimental lattice parameters and unit cell volumes at different pressure up to 20.2 GPa of In_2Se_3.

Phase I	***R3m* (Z=3)**				
P (GPa)	**a_I(Å)**		**c_I(Å)**		**V_I(Å^3)**
0.001	4.028(1)		28.731(6)		403.8(2)
0.3(1)	4.018(1)		28.666(6)		400.8(2)
0.5(1)	4.012(1)		28.622(6)		399.0(2)
Phase II	***C*2/*m* (Z =2)**				
	a_{II}(Å)	**b_{II}(Å)**	**c_{II}(Å)**	**β**	**V_{II}(Å^3)**
1.2(1)	6.828(2)	3.973(1)	9.419(3)	103.25(3)	248.7(2)
1.6(1)	6.819(2)	3.967(1)	9.395(3)	103.25(3)	247.4(2)
4.4(1)	6.763(2)	3.928(1)	9.231(3)	103.30(3)	238.6(2)
5.3(1)	6.745(2)	3.916(1)	9.178(3)	103.32(3)	235.9(2)
6.7(1)	6.717(2)	3.896(1)	9.096(3)	103.34(3)	231.6(2)
8.2(1)	6.687(2)	3.876(1)	9.008(3)	103.37(3)	227.1(2)
9.2(1)	6.667(2)	3.862(1)	8.950(3)	103.39(3)	224.2(2)
10.8(1)	6.635(2)	3.840(1)	8.856(3)	103.42(3)	219.5(2)
11.9(1)	6.613(2)	3.825(1)	8.792(3)	103.44(3)	216.3(2)
Phase III	***R*-3*m* (Z=3)**				
	a_{III}(Å)		**c_{III}(Å)**		**V_{III}(Å^3)**
12.7(1)	3.832(2)		25.16(1)		319.9(5)
14.2(1)	3.823(2)		24.88(1)		314.9(5)
15.1(1)	3.819(2)		24.72(1)		312.2(5)
16.6(1)	3.810(2)		24.44(1)		307.3(5)
18.2(1)	3.802(2)		24.14(1)		302.3(5)
19.2(1)	3.796(2)		23.96(1)		299.1(5)
20.2(1)	3.791(2)		23.78(1)		295.9(5)

Effective coordination number (ECoN)

The mean or ′effective′ coordination number (ECoN) is defined as

$$ECoN = \sum_i w_i \text{ where } w_i = exp\left[1 - \left(\frac{l_i}{l_{av}}\right)^6\right] \text{ and } l_{av} = \frac{\sum_i l_i exp\left[1-\left(\frac{l_i}{l_{min}}\right)^6\right]}{\sum_i exp\left[1-\left(\frac{l_i}{l_{min}}\right)^6\right]}$$

being the l_{min} the smallest bond length in the coordination polyhedron

PCCP

ROYAL SOCIETY OF CHEMISTRY

PAPER

View Article Online
View Journal

Cite this: DOI: 10.1039/d0cp06417c

Structural, vibrational and electronic properties of α′-Ga_2S_3 under compression†

S. Gallego-Parra, *[a] R. Vilaplana,*[b] O. Gomis, [b] E. Lora da Silva,[ac] A. Otero-de-la-Roza,[d] P. Rodríguez-Hernández,[e] A. Muñoz,[e] J. González,[f] J. A. Sans, [a] V. P. Cuenca-Gotor, [a] J. Ibáñez,[g] C. Popescu [h] and F. J. Manjón [a]

Received 11th December 2020,
Accepted 23rd February 2021

DOI: 10.1039/d0cp06417c

rsc.li/pccp

We report a joint experimental and theoretical study of the low-pressure phase of α′-Ga_2S_3 under compression. Theoretical *ab initio* calculations have been compared to X-ray diffraction and Raman scattering measurements under high pressure carried out up to 17.5 and 16.1 GPa, respectively. In addition, we report Raman scattering measurements of α′-Ga_2S_3 at high temperature that have allowed us to study its anharmonic properties. To understand better the compression of this compound, we have evaluated the topological properties of the electron density, the electron localization function, and the electronic properties as a function of pressure. As a result, we shed light on the role of the Ga–S bonds, the van der Waals interactions inside the channels of the crystalline structure, and the single and double lone electron pairs of the sulphur atoms in the anisotropic compression of α′-Ga_2S_3. We found that the structural channels are responsible for the anisotropic properties of α′-Ga_2S_3 and the A′(6) phonon, known as the breathing mode and associated with these channels, exhibits the highest anharmonic behaviour. Finally, we report calculations of the electronic band structure of α′-Ga_2S_3 at different pressures and find a nonlinear pressure behaviour of the direct band gap and a pressure-induced direct-to-indirect band gap crossover that is similar to the behaviour previously reported in other ordered-vacancy compounds, including β-Ga_2Se_3. The importance of the single and, more specially, the double lone electron pairs of sulphur in the pressure dependence of the topmost valence band of α′-Ga_2S_3 is stressed.

Introduction

Research on Ga_2S_3 chalcogenide has increased in recent years due to its promising properties in different applications. For instance, the high specific capacity of Ga_2S_3 (theoretically estimated to be 682–1591 mA h g^{-1})[1–4] makes it a promising anode material candidate in the field of Na-ion batteries, an alternative to the well-known commercial Li-ion batteries. In this context, recently synthesized Ga_2S_3 rods mixed with graphene have shown a reversible specific capacity of 476 mA h g^{-1} (100 cycles, current density 0.4 A g^{-1}).[5] On the other hand, many GaS_4-tetrahedron-based compounds, such as $AgGaGeS_4$,[6] $LiGaS_2$[7] and $Li_2Ga_2GeS_6$,[8] have exhibited large second-harmonic generation (SHG) efficiency and high laser-induced damage threshold (LIDT), necessary for nonlinear optical (NLO) devices. It has been demonstrated that the major contribution to the high birefringence, high SHG and high LIDT in chalcopyrites $AgGaX_2$ and $LiGaX_2$ (X = S, Se, Te) comes from the GaX_4 tetrahedra.[9,10] These results have motivated a systematic research on Ga_2S_3 itself[11] that has proved that both α′ (monoclinic, space group (S.G.) *Cc*, No. 9, $Z = 4$) and γ (cubic "sphalerite", S.G. $F\bar{4}3m$, No. 216) phases have good optical transparency in the IR region and large NLO effects, with SHGs and LIDTs competitive with commercial NLO materials, like $KTiOPO_4$ and $AgGaS_2$. In a wider perspective of the optoelectronic industry, Ga_2S_3 is a wide-band semiconductor (2.5–3.4 eV)[12,13] suitable for a wealth of applications, such as emitters from the

[a] *Instituto de Diseño para la Fabricación y Producción Automatizada, MALTA Consolider Team, Universitat Politècnica de València, 46022 València, Spain. E-mail: sagalpar@doctor.upv.es, rovilap@fis.upv.es*
[b] *Centro de Tecnologías Físicas, MALTA Consolider Team, Universitat Politècnica de València, 46022 Valencia, Spain*
[c] *IFIMUP, Department of Physics and Astronomy, Faculty of Science, University of Porto, Portugal*
[d] *Departamento de Química Física y Analítica, MALTA Consolider Team, Facultad de Química, Universidad de Oviedo, 33006 Oviedo, Spain*
[e] *Departamento de Física, Instituto de Materiales y Nanotecnología, MALTA Consolider Team, Universidad de La Laguna, 38207 San Cristóbal de La Laguna, Spain*
[f] *Ciencias de la Tierra y Física de la Materia Condensada, MALTA Consolider Team, Universidad de Cantabria, 39005, Santander, Spain*
[g] *Institute of Earth Sciences Jaume Almera, MALTA Consolider Team, Consell Superior d'Investigacions Científiques (CSIC), 08028 Barcelona, Catalonia, Spain*
[h] *ALBA-CELLS, MALTA Consolider Team, 08290 Cerdanyola del Valles (Barcelona), Catalonia, Spain*

† Electronic supplementary information (ESI) available. See DOI: 10.1039/d0cp06417c

Structural, vibrational and electronic properties of α'-Ga_2S_3 under compression

S. Gallego-Parra[1]*, R. Vilaplana[2]*, O. Gomis[2], E. Lora da Silva[1,3], A. Otero-de-la-Roza[4], P. Rodríguez-Hernández[5], A. Muñoz[5], J. González[6], J.A. Sans[1], V.P. Cuenca-Gotor[1], J. Ibáñez[7], C. Popescu[8] and F. J. Manjón[1]

[1]*Instituto de Diseño para la Fabricación y Producción Automatizada, MALTA Consolider Team, Universitat Politècnica de València, 46022 València, Spain*
[2] *Centro de Tecnologías Físicas, MALTA Consolider Team, Universitat Politècnica de València, 46022 Valencia, Spain*
[3]*IFIMUP, Department of Physics and Astronomy, Faculty of Science, University of Porto, Portugal*
[4]*Departamento de Química Física y Analítica, MALTA Consolider Team, Facultad de Química, Universidad de Oviedo, 33006 Oviedo, Spain*
[5]*Departamento de Física, Instituto de Materiales y Nanotecnología, MALTA Consolider Team, Universidad de La Laguna, 38207 San Cristóbal de La Laguna, Spain*
[6]*Ciencias de la Tierra y Fisica de la Materia Condensada, MALTA Consolider Team, Universidad de Cantabria, 39005, Santander, Spain*
[7] *Institute of Earth Sciences Jaume Almera, MALTA Consolider Team, Consell Superior d'Investigacions Científiques (CSIC), 08028 Barcelona, Catalonia, Spain*
[8]*ALBA-CELLS, MALTA Consolider Team, 08290 Cerdanyola del Valles (Barcelona), Catalonia, Spain*

*Corresponding authors: S. Gallego-Parra (sagalpar@doctor.upv.es), R. Vilaplana (rovilap@fis.upv.es)

ABSTRACT

We report a joint experimental and theoretical study of the low-pressure phase of α'-Ga_2S_3 under compression. Theoretical *ab initio* calculations have been compared to X-ray diffraction and Raman scattering measurements under high pressure carried out up to 17.5 and 16.1 GPa, respectively. In addition, we report Raman scattering measurements of α'-Ga_2S_3 at high temperature that have allowed us to study its anharmonic properties. To understand better the compression of this compound, we have evaluated the topological properties of the electron density, the electron localization function, and the electronic properties as a function of pressure. As a result, we shed light on the role of the Ga-S bonds, the van der Waals interactions inside the channels of the crystalline structure, and the single and double lone electron pairs of the sulphur atoms in the anisotropic compression of α'-Ga_2S_3. We found that the structural channels are responsible for the anisotropic properties of α'-Ga_2S_3 and the *A'*(6) phonon, known as the breathing mode and associated with these channels, exhibits the highest anharmonic behaviour. Finally, we report calculations of the electronic band structure of α'-Ga_2S_3 at different pressures and find a nonlinear pressure behaviour of the direct band gap and a pressure-induced direct-to-indirect

band gap crossover that is similar to the behaviour previously reported in other ordered-vacancy compounds, including β-Ga_2Se_3. The importance of the single and, more specially, the double lone electron pairs of sulphur in the pressure dependence of the topmost valence band of α'-Ga_2S_3 is stressed.

1. INTRODUCTION

Research on Ga_2S_3 chalcogenide has increased in recent years due to its promising properties in different applications. For instance, the high specific capacity of Ga_2S_3 (theoretically estimated to be 682–1591 mAh g^{-1})[1-4] makes it a promising anode material candidate in the field of Na-ion batteries, an alternative to the well-known commercial Li-ion batteries. In this context, recently synthesized Ga_2S_3 rods mixed with graphene have shown a reversible specific capacity of 476 mAh g^{-1} (100 cycles, current density 0.4 A g^{-1}).[5] On the other hand, many GaS_4-tetrahedron-based compounds, such as $AgGaGeS_4$,[6] $LiGaS_2$[7] and $Li_2Ga_2GeS_6$,[8] have exhibited large second-harmonic generation (SHG) efficiency and high laser-induced damage threshold (LIDT), necessary for nonlinear optical (NLO) devices. It has been demonstrated that the major contribution to the high birefringence, high SHG and high LIDT in chalcopyrites $AgGaX_2$ and $LiGaX_2$ (*X*=S, Se, Te) comes from the GaX_4 tetrahedra.[9,10] These results have motivated a systematic research on Ga_2S_3 itself[11] that has proved that both α' (monoclinic, space group (S.G.) *Cc*, No. 9, Z=4) and y (cubic "sphalerite", S.G. F-43*m*, No. 216) phases have a good optical transparency in the IR region and large NLO effects, with SHGs and LIDTs competitive with commercial NLO materials, like $KTiOPO_4$ and $AgGaS_2$. In a wider perspective of the optoelectronic industry, Ga_2S_3 is a wide-band semiconductor (2.5-3.4 eV)[12, 13] suitable for a wealth of applications, such as emitters from near IR to blue region,[14-17] UV optical absorbers,[18] Terahertz receivers,[19-21] photovoltaic devices,[22, 23] gas sensors,[24, 25] micro-tunable lasers,[26] and fluorescent probe materials.[27]

All the above applications reveal the great versatility of Ga_2S_3 and open exciting prospects for inexpensive, non-toxic, and abundant-element-based devices. Therefore, understanding the behavior of the different phases of Ga_2S_3 is necessary. According to the Ga-S phase diagram,[28, 29] the α' phase is the stable polymorph at room conditions and melts congruently at 1300 K. At high temperatures (HTs) and non-stoichiometric compositions, three phases are found: y phase between 1130-1180 K; α (hexagonal, S.G. $P6_1$, No. 161) and β (hexagonal "wurtzite", S.G. $P6_3mc$, No. 186) phases between 1190 and 1300 K depending on the excess of Ga.[30] Due to the tendency of Al, Ga and In atoms to show four-fold coordination when linked to S, Se and Te atoms, such as in zincblende-like binary *AX* compounds, like GaS, GaSe and GaTe or zincblende-related ternary ABX_2 compounds, like chalcopyrite $AgGaS_2$, $AgGaSe_2$ and $AgGaTe_2$, 1/3 of cations sites are empty in the four existing phases with Ga_2S_3 stoichiometry due to the mismatch between the number of cations and anions. The same occurs in zincblende-related defect chalcopyrite $CdGa_2S_4$, $CdGa_2Se_4$ and $CdGa_2Te_4$ and other chalcogen-based ordered-vacancy compounds (OVCs).[31-33] However, only the α' phase exhibits an ordered array of these cation vacancies. The S atoms are distributed in an almost hexagonal close-packed arrangement in α', α and β phases while they are in a cubic close-packed fashion in the y phase. In fact, α' and

α phases are superstructures of the β phase, which means that Ga sites determine the resulting structure.[34] In fact, if vacancies of the α' phase were filled with cations, we would obtain a distorted wurtzite lattice;[32, 34] i.e. we would reproduce the β phase of Ga_2S_3 but without disordered vacancy arrays.

Figure 1a) shows the monoclinic unit cell of the α' phase. This phase has 5 independent atoms, two Ga (Ga1 and Ga2) and three S (S1, S2 and S3), all occupying 4*a* Wyckoff positions. Vacancies (V) are also represented in **Fig. 1a)**. Both Ga cations are four-fold coordinated, with Ga1 atoms linked to two S1, one S2 and one S3 atoms and Ga2 atoms linked to one S1, two S2 and one S3 atoms. In contrast, the three S atoms are coordinated differently. S1 and S2 are three-fold coordinated, S1 is linked to two Ga1 and one Ga2 atom and S2 is linked to one Ga1 and two Ga2 atoms. In turn, S3 is two-fold coordinated to one Ga1 and one Ga2 atoms. Based on the coordination of Ga and S atoms observed in **Fig. 1a)** and according to the Lewis diagrams (see **Fig. 1b)**), one of the Ga-S bonds in the GaS_4 tetrahedra should be a dative bond. Furthermore, another feature (not emphasized in the literature) must be highlighted: S1 and S2 atoms have one lone electron pair (LEP), while S3 atoms have two LEPs. The greater electrostatic repulsion of these LEPs in comparison to bonded electron pairs[35] explain the decrease in symmetry and the distortion of the S arrangement with respect to the hexagonal wurtzite lattice. In particular, the LEPs give rise to empty channels lying along the *c* axis and pointing towards the ordered cation vacancies (see **Figs. 1c)** and **d)**).[36, 37]

Several efforts have been made to explore the temperature-composition phase diagram of the Ga-S system at room pressure; however, little information is available about the Ga-S system at high pressure (HP). To our knowledge, only two studies have addressed the behaviour of Ga_2S_3 at HP.[38] Using *in situ* X-ray diffraction (XRD) and X-ray near edge structure (XANES) measurements supported by theoretical simulations, a pressure-induced phase transition from the monoclinic α' phase to the rhombohedral tetradymite-type structure (S.G. *R-3m*) was observed at 16 GPa and 1300 K.[38] Curiously, the pressure-induced stabilization of the tetradymite-like phase under pressure was also observed in other A_2X_3 compounds, as α(R)-In_2Se_3.[39] Moreover, the tetradymite-like phase is the typical phase at room conditions of heavy group-15 sesquichalcogenides (β-As_2Te_3, Sb_2Te_3, Bi_2Se_3 and Bi_2Te_3) with exceptional thermoelectric properties and is strongly related to their recently discovered topological insulating properties.[40] A most recent publication has reported Raman scattering (RS) and electrical conductivity measurements under HP, showing that the α'-Ga_2S_3 undergoes to a semiconductor-metal transformation at 11.3 (17.2) GPa under hydrostatic (non-hydrostatic) condition at room temperature.[41] Such phase at those pressures was associated to the *R*-3*m* phase, according to the previous Lai *et al.*'s results.[38] On top of that, two HP transitions have been observed under decompression, at around 8.0 and 3.0 GPa for both hydrostatic and non-hydrostatic conditions.[41] However, the lack of XRD measurements on downstroke hamper a clear identification of such polymorphs.

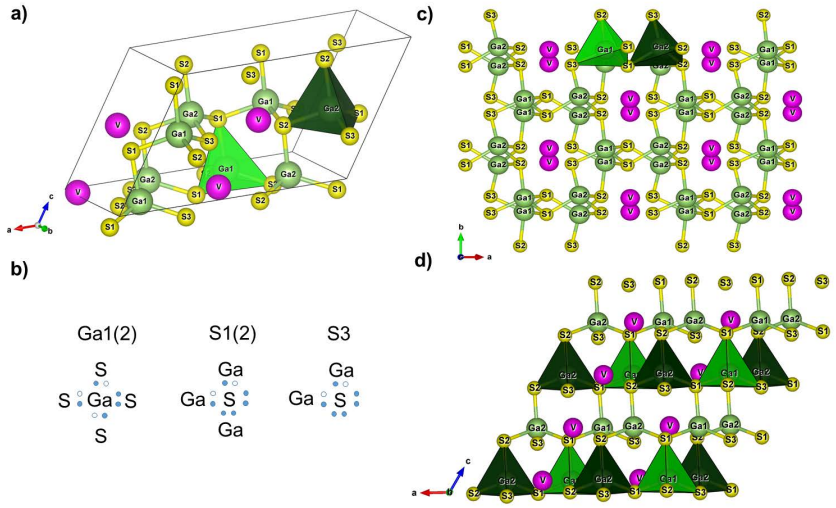

Figure 1. a) Perspective view of α'-Ga_2S_3. Green, yellow and pink balls represent Ga atoms, S atoms and vacancies, respectively. Ga atoms are four-fold coordinated while S1 and S2 atoms on one hand and S3 atoms on the other hand are three- and two-fold coordinated, respectively. b) Lewis dot diagrams for Ga and S atoms and their nearest bonded neighbour atoms. c) View of the α' phase perpendicular to the *c* axis. The arrangement of the vacancies forms the channels along the *c* axis. d) View of the α' phase perpendicular to the *b* axis. Layers based on GaS_4 tetrahedra parallel to the *a*-*b* plane are stacked along the *c* axis; i.e. coincident with the direction of the channels. When vacancies are included, the strong resemblance of the monoclinic structure of the α' phase with the wurtzite structure can be observed.

Cationic LEPs present on oxides and chalcogenides of groups 14 (Ge, Sn and Pb) and 15 (As, Sb and Bi) have been the subject of multiple studies under HP.[42-45] Stereochemically-active cationic LEPs (formed from the cation *s* valence electron pair) occur when the empty p orbital of the cation hybridizes with the antibonding cation *s*-anion *p* orbital. This stabilization is promoted by the small energy separation between the cationic *s* and anionic *p* orbitals.[46] This usually occurs when cations are linked to light chalcogen anions, such as O and S. For Se and Te, with a higher energy of anionic *p* orbitals, the s-p mixing is smaller and cationic inert LEPs are preferred. This seems to be the reason why the rhombohedral layered tetradymite-like structure is present in Sb_2Te_3, Bi_2Se_3 and Bi_2Te_3, as already commented. The behaviour of anionic LEPs at HP has not been studied in these layered chalcogenides and in other chalcogenides with single LEPs, like ordered vacancy compounds (OVCs).[31, 47] For example, in molecular solids like S_8 [48] and thioarsenide molecular crystals As_4S_n (n = 3, 4 and 5)[48], their HP behaviour has been studied,[49-53] but the role played by the double LEPs present in such structures under compression has not been clarified. In this context, we consider that a detailed study of the properties of α'-Ga_2S_3 under compression has not been done. More specifically, the role of the channel-like structure of the vacancies formed by the single and double LEPs of S atoms in the anisotropic compression of the α' phase has not been studied. Therefore, the presence

of single and double LEPs of S atoms in α'-Ga_2S_3 makes this compound an ideal system to evaluate the influence of these two different stereochemically-active anionic LEPs on the pressure behaviour of α'-Ga_2S_3 and could shed light on the behaviour of anionic LEPs in other solids under compression.

The present work is devoted to the study of the structural, vibrational and electronic properties of the α' phase of Ga_2S_3 at HP and addresses the following points: 1) the study of the structural and vibrational properties by means of HP-XRD and HP-RS measurements, complemented with *ab initio* simulations; 2) the study of anharmonic properties arising from the joint study of the HP-RS and HT-RS measurements; 3) the characterization of the different chemical bonds and interactions and the relevance of the single and double LEPs at HP via the Quantum Theory of Atoms In Molecules (QTAIM) and electron localization function (ELF) analysis at different pressures; and finally 4) the understanding of the electronic properties under compression via *ab initio* simulations.

2. EXPERIMENTAL DETAILS

Commercial powders of α'-Ga_2S_3 were purchased from Alfa Aesar, with a high purity (99.99%). For HP measurements, powders were loaded in a 150-μm diameter hole made in an Inconel gasket and inserted in a membrane-type diamond-anvil cell with 350 μm diamond-culet diameter. A 4:1 methanol-ethanol mixture was used as a pressure-transmitting medium (PTM).[54]

Room-temperature powder angle-dispersive HP-XRD measurements up to 17.5 GPa, with cooper as a pressure sensor,[55] were carried out in the BL04-MSPD beamline at ALBA synchrotron facility.[56] The beam was focused by Kirkpartrick-Baez mirrors and images were collected using a Rayonix SX165 CCD detector, with a diameter active area of 165 mm, located at 240 mm from the sample. XRD measurements were performed with a wavelength of 0.4246 Å. The 2D x-ray diffraction area detector data and the calibration with standard LaB_6 were performed with the Python-based DIOPTAS software.[57] Le Bail method was employed in our refinements with the software GSAS-II.[58]

Unpolarized HP-RS measurements up to 16.1 GPa were carried out with a LabRAM HR UV Raman microspectrometer with a thermoelectrically cooled CCD camera and a spectral resolution better than 2 cm^{-1}. Excitation of Raman signal was performed using the He:Ne line (632.8 nm) with a power below 1 mW. The applied pressure was determined by the ruby luminescence method.[59] Raman peaks have been fitted to Voigt profiles, where the spectrometer resolution is taken as the fixed Gaussian width.

3. THEORETICAL DETAILS

Density functional theory (DFT)[60] calculations of α'-Ga_2S_3 have been carried out with the Vienna Ab-initio Simulation Package (VASP).[61] The projected augmented wave (PAW) potentials[62, 63] have been used to describe valence electrons of Ga ($4s^2 3d^{10} 4p^1$) and S ($3s^2 3p^4$) atoms, taking into account the full nodal character of the all-electron charge density in the core region but with an affordable basis-set. Calculations were performed with the generalized gradient approximation (GGA) of Perdew-Burke-

Ernzenhof revised for solids (PBEsol).[64] A plane-wave kinetic-energy cutoff of 380 eV was defined in order to achieve highly converged results. For each relaxed structure, calculations were performed with the automatic k-point generation method included in the VASP package using l=30, that provides a dense special k-mesh of 6x6x5, with Hellman-Feynman forces smaller than 0.006 eV/Å per atom and deviations of the stress tensor from the diagonal hydrostatic form smaller than 0.1 GPa.

Lattice-dynamic calculations of transversal optical (TO) modes were performed at the zone center (Γ-point) of the Brillouin zone. The direct force-constant approach (or supercell method) with the primitive cell was employed for the calculation of the dynamical matrix at the Γ-point.[61, 65] In order to obtain the phonon density of states, a 4x4x4 supercell was used.

The DFT charge densities were analysed with the Critic2 program.[66] The Yu-Trinkle method,[67] implemented in Critic2, was employed to calculate Bader atomic charges and atomic volumes using VASP output files (CHGCAR and AECCAR files). In order to guarantee a smooth pressure behaviour of the topological properties at the bond critical points (BCPs), VASP-optimized structures were recalculated using the linearized augmented plane-waves (LAPW) method implemented in the Elk program, version 6.3.02.[68] For the ELK calculations, we used a 2 x 2 x 2 uniform k-point grid, R_{min} x max $\{|G + k|\}$ equal to 9 and $R^{MT} = 2.4$ a.u. and 2.2 a.u. for Ga and S atoms, respectively. At each pressure, the number of critical points fulfils the Morse zero-sum condition. The kinetic, potential and total energy densities were calculated using the Thomas-Fermi approximation, with the semiclassical gradient correction proposed by Kirzhnits.[69, 70] Finally, the positions of the ELF maxima were located using Critic2 and ELF isosurfaces were obtained with VESTA software[71] by reading the cube files written by Critic2 from ELF3D.OUT files of Elk.

4. STRUCTURAL PROPERTIES UNDER COMPRESSION

Figure 2 shows selected HP-XRD patterns of the α' phase at HP up to 17.5 GPa. At 0.1 GPa, we can distinguish several diffraction peaks at angles below 12 degrees that belong only to the α' phase (at around 4.6, 5.2, 7.0, 7.6, 8.1, 8.9, 11.1 and 11.9 degrees) in good agreement with a previous HP study.[38] Above 12 degrees, our diffraction peaks from the α' phase are overlapped with those from an impurity that was also observed in a previous HP work using commercial powder.[38] Such impurity has been identified as Ga_2O_3 in the commercial sample. For further details, the authors are referred to the Supporting Information (SI) (see **Fig. S1** in the SI). To avoid misunderstanding, we include in **Fig. 2** tick marks for the phases of Ga_2S_3 and Ga_2O_3 and also Cu reflections at certain pressures. It can be observed that emerging diffraction peaks observed at HP come from the splitting of those peaks overlapped from Ga_2O_3 and the α' phase.

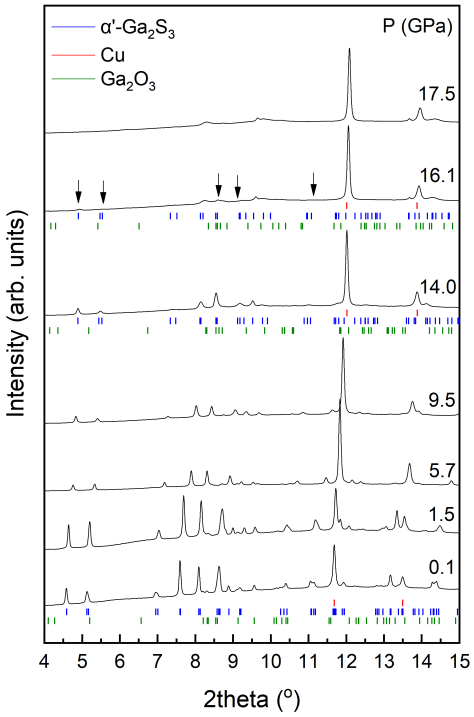

Figure 2. (Color online) Selected XRD patterns of α'-Ga_2S_3 at several pressures. Tick marks corresponding to the α' phase, impurity and Cu reflections are added at a few pressures to enlighten the appearance/disappearance of diffraction peaks. Down arrows show the disappearance of several reflections of the α' phase at 16.1 GPa.

Le Bail refinement of the pattern at 0.1 GPa (**Fig. S1**) yields the following lattice parameters of α'-Ga_2S_3: a=11.121(6) Å, b=6.4093(3) Å, c=7.012(2) Å and β=121.276(7) degrees with a unit-cell volume of 427.16(2) $Å^3$. These values are in good agreement with those reported in earlier works.[36, 37] At HP, the shortening of the different interplanar distances in the α' phase shift the diffraction peaks at higher angles, and the same happens with the impurity and the Cu peaks. Above 3.3 GPa, several overexposed spots start to emerge in the diffraction rings, making difficult to mask such zones. That forces us to perform Le Bail refinements on regions richer in Cu, leading to a deacrease of reflection intensities of α' phase and Ga_2O_3, especially above 5.7 GPa.

At 16.1 GPa, several peak intensities of the α' phase start to decrease notably (marked with vertical arrows in **Fig. 2**). Those peaks disappear completely at 17.5 GPa, which does not allow us to refine the α' phase anymore. At this pressure, a pressure-induced phase transition is observed, in agreement with previous works.[38,41] New peaks are not observed for the HP phase, maybe due to the lack of heating to overcome a large kinetic barrier, as was suggested in **Ref. 38**. Curiously, heating has not been required

for such HP transition in a recent work.[41] In any case, as previously mentioned, in this work we are only concerned with the behaviour of the α' phase at HP, so the nature and behaviour of the HP phase is out of the scope of the present paper.

As can be seen in **Fig. 3a)**, our experimental unit-cell volumes below 2 GPa agree reasonably with those of run-2 in **Ref. 38**. At higher pressures, our experimental unit-cell volume shows a larger compression than that of **Ref. 38**. This mismatch could stem from the less hydrostatic conditions achieved in **Ref. 38** (which used LiF as a PTM) than in this work (we have used 4:1 methanol:ethanol mixture as a PTM). We must stress that the decrease of our experimental unit-cell volume is in good agreement with the behaviour observed in both LDA and GGA-PBEsol theoretical calculations shown in **Fig. 3a)**. Note that our GGA-PBEsol calculations show a more pronounced compression than LDA calculations up to 6 GPa,[38] and that both calculations show a similar compression rate at higher pressures.

Concerning the pressure behaviour of the α' phase, Lai *et al.*[38] employed a 2nd-order Birch-Murnaghan equation of state (BM2-EoS) to evaluate the zero-pressure volume, V_o, and bulk modulus, B_o.[38] This could be reasonable for their run-1 since fixing the pressure derivative, B_o', to 4 allowed them to fit experimental data despite not having enough points. In order to properly determine the order of the BM-EoS for our experimental data and those of run-2 of Lai *et al.* [38], we have plotted the normalised stress, F_E, vs finite strain, f_E, (**Fig. S2**) by employing EosFit-7c software.[72] It can be observed that both our experimental data (**Fig. S2a)**) and that from Lai *et al.* (**Fig. S2b)**) fit better to a BM3-EoS than to a BM2-EoS (see **Table 1**) since B_o' values of both sets of experimental data, which are in agreement between them, are far from 4. In addition, both experimental data sets show a similar B_o and V_o.

Table 1. Zero-pressure volume (V_o), bulk modulus (B_o) and pressure derivative (B_o') from BM3-EoS. Our experimental (Exp) and theoretical (GGA-PBEsol) values are compared to experimental (Run-2) and theoretical (LDA) data from **Ref. [38].** The same parameters are shown for the isostructural β-Ga_2Se_3.

	α'-Ga_2S_3				**β-Ga_2Se_3**	
	Exp	Run-2[38]	GGA-PBEsol	LDA[38]	Exp	GGA-PBE[73]
V_o (Å^3)	427.8 (3)	429 (2)	423.1 (3)	411.1 (3)	488.4[120]	467.5
B_o(GPa)	47 (5)	49 (5)	38.0 (6)	49.6 (8)	51[74]	39.9
B_o'	5 (1)	6 (1)	5.3 (1)	4.1 (2)		4.7

Importantly, the experimental B_o values are between those of GGA-PBEsol (**Fig. S2c)**) and LDA (**Fig. S2d)**) calculations. The former is better fitted with a BM3-EoS while the latter is better fitted with a BM2-EoS. For the sake of comparison, we have also fitted the LDA data to a BM3-EoS (see **Table 1**). GGA-PBEsol data predict a softer behaviour of α'-Ga_2S_3 at HP than previously reported LDA data.[38] On the other hand, the B_o and B_o' values for α'-Ga_2S_3 are in agreement with those values previously

reported for isostructural β-Ga_2Se_3 (see **Table 1**).[73, 74] Channels are expected to shrink on compression, thus leading to a low B_0 value and a values of B_0' much higher than 4, as occurs in other compounds with channels caused by LEPs.[42, 75] The obtained B_o' values for α'-Ga_2S_3 are only slightly larger than 4 for both experimental and theoretical data. A deeper study of the pressure behaviour of the LEPs forming the channels will be later provided when the evolution of the charge density at HP is analyzed.

The pressure dependence of the lattice parameters and monoclinic β angle of α'-Ga_2S_3 is shown in **Fig. 3b)** and its inset. In general, there is a good agreement between our experimental and theoretical data on compression. We can observe that GGA-PBEsol data are closer to the experimental lattice parameters than LDA, particularly below 4 GPa. The most striking feature of the α' phase on compression is the change in behavior of the β angle at HP. The experimental (theoretical) β angle shows a negligible pressure dependence below 4 GPa (8 GPa) and a decrease above this pressure. Therefore, both experimental and theoretical data show a symmetrisation of the monoclinic structure at HP.

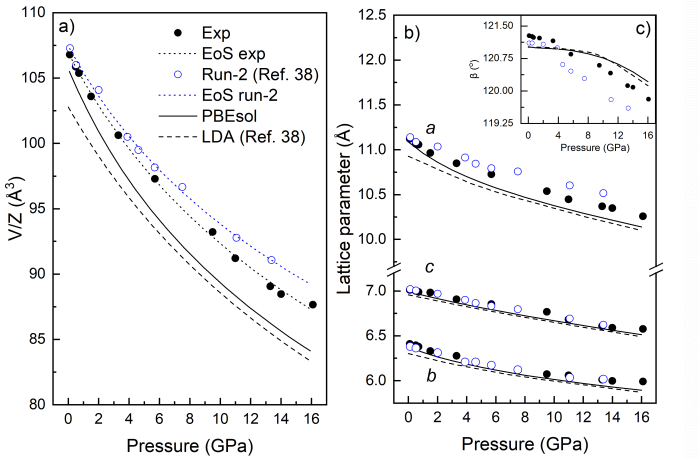

Figure 3. a) Experimental (black solid circles) and theoretical GGA-PBEsol (black solid line) pressure dependence of the unit-cell volume of α'-Ga_2S_3. Experimental Run-2 (blue empty circles) and theoretical LDA (black dash line) from **Ref. 38** are also plotted for comparison. Both experimental data are fit to a BM3-EoS (dotted lines). b) Pressure dependence of the lattice parameters *a*, *b* and *c* of α'-Ga_2S_3. The inset shows the pressure dependence of the monoclinic β angle.

Regarding the axial bulk modulus of the α' phase, Lai *et al.* reported a quasi-isotropic behaviour based on the modified BM2-EoS.[38] In order to revise this assessment, we have first tabulated the zero-pressure axial compressibilities, defined as $\kappa_x = -\frac{1}{x}\frac{\partial x}{\partial P}$. As **Table 2** shows, the *b* axis is the most compressible for our experimental data and those from run-2 in **Ref. 38**. However, theoretical calculations predict the *a* axis to be the most compressible. Our experimental and theoretical data reflect a higher axial compressibility than the results from **Ref. 38**. Indeed, *a* and *b* axes are the most compressible axes of the α' phase. In view of **Table 2**, the α' phase does not have a

quasi-isotropic behaviour. In any case, it must be stressed that the conclussions reached in the paragraph as a result of fitting each lattice parameter of monoclinic α'-Ga_2S_3 to a BM3-EoS or a Murnaghan-EoS cannot totally describe the change of the crystal at HP because the β angle also changes with pressure. Consequently, a more elaborate analysis should be done of the axial bulk moduli in monoclinic and triclinic systems.

For monoclinic systems, the non-orthogonality in the three crystallographic axes implies non-zero shear stress when each axis is compressed. Therefore, a good description of the axial compressibility requires the study of the isothermal compressibility tensor. For this purpose, we have used the software PASCAL[76] with the Eulerian approximation[77] to obtain both orthogonal principal axis ev_i and their compressibilities λ_i by diagonalizing the isothermal compressibility tensor (see **Table 2**). These parameters have been tabulated in a range of pressures from 0 to 14 GPa for our experimental and theoretical data and that from Lai *et al*.[38] It can be observed that ev_2 coincides with the *b* axis and shows an intermediate compressibility. On the other hand, ev_1 and ev_3, contained in the *a*-*c* plane, are the directions of maximum and minimum compressibilities, respectively. We find that the direction of maximum compressibility (ψ_{max}, measured to the *c* axis, from *c* to *a*) for run-2 in **Ref. 38** differs almost 27 degrees from our experimental data and theoretical calculations. We must stress that the compressibilities λ_1 and λ_2 imply between the 70-80 % of the total compression. Concerning ev_3, the direction of minimum compression (ψ_{min}, measured to the *c* axis, from *c* to *a*), is quite similar in both our results and those from **Ref. 38**, with an angle between 154 and 168 degrees.

Table 2. Axial compressibilities, principal axes (ev_i) and their compressibillities (λ_i), and angles of maximum (ψ_{max}) and minimum compression (ψ_{min}) in α'-Ga_2S_3 from 0 to 14 GPa. Our experimental (Exp) and theoretical (GGA-PBEsol) data are compared to experimental (Run-2) and theoretical (LDA) data from **Ref. 38**. ψ_{max} and ψ_{min} are measured to the *c* axis (from c to a).

	Exp	**Run-2[38]**	**GGA-PBEsol**	**LDA[38]**
κ_a (10^{-3} GPa)	9.05	6.36	10.98	7.49
κ_b (10^{-3} GPa)	12.76	8.86	9.62	6.85
κ_c(10^{-3} GPa)	4.317	4.93	5.39	4.82
λ_1 (TPa^{-1})	5.53	4.81	5.04	5.02
ev_1	(-0.963, 0, -0.270)	(-0.833, 0, 0.553)	(-0.940, 0, -0.341)	(-0.958, 0, -0.286)
λ_2 (TPa^{-1})	5.05	4.57	4.52	4.35
ev_2	(0, 1, 0)	(0, 1, 0)	(0, 1, 0)	(0, 1, 0)
λ_3 (TPa^{-1})	3.29	2.52	3.88	3.68
ev_3	(-0.231, 0, -0.973)	(-0.436, 0, -0.900)	(-0.201, 0, -0.980)	(-0.224, 0, -0.975)
ψ_{max} (º)	68.6	43.0	71.7	69.4
ψ_{min} (º)	158.2	132.5	164.6	159.2

Figure 4 helps to visualize how the principal axes are related to the channels in the crystalline structure. It can be seen that ev_2 is perpendicular to the channels, along the direction connecting S1 atoms (**Fig. 4a)**). On the other hand, ev_1 involves the small section of the channels. Specifically, the direction of ev_1 is perpendicular to the array of S2 and S3 atoms along the *c* axis (**Fig. 4b)**). Therefore, we can say that the empty channels, concretely along their cross-sections, are responsible for most of the compression of the α' phase. The minimum direction of compression, ev_3, implies that the stiffest direction is almost perpendicular to the layers formed by coplanar GaS_4 polyhedra along the a-b plane (**Fig. 4b)**). We can conclude, in view of the principal axes and their compressibilities, that the α' phase shows a high anisotropy due not only to its monoclinic symmetry but also to the presence of channels along the *c*-axis of the structure.

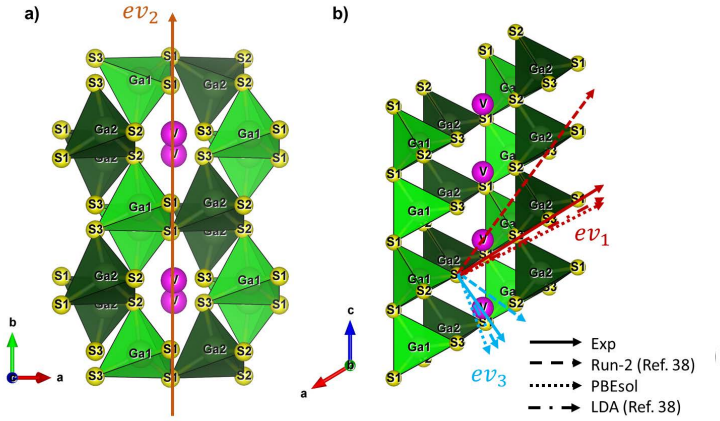

Figure 4. a) View of α'-Ga_2S_3 perpendicular to *c* axis where ev_2 is located along *b* axis, covering the major section of the vacancy channels. ev_2 refers to the intermediate direction of compression. b) View of α'-Ga_2S_3 perpendicular to *b* axis, parallel to *a*-*c* plane. ev_1 intersects the small cross-section of the vacancy channels, meanwhile ev_3 is almost normal to the GaS_4-based layers. ev_1 and ev_3 refer to the maximum and the minimum direction of compression, respectively. Ga and S atoms and vacancies are shown in green, yellow and pink, respectively.

We turn now to evaluate the role of sulfur LEPs in the compression of α'-Ga_2S_3. First, we studied the change in the GaS_4 polyhedra at HP. For that purpose, the pressure dependence of the relative volume, V/V_o, of the two different GaS_4 tetrahedra was compared to that the unit-cell volume (see **Fig. S3**). A fit to a BM3-EoS yields B_o = 123.0 (99.1) GPa and B_o' = 3.9 (6.1) for the $Ga1S_4$ ($Ga2S_4$) tetrahedron; i.e. both tetrahedra show a different pressure behaviour despite their similar environment. Clearly, the Ga polyhedral bulk moduli are more than double than that of the unit-cell volume (see **Table 1**), thus reflecting that the major contribution to the compression of the α' structure comes from the compression of the empty channels of the structure generated by the sulfur LEPs.

To study their similarities and differences, we have analysed the influence of pressure on both GaS_4 polyhedra by examining the calculated Ga-S bond lengths, their compressbilities, effective coordination number (ECoN), distortion index, bond angle variation and quadratic elongation with the software VESTA.[71] **Figure 5a)** and **5b)** plot the change in the Ga-S bond lengths of $Ga1S_4$ and $Ga2S_4$ tetrahedra, respectively. In both tetrahedra, the three longer Ga-S bonds involve the S1 and S2 atoms (those with only one LEP), meanwhile the shortest Ga-S bond refers to the S3 atoms (with double LEPs) (**Fig. 1b)**). Connecting with the Lewis diagram depicted in **Fig. 1b)**, it is clear that Ga-S3 bonds can not be dative due to the double LEPs of S3 atoms. Therefore, in each GaS_4 tetrahedron the dative bond must be associated with either the Ga-S1 or the Ga-S2 bond. The dative bond in one of these two GaS_4 tetrahedra leads to different Ga-S bond lengths in both tetrahedra, and therefore, their different pressure dependence.

Figure 5c) and **5d)** show the compressibility of each Ga-S bond for both tetrahedra when fitted to a Murnaghan-EoS. As expected, we found that the three longer Ga-S bonds in both tetrahedra are more compressible than the shortest bond. Additionally, the Ga2 tetrahedron shows two bonds with a high compressibility (above $4 \cdot 10^{-3}$ GPa^{-1}) at low pressures while the Ga1 tetrahedron shows only one bond with a high compressibility. This difference explains the softer behaviour of the Ga2 tetrahedron than the Ga1 tetrahedron at low pressure. On the other hand, the longest Ga1-S1 bond in the $Ga1S_4$ tetrahedron, named Ga1-S1*, behaves in an anomalous way: its compressibility increases slightly up to 4 GPa, and then becomes almost constant up to 16 GPa, showing the largest bond compressibility above 11 GPa. A careful examination of the structure shows that bonds Ga1-S1* and Ga2-S2* (the longest distance between Ga2-S2 atoms) are perpendicular to the layers (**Fig. 1c)**); i.e. they are almost in the same direction of the ev_3. This result means that the direction of minimum compressibility is in fact related to how the bonds Ga1-S1* and Ga2-S2* are compressed. In fact, we could tentatively identify the Ga1-S1* and Ga2-S2* bonds as dative if we attend to the anomalous pressure dependence of their compressibilities and their relation with the direction of minimum compressibility.

The ECoN and distortion index (see **Figure S4a)**) are equal for both GaS_4 tetrahedra at 0 GPa; however, the $Ga2S_4$ tetrahedron has a slightly higher ECoN than the $Ga1S_4$ tetrahedron at HP and, consequently, a smaller distortion index. Largest differences are observed in the bond angle variance and quadratic elongation (**Fig. S4b)**). These parameters are larger for the $Ga1S_4$ tetrahedron over the entire pressure range. Curiously, both tetrahedra reach almost the same value of these parameters near 16 GPa, thus suggesting that Ga atoms are increasingly displaced from their centroid in both polyhedra as pressure increases and reach similar values just prior to the phase transition. The increase of both parameters is more remarkable in the $Ga2S_4$ tetrahedron, where the Ga2 atom is strongly shifted towards the S1-S2-S3 plane (inset of **Figure S4b)**). Concretely, this increasing distortion under compression can be rooted in the different compressibilities of the Ga1-S1* and Ga2-S2* bonds, tentatively proposed as dative, compared to the other Ga-S bonds. Indeed, the increasing distortions in both polyhedra likely cause a structural instability leading to the phase transition that occurs near 16 GPa on α' phase, as we have observed (see **Fig. 2**) and was already reported in **Ref. 38** and **41.**

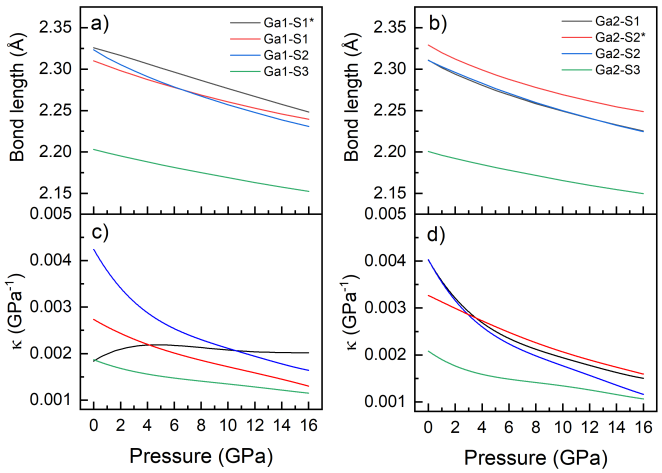

Figure 5. (Color online) Pressure dependence of Ga-S bond lengths and compressibilities in the two GaS_4 polyhedra: a) and c) for $Ga1S_4$ and b) and d) for $Ga2S_4$ polyhedra. Ga1-S1* and Ga2-S2* refer the longest bond lengths between the Ga1-S1 and Ga2-S2 atoms, respectively.

Finally, in order to understand the changes observed in the Ga-S bonds we have followed the relative change of the free theoretical atomic coordinates (x,y,z) of the unequivalent Ga and S atoms at HP, as can be seen in **Figs. S5, S6** and **S7** in the SI and schematized in **Figs. S8** and **S9** in the SI. Among all the features observed, included in the SI, we must stress the symmetrisation of the structure with increasing pressure, as clearly shown by the z coordinate of the Ga2 atom (see **Fig. S7b)**). This coordinate tends to 0 close to 16 GPa thus suggesting a phase transition above that pressure, in agreement with our HP-XRD measurements and previous works.[38, 41]

To summarize the structural part, we have found a good agreement between our experimental and theoretical results in the pressure dependence of the lattice parameters and the bulk modulus. Concerning the bulk modulus, thanks to the data of **Ref. 38** and our own results, we have demonstrated a more compressible pressure behaviour of the α' phase that was previously reported and in agreement with the pressure behaviour β-Ga_2Se_3.[79] On the other hand, our results for lattice parameters match quite well with those published in **Ref. 38**; however, we have performed a detailed analysis of the pressure dependence of the axial compressibility in a monoclinic symmetry, like that of the α' phase, by obtaining the pressure dependence of the principal axes given by the isothermal compressibility tensor. As a result, we have obtained that the compression of α'-Ga_2S_3 is rather anisotropic and that the principal axes with the maximum and intermediate compressibilities are related with the cross-sections of the channels. Moreover, the study of the Ga polyhedral volumes have revealed that the high bulk modulus of both GaS_4 tetrahedra and their low contribution to the relative volume shows the dominant role of the channels in the compression of the α' phase. Curiously, despite the high bulk moduli of both GaS_4 tetrahedra, they experiment a high distortion at HP and show a different compression due to the existence of a dative Ga-S bond in one of the two polyhedra. In particular,

the bond angle variance and quadratic elongation show the largest values (almost equal for both tetrahedra) at 16 GPa. Indeed, this increase of the distortion of both GaS_4 tetrahedra and the symmetrisation of the Ga2 atoms points out to a phase transition above 16 GPa towards a more symmetric HP phase, as previously reported.[38,41]

5. VIBRATIONAL PROPERTIES UNDER COMPRESSION AND THERMAL EXPANSION. ANHARMONIC PROPERTIES.

5.1 Vibrational properties at HP

Now we turn to our HP- and HT-RS measurements on α'-Ga_2S_3. Group theory predicts for the non-centrosymmetric α' phase 27 IR- and Raman-active optical modes at Γ = 13 *A*' + 14 *A*'', plus three acoustic modes (2 *A*' + 1 *A*''). We have to note that all *A'* and *A''* modes are both Raman- and IR-active; therefore, can show transversal optic (TO) and longitudinal optic (LO) components; i.e. two peaks can eventually be observed for each mode. This means that up to 54 vibrational modes can be observed in the Raman and IR spectrum of α'-Ga_2S_3. In this work, experimental modes with TO and LO counterparts are indicated in the Tables and Figures; otherwise only TO counterpart is referred.

Figure 6 shows normalized HP-RS spectra up to 16.1 GPa. All the observed Raman modes have been attributed to the α' phase with no mode corresponding to the Ga_2O_3 impurity. We have observed changes in the Raman spectrum at 15.1 GPa, with broad peaks appearing at 150, 210, 410 and 460 cm^{-1}. The new broad peaks increase their intensities at higher pressures, being that located a 410 cm^{-1} the most intense. These features present at 15.1 GPa, and even more remarkable at 16.1 GPa, show the onset of the pressure-induced phase transition observed by our HP-XRD measurements and in previous works.[38,41] In fact, recent HP-RS measurement locate the onset of the phase transition at 11.3 and 17.2 GPa under hydrostatic (helium as PTM) and non-hydrostatic (no PTM) conditions, respectively.[41] Therefore, the slight differences in this transition pressure could come from the different hydrosticity conditions achieved in both the present work and the previous ones.[38, 41] The RS spectra of **Fig. 6** are in agreement with those published recently in **Ref. 41**, only differing in the transition pressure, as already commented, and the lack of measurements below 100 cm^{-1} in **Ref. 41**. Unfortunately, we can merely make a visual comparison between our HP-RS measurements and those from **Ref. 41** due to the lack of assignment of the symmetry and pressure coefficients of the observed Raman modes.

The RS spectrum of the α' phase can be divided into two regions: the low-frequency region (below 200 cm^{-1}) and the high-frequency region (above 200 cm^{-1}). According to Lucazeau *et al.*, modes at the low (high)-frequency regions correspond to bending (stretching) vibrations of the GaS_4 tetrahedra.[78] We have observed and followed the pressure dependence of 26 Raman-active modes. As observed in previous studies,[20, 22, 25, 26, 78-82] the RS spectrum at 0.5 GPa is dominated by the breathing mode near 230 cm^{-1}, which is assigned to the *A*' symmetry. This peak is related with the symmetric stretching vibration of S atoms around the vacancies in the S atom-vacancy direction, and it derives from the symmetric Ga-S stretching vibrations of GaS_4 units.[20, 26, 78, 79]

It is worth mentioning that the breathing mode is also found in adamantine OVCs of AGa_2S_4 stoichiometry,[31, 83, 84] which are synthesized from Ga_2S_3 and several binary *A*S (*A*= Zn, Cd and Hg) compounds. Their crystalline structures are strongly dominated by the Ga_2S_3 compound and have ordered vacancies, therefore explaining the presence of the breathing mode.[80-82] Moreover, the symmetric stretching mode of S anions around Ga cations has been also observed in GaS near 190 cm^{-1};[85] i.e. at a smaller frequency than the breathing mode in Ga_2S_3, likely due to the influence of the Ga-Ga bond in the vibration of the Ga_2S_6 units in GaS. Finally, we can mention that RS spectra with similarities to that of Ga_2S_3 have also been recently reported for the mc64 and mC16 polymorphs of $CsGaS_2$, constituted by corner-sharing and edge-sharing GaS_4 units, respectively, and showing no cation vacancies in their structures.[86]

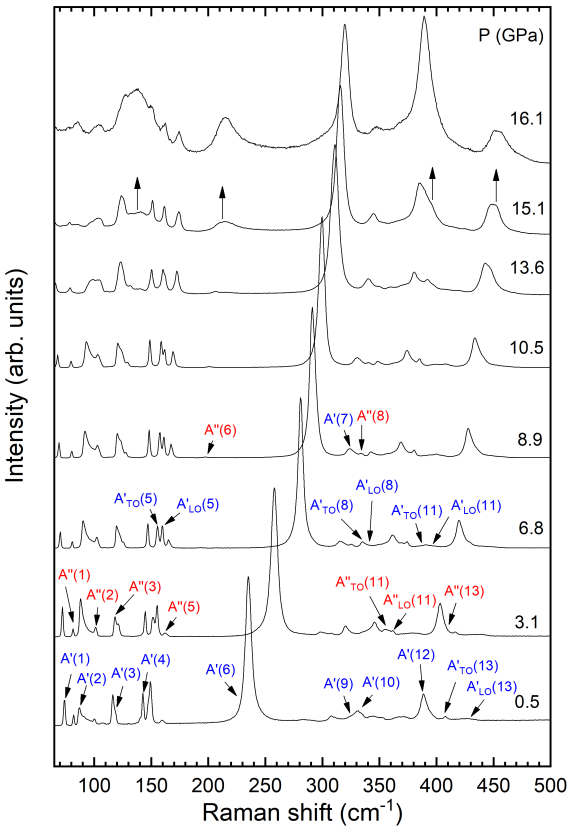

Figure 6. (Color online) RS spectra of α'-Ga_2S_3 at selected pressures. The different *A'* and *A''* modes have been tentatively identified in the RS spectra.

To better understand the vibrational modes attributed in **Fig. 6**, we have plotted the atomic displacements of some of the more representative Raman-active modes of α'-Ga_2S_3 in **Figs. S10** to **S19** in the SI. In short, we have observed that modes below 200 cm^{-1} are mainly a mixture of Ga-S bending modes and external modes of the GaS_4

units due to translation and rotation of the tetrahedra (see **Figs. S10** to **S14**). Between 200 and 300 cm^{-1}, modes are mainly Ga-S bending modes with some admixture of Ga-S stretching modes. In particular, the strongest Raman mode is the breathing mode near 230 cm^{-1} and corresponds to the *A'*(6) mode; a mixture of Ga-S bending modes leaded by displacements of S1, S2 and S3 atoms (see **Fig. S15**). The concerted displacements of S atoms lead to a strong symmetric Ga-S stretching mode of S atoms vibrating around the vacancy and to a small symmetric Ga-S stretching v_1 mode of the GaS_4 units.[77] This is the reason why this mode is also known as the breathing mode of the vacancy. Finally, modes above 300 cm^{-1} are mainly asymmetric Ga-S stretching modes (deriving from the v_3 mode of GaS_4 units)[77] with some admixture of Ga-S bending modes (see **Figs. S16** to **S19**).

We now turn to analyze the contribution of the different atoms to each vibrational region. For that reason, we have studied the one-phonon density of states (1-PDOS) at 0 GPa (see **Fig. S20**). Notably, our 1-PDOS is similar to that found in the Materials Project Database.[87] The 1-PDOS shows that the high-frequency region (above 200 cm^{-1}) can be subdivided into three parts: low (200-300 cm^{-1}), medium (300-350 cm^{-1}), and high (above 350 cm^{-1}). The contributions of Ga and S atoms are rather similar in the low-frequency region (below 200 cm^{-1}) and in the low part of the high-frequency region (200-300 cm^{-1}). However, in the medium and high parts of the high-frequency region there is a much larger contribution of S atoms than of Ga atoms. Concretly, S1 and S2 atoms (both with three-fold coordination) are predominant in the medium frequency region, meanwhile the S3 atoms (with two-fold coordination) contribute mainly in the high part of the high-frequency region. On the other hand, it is remarkable that the S3 atoms vibrate with low amplitudes when S1 and S2 atoms vibrate with higher amplitudes and conversely. This can be understood as a way to minimize the electrostatic repulsion between the double LEPs from S3 atoms and the single LEPs of S1 and S2 atoms.

The same three phononic gaps observed on the 1-PDOS of α'-Ga_2S_3 are seen in β-Ga_2Se_3, whose 1-PDOS can be found in the Materials Projects database.[87] A further comparision can be made if we take into account other OVCs of AGa_2S_4 stoichiometry (*A* = Zn, Cd and Hg) with tetragonal defect chalcopyrite structure (S.G. $I\bar{4}$, No. 82, Z=2),[87] which exhibit only two phononic gaps. On the other hand, the wurtzite type-structure such as ZnS, with no vacancies, only exhibits one phononic gap in its 1-PDOS.[87, 88] In this context, we can assume that the presence of vacancies in a compound gives rise to more inequivalent atoms in the asymmetric unit cell (five for α'-Ga_2S_3, four for AGa_2S_4 and two for wurtzite type-structure). Curiously, the more inequivalent atoms, the more phononic gaps can occur in the 1-PDOS. The same trend cannot be observed in OVCs with AGa_2Se_4 stoichiometry,[87] that even do not have a single phononic gap. The reason is the overlapping of the different regions due to the reduced range of frequencies where all phonons occur as a consequence of the higher mass of Se than S. Therefore, the appearance of these phononic gaps seems to clearly depend on the mass of the atoms.

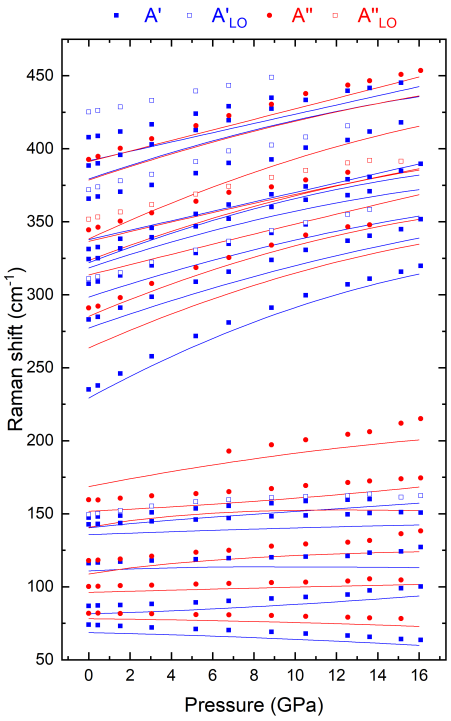

Figure 7. Pressure dependence of the theoretical (solid lines) and experimental (symbols) Raman-active mode frequencies of α'-Ga_2S_3.

Figure 7 shows the pressure dependence of the experimental and theoretical Raman-active mode frequencies of the α' phase. Note that theoretical mode frequencies refer only to the TO counterpart. In order to do the tentative assignment of the experimental Raman-active modes shown both in **Fig. 7** and **Table S1**, we have compared our experimental frequencies and pressure coefficients with those for the TO components of the theoretical vibrational modes and also with the frequencies at room pressure reported in previous works. As observed, the rather good agreement of experimental and theoretical frequencies and pressure coefficients has allowed us to tentatively assign the symmetry of each experimental mode observed in the α' phase (see **Table S1**). It must be recalled that all *A'* and *A''* modes can show a TO-LO splitting, so two modes can be expected for each theoretically predicted mode in both RS and IR spectra. Therefore, the relatively similar frequencies shown for several *A'* and *A''* modes, coming from Raman- and IR-active modes if symmetry would be higher,[78] could be the TO and LO component of a single mode. In this respect, we have tentatively assigned the LO counterparts of some phonons to modes whose pressure coefficients do not match well with theoretical TO modes of similar frequencies.

As regards the pressure coefficients, we have found that the *A'*(6) mode has the highest pressure coefficient (~8.0 cm^{-1}/GPa) of all vibrational modes, as occurs for the breathing mode of isostructural β-Ga_2Se_3 (at 155 cm^{-1})[72] and for the breathing mode

(A^1 mode) of defect chalcopyrites as $ZnGa_2S_4$, $CdGa_2S_4$ and $HgGa_2S_4$.[31, 83, 84] In the low-frequency region, most modes of α'-Ga_2S_3 show a very small pressure coefficient. Moreover, the *A'*(1) and *A''*(1) modes; i.e. those with the lowest frequency, exhibit negative pressure coefficients. This has also been observed in a number of compounds, including adamantine-type AB_2X_4 OVCs.[31, 47, 83, 84] The anomalous decrease of the frequency with increasing pressure of many Raman-active low-frequency modes cannot be explained by an increase of the cation-anion distances with increasing pressure in all these compounds. Instead, it is likely related to an instability of those structures to hydrostatic compression that is evidenced by negative pressure coefficients of low-frequency vibrational modes at the Brillouin zone edge of the cubic lattice (mainly coming from acoustic branches folded into the zone center of low-symmetry structures).[89] In the low-frequency region, the overlapped Raman peaks are easily discerned thanks to their intensities. According to the idealised P.G. proposed by Lucazeau for the α' phase,[78] the *A'* modes derive from Raman-active modes and the *A''* modes from IR-active, therefore giving arise a higher intensity for the former than for the latter. As an exception, the *A''*(3) mode is identified as more intense than the *A'*(3) mode and both modes have been confirmed by the agreement between their experimental and theoretical pressure coefficients (see **Table S1**). In terms of pressure coefficients, the mode at the right side of the $A'_{TO}(5)$ mode does not match well with the theoretically predicted for the *A''*(4) mode; therefore it has been labelled as $A'_{LO}(5)$. On the other hand, the high-frequency region shows a massive overlapping of the Raman peaks, and their low intensity hampers their uncoupling even at high pressure except for the *A'*(12) mode that was also previously observed.[20, 25, 78, 90] In this region, we consider that the theoretically predicted *A''*(7), *A''*(9), *A''*(10), *A''*(12), *A''*(14) modes have not been experimentally observed either in this work or in previous ones. Instead, we have tentatively assigned the LO counterparts of the *A'*(8), *A''*(11), *A'*(11) and *A'*(13) modes in view of the mismatch between their pressure coefficients with those theoretically predicted and the higher frequencies observed. The modes of the high-frequency region exhibit higher pressure coefficients than in the low-frequency region (see **Table S1**). It must be noticed that the theoretical mode frequencies in the high-frequency range underestimate those observed experimentally, mainly above 325 cm^{-1} from the *A''*(11) to the $A'_{LO}(13)$ modes (**Fig. 7**). Moreover, it can be noticed that, in general, the modes at the lower part of the high-frequency region show larger pressure coefficients than those at the high part of the high-frequency region and are more separated at 0 (162 cm^{-1}) than at 12 GPa (135 cm^{-1}). These features of these modes, related to TO and LO modes from the cubic structure, respectively, indicate a decrease of the LO-TO splitting on increasing pressure as expected from the more covalent character of the compound on increasing pressure as is also observed in adamantine-type AB_2X_4 OVCs.[31, 47, 83, 84]

In order to evaluate the anharmonicity of each vibrational mode, we have calculated the isothermal mode Grüneisen parameter, γ_i^T (**Eq. 1** in the SI). In general, we observe a good agreement between theoretical and experimental γ_i^T. Excluding the *A'*(1) and *A''*(1) modes, which exhibit negative γ_i^T, most modes show positive γ_i^T values between 0 and 1. The only exception is the breathing mode *A'*(6) that features the highest γ_i^T with a value above 1. This result highlights the high anharmonicity of the stretching vibration of S atoms around the cation vacancies. Taking into account the

microscopic definition (**Eq. 3** in the SI), the isothermal averaged Grüneisen parameter, γ_{av}^{T}, obtained for the α' phase from our experimental and theoretical data are 0.49 and 0.44, respectively. These values are in a good agreement with the common range for γ_{av}^{T} in tetrahedral compounds (between 0.5 and 1.5).[91]

5.2 Vibrational properties at HT

Figure 8 shows the normalized Raman spectra in the α' phase at room pressure and at selected temperatures. To assign the corresponding symmetry to each mode observed at HT, we have used the mode frequencies calculated at 0 GPa. However, due to the lack of lattice-dynamical calculations at HT, we were not able to decouple *A''*(3) and *A'*(3) modes. For that reason, we have noted them as the *A''*(3)/*A'*(3) mode. From 300 to 923 K, all observed modes shift to lower frequencies, even the the *A'*(1) and *A''*(1) modes that show softening at HP. At 948 K, the mode intensities decrease significantly and only the *A''*(3)/*A'*(3), *A'*(4), *A'*(5), *A'*(6), *A'*(12) modes from the α' phase can be discerned. However, new peaks arise at 160, 200, 320 and 410 cm^{-1} at this temperature. At temperatures above 1000 K, all modes of the α'-phase disappear but the new modes persist (see **Fig. S21**). The disappearance of the Raman-active modes of the α' phase is consistent with its melting point at about 1300 K.[28, 29] Therefore, we attribute the new Raman peaks above 948 K to the impurity of Ga_2O_3 present in the sample (see discussion in the SI in relation to **Fig. S21**).

Figure S22 shows the temperature dependence of the observed mode frequencies in α'-Ga_2S_3 and temperature coefficients are summarized in **Table S2**. The mode frequencies show a normal shift to lower frequencies as temperature increases, even the *A'*(1), *A'*(7), *A''*(8), *A'*(9) and A''_{LO}(11) modes. However, these modes exhibit a positive linear temperature coefficient but a negative nonlinear coefficient, dominating their temperature dependence behaviour. Moreover, we can observe that the modes from the high-frequency region are more sensitive to temperature than those in the low-frequency region.

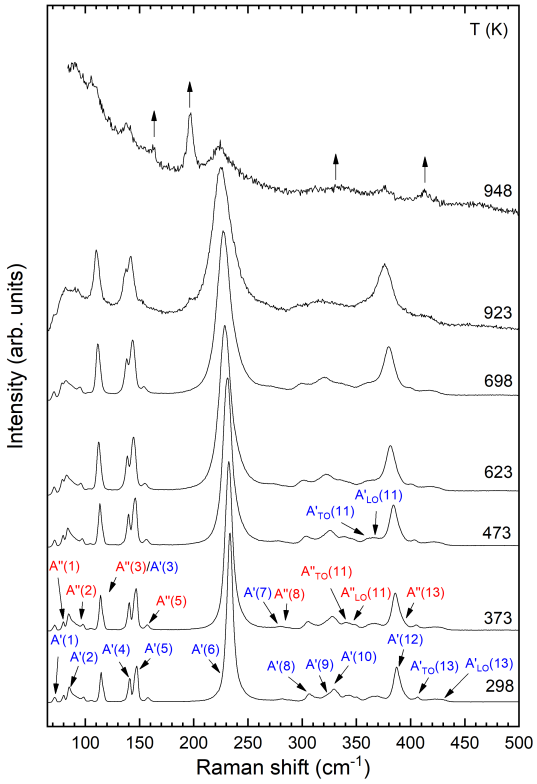

Figure 8. RS spectra of α'-Ga_2S_3 at selected temperatures. Up arrows show the appeareance of new peaks at 948 K.

According to the Klemens model (**Eq. 5** in the SI), we have obtained the cubic and quartic anharmonic contributions, i.e. A and B coefficients, and their absolute ratio |A/B| for all the experimentally observed modes under HT. As can be observed in **Table S2**, low-frequency modes show |A/B| values above 1; i.e. with cubic anharmonic contributions dominating over quartic contributions. On the contrary, the |A/B| ratio is lower than 1 in the high-frequency region, leading to a major contribution of quartic anharmonic contributions.[92] Therefore, we can confirm that high-frequency modes have an important nonlinear temperature dependence (higher b_2 coefficients), where fourth-order processes are quite relevant. As an exception, the low-frequency *A'*(1) and *A''*(5) modes have a similar |A/B| ratio as the high-frequency modes, thus indicating a relevant contribution of fourth-order processes in these modes. In contrast, the high-frequency *A'*(8) and *A'*(10) modes have a similar |A/B| ratio as the low-frequency modes, with a clear third-order processes dominance. Concerning the *A'*(6) mode, it shows the highest |A/B| ratio so it has the highest contribution of third-order processes.

Since the *A'*(6) mode is not overlapped with other modes, we have analysed its linewidth (full width at half maximum, FWHM) under HT (**Eq. 6** from SI). The fit of

FWHM data of the *A'*(6) mode at HT to **Eq. 6** in the SI yields Γ_o = 4.15 cm^{-1}, C = 0.002 cm^{-1} and D = $5.62 \cdot 10^{-7}$ cm^{-1}, where C and D are the cubic and quartic anharmonic contributions, respectively. These values again indicate a dominance of third-order processes in the phonon-phonon coupling of the breathing mode at low temperatures. However, fourth-order processes become dominant in the FWHM shift above 300 K (see **Fig. S23**).

On the other hand, we have calculated the isobaric and isochoric mode Grüneisen parameters, γ_i^P and γ_i^V, in order to estimate the implicit and explicit effects that govern the frequency shifts observed at HT (**Eq. 7** and **8** in the SI). **Table S2** summarizes γ_i^P, γ_i^T and γ_i^V for each experimental Raman-active mode at room temperature. If the quasiharmonic approximation is valid, each γ_i^V must be equal to 0, which means a negligible explicit effect. In fact, we observe that γ_i^V values are quite similar to those of γ_i^P for the α' phase, so that there is a high contribution of the phonon-phonon coupling to the total thermal frequency shift.

In order to visualize the contribution of the implicit and explicit effects for each mode,[93, 94] we have plotted in **Fig. 9** the isobaric temperature derivative (the total thermal effect, the left-hand side of the **Eq. 7** in the SI) vs the isothermal pressure derivative (the implicit effect, the first term in the right-hand side of the **Eq. 7** in the SI). The dashed lines are labelled with its corresponding implicit fraction, η_i (**Eq. 9** in the SI), which specifies the ratio of the implicit and total effects. For η_i = 0 (γ_i^T = 0) there is only contribution of the explicit effect to the mode frequency shift at HT. On the other hand, for η_i = 1 (γ_i^V = 0) the implicit effect is responsible for the mode frequency shift at HT. Finally, for η_i = 0.5 (γ_i^T = γ_i^V), both effects are comparable and for values η_i > 1 (γ_i^V < 0) both effects have opposite signs. Notice that negative η_i is similar to η_i > 1, but only changing which effect is negative (γ_i^T < 0). **Table S2** shows η_i for each mode observed. In view of **Fig. 9**, we can see that most modes have η_i < 0.5, implying a predominantly explicit effect. The modes of the low-frequency region (0.01 < η_i < 0.09) exhibit a higher explicit effect than those of the high-frequency region (0.07 < η_i < 0.30). A high contribution of the explicit effect has also been observed in several transition metal dichalcogenides.[94, 95] Concerning the lowest frequency modes, the *A'*(1) and *A''*(1) modes have negative η_i, the latter with a higher explicit effect than the former. These negative η_i stem from their softening behaviour under HP, as has been observed for many modes on As_2S_3, β-$GeSe_2$, $SnGeS_3$ and SnSe.[43, 96-98] On the other hand, the *A'*(9) and *A''*(8) modes from the high-frequency region show η_i > 1, with a highly relevant implicit effect, but small explicit effect of the opposite sign. For the *A'*(6) mode (the breathing mode), the explicit contribution is almost three times higher than the implicit one ($\eta_i \approx 0.25$).

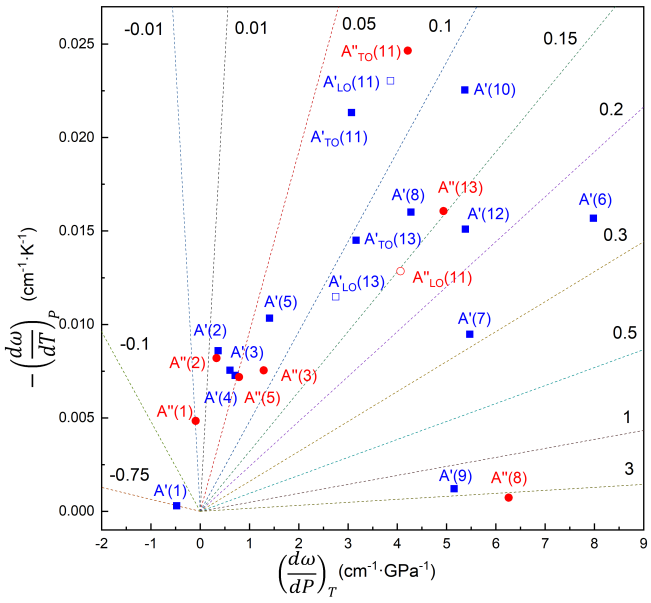

Figure 9. Correlation between the temperature and pressure derivatives of the experimental Raman-active mode frequencies. Dashed lines are labelled by the corresponding implicit fraction.

In summary, we have studied the pressure and temperature dependence of the Raman-active modes of the α' phase, evidencing the onset of the pressure-induced phase transition at 15.1 GPa and its thermal stability until reaching the melting point at about 1300 K. Moreover, the combination of the experimental measurements and theoretical calculations has allowed us to assign tentatively the symmetries of the experimentally observed Raman-active modes. On the other hand, our calculations have lead us to highlight the mixed bending-stretching character of the Raman-active modes, with a remarkable vibration amplitude of Ga and S1 and S2 (S3) atoms in the low-frequency region and lower (high) part of the high-frequency region, respectively. Finally, the combination of HP-RS and HT-RS measurements has enabled us to address the anharmonic effects, yielding a relevant contribution of third (fourth)-order processes in the low (high)-frequency region and a high dominance of the implicit effect in most modes. Particularly, the breathing mode features the highest anharmonicity at HP (γ_i^T) and the highest contribution to the third-order processes to its frequency and FWHM at HT.

6. TOPOLOGICAL ANALYSIS OF THE ELECTRON DENSITY UNDER COMPRESSION

Bader's quantum theory of atoms in molecules (QTAIM)[99] is based on a partition of any electronic system in real space into non-overlapping basins, whose interatomic surfaces satisfy the zero-flux condition. Critical points (CPs) are those points where $\nabla\rho(r)$ vanishes. For the chemical point of view, the bond critical points (BCPs) are CPs linking every pair of atoms along a unique path, the bond path. The nature and

strength of these interatomic bonds can be evaluated using the properties at the BCPs. The basin partition also allows the integration of atomic properties, like atomic volumes and atomic charges. Concerning the α' phase, **Fig. S24a), 24b)** and **24c)** show the evolution of atomic volumes, Bader atomic charges (Q_i) and charge transfers (CT_i) for S and Ga atoms under compression, respectively. Due to the more diffuse distribution of $\rho(r)$ in anions than cations,[100] the S basins have larger volume than Ga basins, around twice at 0 GPa (see **Fig. S24a)**). Furthermore, S3 atoms (with double LEPs) have a larger atomic volume in comparison to S1 and S2 atoms (with single LEPs). Since all basin properties are additive and these basins fill the space to give the total unit-cell volume, macroscopic properties, such as the bulk modulus, can be obtained by the volume-weighted sum of the contributions in each basin (**Eq. 10** in the SI).

According to this fraction, the S atoms represent 75% of the unit-cell volume and, therefore, their contribution dominates the crystal compressibility, in the same way as oxygen and halogen anions dominate in oxide spinels and alkali halides.[101] By fitting each $V_i(P)$ to a BM3-EoS (not shown), we have obtained for S1(2), S3, Ga1, and Ga2 basins a bulk modulus of 38.5, 31.9, 80.0, and 66.4 GPa, respectively. In this way, a global bulk modulus of 45.0 GPa is obtained for the α' phase in reasonable agreement with experimental and theoretical values (see **Table 1**). The above results show that the Ga basins are less compressible than the S basins. This is consistent with the high bulk modulus of both GaS_4 tetrahedra as compared to the total volume bulk modulus, as previously discussed. On the other hand, the smaller bulk modulus of S3 atoms compared to S1(2) atoms is explained by the greater compressibility of the double LEPs than the single LEPs. This point reinforces our previous statement that the compressibility of the α' phase is dominated by the channels, whose behaviour under compression is determined by single and double LEPs inside the channels.

The Bader charges of the different basins, Q_i, under compression (see **Fig. S24 b)**) are far from their nominal oxidation states (OS_i). These deviations increase under increasing pressure, thus pointing to a decrease of the ionicity of the compound at HP. It is worth noting the difference in terms of atomic charge between S1(2) and S3 atoms, probably due to the different number of LEPs. In order to emphasize the change in ionicity, we have plotted the charge transfer (**Fig. S24 c)**), using the **Eq. 11** in the SI. The CT of Ga1, Ga2 and S1 basins decrease almost linearly. For the S2 basins, the CT flattens above 8 GPa, and for the S3 basins it decays nonlinearly. Again, the presence of the double LEPs on the S3 atoms is seen, not only in terms of CT, but also in the pressure dependence of this dimensionless parameter. Moreover, the fact that S2 atoms face the S3 atoms along the channels could explain the CT flattening of the S2 basins above 8 GPa. To get a global idea of the ionicity of the whole unit cell, we can average the CT for all the basins.[102] As a result, we have tabulated an average CT of 39.2 and 38.5 at 0 and 16 GPa, respectively. Both averaged CTs fall in the range of polar compounds (30-60), including most III-V crystals and nitrides,[102] and suggests a slight decrease in the ionicity of α'-Ga_2S_3 at HP.

To obtain relevant information about the chemical bonds present in the α' phase, we now turn to inspect the topological properties of the BCPs (**Fig. S25**). While Ga-S

BCPs are located along Ga-S bonds, S-S BCPs fill the channels, except for the S3-S3 BCPs. The appearance of the S-S BCPs occurs because anionic basins share their surfaces not only with cation basins, but with nearest anionic basins as well. In this sense, the S-S BCPs found are associated to the shared IASs among the S basins. Most of the S-S BCPs involve contacts between S3 atoms with other S3 atoms and with S1 and S2 atoms. The BCPs related to the S3 atoms indicate a distorted form of the S3 basins, which is likely associated with the double LEPs present inside the S3 basins.

Figure 10 a) and **b)** show the pressure dependence of $\rho(r)$ and its Laplacian, $\nabla^2\rho(r)$, for every BCP, hereafter named ρ_b and $\nabla^2\rho_b$. We can distinguish the chemical interactions into two great realms depending on the sign of the Laplacian:[99] $\nabla^2\rho_b < 0$ for shared-shell (SS) interactions (covalent and polar bonds) and $\nabla^2\rho_b > 0$ for closed-shell (CS) interactions (ionic bonds, H-bonds and van der Waals (vdW) interactions). According to these criteria, all BCPs of α'-Ga_2S_3 are found to exhibit CS interactions. In particular, Ga-S interactions are categorized with ionic bonding due to the high ρ_b and $\nabla^2\rho_b$ of Ga-S BCPs. Conversely, S-S interactions are typical vdW interactions due to their low values of these topological properties in S-S BCPs. Due to the non-directionality of the vdW interactions, these S-S BCPs at certain positions in the crystal inform about vdW interactions inside the channels. For every BCP, the ρ_b and its $\nabla^2\rho_b$ increase at HP, as expected. However, the $\nabla^2\rho_b$ for the Ga2-S3 BCP increases smoothly until it decreases slightly above 14 GPa. We discuss this result below. For S-S BCPs, this increase indicates the increase of the vdW interactions inside the channels. Among these BCPs, S3-S3 BCPs experiment the smallest increase of the vdW interaction on compression since they are located between the S3 atoms and not along the channels per se.

Other topological properties than $\rho(r)$ and its Laplacian, $\nabla^2\rho(r)$, can be considered to describe the nature of the chemical bonds such as the local energy densities, $G(r)$, $V(r)$ and $H(r)$ refering to the kinetic, potential and total energy densities, respectively. On the other hand and considering the BCPs, where $\nabla\rho(r) = 0$ and the Kirzhnits[103] approximation holds, the H_b/ρ_b, G_b/ρ_b and $|V_b|/G_b$ ratios give adimensional numbers that can be used for the chemical bonding classification. Furthermore, these ratios allow comparing with other systems since they are intrinsic properties and not extrinsic properties as $\rho(r)$ and its Laplacian, $\nabla^2\rho(r)$.[100, 104-109] The first was introduced by Espinosa[108] and stablishes $H_b/\rho_b < 0$ for SS interactions (covalent and polar bonds) and $H_b/\rho_b > 0$ for CS interactions (ionic bonds, H-bonds and vdW interactions); the second was proposed to distinguish in a more generic way between SS interactions ($G_b/\rho_b < 1$) and CS interactions ($G_b/\rho_b > 1$).[107] Lastly, the $|V_b|/G_b$ ratio establishes three chemical bonding regions: a) a pure CS interaction ($|V_b|/G_b < 1$, $\nabla^2\rho_b > 0$); b) a pure SS interaction ($|V_b|/G_b > 2$, $\nabla^2\rho_b < 0$); and c) a transit CS interaction ($1 < |V_b|/G_b < 2$, $\nabla^2\rho_b > 0$). Therefore, knowing these density energies and their ratios we can evaluate the pressure dependence of G_b and V_b and properly characterize the different chemical bonds and their variation under compression.

Figure 11 a), b) and **c)** shows the pressure dependence of the H_b/ρ_b, G_b/ρ_b and $|V_b|/G_b$ ratios. In view of these ratios at zero pressure and having in mind **Fig. 10**, we

can discern the nature of the chemical bonding according to the classification scheme of **Ref.** [100]. In this way, Ga-S bonds can be described as polar bonds (small ρ_b, positive $\nabla^2\rho_b$, $H_b/\rho_b < 0$, $G_b/\rho_b > 0$ and $1 < |V_b|/G_b < 2$), meanwhile S-S BCPs evidence the vdW interactions along the channels (smaller ρ_b than Ga-S BCPs, positive $\nabla^2\rho_b$, $H_b/\rho_b > 0$, $G_b/\rho_b > 0$ and $|V_b|/G_b < 1$). Among the Ga-S bonds, we can distinguish two types: Ga1(2)-S3 and Ga1(2)-S1(2) bonds. The former exhibit the highest absolute values of these ratios, the highest ρ_b and the highest $\nabla^2\rho_b$ for the Ga2-S3 and a similar $\nabla^2\rho_b$ for the Ga1-S3 in comparison to other Ga-S bonds. On other hand, Ga1(2)-S1(2) bonds exhibit intermediate absolute values of the ratios, as well as intermediate values of ρ_b and $\nabla^2\rho_b$. We must stress that using the values of ρ_b and the sign of $\nabla^2\rho_b$ as a criterion to classify the chemical bonding is critical to establish a clear difference between ionic interactions (CS) and polar bonds (SS). We can easily compare these interactions with those found in other systems, like cation-cation polar bonds in $CaAl_2Si_2$-type structures[104] or Ti-S bonds in layered TiS_2[110], and anion-anion vdW interactions in layered SnS_2[104] and TiS_2.[110]

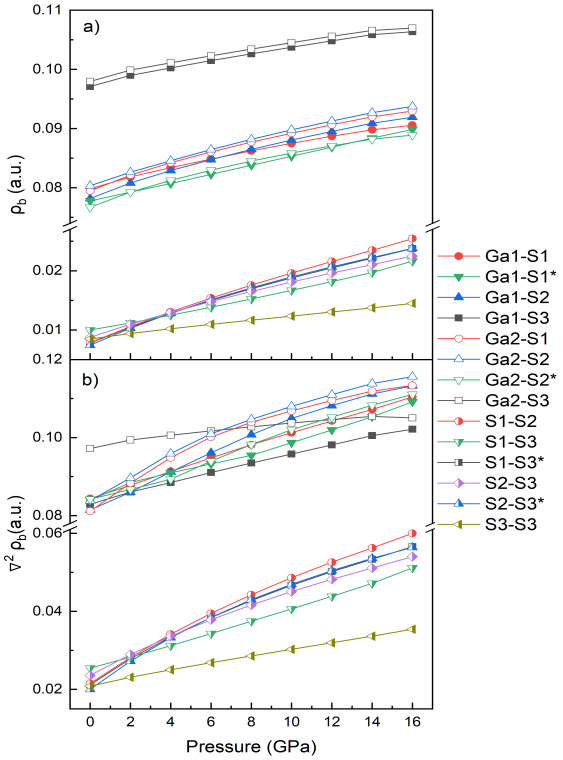

Figure 10. (Color online) Pressure dependence of the charge density $(\rho(r))$ and its laplacian $(\nabla^2\rho(r))$ for the BCPs.

Concerning the Ga-S bonds and their ratios under compression, their values are inside the range considered for polar Ga-S bonds. We can observe an increase of the absolute

value of the H_b/ρ_b ratio due to the increase of the prevalence of V_b under compression (**Fig. 11a)**), at the same time that G_b increases (**Fig. 11b)**). However, the increase of G_b overcomes the increase of V_b for most Ga-S bonds (**Fig. 11c)**). Again, the Ga2-S3 bond stands out as an exception, where the increase of V_b is the most relevant. This explains the almost flat pressure behaviour of its Laplacian and its decrease above 16 GPa. Indeed, this fact shows that the Ga1-S3 and Ga2-S3 bonds are not equivalent and they could be related with the symmetrisation of the relative z coordinate of the Ga2 atoms at HP (see **Fig. S7**), which drives to the phase transition observed in **Ref. 38**. On the other hand, since Ga-S bonds are considered as transit CS interactions ($1 < |V_b|/G_b < 2$, $\nabla^2\rho_b > 0$), the greater is the absolute value of H_b/ρ_b ratio, the more covalent and stronger is the bond.[108] In this sense, Ga1(2)-S3 bonds are more covalent and stronger than the rest of the Ga-S bonds.

More surprising are the S-S interactions and their behaviour under pressure. As was observed in Ga-S bonds, both V_b and G_b increase under compression (**Fig. 11a)** and **Fig. 11b)**), but contrary to Ga-S bonds, G_b is dominant at zero pressure, resulting in $H_b > 0$ (**Fig.11a)**). In the same trend of Ga2-S3 bonds, the increase of V_b under compression is higher than the increase of G_b (**Fig. 11c)**) for the S-S interactions, but with $|V_b|/G_b < 1$ at 0 GPa. It is between 10 and 14 GPa where the interactions between S-S atoms change, from $H_b/\rho_b > 0$ to < 0 and $|V_b|/G_b < 1$ to > 1. This change means an increment of the charge concentration in the channels, increasing the vdW interactions due to the decrease of S-S distances. Indeed, the increasing charge concentration in the channels might promote the phase transition observed at 16 GPa. Again, we can find an exception in the S3-S3 interactions, whose ratios are in the whole range of pressures inside the range of values attributed to vdW interactions.

Concerning the proposed dative bonds, Ga1-S1* and Ga2-S2*, they exhibit the smallest ρ_b, intermediate positive $\nabla^2\rho_b$, highest H_b/ρ_b, smaller G_b/ρ_b and $|V_b|/G_b$ compared to the other Ga-S bonds. Moreover, the trend of these properties on compression for both proposed dative bonds is not as soft as it can be seen for the other Ga-S bonds (**Fig. 11a), 11b)** and **11c)**). Therefore, in terms of these topological properties and their pressure dependence, we can stablish differences on theses properties to tentatively assign the Ga1-S1* and Ga2-S2* bonds as dative. In order to highlight other relevant differences between covalent and dative bonds, we analysed the ELF of the α' phase. In particular, we evaluated the one-dimensional ELF profile (1D-ELF) along the Ga-S bonds in both GaS_4 tetrahedra (**Fig. S26**). Thanks to the ELF, we can observe the different shell structure of atoms.[111] In an ionic compound, each maximum in the 1D-ELF corresponds to a closed shell of an atom. Conversely, along the covalent bond between two atoms, the 1D-ELF has a maximum at the centre of the bond. In our case, where polar bonds are present, the valence shells are deformed.[112] The 1D-ELF along the Ga1(2)-S3 bond is the only one that looks like different to other 1D-ELFs; however, the double LEP of S3 atoms impede them to form dative bonds with the bonded Ga. For the rest of the Ga-S bonds, the 1D-ELF does not allow us to distinguish between covalent and dative bonds existing in the α'-Ga_2S_3.

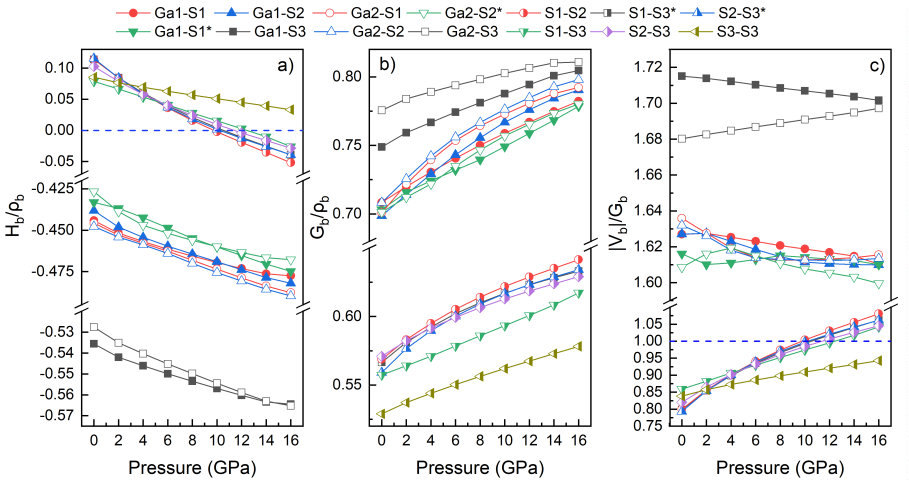

Figure 11. Pressure dependence of the a) H_b/ρ_b, b) G_b/ρ_b and c) $|V_b|/G_b$ ratios for the BCPs.

The maxima of the ELF can also be used to locate the position of the LEPs associated to the sulfur atoms. **Fig. 12a)** shows the representation of the ELF ($\eta = 0.87$) isosurface at 0 GPa, with the single and double LEPs of S1(2) and S3 atoms located inside the channels. At the ELF isosurface level chosen, we have plotted the LEPs with their respective maxima at several pressures, as can be seen in **Fig. 12b)**. As pressure increases, the volume of the single and double LEPs is reduced. This observation supports our assertion that the compressibility of the channels, and of the overall α' phase, is ruled by the compressibility of the LEPs. The shape of the LEPs also changes with pressure. In particular, the ELF maxima corresponding to the double LEP are more separated under compression. This separation is evidenced by the angle between the double LEP and the S3 atom (**Fig. 13**) that increases from 118.5 to 131.6 degrees from 0 to 14 GPa, and is followed by a decrease at 16 GPa. This decrease at 16 GPa may suggest that the system undergoes an instability around this pressure which is related to the phase transition. On the other hand, the overall increase of LEP-S3-LEP angle with increasing pressure can be explained by the increasing repulsion of the S3 LEPs. The opening of the LEP-S3-LEP angle is a distortion of the S3 environment that affects to the surrounding Ga1(2) atoms. In fact, the Ga1-S3-Ga2 angle varies from 104.9 to 97.5 degrees from 0 to 16 GPa showing also a small jump between 14 and 16 GPa indicative of the instability (**Fig. 13**).

In summary, QTAIM analysis of the electronic structure has allowed to explore the properties of the basin volumes. From the individual basin volumes we have obtained an averaged bulk modulus in agreement with the experimental and theoretical values reported in **Table 1**. Additionally, the pressure behaviour of the atomic charge and their charge transfer show a slight decrease in the ionicity of the compound with increasing pressure in agreement with the decrease of the LO-TO splitting of the Raman-active modes. Concerning the BCPs, both the charge density and its Laplacian, in addition with the three H_b/ρ_b, G_b/ρ_b and $|V_b|/G_b$ ratios, drives a clear

classification of the Ga-S bonds and S-S interactions as polar bonds and vdW interactions, respectively. The ELF and its isosurface has helped us locate the single and double LEPs along the channels and to visualize how anion LEPs in α'-Ga_2S_3 evolve under compression. In particular, the double LEP of S3 atoms separate with increasing pressure, distorting the environment of S3-bonded Ga1(2) atoms.

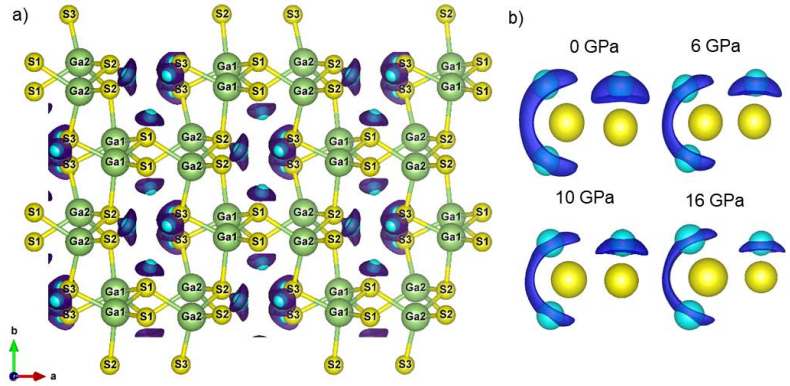

Figure 12. a) View of α'-Ga_2S_3 perpendicular to the *c* axis with the single and double LEPs along the channels at 0 GPa. b) Detail of the single and double LEP volume of the S1 and S3 atoms, respectively, at selected pressures (ELF isosurfaces at $\eta = 0.87$).

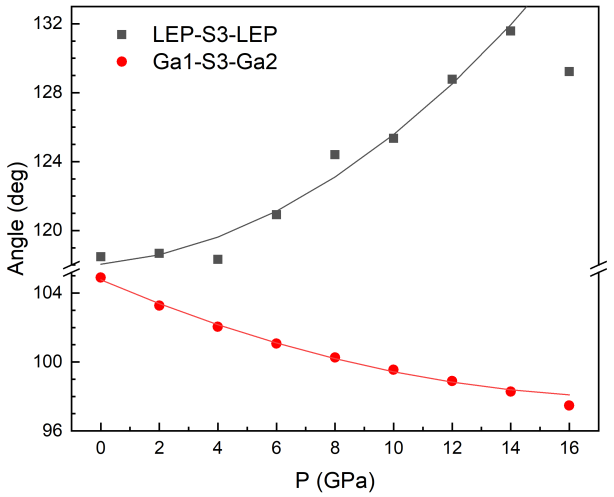

Figure 13. Pressure dependence of the LEP-S3-LEP and Ga1-S3-Ga2 angles.

7. ELECTRONIC PROPERTIES UNDER COMPRESSION

The electronic band structure of α'-Ga_2S_3 at 0 GPa has been already reported[87] and its behaviour at HP was partially studied by means of the electronic total density of states (EDOS).[38, 41] Specifically, both a decrease of the band gap from 1.9 to 1.6 eV between 0 and 9.3 GPa[38] and a increase of the band gap from 1.7 to 2.1 eV between 0 to 8 GPa[41] have been reported. Curiously, contradictory those results were strikingly different to those previously reported for isostructural β-Ga_2Se_3, that showed an increase of the band gap with pressure from optical absorption measurements[113] and that were supported by theoretical calculations.[74] Furthermore, those calculations additionally predicted a decrease of the direct band gap above 7.5 GPa in β-Ga_2Se_3. The unusual nonlinear behaviour of the direct band gap of β-Ga_2Se_3 was explained by a conduction band anticrossing of the two lowermost conduction bands (CBs) at the Γ point, resulting from the presence of the ordered vacancies in the structure of β-Ga_2Se_3.[74] In fact, the same behavior of the direct band gap was observed in OVCs, like $CdGa_2Se_4$,[74] $HgGa_2Se_4$,[74] $MgGa_2Se_4$[114] and $CdGa_2S_4$.[115] Therefore, it was proposed that this nonlinear behaviour must be rooted in the presence of ordered vacancies in OVCs, regardless of the composition and the structure. Consequently, on the basis of the reported contradictory data we have studied the behavior of the electronic band structure of α'-Ga_2S_3 under compression by means of theoretical calculations.

Figure 14 shows the electronic band structure together with the EDOS and partial electronic density of states (pEDOS) of α'-Ga_2S_3 at zero pressure (plotted with the SUMO package[116]). High symmetry directions in the BZ have been chosen according the Seek-path tool.[117, 118] The first BZ and its relevant high symmetry points of α'-Ga_2S_3 are shown in **Figure S27**. From the electronic band structure, we observed that the valence band (VB) shows the valence band maximum (VBM, green points) at the Γ point. Similarly, the CB minimum (CBM, red points) is also at the Γ point, thus yielding a direct band gap of 1.81 eV. Our direct band gap energy is quite similar to the reported 1.9 and 1.7 eV from **Refs. 38** and **41**, respectively. As expected for conventional DFT calculations, these theoretical direct band gaps are smaller than the experimental values that fall in the range of 2.4-3.5 eV.[14, 119]

The contribution of the atomic orbitals to the EDOS is shown in **Figure 14**. It is well known that the anion *p* (cation *s*) orbitals have a major contribution to the top (bottom) of the VB (CB) in heteropolar semiconductors. This is in agreement with our results for α'-Ga_2S_3. The VB is mainly composed by S 3*p* orbitals, specifically the high energy orbitals with the single and double LEPs, which have a strong *p* character. On the other hand, the Ga 4*s*, 3*d* and S 3*p* orbitals contribute equally to the CB. The contribution of the atomic orbitals of S1, S2, S3, Ga1 and Ga2 atomic to the pEDOS at 0 GPa is shown in **Fig. S28a)**. The top of the VB is mainly contributed by S3 3p orbitals, exhibiting a higher contribution of the double LEPs of the S3 atoms over the single LEPs of S1(2) atoms. On the other hand, the bottom of the CB has dominant contributions from Ga 4s and S 3p orbitals and the topmost of the CB is mainly contributed by Ga 4p orbitals and S 3p orbitals.

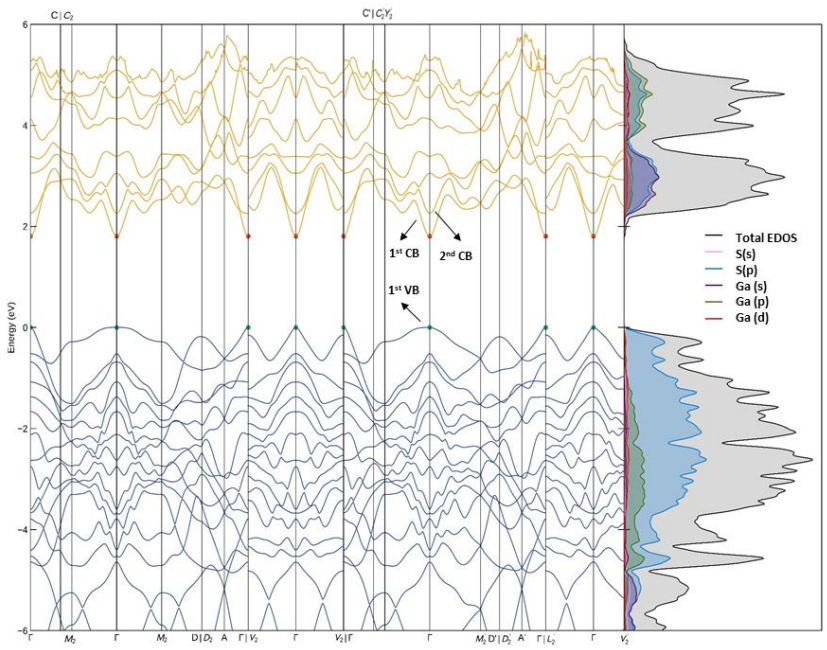

Figure 14. Electronic band structure and PDOS of α'-Ga_2S_3 at 0 GPa. Red and green points mark the position of the conduction band minimum and valence band maximum, respectively. The 1st valence band (VB) and the 1st and 2nd conduction bands (CB) are labelled.

The theoretical pressure dependence of the direct and indirect band gap of the α'-Ga_2S_3 is shown in **Fig. 15a)**. The behaviour of the direct band gap under HP resembles quite well to that observed in other OVCs, especially in β-Ga_2Se_3:[74, 113] It increases up to around 7.5 GPa, and then decreases above that pressure. Concerning the direct-to-indirect band gap crossover, it occurs at around 5.5 GPa in α'-Ga_2S_3. A similar direct-to-indirect band gap crossover was also predicted to occur around 6.0 GPa in β-Ga_2Se_3.[74] **Fig. 15b)** depicts the pressure dependence of the VBM and the lowest three CBs at the Γ point, together the lowest CBM at the V_2' point. We can clearly observe the direct-to indirect band gap crossover near 5.5 GPa and the conduction band anticrossing at the Γ point at around 7.5 GPa. It is curious that both α'-Ga_2S_3 and β-Ga_2Se_3 pass through the same changes in their band gap at similar pressures (**Figure 15a)** and **Figure 4a)** of **Ref.** [74]), despite the difference of the anion and that the nature of the indirect band gap and its pressure dependence are different. Finally, concerning the theoretical pressure dependence of the band gap in α'-Ga_2S_3 reported in **Ref. 38**, we think that the pressure behavior reported in **Ref. 38** likely corresponds to the indirect band gap (see **Fig. 15a)**), which seems to be more underestimated within LDA[38] than with our GGA-PBEsol calculations. On the other hand, the pressure dependence of the band gap reported up to 8 GPa in **Ref. 41** is quite similar to our results because of the use the GGA functional. However, they have not reported

neither the direct-to-indirect band gap crossover at around 5.5 GPa nor the decrease of the direct band gap above 8 GPa showed in **Fig. 15a)**. In this context, we think that the reason why we have observed the indirect band gap is because we have used the complex k path suggested by the Seek-path tool[117, 118] to calculate the complex electronic band structure of the monoclinic Cc phase instead of the simple path used in the Materials Project Database.[87]

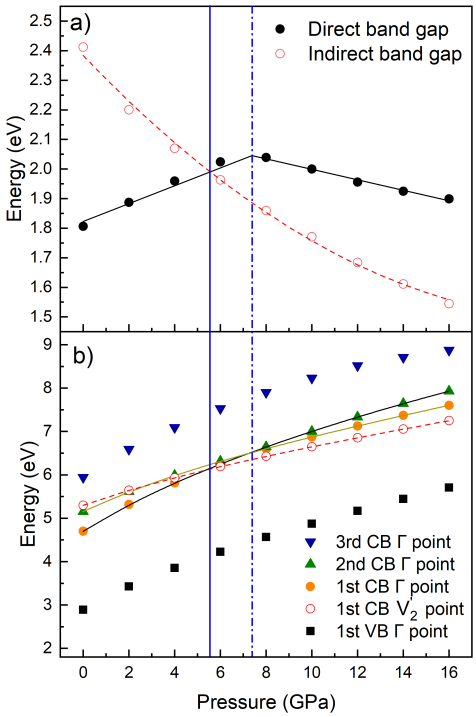

Figure 15. (Color online) a) Pressure dependence of the theoretical direct and indirect band gaps in α'-Ga_2S_3. b) Pressure dependence of the calculated energies of the three lowest conduction band (CB) minima and valence band (VB) maximum at the Γ point, together with the CB minimum at the V_2' point. Blue solid (dash) line indicate the pressure for the the direct-to-indirect band gap crossover (conduction band anticrossing of the direct band gap) at 5.5. (7.5) GPa.

In order to quantitatively analyze the changes of the topmost VB and lowermost CBs, we have tabulated the relative pressure coefficients for the band energies, yielding 8.1, 6.0, 3.9 and 3.0 GPa^{-1} for the 1st VB, 1st and 2nd CB at the Γ point and 1st CB at the V_2' point, respectively. In view of these relative pressure coefficients, the energy of the 1st VB at the Γ point (VBM) is the most sensitive under compression. This should not be surprising since the single and double LEPs occupy the high energy levels of the VB. At increasing pressure, the closing of the channels increases the repulsion of the LEPs, especially among those of the double LEPs, driving a strong increase of the

VBM energy. We must also stress the larger relative pressure coefficients of the 1st and 2nd CB at the Γ point in comparison to that of the 1st CB at the V_2' point leads to the direct-to-indirect band gap crossover at 5.5 GPa. In the same way, the larger relative pressure coefficient of the 1st in comparison with the 2nd CB at the Γ point leads to the anticrossing of the two lowermost CB bands of the direct band gap near 7.5 GPa, thus resulting in a change of pressure coefficient for the direct band gap at this pressure. In summary, our results for α'-Ga_2S_3 show a nonlinear pressure dependence of the direct band gap in good agreement with the expected behavior for all OVCs, as first stated in **Ref. 74**.

The electronic band structure at 6 GPa is shown in **Figure S29** to evidence the indirect band gap Γ-V_2' on α'-Ga_2S_3. A more detailed view of the pEDOS at 6 GPa of **Fig. S29** is illustrated **Fig. S28b)** for each atom. We can observe a more distribuited contribution of Ga 4*s*, 3*d* and 4*p* orbitals throughout the CB, as S 3*s* and 3*p* orbitals do. This important contribution is more remarkable at 16 GPa (**Fig. S28c)**), where the atomic orbitals from Ga and S atoms are more equally distributed over the CB.

As noted above, the most sensitive pressure behaviour of the VBM is rooted in the strong repulsion of the LEPs located in the channels, as a consequence of their approach with increasing pressure. According to **Fig. 5c)** and **5d)**, the Ga-S bond compressibilities decay to a greater extent (except for the Ga1-S1* bond) below 7.5 GPa. At the same time, the charge transfers decrease smoothly (**Fig. S24c)**) as a consequence of the increased covalent nature and strength of the Ga-S bonds (**Fig. 11a)** and **11c)**) under compression. Moreover, the repulsion between the LEPs of the S3 atoms is moderate below 7.5 GPa (**Fig. 13**). Therefore, it is around 7.5 GPa where various changes in the trends mentioned are observed. These results allow us to tentatively suggest that the nonlinear pressure dependence of the direct band gap near 7.5 GPa could be related to the slight decrease of the compressibilities, as a result of the prevalence of the repulsive forces between the nuclei, and the increase of the vdW interactions along the channels (**Fig. 11a)** and 11**c)**). These latter are caused by the higher increase of the repulsion between the LEPs of the S3 atoms as a consequence of the closing of the channels.

In summary, we have reported in this section the pressure dependence of the direct and indirect band gaps of α'-Ga_2S_3. Our results evidence a clear similarity between the behaviour of the electronic band structure of α'-Ga_2S_3 under compression and those of other OVCs, especially with isostructural β-Ga_2Se_3. In particular, we have found a nonlinear behavior of the direct band gap and a direct-to-indirect band gap crossover, as in β-Ga_2Se_3. This similarity was not reported in two previous works that also analysed the electronic band structure of α'-Ga_2S_3 under compression. Additionally, we have emphasized the role of the anion LEPs, contributing mainly to the topmost VB, in the changes of the electronic band structure of α'-Ga_2S_3 under compression.

8. CONCLUSIONS

In this work, we have performed HP-XRD, HP-RS and HT-RS measurements on α'-Ga_2S_3, in addition to *ab initio* calculations. With our experimental HP-XRD measurements and theoretical results, we have revised the pressure dependence of the volume and lattice parameters of α'-Ga_2S_3 in comparison with previously data.[38] In particular, we have shown that the unit-cell volume vs. pressure is better fitted to a BM3-EoS, with a softer behaviour under compression than previously reported[38] and in agreement with the pressure behaviour β-Ga_2Se_3.[79] We have reported the isothermal compressibility tensor between 0 and 14 GPa and its principal axes with the maximum, minimum and intermediate compressibilities and their relation with the channels of the structure. In particular, the maximum and intermediate compressibilities are related to the cross-sections of the channels. The role of the channels in the anisotropic pressure behaviour of the unit cell is highlighted. In particular, we have found that the channel compressibility governs the unit-cell volume compressibility and that the two GaS_4 tetrahedra become more distorted at increasing pressure, with the distortion of both tetrahedra being equal at 16 GPa. This result, in addition to the symmetrisation of the z coordinate of Ga2 atoms, points out to the pressure induced phase transition observed at 16 GPa, as already reported in **Ref. 38** and **41**.

HP-RS measurements in α'-Ga_2S_3 have allowed us to tentatively assign the symmetries of the observed Raman-active modes, to give the pressure coefficients of the Raman-active modes and to reveal structural changes above 15.1 GPa, in agreement with the pressure-induced phase transition reported previously.[38, 41] Besides, HT-RS measurements have shown the thermal stability until reaching the melting point at about 1300 K. Our lattice-dynamic calculations and the Lucazeau's idealized model[78] have allowed us to assign the symmetry of most of the observed Raman modes. Additionally, our calculations have lead us to highlight the mixed bending-stretching character of the Raman-active modes, with a remarkable vibration amplitude of Ga and S1 and S2 (S3) atoms in the low-frequency region and lower (high) part of the high-frequency region, respectively. The anharmonic effects of the different experimentally observed Raman modes have been studied, showing their different cubic and quartic anharmonic contributions, with a predominance of the implicit effect in most modes. In particular, the $A'(6)$ mode, the breathing mode related to the vacancies, has the highest anharmonicity and cubic anharmonic contribution at HP and HT, respectively.

The study of the topology of the electron density at HP within the QTAIM method has allowed us to explore the properties of the basin volumes and confirm the bulk modulus as well the increase of the covalency (decrease of the ionicity) of the compound with increasing pressure. Additionally, it has allowed us to classify the different chemical bonds in the structure and has evidenced the strengthening of the Ga-S bonds at increasing pressure and the increase of the vdW interactions along the channels, especially above 10 GPa. On the other hand, we have tentatively assigned

the Ga1-S1* and Ga2-S2* bonds as dative bonds attending to the notable differences in bond lengths, compressibilities and topological properties of these two bonds with respect to the other Ga-S bonds. Thanks to the ELF, we have visually evaluated the decreasing volume of single and double LEPs and the increasing angle between the double LEPs of the S3 atoms at HP. This angle shows a decrease around 16 GPa that may suggest an incipient instability related to the first-order phase transition already commented. Moreover, we have presented the use of the topological properties as ρ_b, $\nabla^2\rho_b$ and the H_b/ρ_b, G_b/ρ_b and $|V_b|/G_b$ ratios as an easy methodology to evaluate the chemical interactions within a system and enabling the comparison with others, in addition to studying the pressure dependence of these interactions.

Finally, our calculated electronic band structures at HP have evidenced a strong nonlinear pressure behaviour of the direct band gap and a pressure-induced direct-to-indirect band gap crossover. Both features are similar to those previously reported for isostructural β-Ga_2Se_3 and other OVCs. Moreover, we have shown that, as in other OVCs, the VBM in α'-Ga_2S_3 shows a very large pressure coefficient that is related to the strong contribution of anionic LEPs. In this context, there is a greater relevance for the topmost VB of the double anion LEPs in α'-Ga_2S_3 than in less complex OVCs. In α'-Ga_2S_3, the strong compression of the anion LEPs leads to a strong increase of the VBM energy so LEPs play a similar role as in adamantine-based OVCs, like $CdGa_2S_4$. The strong compression of these LEPs explains the strong increase of the VBM energy and the nonlinear dependence of the direct band gap.

In summary, the present work has been aimed at understanding in detail the behaviour of the low-pressure phase of α'-Ga_2S_3 under compression. Our study has shown that the HP properties of α'-Ga_2S_3 are similar to those of β-Ga_2Se_3 and other adamantine-based OVCs. Therefore, this work has contributed to stablish a general behaviour under compression of materials with unpaired anion electrons in the crystalline structure.

9. ACKNOWLEDGMENTS

The authors thank the financial support from Spanish Research Agency (AEI) under projects MALTA Consolider Team network (RED2018-102612-T) and projects MAT2016-75586-C4-2/3-P, FIS2017-83295-P, PID2019-106383GB-42/43, and PGC2018-097520-A-100, as well as from Generalitat Valenciana under Project PROMETEO/2018/123 (EFIMAT). A. M., and P. R.-H acknowledge computing time provided by Red Española de Supercomputación (RES) and MALTA-Cluster and E.L.D.S. acknowledges Marie Sklodowska-Curie Grant No. 785789-COMEX from the European Union's Horizon 2020 research and innovation program. J. A. S. also wants to thank the Ramon y Cajal fellowship (RYC-2015-17482) for financial support. We also thank ALBA synchrotron light source for funded experiment 2017022088 at the MSPD-BL04 beamline.

10. REFERENCES

1. J. Wang, W. Yuan and M. Li, *J. Cryst. Growth*, 2007, **307**, 59-65.
2. H. Okamoto and T. Massalski, *J. Phase Equilib. Diffus.*, 1991, **12**, 148-168.
3. A. Pelton and S. Larose, *Bulletin of Alloy Phase Diagrams*, 1990, **11**, 347-353.
4. H. Okamoto, *J. Phase Equilib. Diffus.*, 2010, **31**, 206-206.
5. P. Wang, M. Liu, F. Mo, Z. Long, F. Fang, D. Sun, Y.-N. Zhou and Y. Song, *Nanoscale*, 2019.
6. Y. Ni, H. Wu, Z. Wang, M. Mao, G. Cheng and H. Fei, *J. Cryst. Growth*, 2009, **311**, 1404-1406.
7. L. Isaenko, I. Vasilyeva, A. Merkulov, A. Yelisseyev and S. Lobanov, *J. Cryst. Growth*, 2005, **275**, 217-223.
8. Y. Kim, I.-s. Seo, S. W. Martin, J. Baek, P. Shiv Halasyamani, N. Arumugam and H. Steinfink, *Chem. Mater.*, 2008, **20**, 6048-6052.
9. L. Bai, Z. Lin, Z. Wang, C. Chen and M.-H. Lee, *J. Chem. Phys.*, 2004, **120**, 8772-8778.
10. L. Bai, Z. Lin, Z. Wang and C. Chen, *J. Appl. Phys.*, 2008, **103**, 083111.
11. M.-J. Zhang, X.-M. Jiang, L.-J. Zhou and G.-C. Guo, *J. Mater. Chem. C*, 2013, **1**, 4754-4760.
12. H. El Shaikh, M. Abdal-Rahman, A. Belal and I. Ashraf, *J. Phys. D: Appl. Phys.*, 1996, **29**, 466.
13. W.-T. Kim, H.-S. Kim, Y.-G. Kim and S.-R. Hahn, *Journal of materials science letters*, 1987, **6**, 479-480.
14. C.-S. Yoon, F. Medina, L. Martinez, T.-Y. Park, M.-S. Jin and W.-T. Kim, *Appl. Phys. Lett.*, 2003, **83**, 1947-1949.
15. J. Ren, B. Li, G. Yang, W. Xu, Z. Zhang, M. Secu, V. Bercu, H. Zeng and G. Chen, *Optics letters*, 2012, **37**, 5043-5045.
16. I. Sastry, C. Bacalski and J. McKittrick, *J. Electrochem. Soc.*, 1999, **146**, 4316-4319.
17. T. Aono and K. Kase, *Solid state communications*, 1992, **81**, 303-305.
18. C.-H. Ho and H.-H. Chen, *Sci. Rep.*, 2014, **4**, 6143.
19. S. Al Garni and A. Qasrawi, *J. Electron. Mater.*, 2017, **46**, 4848-4856.
20. K. A. Kokh, Z.-M. Huang, J.-G. Huang, Y.-Q. Gao, B. Uralbekov, J. Panomarev, I. Lapin, V. Svetlichnyi, G. Lanskii and Y. M. Andreev, *Mater. Res. Bull.*, 2016, **84**, 462-467.
21. Z. Huang, J.-G. Huang, K. Kokh, V. Svetlichnyi, A. Shabalina, Y. M. Andreev and G. Lanskii, *Ga_2S_3: Optical properties and perspectives for THz applications*, in *2015 40th International Conference on Infrared, Millimeter, and Terahertz waves (IRMMW-THz)*, 2015.
22. C. Jastrzebski, D. J. Jastrzebski, V. Kozak, K. Pietak, M. Wierzbicki and W. Gebicki, *Materials Science in Semiconductor Processing*, 2019, **94**, 80-85.
23. M. Zervos, A. Othonos, V. Gianneta, A. Travlos and A. G. Nassiopoulou, *J. Appl. Phys.*, 2015, **118**, 194302.
24. S. Alharbi and A. Qasrawi, *Plasmonics*, 2017, **12**, 1045-1049.
25. C.-H. Ho, M.-H. Lin, Y.-P. Wang and Y.-S. Huang, *Sens. Actuators, A*, 2016, **245**, 119-126.

26. L. Wang and C. Tu, *Nanotechnol.*, 2020, **31**, 165603.
27. Z. M. Hu, G. T. Fei and L. De Zhang, *Mater. Lett.*, 2019, **239**, 17-20.
28. M. Pardo, M. Guittard, A. Chilouet and A. Tomas, *J. Solid State Chem.*, 1993, **102**, 423-433.
29. R. Lieth, H. Heijligers and C. vd Heijden, *J. Electrochem. Soc.*, 1966, **113**, 798-801.
30. M. Guymont, A. Tomas, M. Pardo and M. Guittard, *phys. status solidi (a)*, 1989, **113**, K5-K7.
31. S. Gallego-Parra, O. Gomis, R. Vilaplana, H. M. Ortiz, E. Perez-Gonzalez, R. Luna, P. Rodríguez-Hernández, A. Muñoz, V. Ursaki and I. Tiginyanu, *J. Appl. Phys.*, 2019, **125**, 115901.
32. F. J. Manjon and O. Gomis, in *Pressure-Induced Phase Transitions in AB_2X_4 Chalcogenide Compounds*, eds. F. J. Manjon, I. M. Tiginyanu and V. Ursaki, Springer, Berlin, 2013, vol. 189, ch. AB_2Se_4 Ordered-Vacancy Compounds at High Pressures, pp. 163-184.
33. F. J. Manjon and R. Vilaplana, in *Pressure-Induced Phase Transitions in AB_2X_4 Chalcogenide Compounds*, eds. F. J. Manjon, I. M. Tiginyanu and V. V. Ursaki, Springer, Berlin, 2013, vol. 189, ch. AB_2S_4 Ordered-Vacancy Compounds at High Pressures, pp. 133-161.
34. A. Tomas, M. Guymont, M. Pardo, M. Guittard and J. Flahaut, *phys. status solidi (a)*, 1988, **107**, 775-784.
35. a. R. Gillespie and R. Nyholm, *Quarterly Reviews, Chemical Society*, 1957, **11**, 339-380.
36. J. Goodyear and G. Steigmann, *Acta Crystallogr.*, 1963, **16**, 946-949.
37. C. Jones, J. Bryan, K. Kirschbaum and J. Edwards, *Z. fur Krist. - New Cryst. Struct.*, 2001, **216**, 349-350.
38. X. Lai, F. Zhu, S. Qin, D. Chen, Y. Li, K. Yang and X. Wu, *J. Appl. Phys.*, 2014, **116**, 193507.
39. R. Vilaplana, S. G. Parra, A. Jorge-Montero, P. Rodríguez-Hernández, A. Munoz, D. Errandonea, A. Segura and F. J. Manjón, *Inorg. Mater.*, 2018, **57**, 8241-8252.
40. F. Manjón, R. Vilaplana, O. Gomis, E. Pérez‐González, D. Santamaría‐Pérez, V. Marín‐Borrás, A. Segura, J. González, P. Rodríguez‐Hernández and A. Muñoz, *phys. status solidi (b)*, 2013, **250**, 669-676.
41. L. Yang, J. Jiang, L. Dai, H. Hu, M. Hong, X. Zhang, H. Li and P. Liu, *J. Mater. Chem. C*, 2021, **9**, 2912-2918.
42. A. L. Pereira, J. A. Sans, R. Vilaplana, O. Gomis, F. Manjón, P. Rodriguez-Hernandez, A. Muñoz, C. Popescu and A. Beltrán, *J. Phys. Chem. C*, 2014, **118**, 23189-23201.
43. V. P. Cuenca-Gotor, J. Á. Sans, O. Gomis, A. Mújica, S. Radescu, A. Munoj, P. Rodriguez-Hernadez, E. L. Da Silva, C. Popescu, J. Ibañez, R. Vilaplana and F. J. Manjon, *Phys. Chem. Chem. Phys.*, 2020.
44. I. Efthimiopoulos, J. Kemichick, X. Zhou, S. V. Khare, D. Ikuta and Y. Wang, *The Journal of Physical Chemistry A*, 2014, **118**, 1713-1720.

45. M. Xu, S. Jakobs, R. Mazzarello, J.-Y. Cho, Z. Yang, H. Hollermann, D. Shang, X. Miao, Z. Yu and L. Wang, *J. Phys. Chem. C*, 2017, **121**, 25447-25454.
46. A. Walsh, D. J. Payne, R. G. Egdell and G. W. Watson, *Chemical Society Reviews*, 2011, **40**, 4455-4463.
47. O. Gomis, R. Vilaplana, F. J. Manjón, E. Pérez-González, J. López-Solano, P. Rodríguez-Hernández, A. Muñoz, D. Errandonea, J. Ruiz-Fuertes, A. Segura, D. Santamaria-Pérez, I. M. Tiginyanu and V. Ursaki, *J. Appl. Phys.*, 2012, **111**, 013518.
48. G. V. Gibbs, A. F. Wallace, R. Downs, N. L. Ross, D. F. Cox and K. M. Rosso, *Physics and Chemistry of Minerals*, 2011, **38**, 267-291.
49. C. Hejny, R. Sagl, D. M. Többens, R. Miletich, M. Wildner, L. Nasdala, A. Ullrich and T. Balic-Zunic, *Physics and Chemistry of Minerals*, 2012, **39**, 399-412.
50. S. Vaidya and G. Kennedy, *J. Phys. Chem. Solids*, 1972, **33**, 1377-1389.
51. G. Lepore, T. B. Ballaran, F. Nestola, L. Bindi, D. Pasqual and P. Bonazzi, *Mineralogical Magazine*, 2012, **76**, 963-973.
52. M. Tuktabiev, S. Popova, V. Brazhkin, A. Lyapin and Y. Katayama, *J. Phys.: Condens. Matter*, 2009, **21**, 385401.
53. T. Chattopadhyay, A. Werner and H. Schnering, *J. Phys. Chem. Solids*, 1982, **43**, 919-923.
54. S. Klotz, J. C. Chervin, P. Munsch and G. Le Marchand, *J. Phys. D: Appl. Phys.*, 2009, **42**, 075413.
55. A. Dewaele, P. Loubeyre and M. Mezouar, *Phys. Rev. B*, 2004, **70**, 094112.
56. F. Fauth, I. Peral, C. Popescu and M. Knapp, *Powder Diffr.*, 2013, **28**, S360-S370.
57. C. Prescher and V. B. Prakapenka, *High Pressure Res.*, 2015, **35**, 223-230.
58. B. H. Toby and R. B. Von Dreele, *J. Appl. Crystallogr.*, 2013, **46**, 544-549.
59. H. K. Mao, J. A. Xu and P. M. Bell, *J. Geophys. Res.: Solid Earth*, 1986, **91**, 4673-4676.
60. P. Hohenberg and W. Kohn, *Physical review*, 1964, **136**, B864-B871.
61. G. Kresse and J. Hafner, *Phys. Rev. B*, 1993, **47**, 558-561.
62. P. E. Blöchl, *Phys. Rev. B*, 1994, **50**, 17953-17979.
63. G. Kresse and D. Joubert, *Phys. Rev. B*, 1999, **59**, 1758-1775.
64. J. P. Perdew, A. Ruzsinszky, G. I. Csonka, O. A. Vydrov, G. E. Scuseria, L. A. Constantin, X. Zhou and K. Burke, *Phys. Rev. Lett.*, 2008, **100**, 136406.
65. Computer Code Phonon, see: http://www.computingformaterials.com/index.html).
66. A. Otero-de-la-Roza, E. R. Johnson and V. Luaña, *Computer Physics Communications*, 2014, **185**, 1007-1018.
67. M. Yu and D. R. Trinkle, *J. Chem. Phys.*, 2011, **134**, 064111.
68. Elk code, *The Elk FP-LAPW code*, http://elk.sourceforge.net/).
69. D. Kirzhnits, *Soviet Phys. JETP*, 1957, **5**.
70. D. A. Kirzhnits, *American Journal of Physics*, 1967, **35**, 1166-1167.
71. K. Momma and F. Izumi, *J. Appl. Crystallogr.*, 2011, **44**, 1272-1276.

72. J. Gonzalez-Platas, M. Alvaro, F. Nestola and R. Angel, *J. Appl. Crystallogr.*, 2016, **49**, 1377-1382.
73. M. Takumi, Y. Koshio and K. Nagata, *phys. status solidi (b)*, 1999, **211**, 123-129.
74. F. J. Manjón, O. Gomis, P. Rodríguez-Hernández, E. Pérez-González, A. Muñoz, D. Errandonea, J. Ruiz-Fuertes, A. Segura, M. Fuentes-Cabrera, I. M. Tiginyanu and V. Ursaki, *Phys. Rev. B*, 2010, **81**, 195201.
75. J. A. Sans, R. Vilaplana, E. L. da Silva, C. Popescu, V. P. Cuenca-Gotor, A. n. Andrada-Chacón, J. Sánchez-Benitez, O. Gomis, A. L. Pereira and P. Rodríguez-Hernández, *Inorg. Mater.*, 2020.
76. M. J. Cliffe and A. L. Goodwin, *J. Appl. Crystallogr.*, 2012, **45**, 1321-1329.
77. L. D. Landau, A. Kosevich, L. P. Pitaevskii and E. M. Lifshitz, 1986.
78. G. Lucazeau and J. Leroy, *Spectrochimica Acta Part A: Molecular Spectroscopy*, 1978, **34**, 29-32.
79. A. Miller, A. MacKinnon and D. Weaire, in *Solid State Phys.*, Elsevier, 1982, vol. 36, pp. 119-175.
80. C. Julien, S. Barnier, I. Ivanov, M. Guittard, M. Pardo and A. Chilouet, *Mater. Sci. Eng., B*, 1999, **57**, 102-109.
81. S. Barnier, M. Palazzi, M. Massot and C. Julien, *Solid State Ionics*, 1990, **44**, 81-86.
82. C. Julien, S. Barnier, M. Massot and M. Pardo, *Mater. Res. Bull.*, 1994, **29**, 785-794.
83. V. V. Ursaki, I. I. Burlakov, I. M. Tiginyanu, Y. S. Raptis, E. Anastassakis and A. Anedda, *Phys. Rev. B*, 1999, **59**, 257.
84. R. Vilaplana, M. Robledillo, O. Gomis, J. A. Sans, F. J. Manjón, E. Pérez-González, P. Rodríguez-Hernández, A. Muñoz, I. M. Tiginyanu and V. V. Ursaki, *J. Appl. Phys.*, 2013, **113**, 093512.
85. M. J. Taylor, *J. Raman Spectrosc.*, 1973, **1**, 355-358.
86. D. Friedrich, M. Schlosser, R. Weihrich and A. Pfitzner, *Inorganic Chemistry Frontiers*, 2017, **4**, 393-400.
87. A. Jain, S. P. Ong, G. Hautier, W. Chen, W. D. Richards, S. Dacek, S. Cholia, D. Gunter, D. Skinner and G. Ceder, *Apl Materials*, 2013, **1**, 011002.
88. Y. C. Cheng, C. Q. Jin, F. Gao, X. L. Wu, W. Zhong, S. H. Li and P. K. Chu, *J. Appl. Phys.*, 2009, **106**, 123505.
89. G. Abstreiter, M. Cardona and A. Pinczuk, in *Light Scattering in Solids IV*, Springer, 1984, pp. 5-150.
90. T. Ahamad and S. M. Alshehri, *Green Synthesis and Characterization of Gallium (III) Sulphide (α-Ga_2S_3) Nanoparicles at Room Temperature*, in *Nano Hybrids*, 2014.
91. S. A. Miller, P. Gorai, B. R. Ortiz, A. Goyal, D. Gao, S. A. Barnett, T. O. Mason, G. J. Snyder, Q. Lv and V. Stevanović, *Chem. Mater.*, 2017, **29**, 2494-2501.
92. A. Link, K. Bitzer, W. Limmer, R. Sauer, C. Kirchner, V. Schwegler, M. Kamp, D. Ebling and K. Benz, *J. Appl. Phys.*, 1999, **86**, 6256-6260.
93. R. Zallen and E. Conwell, *Solid State Communications*, 1979, **31**, 557-561.

94. B. A. Weinstein and R. Zallen, in *Light Scattering in Solids IV*, Springer, 1984, pp. 463-527.
95. S. V. Bhatt, M. Deshpande, V. Sathe, R. Rao and S. Chaki, *J. Raman Spectrosc.*, 2014, **45**, 971-979.
96. J. Besson, J. Cernogora, M. Slade, B. Weinstein and R. Zallen, *Physica B+C*, 1981, **105**, 319-323.
97. Z. Jakšić, *phys. status solidi (b)*, 2003, **239**, 131-143.
98. I. Efthimiopoulos, M. Berg, A. Bande, L. Puskar, E. Ritter, W. Xu, A. Marcelli, M. Ortolani, M. Harms and J. Müller, *Phys. Chem. Chem. Phys.*, 2019, **21**, 8663-8678.
99. R. Bader, *Journal*, 1990.
100. C. Gatti, *Z. Kristallogr. Cryst. Mater.*, 2005, **220**, 399-457.
101. A. M. Pendás, A. Costales, M. Blanco, J. Recio and V. Luaña, *Phys. Rev. B*, 2000, **62**, 13970.
102. P. Mori-Sánchez, A. M. Pendás and V. Luaña, *J. Am. Chem. Soc.*, 2002, **124**, 14721-14723.
103. H. Yang, P. Boulet and M.-C. Record, *Computational and Theoretical Chemistry*, 2020, 112784.
104. J. Zhang, L. Song, M. Sist, K. Tolborg and B. B. Iversen, *Nat. Commun.*, 2018, **9**, 4716.
105. R. Bianchi, G. Gervasio and D. Marabello, *Inorg. Mater.*, 2000, **39**, 2360-2366.
106. H. Yang, P. Boulet and M.-C. Record, *J. Solid State Chem.*, 2020, **286**, 121266.
107. R. F. Bader and H. Essén, *J. Chem. Phys.*, 1984, **80**, 1943-1960.
108. E. Espinosa, I. Alkorta, J. Elguero and E. Molins, *J. Chem. Phys.*, 2002, **117**, 5529-5542.
109. T. Lankau and C. H. Yu, *The Journal of Physical Chemistry A*, 2020, **124**, 3795-3804.
110. H. Kasai, K. Tolborg, M. Sist, J. Zhang, V. R. Hathwar, M. Ø. Filsø, S. Cenedese, K. Sugimoto, J. Overgaard and E. Nishibori, *Nat. Mater.*, 2018, **17**, 249-252.
111. A. D. Becke and K. E. Edgecombe, *J. Chem. Phys.*, 1990, **92**, 5397-5403.
112. M. Kohout and A. Savin, *Journal of computational chemistry*, 1997, **18**, 1431-1439.
113. M. Takumi, T. Ueda, Y. Koshio, H. Nishimura and K. Nagata, *phys. status solidi (b)*, 2001, **223**, 271-274.
114. J. González, R. Rico, E. Calderón, M. Quintero and M. Morocoima, *phys. status solidi (b)*, 1999, **211**, 45-49.
115. H. A. Rahnamaye Aliabad, S. Basirat and I. Ahmad, *J. Mater. Sci.: Mater. Electron.*, 2017, **28**, 16476-16483.
116. A. M. Ganose, A. J. Jackson and D. O. Scanlon, *Journal of Open Source Software*, 2018, **3**, 717.
117. Y. Hinuma, G. Pizzi, Y. Kumagai, F. Oba and I. Tanaka, *Computational Materials Science*, 2017, **128**, 140-184.
118. A. Togo and I. Tanaka, *arXiv preprint arXiv:1808.01590*, 2018.

119. O. Madelung, *Semiconductors: data handbook*, Springer Science & Business Media, 2012.
120. D. Lübbers and V. Leute, *J. Solid State Chem.*, 1982, **43**, 339-345.

Supplementary Information of

Structural, vibrational and electronic properties of α'-Ga_2S_3 under compression

S. Gallego-Parra[1]*, R. Vilaplana[2]*, O. Gomis[2], E. Lora da Silva[1,3], A. Otero-de-la-Roza[4], P. Rodríguez-Hernández[5], A. Muñoz[5], J. González[6], J.A. Sans[1], V.P. Cuenca-Gotor[1], J. Ibáñez[7], C. Popescu[8] and F. J. Manjón[1]

[1]*Instituto de Diseño para la Fabricación y Producción Automatizada, MALTA Consolider Team, Universitat Politècnica de València, 46022 València, Spain*
[2] *Centro de Tecnologías Físicas, MALTA Consolider Team, Universitat Politècnica de València, 46022 Valencia, Spain*
[3]*IFIMUP, Department of Physics and Astronomy, Faculty of Science, University of Porto, Portugal*
[4]*Departamento de Química Física y Analítica, MALTA Consolider Team, Facultad de Química, Universidad de Oviedo, 33006 Oviedo, Spain*
[5]*Departamento de Física, Instituto de Materiales y Nanotecnología, MALTA Consolider Team, Universidad de La Laguna, 38207 San Cristóbal de La Laguna, Spain*
[6]*Ciencias de la Tierra y Fisica de la Materia Condensada, MALTA Consolider Team, Universidad de Cantabria, 39005, Santander, Spain*
[7] *Institute of Earth Sciences Jaume Almera, MALTA Consolider Team, Consell Superior d'Investigacions Científiques (CSIC), 08028 Barcelona, Catalonia, Spain*
[8]*ALBA-CELLS, MALTA Consolider Team, 08290 Cerdanyola del Valles (Barcelona), Catalonia, Spain*

*Corresponding authors: S. Gallego-Parra (sagalpar@doctor.upv.es), R. Vilaplana (rovilap@fis.upv.es)

Structural properties

Alfa Aesar product specification certifies the existence of a small amount of oxide, Ga_2O_3, in the commercial powders of Ga_2S_3. At room conditions, Ga_2O_3 exhibits a monoclinic β phase (S.G. C2/m, No 12). By means of Le Bail refinements, we have succeeded in indexing α'-Ga_2S_3 together with β-Ga_2O_3 in our XRD pattern at 0.1 GPa, as depicted in **Fig. S1**. Those peaks coming from the β-Ga_2O_3 are located at around 8.20, 8.30, 9.10, 9.50, 10.13 and 12.30 degrees. It is worthy to stress the high intensity of the diffraction peaks from β-Ga_2O_3 at 8.20, 8.30 and 9.50 degrees. The high structure factor values of these peaks explain these high intensities, even at the very low concentration in our commercial powders of Ga_2S_3.

According the Lai et al.'s patterns,[1] they found peaks associated with the impurity, concretely, at 0.39 $Å^{-1}$ in Run-1 (0.0001 GPa, **Fig. 1** of **Ref. 1**) and additionally other peak at 0.3 $Å^{-1}$ in Run-2 (0.1 GPa, **Fig. 2** of **Ref. 1**). Since the limited number of peaks, they could not identify such an impurity. In our HP-XRD conditions, these peaks must be located at 7.30 and 9.5 degrees. That peak observed at 9.5 degrees corresponds with the most intense peak observed of β-Ga_2O_3 in our measurement at 0.1 GPa (**Fig. S1**). However, we have not observed the peak at 7.30 degrees. Therefore, this must correspond to other impurity different from β-Ga_2O_3. To avoid confusion, henceforth we will refer to the β-Ga_2O_3 as the only impurity in our work.

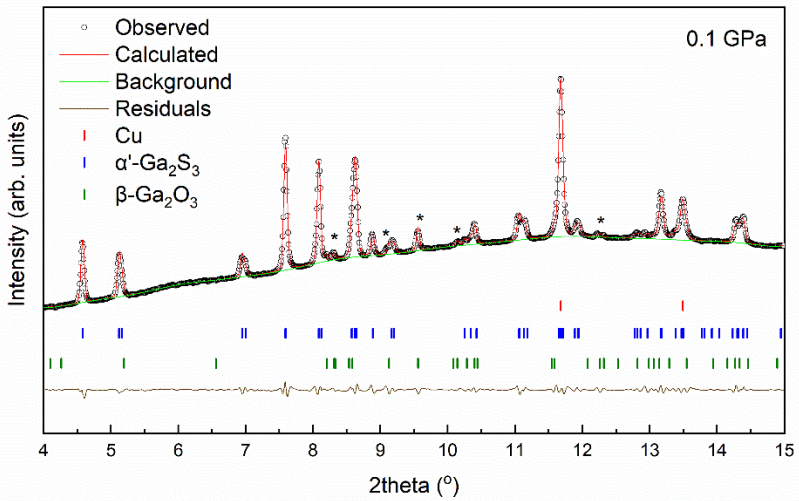

Figure S1. Experimental powder XRD pattern (open circles) of α'-Ga_2S_3 measured at 0.1 GPa. Le Bail refinement (red line) with the used background (green line) and residuals (black line) are also shown. Tick marks correspond to α'-Ga_2S_3, β-Ga_2O_3 and Cu reflections, respectively. Asterisks indicate those diffraction peaks observed from the β-Ga_2O_3.

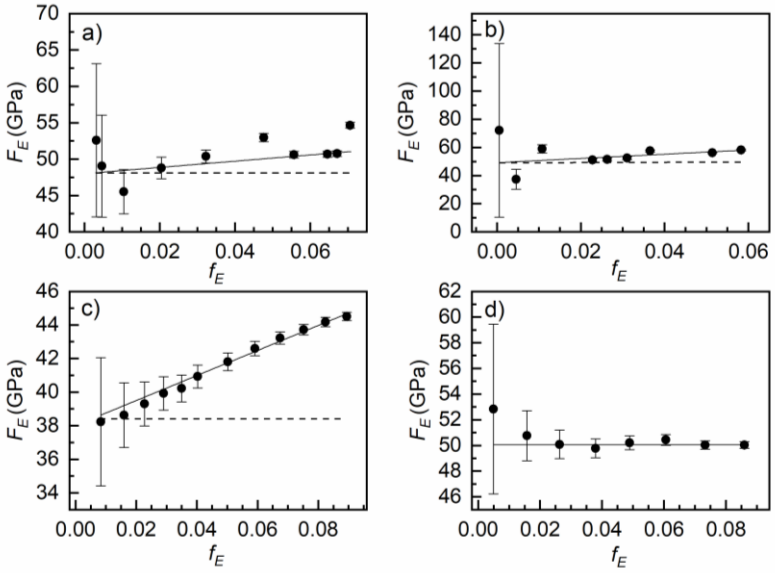

Figure S2. Normalized stress, F_E, vs finite strain, f_E, for a) our experimental data and b) experimental data from run-2 in **Ref. 1**, c) our GGA-PBEsol calculations and d) LDA calculations from **Ref. 1** for the α' phase. Horizontal dash lines serve as a reference of $B_o' = 4$.

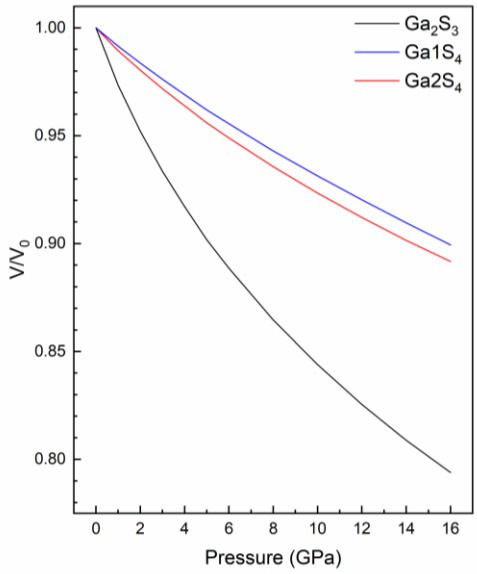

Figure S3. Pressure dependence of the relative volumes in α'-Ga_2S_3 corresponding to the unit-cell and to the $Ga1S_4$ and $Ga2S_4$ tetrahedra.

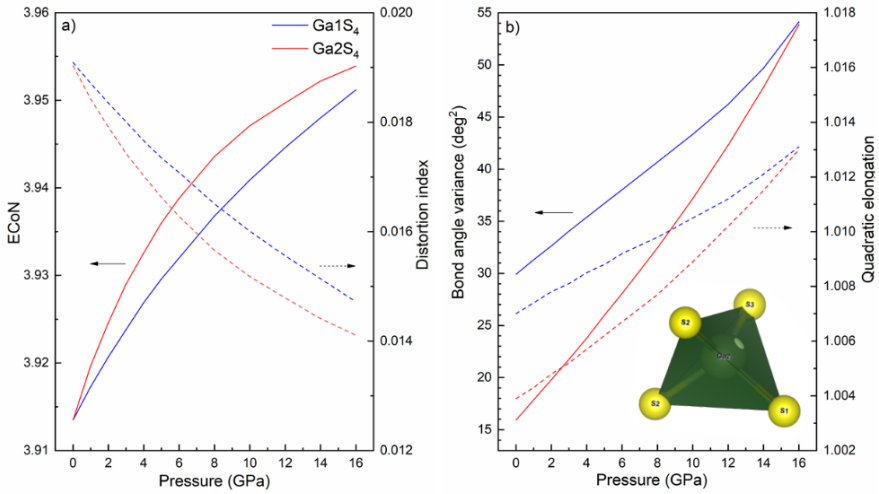

Figure S4. Pressure dependence of the a) ECoN and distortion index and b) bond angle variance and quadratic elongation in $Ga1S_4$ and $Ga2S_4$ polyhedra. Inset on b) depicts the Ga2 atom out the centroid of the $Ga2S_4$ tetrahedra at 14 GPa.

Figs. S5, S6 and **S7** show the relative change of the free theoretical atomic coordinates (x,y,z) of the unequivalent Ga and S atoms at HP. In general, it can be inferred that S atoms move more than Ga atoms at HP. However, we must highlight the particular features observed in each figure. As **Fig. S5 a)** shows, S1 and S2 atoms displace along the positive *a* axis while S3 atoms move in the opposite direction (**Fig. S5 b)**). Moreover, the change of the atomic parameters of the S3 atom is considerably larger than those of S1 and S2 atoms. These movements lead to the closing of the channels (see **Fig. S8 c)**). Concerning the Ga atoms, below ~4 GPa, Ga1 and Ga2 atoms move along the positive and negative *a* axis, respectively, which also leads to the closure of the channels (**Fig. S8 a)**). Above that pressure, Ga1 and Ga2 atoms start to move in the opposite direction as if there was some kind of repulsion along the *a* axis (**Fig. S5 a)**). Along the positive *b* axis, S atoms again move in a more pronounced way than Ga atoms (**Fig. S6**). Again around 4 GPa, Ga2 atoms change the movement direction from the positive to the negative *b* axis as if there were a repulsive effect above that pressure.

Figure S8 shows the displacement of S and Ga atoms in the *a*-*b* plane. Below ~4 GPa, Ga atoms move approximately symmetrically along the *b* axis (**Fig. S8 a)**). Above ~4 GPa they also move in a similar trend, where the axis of symmetry is now at around 60 degrees, measured to the *b* axis, from *a* to *b* (**Fig. S8 b)**). More surprising is how S and Ga atoms move along the z axis; i.e. along the direction normal to the *a*-*b* plane (**Fig. S7**). S1 and Ga1 atoms displace along the positive z cartesian axis, while S2 atoms move slightly in the opposite direction (**Fig. S7 a)**). In contrast, S3 atoms move along the positive z axis up to around 2 GPa and in the negative direction above that pressure. The most striking feature is that the relative z coordinate of the Ga2 atoms steadily decreases to 0 above 16 GPa (see **Fig. S7 b)**); i.e. it points to a symmetrisation

of the structure that ends in the phase transition that has been observed above this pressure (see **Fig. 2**).

Figure S9 shows the displacements along the z cartesian axis of the S and Ga atoms. We have remarked that Ga1 and Ga2 atoms move in the opposite direction (**Fig. S9 a)**), bearing in mind that atom Ga2 changes its z coordinate much faster than atom Ga1, as already commented. **Figure S9 b)** and **Figure S9 c)** emphasize the change in the direction of movement of the S3 atom below and above 2 GPa, respectively. Therefore, the analysis of the atomic movements at HP shows a tendence of the monoclinic structure to a symmetrisation at HP.

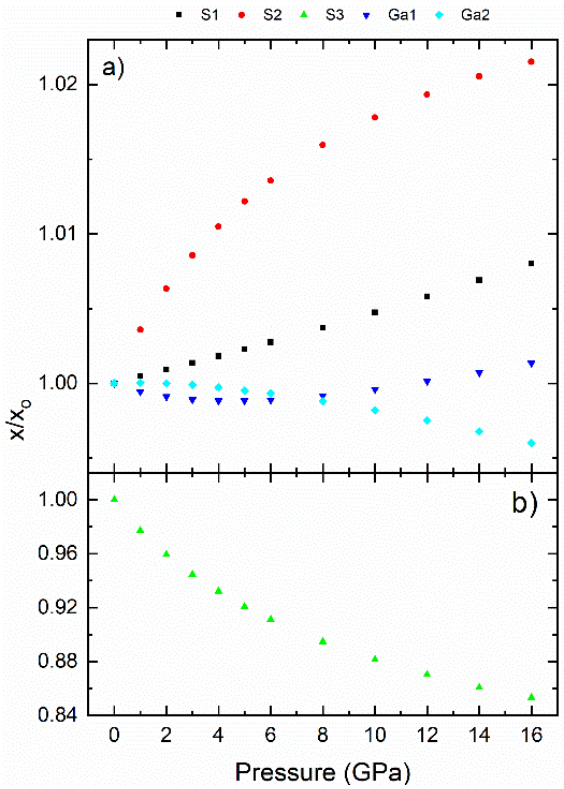

Figure S5. Relative change of the theoretical *x* atomic coordinate of independent a) S1, S2, Ga1 and Ga2 atoms and b) S3 atoms of the α' phase on increasing pressure.

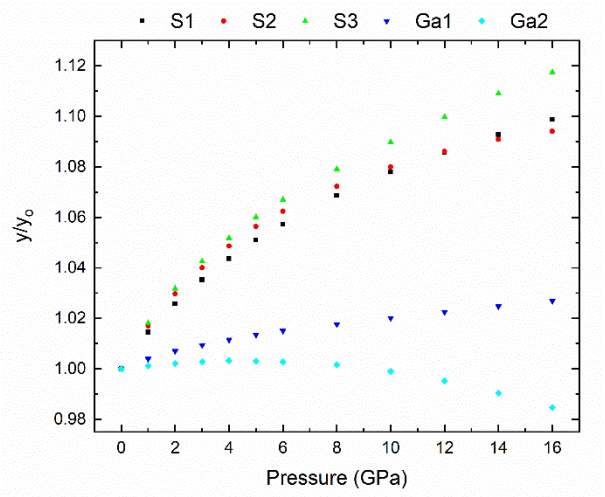

Figure S6. Relative change of the theoretical y atomic coordinate of all the independent atoms of the α' phase on increasing pressure.

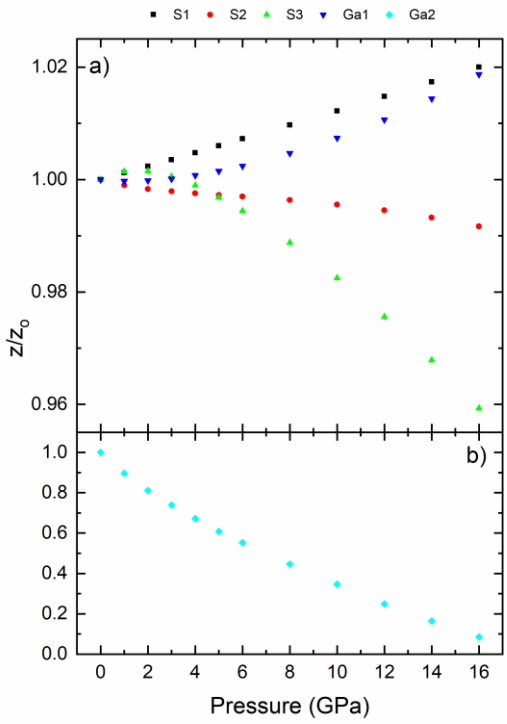

Figure S7. Relative change of the theoretical *z* atomic coordinate of independent a) S1, S2, S3 and Ga1 atoms and b) Ga2 atoms of the α' phase on increasing pressure.

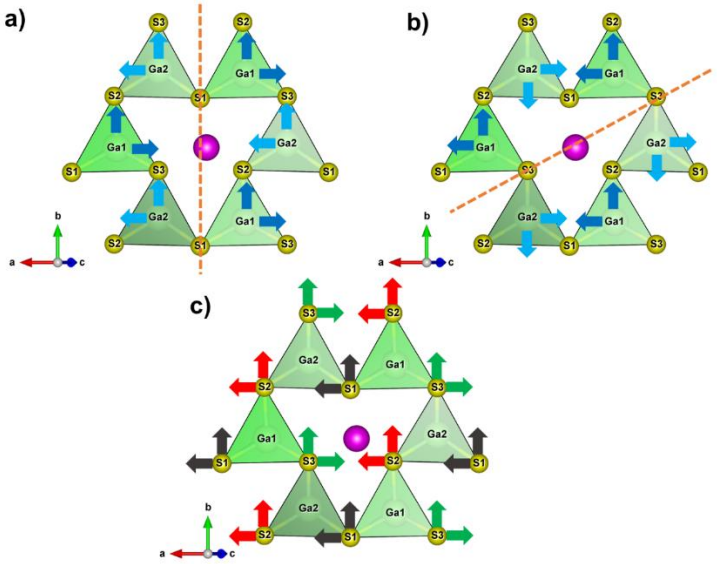

Figure S8. Schemes of the Ga_2S_3 structure around the vacancy. Arrows of each atom indicate the directions *x* and *y* of displacement of Ga atoms before a) and after 4 GPa b), and S atoms c) with increasing pressure. Dashed lines indicate the axis of symmetry about which the movement of Ga atoms is symmetrical. This axis is a) paralel to the *b* axis before 4 GPa and b) at around 60 degrees (measured to the *b* axis, from *a* to *b*) after 4 GPa.

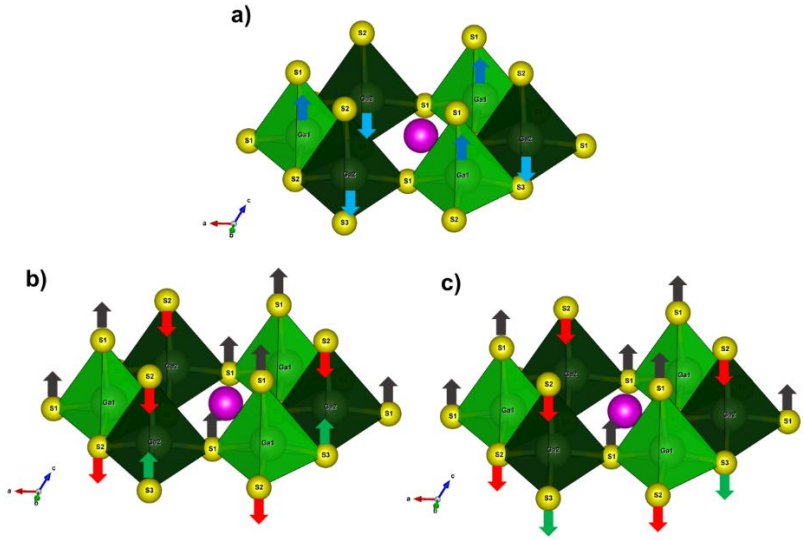

Figure S9. Schemes of α'-Ga_2S_3 around the vacancy. Arrows of each atom indicate the direction *z* of displacement of Ga atoms a) and S atoms b) before and c) after 2 GPa.

Vibrational properties

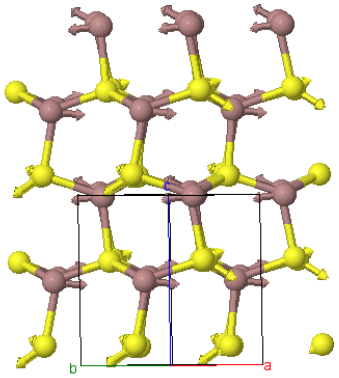

Figure S10. Scheme of the atomic vibrations of the *A'*(1) mode of α'-Ga_2S_3 around 74 cm^{-1}. This mode is a shear layer-like mode with all Ga and S atoms almost in the same plane of the wurtzite lattice vibrating out-of-phase with respect to all atoms of neighbour planes. It can be considered as a translation of the GaS_4 unit, despite it is a translation of the GaS_3 unit. Vibrations are observed thanks to software J-ICE.[2]

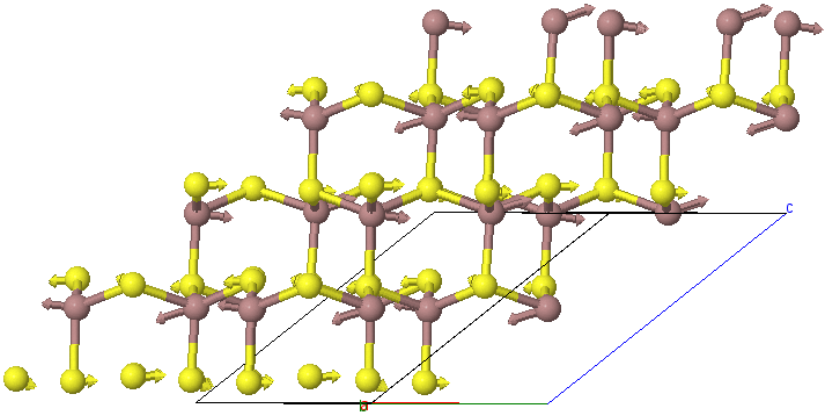

Figure S11. Scheme of the atomic vibrations of the *A''*(1) mode of α'-Ga_2S_3 around 82 cm^{-1}. This mode is also a shear layer-like mode with all Ga and S atoms almost in the same plane of the wurtzite lattice vibrating out-of-phase with respect to all atoms of neighbour planes. It can be considered as a translation of the GaS_4 unit, despite it is a translation of the GaS_3 unit. Note that this mode and the previous one are the two non-degenerate shear modes of typical shear E rigid modes of layered materials; i.e. atoms in both modes vibrate in perpendicular direction.

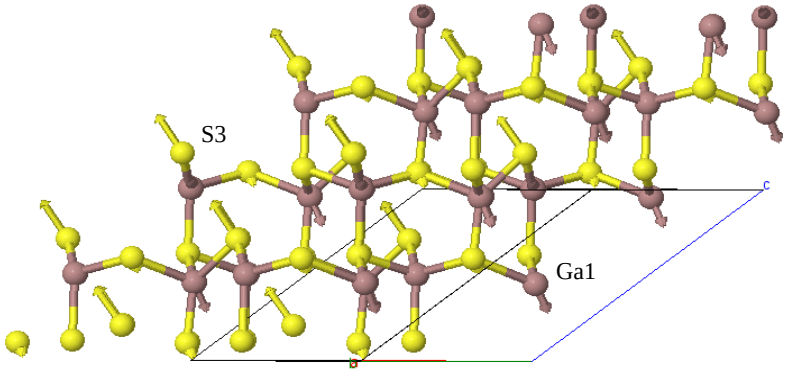

Figure S12. Scheme of the atomic vibrations of the *A'*(2) mode of α'-Ga_2S_3 around 87 cm^{-1}. This mode is mainly characterized by a strong movement of the S1 atom almost in perpendicular direction to the atomic planes of the wurtzite lattice. It also shows Ga1 atoms moving in opposite direction with respect to S3 atoms.

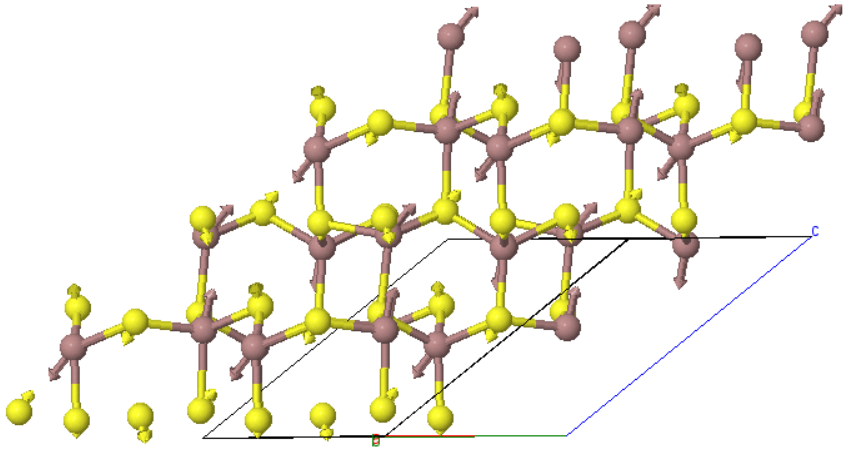

Figure S13. Scheme of the atomic vibrations of the *A''*(2) mode of α'-Ga_2S_3 around 100 cm^{-1}. This mode is a kind of compressional layer-like mode with all Ga and S atoms almost in the same plane of the wurtzite lattice vibrating out-of-phase with respect to all atoms of neighbour planes.

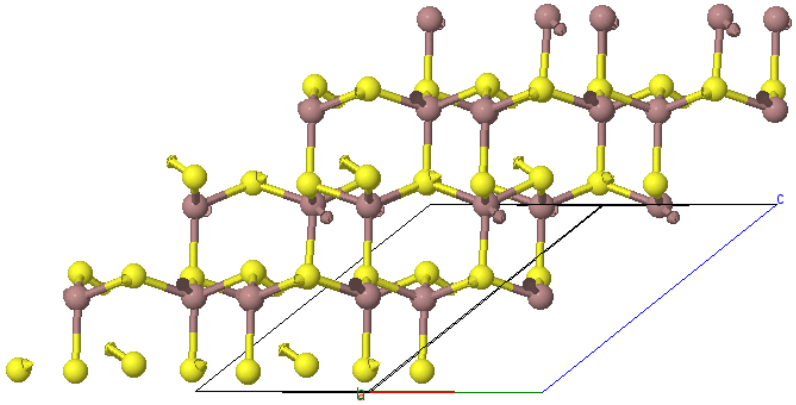

Figure S14. Scheme of the atomic vibrations of the *A'*(5) mode of α'-Ga_2S_3 around 147 cm^{-1}. This mode is a pure υ_4 bending mode of GaS_4 tetrahedra characterized by concerted movements of Ga and specially S3 atoms (that vibrate out-of-phase with respect to those of the neighbour layers).

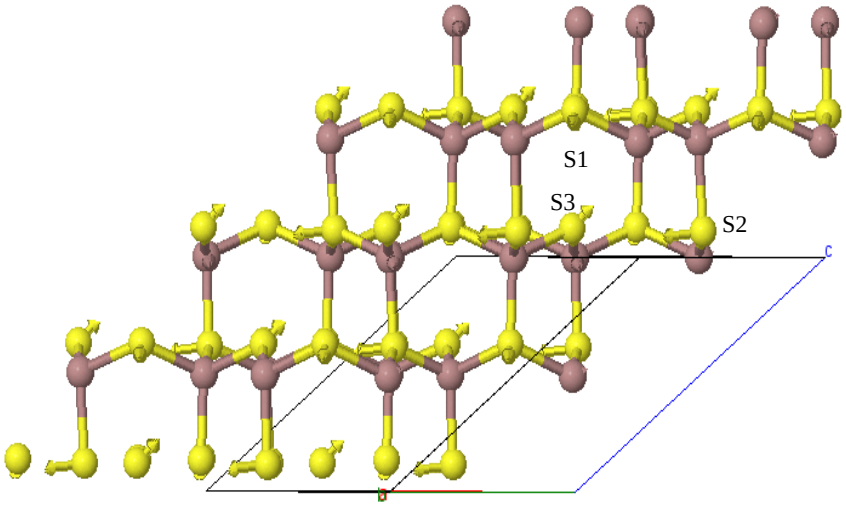

Figure S15. Scheme of the atomic vibrations of the *A'*(6) mode. The strongest Raman mode of α'-Ga_2S_3 around 234.6 cm^{-1}. This mode is a mixture of bending modes leaded by displacements of S1, S2 and S3 atoms. The concerted displacement of S atoms leads considerable symmetric stretching of S atoms around the vacancy and to a small symmetric Ga-S stretching υ_1 mode of the GaS_4 unit. This is why this mode is known also as the breathing mode of the vacancy. Note and S3 atom moves in the direction of the bisector of both cation vacancies around it (upward right in the figure), S2 atom vibrates against its neighbour vacancy (downward left in the figure), and S1 atom vibrates against its neighbour vacancy (downward front in the figure).

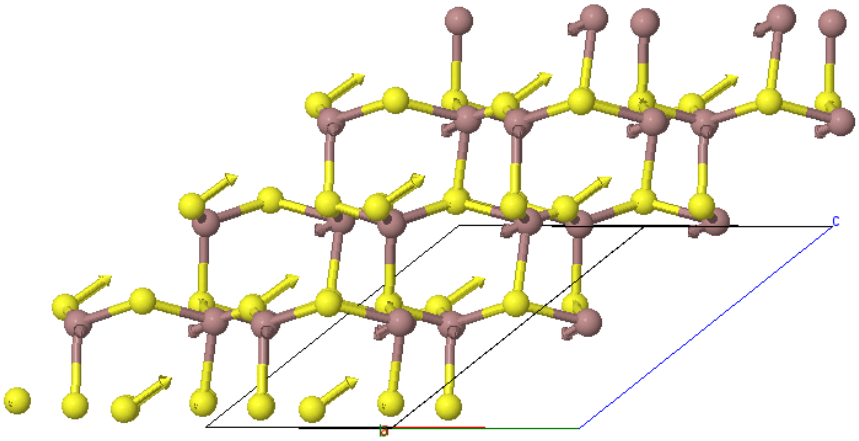

Figure S16. Scheme of the atomic vibrations of the *A'*(12) mode. The second strongest Raman mode of α'-Ga_2S_3 around 387 cm^{-1} is an asymmetric Ga-S stretching υ_3 vibration characterized mainly by S3 atomic vibrations (moving in-phase in the different layers) in the direction of the bisector of both cation vacancies around it (upward right in the figure), while Ga1 atoms (also moving in-phase in the different layers), but in opposite phase with respect to S3 atoms (downward left in the figure).

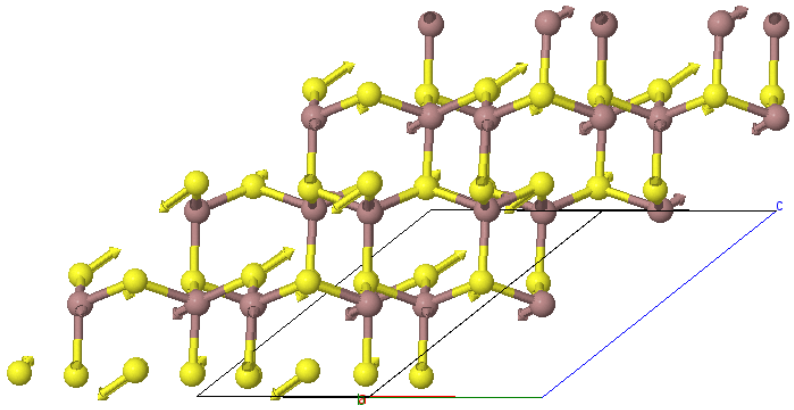

Figure S17. Scheme of the atomic vibrations of the *A''*(13) mode. This mode of α'-Ga_2S_3 around 392 cm^{-1} is an asymmetric Ga-S stretching υ_3 vibration characterized mainly by S3 atoms vibrations (moving out-of-phase in the different layers) in the direction of the bisector of both cation vacancies around it (upward right in the figure), while Ga1 atoms (also moving out-of-phase in the different layers), but in opposite phase with respect to S3 atoms (downward left in the figure).

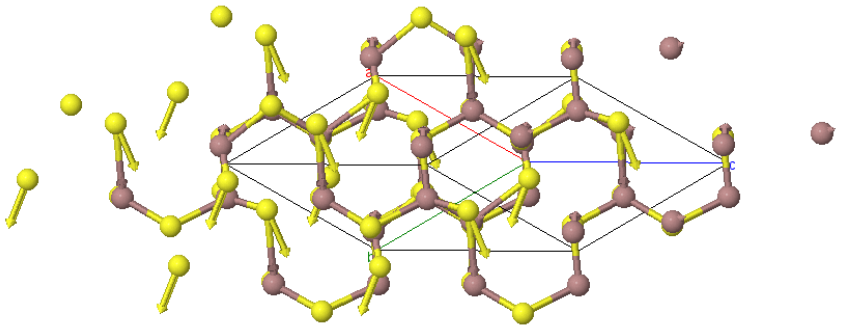

Figure S18. Scheme of the vibration of the *A''*(14) mode of α'-Ga_2S_3 around 407 cm^{-1}. This mode is an asymmetric Ga-S stretching υ_3 vibration characterized mainly by an in-phase movement of all S3 atoms in the direction of the two Ga atoms linking the S3 atom. View along the direction perpendicular to the wurtzite-like layers.

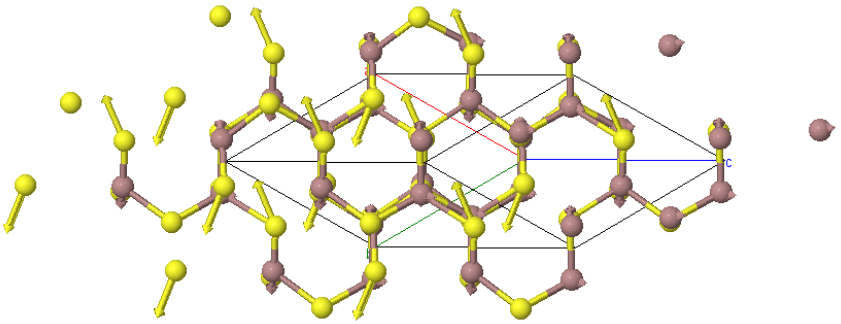

Figure S19. Scheme of the vibration of the *A'*(13) mode of α'-Ga_2S_3 around 425 cm^{-1}. This mode is an asymmetric Ga-S stretching υ_3 vibration characterized mainly by an out-of-phase movement of the closest S3 atoms in the direction of the two Ga atoms linking the S3 atom. View along the direction perpendicular to the wurtzite-like layers.

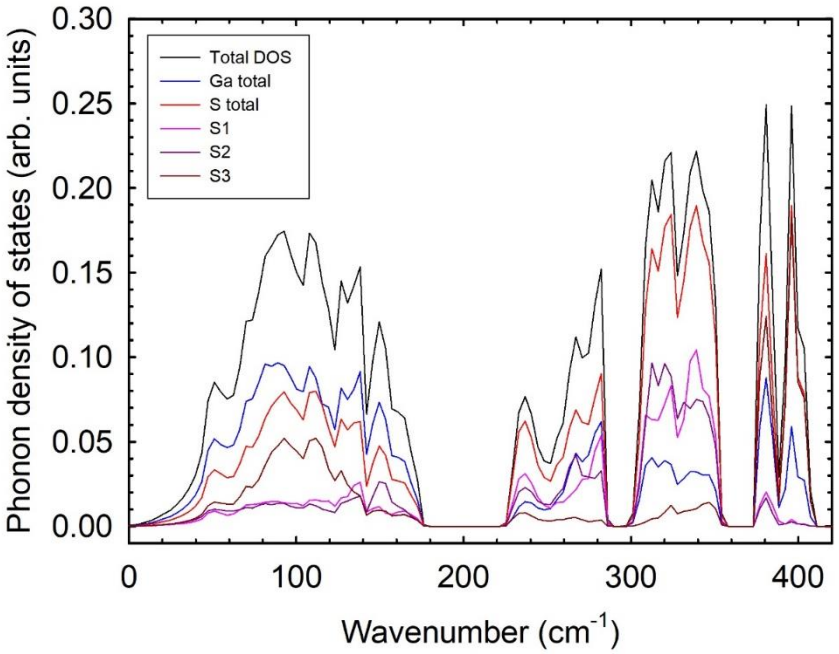

Figure S20. Theoretical one-phonon density of states of α'-Ga_2S_3 at 0 GPa. The total as well as the partial contribution of Ga and S atoms to the different vibrations is plotted. The individual contribution of the S atoms is also plotted in order to show the different contributions of S1, S1 and S3 atoms. Individual contribution of the Ga atoms is not plotted since both Ga1 and Ga2 atoms show similar contributions in all the regions.

Figure S21 shows the normalized Raman spectra at 1048 and 1123 K. It can be seen that at these high temperatures all modes of α'-Ga_2S_3 have completely disappeared (see the comparison with the spectrum at 948 K in **Figure 8** of the main text). Moreover, two broad peaks emerge in the range from 500 to 800 cm^{-1}. These new peaks cannot be due to a temperature-induced phase transition of the α'-phase, because it melts congruently at about 1300 K.[3, 4] Therefore, we consider that these new peaks must come from the Ga_2O_3 impurity observed in our HP-XRD measurements. β-Ga_2O_3 exhibits 15 Raman-active optical modes $\Gamma = 10A_g + 5B_g$. Thanks to **Ref. 5** (see **Table 1**), we can confirm the presence of the β-Ga_2O_3 by assigning the symmetry of each mode observed in our Raman spectra, as can be seen in **Figure S21**. The A_g modes are observed in the XX, YY, ZZ and XY directions and the B_g modes in the YZ and XZ directions. For this reason, several modes cannot be seen properly in our unpolarised HT-RS measurements where several modes are overlapped. We have to notice that the Raman signals shown in **Fig. S21** are quite weak (RS spectra are shown with 50x factor in comparison with that of the α' phase) and that this observation is coherent with the small fraction of β-Ga_2O_3 in the original sample.

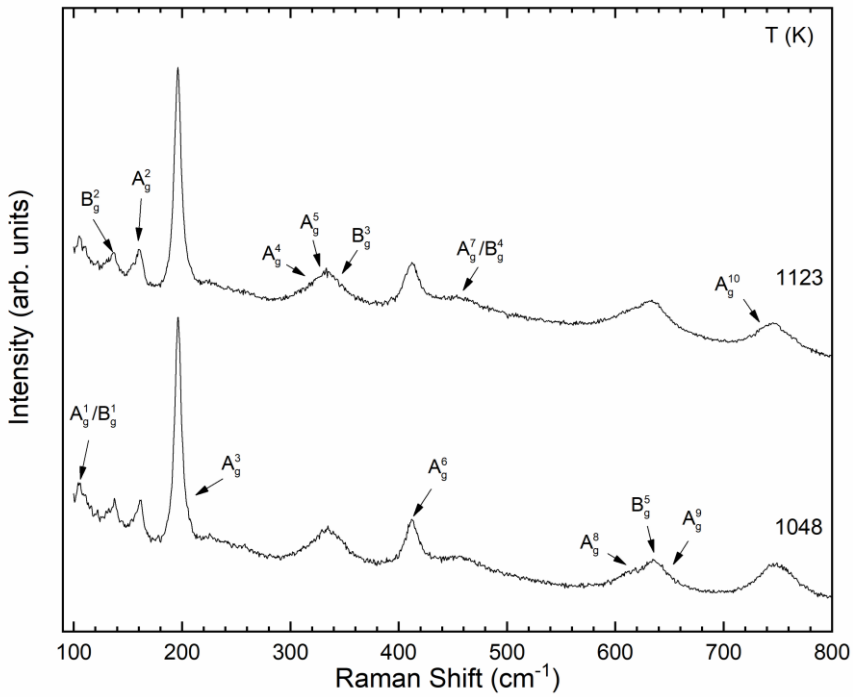

Figure S21. HT normalized Raman spectra of β-Ga_2O_3 at 1048 and 1123 K.

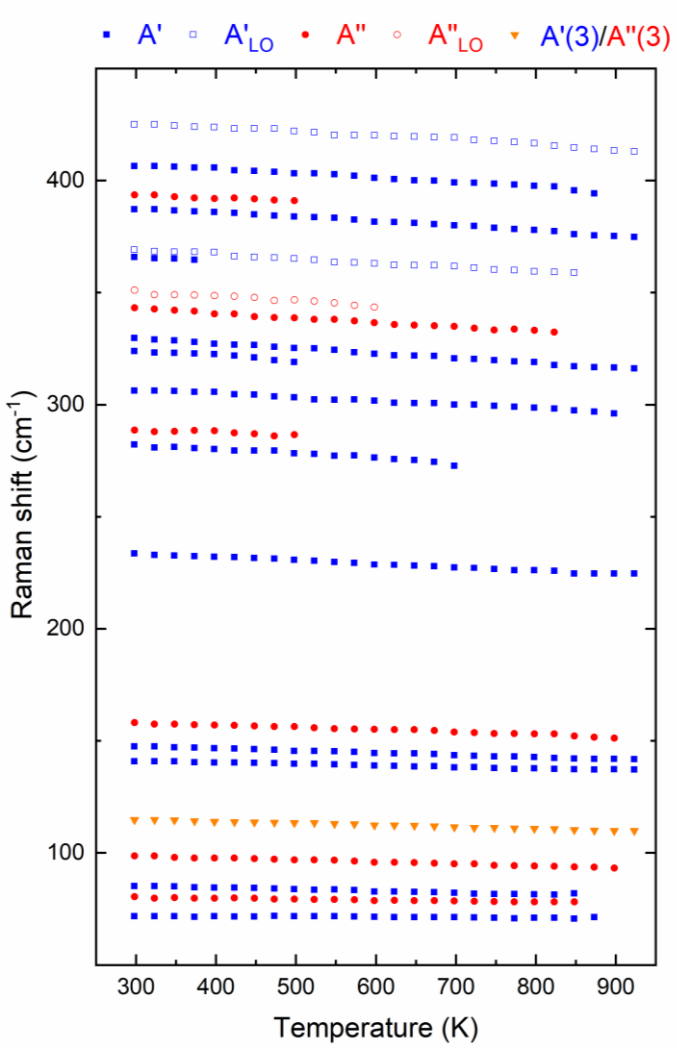

Figure S22. Temperature dependence of the experimental Raman-active mode frequencies of α'-Ga_2S_3.

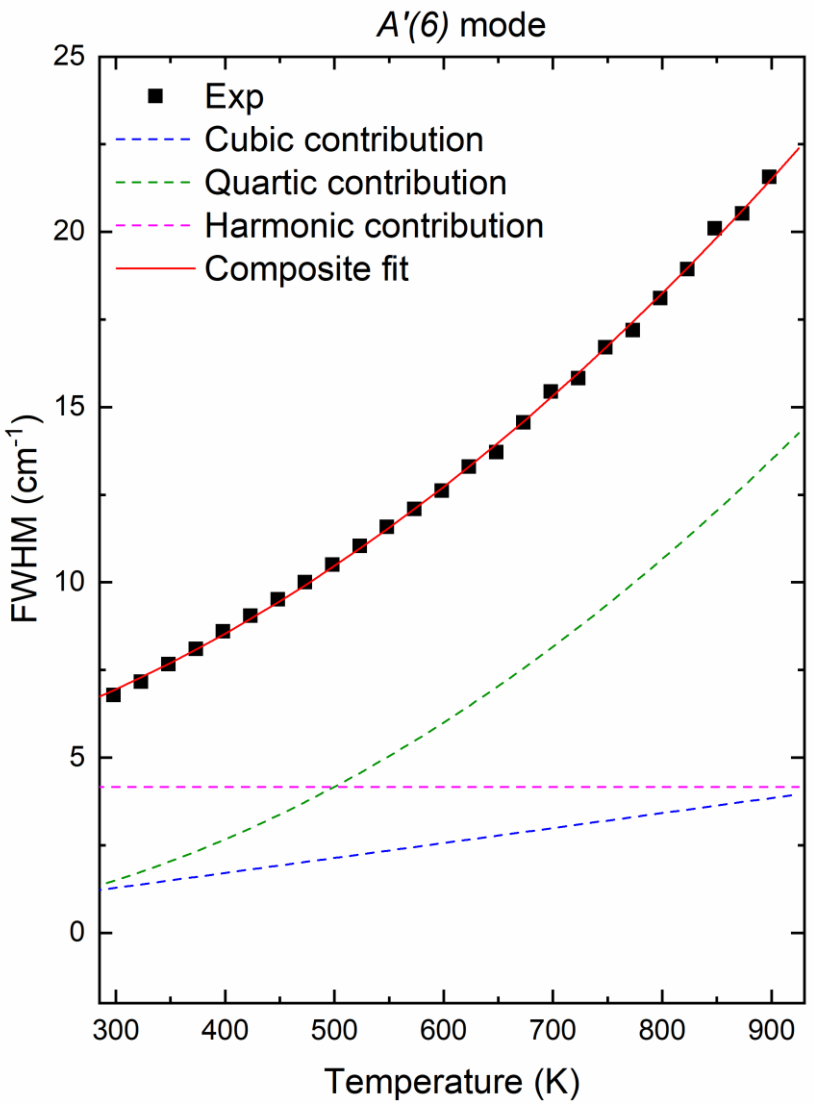

Figure S23. Temperature dependence of the FWHM of the *A'*(6) mode. Cubic, quartic and harmonic contributions are shown.

The isothermal mode Grüneisen parameter, γ_i^T, has been tabulated under the quasi-harmonic approximation according to the following equation:[6]

$$\gamma_i^T = (B_0/\omega_i)(d\omega_i/dP) \quad (1)$$

where ω_i and B_0 are the frequency of each mode and the isothermal bulk modulus, respectively. On the other hand, the isothermal averaged Grüneisen parameter from the macroscopic definition, γ_{av}^T, is defined as:[7]

$$\gamma_{av}^T = 3\alpha V_m B_0/C_v \quad (2)$$

expressed in terms of thermal expansion coefficient, α, molar volume, V_m, and molar heat capacity, C_v. From the microscopic definition, γ_{av}^T can be obtained as:

$$\gamma_{av}^T = \sum C_i\gamma_i/C_v \quad (3)$$

where C_i corresponds to the Einstein molar heat capacity and C_v is defined as $C_v = \sum C_i$. In particular, C_i is obtained as a function of the energy of each mode, $E_i = hv_i$, as:

$$C_i = R\frac{(E_i/k_BT)^2 e^{E_i/k_BT}}{(e^{E_i/k_BT}-1)^2} \quad (4)$$

where v_i is the frequency in Hz, *T* the temperature, and k_B, h and *R* are the Boltzmann, Planck and ideal gas constants, respectively.

The simplest model proposed by Klemens allows us to qualitatively describe the mode frequency shift at HT as a function of the phonon-phonon coupling as follows:[8-10]

$$\omega_i = \omega_{io} + A\left[1+\frac{2}{e^x-1}\right] + B\left[1+\frac{3}{e^y-1}+\frac{3}{(e^y-1)^2}\right] \quad (5)$$

where A and B are the cubic and quartic anharmonic contributions; i.e., decays of one phonon through third- and fourth-order processes into two or three modes of frequency $\omega_o/2$ or $\omega_o/3$, respectively, and where the exponents refer to $x = \hbar\omega_o/2k_BT$ and $y = \hbar\omega_o/3k_BT$, being ħ the reduced Planck's constant. It has to be said that **Eq. 5** has another term in the right side, which takes into account the mode shift at HT due to the thermal expansion of the lattice.[11-13] We do not have HT-XRD measurements to obtain the temperature dependence of the thermal expansion to consider this missing term. However, this is an approach to get knowledge of the third- and fourth-order processes that govern the temperature dependence of the modes.[8, 9]

The FWHM varies at HT due to the phonon-phonon coupling according the equation:[8]

$$\Gamma_i = \Gamma_{io} + C\left[1+\frac{2}{e^x-1}\right] + D\left[1+\frac{3}{e^y-1}+\frac{3}{(e^y-1)^2}\right] \quad (6)$$

where C and D are the cubic and quartic anharmonic contributions, respectively.

Under the assumption of the quasiharmonic approximation, the mode frequency shifts observed at HP are the result of the variation of bond distances and thus their force constants. However, such an assumption is not fulfilled at HT since the mode frequency shifts observed in RS spectra depend on two effects: the volume (implicit) effect caused by the lattice thermal expansion and the temperature (explicit) effect related to phonon-phonon coupling.[14-16] These two contributions can be decoupled thanks to HP-RS and HT-RS measurements as follows:

$$\left(\frac{d\omega_i}{dT}\right)_P = -\frac{\alpha}{\beta}\left(\frac{d\omega_i}{dP}\right)_T + \left(\frac{d\omega_i}{dT}\right)_V \quad (7)$$

where β is the volume compressibility. The left-hand side of the **Eq. 7** is the isobaric temperature derivative of the mode frequency; that is, the total effect of the temperature on the mode shift, obtained from our HT-RS measurements. The first term in the right-hand side is the isothermal pressure derivative of the mode frequency, the implicit effect, obtained from our HP-RS measurements. The second term is the isochoric temperature derivative of the mode frequency; i.e. the explicit effect. We can reformulate the **Eq. 7** in terms of the mode Grüneisen parameters: [13, 17]

$$\gamma_i^P = \gamma_i^T + \gamma_i^V \quad (8)$$

where the isobaric and isochoric mode Grüneisen parameters are $\gamma_i^P = (-1/\alpha\omega_i)(d\omega_i/dT)_P$ and $\gamma_i^V = (-1/\alpha\omega_i)(d\omega_i/dT)_V$, respectively.[13, 14] Therefore, we can evaluate the relevance of the explicit effect, γ_i^V, for each mode with **Eq. 8**. From **Eq. 2**, we have obtained the experimental α = 1.03·10^{-5} K^{-1}, required to calculate γ_i^P.

The implicit fraction, η_i is given by: [18]

$$\eta_i = \frac{\alpha}{\beta}\frac{(d\omega_i/dP)_T}{(d\omega_i/dT)_P} = \frac{\gamma_i^T}{\gamma_i^P} \quad (9)$$

Table S1. Zero-pressure theoretical (only TO) and experimetal frequencies, pressure coefficients, and isothermal mode Grüneisen parameter of the Raman-active modes of the α' phase. The evolution of the mode frequencies as a function of pressure has been fitted to $\omega = \omega_o + a_1 P + a_2 P^2$ (ω_0 in cm^{-1}, a_1 in $cm^{-1}\cdot GPa^{-1}$ and a_2 in 10^{-2} $cm^{-1}\cdot GPa^{-2}$). For comparison, zero-pressure frequencies corresponding to Raman and IR experiments from **Ref. 19** are also shown.

	Theoretical				**Experimental**			
Mode	ω_0	a_1	a_2	γ_i^T	ω_0	a_1	a_2	γ_i^T
A'(1)	68.7	-0.3	-1.4	-0.2	74, 72[a]	-0.5	-0.9	-0.3
A''(1)	78.1	-0.2	-1.1	-0.1	82, 80[a]	-0.1	-1.0	-0.1
A'(2)	81.5	0.5	2.0	0.2	87, 86[a]	0.4	2.1	0.2
A''(2)	96.2	0.4	-0.4	0.2	100, 93(TO)[b], 98(LO)[a]	0.3	-0.4	0.2
A''(3)	110.0	1.7	-5.0	0.6	118, 115[b]	1.3	-2.0	0.5
A'(3)	111.3	0.6	-3.2	0.2	116, 114(TO)[a], 116(LO)[a]	0.6	-1.8	0.2
A'(4)	135.7	0.5	-0.7	0.2	143, 141[a]	0.7	-1.1	0.2
A'(5)	140.2	1.6	-5.4	0.4	147(TO), 146[a] 150(LO), 147[a]	1.4 2.0	-3.0 -7.4	0.5 0.6
A''(4)	145.7	0.8	-0.8	0.2	148[b]			
A''(5)	151.8	0.7	2.4	0.2	159	0.8	1.2	0.2
A''(6)	168.6	2.8	-4.7	0.6	177, 172[b]	2.7	-3.5	0.7
A'(6)	229.3	7.7	-14.9	1.3	235, 233[a]	8.0	-17.5	1.6
A''(7)	263.6	6.3	-11.4	0.9	280[a]			
A'(7)	277.2	5.0	-7.0	0.7	283, 284[b]	5.5	-9.1	0.9
A''(8)	285.3	6.0	-11.3	0.8	290, 300[b]	6.3	-14.2	1.0
A'(8)	298.4	4.6	-7.2	0.6	307(TO), 307[a] 310(LO)	4.3 4.1	-3.7 -3.8	0.7 0.6
A''(9)	313.5	3.6	-0.8	0.4	326[b]			
A'(9)	318.4	4.8	-8.9	0.6	324, 321[a]	5.2	-12.6	0.7
A'(10)	322.0	5.4	-10.5	0.6	331, 329[a]	5.4	-12.0	0.8
A''(10)	323.5	5.4	-9.4	0.6	335[b]			
A''(11)	336.5	3.4	-1.8	0.4	344(TO), 343[b] 351(LO), 355[b]	4.2 4.1	-8.7 -8.3	0.6 0.5
A'(11)	337.8	3.2	0.2	0.4	366(TO), 368[a] 372(LO)	3.1 3.9	2.0 -3.5	0.4 0.5
A''(12)	338.2	6.6	-10.9	0.7	364[b]			
A''(13)	378.5	4.8	-7.6	0.5	393, 390[b]	4.9	-7.1	0.6
A'(12)	379.3	4.8	-7.8	0.5	388, 386[a]	5.4	-10.4	0.7
A''(14)	391.4	3.3	-0.5	0.3	411(TO)[b] 417(LO)[b]			

A'(13)	391.6	3.6	0.3	0.3	407(TO), 404[a] 425(LO)	3.2 2.8	-0.3 -0.3	0.4 0.3

Table S2. Room-temperature experimental frequencies and temperature coefficients, as obtained from our HT-RS measurements, where mode frequencies have been fitted to $\omega = \omega_o + b_1 T + b_2 T^2$ (ω_0 in cm^{-1}, b_1 in $cm^{-1}\cdot GPa^{-1}$ and b_2 in 10^{-2} $cm^{-1}\cdot GPa^{-2}$). Experimental cubic and quartic anharmonic contributions and their absolute ratio are appened. Experimental isobaric, isothermal and isochoric mode Grüneisen parameters are also shown as estimations of the total, implicit and explicit effects. The related implicit fraction, η_i, is included.

Mode	ω_0	b_1	b_2	**A**	**B**	**|A/B|**	γ_i^P	γ_i^T	γ_i^V	η_i
A'(1)	72	0.1	-0.2	0.01	-0.02	0.38	0.4	-0.3	0.7	-0.77
A''(1)	80	-0.6	0.1	-0.05	0.02	3.17	5.9	-0.1	5.9	-0.01
A'(2)	85	-1.0	0.2	-0.10	0.03	3.17	9.8	0.2	9.6	0.02
A''(2)	99	-0.7	-0.1	-0.09	-0.02	3.63	8.1	0.2	7.9	0.02
A''(3)*	115	-0.7	-0.1	-0.09	-0.03	2.79	6.4	0.5	5.9	0.08
A'(3)*	115	-0.7	-0.1	-0.09	-0.03	2.79	6.4	0.2	6.1	0.04
A'(4)	141	-0.8	0.1	-0.13	0.04	3.29	5.0	0.2	4.8	0.05
A'(5)	148	-1.1	0.1	-0.19	0.03	5.43	6.8	0.4	6.4	0.07
A''(4)										
A''(5)	158	-0.4	-0.6	-0.07	-0.28	0.24	4.4	0.2	4.2	0.05
A''(6)										
A'(6)	234	-1.6	0.1	-0.44	0.06	6.93	6.4	1.6	4.8	0.25
A''(7)										
A'(7)	282	0.7	-2.7	0.22	-4.21	0.05	3.3	0.9	2.4	0.28
A''(8)	288	3.2	-5.4	1.03	-8.51	0.12	0.2	1.0	-0.8	4.14
A'(8)	307	-1.5	-0.1	-0.54	-0.27	2.03	5.1	0.7	4.4	0.13
A''(9)										
A'(9)	324	6.4	-10.9	2.32	-21.01	0.11	0.4	0.7	-0.4	2.05
A'(10)	330	-2.3	0.1	-0.89	0.18	5.09	6.6	0.8	5.9	0.11
A''(10)										
A''(11)	343(TO) 350(LO)	-2.9 0.5	0.8 -2.9	-1.19 0.19	1.97 -7.03	0.61 0.03	7.0 3.6	0.6 0.5	6.4 3.0	0.08 0.15
A'(11)	366(TO) 369(LO)	-6.7 -2.7	7.6 0.7	-2.94 -1.19	21.57 2.04	0.14 0.58	5.7 6.1	0.4 0.5	5.3 5.6	0.07 0.08
A''(12)										
A''(13)	394	-2.6	1.6	-1.19	5.07	0.23	4.0	0.6	3.4	0.15
A'(12)	387	-1.0	-0.9	-0.45	-2.54	0.18	3.8	0.6	3.1	0.17
A''(14)										

A'(13)	407(TO) 425(LO)	-0.9 -0.4	-1.0 -1.2	-0.42 -0.21	-3.12 -4.34	0.13 0.05	3.5 2.6	0.4 0.3	3.1 2.3	0.10 0.12

Topological properties

The bulk modulus can be obtained from the different B_{oi} of each basin by the volume-weighted sum of the contributions as follows: [20]

$$\frac{1}{B_o} = \sum f_i \frac{1}{B_{oi}} \tag{10}$$

where $f_i = \frac{V_i}{V}$ is the fraction of the unit-cell volume occupied by the basin i.

The charge transfer is related with the Bader charges, Q_i, and the nominal oxidation states, OS_i, by means of the following relation:[21]

$$CT_i = \frac{Q_i}{OS_i} \tag{11}$$

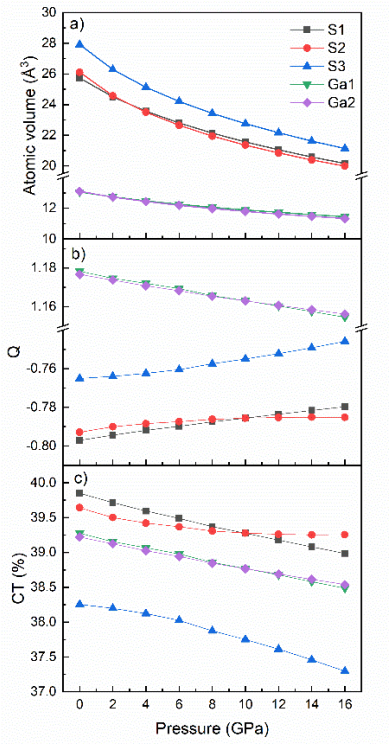

Figure S24. Pressure dependence of a) atomic volumes, b) Bader atomic charges (Q_i) and c) charge transfers (CT_i) of the Ga and S basins.

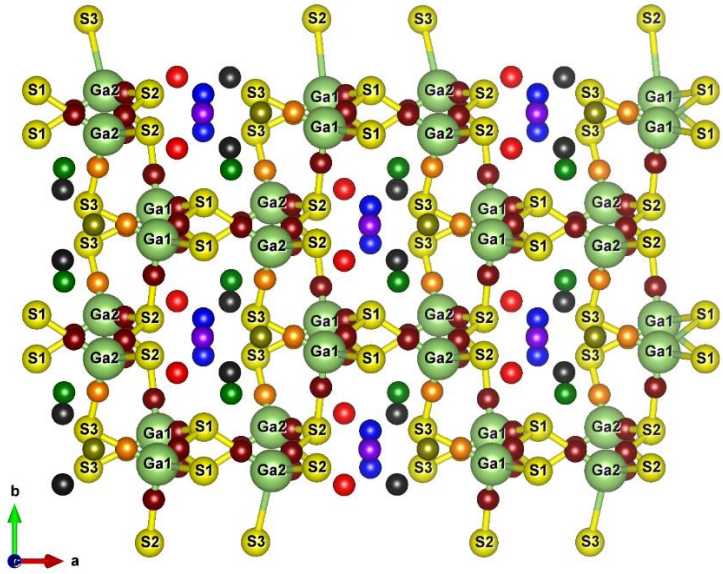

Figure S25. View of α'-Ga_2S_3 perpendicular to the *c*-axis with the bond critical points (BCPs). Orange and brown balls refer to Ga-S BCPs. The former is related with the S3 atoms and the latter with the S1 and S2 atoms. Red balls indicate the S1-S2 BCPs. The S1 and S2 atoms have also BCPs with the S3 atoms. They are represented with balls as follows: green (dark) balls refer to S1-S3(S3*) and violet (blue) refer to S2-S3(S3*), respectively. Asterisks indicate those atoms separated a longer distance. S-S BCPs are inside the channels, except the S3-S3 BCPs (gold balls) that are found between S3-S3 atoms.

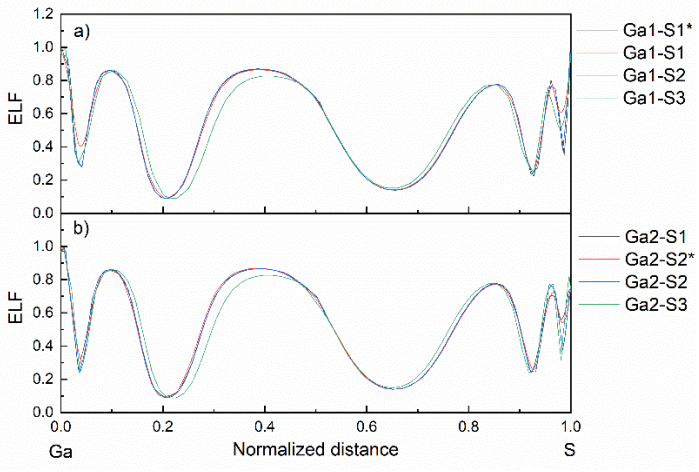

Figure S26. Theoretical all-electron 1D-ELF between Ga-S bonds for a) $Ga1S_4$ and b) $Ga2S_4$ tetrahedra at 0 GPa.

Electronic properties

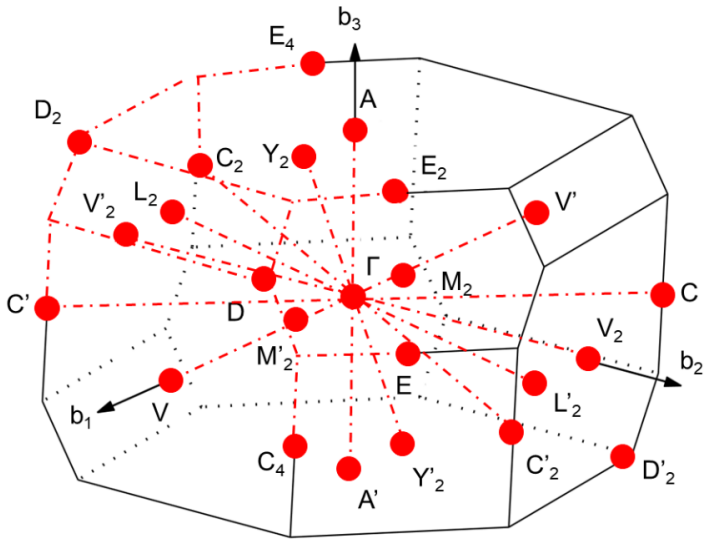

Figure S27. The first Brillouin zone (BZ) and relevant high symmetry points of α'-Ga_2S_3.

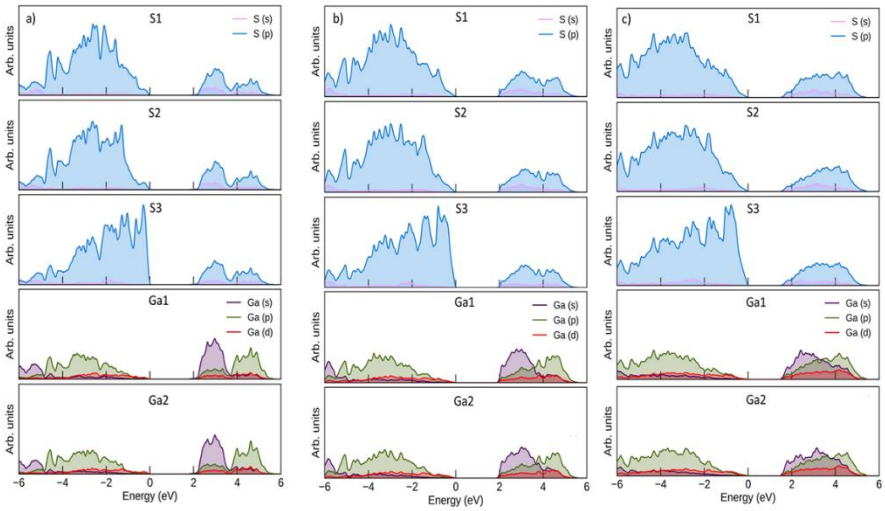

Figure S28. Atomic contributions to the electronic density of states (EDOS) of α'-Ga_2S_3 at different pressures: a) 0 GPa, b) 6 GPa, and c) 16 GPa.

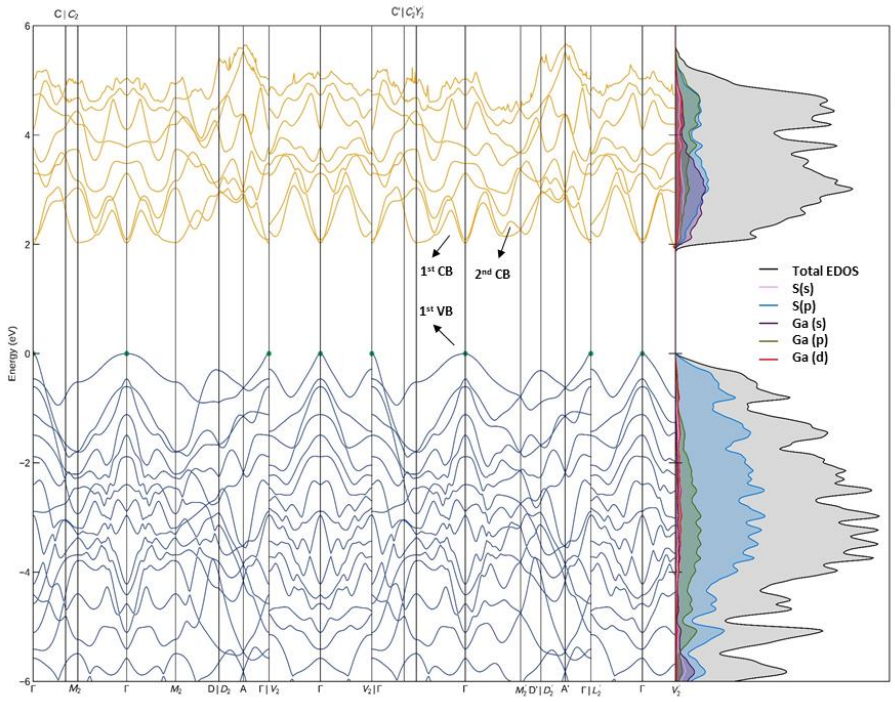

Figure S29. Electronic band structure and total and partial electronic density of states (EDOS) in α'-Ga_2S_3 at 6 GPa. The 1st valence band (VB) and the 1st and 2nd conduction bands (CB) are labelled.

References

1. X. Lai, F. Zhu, S. Qin, D. Chen, Y. Li, K. Yang and X. Wu, *J. Appl. Phys.*, 2014, **116**, 193507.
2. P. Canepa, R. M. Hanson, P. Ugliengo and M. Alfredsson, *J. Appl. Crystallogr.*, 2011, **44**, 225-229.
3. R. Lieth, H. Heijligers and C. vd Heijden, *J. Electrochem. Soc.*, 1966, **113**, 798-801.
4. M. Pardo, M. Guittard, A. Chilouet and A. Tomas, *J. Solid State Chem.*, 1993, **102**, 423-433.
5. T. Onuma, S. Fujioka, T. Yamaguchi, Y. Itoh, M. Higashiwaki, K. Sasaki, T. Masui and T. Honda, *J. Cryst. Growth*, 2014, **401**, 330-333.
6. E. Grüneisen, *Annalen der Physik*, 1912, **344**, 257-306.
7. T. H. K. Barron, *Annals of Physics*, 1957, **1**, 77-90.
8. M. Balkanski, R. Wallis and E. Haro, *Phys. Rev. B*, 1983, **28**, 1928.
9. E. Sarantopoulou, C. Raptis, S. Ves, D. Christofilos and G. Kourouklis, *J. Phys.: Condens. Matter*, 2002, **14**, 8925.
10. S. Bevara, K. K. Mishra, S. J. Patwe, T. Ravindran, M. K. Gupta, R. Mittal, P. S. R. Krishna, A. K. Sinha, S. N. Achary and A. K. Tyagi, *Inorg. Mater.*, 2017, **56**, 3335-3348.
11. J. E. Spanier, R. D. Robinson, F. Zhang, S.-W. Chan and I. P. Herman, *Phys. Rev. B*, 2001, **64**, 245407.
12. M. Deshpande, S. V. Bhatt, V. Sathe, R. Rao and S. Chaki, *Phys. B*, 2014, **433**, 72-78.
13. G. Kourouklis and E. Anastassakis, *phys. status solidi (b)*, 1989, **152**, 89-99.
14. G. Lucazeau, *J. Raman Spectrosc.*, 2003, **34**, 478-496.
15. P. Peercy and B. Morosin, *Phys. Rev. B*, 1973, **7**, 2779.
16. B. A. Weinstein and R. Zallen, in *Light Scattering in Solids IV*, Springer, 1984, pp. 463-527.
17. S. V. Bhatt, M. Deshpande, V. Sathe, R. Rao and S. Chaki, *J. Raman Spectrosc.*, 2014, **45**, 971-979.
18. R. Zallen and E. Conwell, *Solid State Communications*, 1979, **31**, 557-561.
19. G. Lucazeau and J. Leroy, *Spectrochimica Acta Part A: Molecular Spectroscopy*, 1978, **34**, 29-32.
20. A. M. Pendás, A. Costales, M. Blanco, J. Recio and V. Luaña, *Phys. Rev. B*, 2000, **62**, 13970.
21. P. Mori-Sánchez, A. M. Pendás and V. Luaña, *J. Am. Chem. Soc.*, 2002, **124**, 14721-14723.

PCCP

ROYAL SOCIETY OF CHEMISTRY

PAPER

View Article Online
View Journal | View Issue

Cite this: *Phys. Chem. Chem. Phys.*, 2021, **23**, 23625

Pressure-induced order–disorder transitions in β-In_2S_3: an experimental and theoretical study of structural and vibrational properties†

Samuel Gallego-Parra, *[a] Óscar Gomis, *[b] Rosario Vilaplana, [b] Vanesa Paula Cuenca-Gotor, [a] Domingo Martínez-García, [c] Plácida Rodríguez-Hernández, [d] Alfonso Muñoz, [d] Aldo Romero, [e] Arnab Majumdar, [fg] Rajeev Ahuja, [fh] Catalin Popescu [i] and Francisco Javier Manjón [a]

Received 30th June 2021,
Accepted 11th October 2021

DOI: 10.1039/d1cp02969j

rsc.li/pccp

This joint experimental and theoretical study of the structural and vibrational properties of β-In_2S_3 upon compression shows that this tetragonal defect spinel undergoes two reversible pressure-induced order–disorder transitions up to 20 GPa. We propose that the first high-pressure phase above 5.0 GPa has the cubic defect spinel structure of α-In_2S_3 and the second high-pressure phase (ϕ-In_2S_3) above 10.5 GPa has a defect α-$NaFeO_2$-type ($R\bar{3}m$) structure. This phase, related to the NaCl structure, has not been previously observed in spinels under compression and is related to both the tetradymite structure of topological insulators and to the defect $LiTiO_2$ phase observed at high pressure in other thiospinels. Structural characterization of the three phases shows that α-In_2S_3 is softer than β-In_2S_3 while ϕ-In_2S_3 is harder than β-In_2S_3. Vibrational characterization of the three phases is also provided, and their Raman-active modes are tentatively assigned. Our work shows that the metastable α phase of In_2S_3 can be accessed not only by high temperature or varying composition, but also by high pressure. On top of that, the pressure-induced β–α–ϕ sequence of phase transitions evidences that β-In_2S_3, a $B_2^{III}X_3^{V}$ compound with an intriguing structure typical of $A^{II}B_2^{III}X_4^{VI}$ compounds (intermediate between thiospinels and ordered-vacancy compounds) undergoes: (i) a first phase transition at ambient pressure to a disordered spinel-type structure (α-In_2S_3), isostructural with those found at high pressure and high temperature in other $B_2^{III}X_3^{V}$ compounds; and (ii) a second phase transition to the defect α-$NaFeO_2$-type structure (ϕ-In_2S_3), a distorted NaCl-type structure that is related to the defect NaCl phase found at high pressure in $A^{II}B_2^{III}X_4^{VI}$ ordered-vacancy compounds and to the defect $LiTiO_2$-type phase found at high pressure in $A^{II}B_2^{III}X_4^{VI}$ thiospinels. This result shows that In_2S_3 (with its intrinsic vacancies) has a similar pressure behaviour to thiospinels and ordered-vacancy compounds of the $A^{II}B_2^{III}X_4^{VI}$ family, making β-In_2S_3 the union link between such families of compounds and showing that group-13 thiospinels have more in common with ordered-vacancy compounds than with oxospinels and thiospinels with transition metals.

[a] *Instituto de Diseño para la Fabricación y Producción Automatizada, MALTA Consolider Team, Universitat Politècnica de València, 46022 València, Spain. E-mail: sagalpar@doctor.upv.es*
[b] *Centro de Tecnologías Físicas, MALTA Consolider Team, Universitat Politècnica de València, 46022 València, Spain. E-mail: osgohi@fis.upv.es*
[c] *Departamento de Física Aplicada-ICMUV-MALTA Consolider Team, Universitat de València, c/Dr. Moliner 50, 46100 Burjassot (València), Spain*
[d] *Departamento de Física, Instituto de Materiales y Nanotecnología, MALTA Consolider Team, Universidad de La Laguna, 38207 San Cristóbal de La Laguna, Spain*
[e] *Physics Department, West Virginia University, Morgantown, 26505, USA*
[f] *Department of Physics and Astronomy, Uppsala University, Box 516, Uppsala, SE-75120, Sweden*
[g] *Département de Physique and Regroupement Québécois sur les Matériaux de Pointe, Université de Montréal, C. P. 6128, Succursale Centre-Ville, Montréal, Québec H3C 3J7, Canada*
[h] *Department of Physics, Indian Institute of Technology Ropar, Rupnagar 140001, Punjab, India*
[i] *ALBA-CELLS, MALTA Consolider Team, 08290 Cerdanyola del Valles (Barcelona), Catalonia, Spain*
† Electronic supplementary information (ESI) available. See DOI: 10.1039/d1cp02969j

Pressure-induced order-disorder transitions in β-In_2S_3: an experimental and theoretical study of structural and vibrational properties

Samuel Gallego-Parra,[1*] Óscar Gomis,[2*] Rosario Vilaplana,[2] Vanesa Paula Cuenca-Gotor,[1] Domingo Martínez-García,[3] Plácida Rodríguez-Hernández,[4] Alfonso Muñoz,[4] Aldo Romero,[5] Arnab Majumdar,[6,7] Rajeev Ahuja,[6,8] Catalin Popescu[9] and Francisco Javier Manjón[1]

[1]*Instituto de Diseño para la Fabricación y Producción Automatizada, MALTA Consolider Team, Universitat Politècnica de València, 46022 València, Spain*
[2]*Centro de Tecnologías Físicas, MALTA Consolider Team, Universitat Politècnica de València, 46022 València, Spain*
[3]*Departamento de Física Aplicada-ICMUV-MALTA Consolider Team, Universitat de València, c/Dr. Moliner 50, 46100 Burjassot (València), Spain*
[4]*Departamento de Física, Instituto de Materiales y Nanotecnología, MALTA Consolider Team, Universidad de La Laguna, 38207 San Cristóbal de La Laguna, Spain*
[5]*Physics Department, West Virginia University, Morgantown, 26505, USA*
[6]*Department of Physics and Astronomy, Box 516, Uppsala University, Uppsala, SE-75120, Sweden*
[7]*Département de Physique and Regroupement Québécois sur les Matériaux de Pointe, Université de Montréal, C. P. 6128, Succursale Centre-Ville, Montréal, Québec H3C 3J7, Canada*
[8]*Department of Physics, Indian Institute of Technology Ropar, Rupnagar 140001, Punjab, India*
[9]*ALBA-CELLS, MALTA Consolider Team, 08290 Cerdanyola del Valles (Barcelona), Catalonia, Spain*

*Corresponding authors: S. Gallego-Parra (sagalpar@doctor.upv.es), O. Gomis (osgohi@fis.upv.es)

ABSTRACT

This joint experimental and theoretical study of the structural and vibrational properties of β-In_2S_3 upon compression shows that this tetragonal defect spinel undergoes two reversible pressure-induced order-disorder transitions up to 20 GPa. We propose that the first high-pressure phase above 5.0 GPa has the cubic defect spinel structure of α-In_2S_3 and the second high-pressure phase (ϕ-In_2S_3) above 10.5 GPa has a defect α-$NaFeO_2$-type (*R*-3*m*) structure. This phase, related to the NaCl structure, has not previously observed in spinels under compression and is related to both the tetradymite structure of topological insulators and to the defect $LiTiO_2$ phase observed at high pressure in other thiospinels. Structural characterization of the three phases shows that α-In_2S_3 is softer than β-In_2S_3 while ϕ-In_2S_3 is harder than β-In_2S_3. Vibrational characterization of the three phases is also provided, and their Raman-active modes tentatively assigned. Our work shows that the metastable α phase of

In_2S_3 can be accessed not only by high temperature or varying composition but also by high pressure. On top of that, the pressure-induced β-α-φ sequence of phase transitions evidences that β-In_2S_3, a $B^{III}{}_2X^{V}{}_3$ compound with an intriguing structure typical of $A^{II}B^{III}{}_2X^{VI}{}_4$ compounds (intermediate between thiospinels and ordered-vacancy compounds) undergoes: i) a first phase transition at ambient pressure to a disordered spinel-type structure (α-In_2S_3), isostructural with those found at high pressure and high temperature treatment in other $B^{III}{}_2X^{V}{}_3$ compounds; and ii) a second phase transition to the defect α-$NaFeO_2$-type structure (ϕ-In_2S_3), a distorted NaCl-type structure that is related to the defect NaCl phase found at high pressure in $A^{II}B^{III}{}_2X^{VI}{}_4$ ordered-vacancy compounds and to the defect $LiTiO_2$-type phase found at high pressure in $A^{II}B^{III}{}_2X^{VI}{}_4$ thiospinels. This result shows that In_2S_3 (with its intrinsic vacancies) has a similar pressure behaviour than thiospinels and ordered-vacancy compounds of the $A^{II}B^{III}{}_2X^{VI}{}_4$ family, making β-In_2S_3 the union link between such families of compounds and showing that group-13 thiospinels have more in common to ordered-vacancy compounds than to oxospinels and thiospinels with transition metals.

1. INTRODUCTION

Spinels constitute a class of technologically important materials used in a wide range of applications, such as in dielectrics, sensors, solar cells, and energy materials. High-performance In-based nontoxic (Cd free) semiconductors are under the attentive watch of the industry to implement reliable and eco-friendly devices due to the environmental and biological issues concerning the use of toxic semiconductors in an ever-increasing demand for solar cells. In this context, In-based semiconductors, like spinel-type In_2S_3, have drawn a relevant interest for buffer layers to replace CdS. More specifically, several works have evaluated In_2S_3-buffered thin films in solar cells, achieving efficiencies between 12.9 and 16.4% by various deposition techniques.[1-3] These results make In_2S_3 a worthy competitor of CdS in solar cells. Moreover, as an n-type semiconductor, In_2S_3 exhibits a bandgap around 2.2 eV (depending on the growth conditions),[4-6] a high optical transmission in the visible region,[7] modest electrical transport properties,[8] a low lattice thermal conductivity[9], and excellent chemical stability.

Due to the above properties, different In_2S_3 phases have been exploited not only in buffer layers, but also in other devices and applications, such as photodetectors, lithium-ion batteries, oxygen sensors, as well as in thermoelectric, luminescent, and photocatalytic applications.[10-16] Up to three phases of In_2S_3 have been described at ambient pressure and different temperatures: i) the β phase, with tetragonal defect spinel structure (space group (S.G.) $I4_1/amd$, Z=16, **Fig. 1a)**) at ambient temperature; ii) the α phase, with cubic defect spinel structure (S.G. Fd-3m, Z=10.67, **Fig. 1b)**) above 749 K; and iii) the γ phase, with trigonal structure (S.G. P-3m1, Z=1) above 1100 K.

The stable phase at ambient conditions, β-In_2S_3, features In cations occupying 2/3 of tetrahedral (Td) positions, the Td(8e) sites, and totally occupying octahedral positions (Oh), the Oh(16h), and Oh(8c) sites. Curiously, 1/3 of the Td positions, the Td(4a)

sites, are empty.[17-21] No other $B^{III}{}_2X^{VI}{}_3$ compound shows the defect spinel structure at ambient pressure to our knowledge and only Al_2S_3 and Al_2Se_3 are known to show this phase at high pressure (HP) and high temperature (HT).[22, 23] Indeed, the empty Td(4a) sites can be treated as ordered vacancies, so β-In_2S_3 is in fact the only In-based ordered-vacancy compound (OVC). In this context, β-In_2S_3 can be considered a defective $A^{II}B^{III}{}_2X^{VI}{}_4$ compound (it can be reformulated as $In_{0.66}In_2S_4$ and found at the ICSD database). This material is located between $A^{II}B^{III}{}_2X^{VI}{}_4$ compounds with cubic spinel structure and those with defect chalcopyrite and defect stannite (or famatinite) structures.

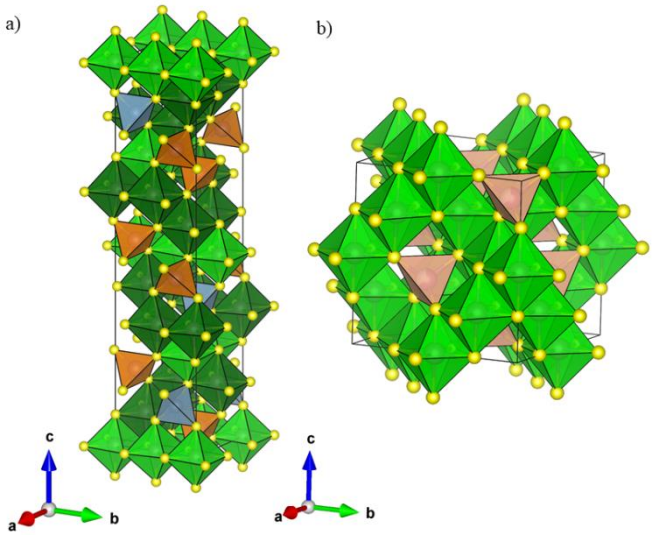

Figure 1. a) Crystal structure of β-In_2S_3. Ordered cation vacancies are located in Td(4a) sites (blue tetrahedra). In atoms are placed in Td(8e), Oh(8c), and Oh(16c) sites (orange tetrahedra, green and dark green octahedra). b) Crystal structure of α- In_2S_3. Fractional occupation of In atoms occurs in Td(8a) sites (light orange tetrahedra) coming from Td(8e) and Td(4a) sites of the β phase. Oh(8a) sites are fully occupied by In atoms.

On the other hand, α-In_2S_3 is a phase characterized by a single Td site, the Td(8a) site, which is shared by vacancies and In atoms as a consequence of the order-disorder transition taking place in In_2S_3 above 749 K. In other words, above that temperature vacancies spread over all Td(4a) and Td(8e) sites of the β phase and the structure changes from tetragonal to cubic with a single Td site in the structure.[18, 24-26] The cubic defect spinel phase was also observed in Al_2S_3 both when Al is partially substituted by a 2% As[27] and in Al_2S_3 and Al_2Se_3 at HP-HT conditions (4 GPa and 673 K).[23] The HT β-α phase transition (PT) in In_2S_3 has been revisited quite recently.[28] In addition, several recent studies have studied the β-α PT at ambient conditions.[29, 30] Aluminium substitution in β-In_2S_3 at relatively high concentration leads to chemical disordering between In and Al cations in the Td(8e) and Td(4a) sites and thus inducing the β-α PT.[29] On the other hand, an extensive study on the β → α PT has been carried out by playing with the composition, *x*, in $In_{1-x}Vac_xIn_2S_4$, where Vac stands for the

vacancy.[30] This β → α PT has been induced by Se(Te)-for-S substitution as well.[31] Therefore, in view of these studies, the β-α PT can be triggered by HT or by composition.

Above 1100 K, another order-disorder transition occurs with vacancies being randomly distributed over both Td and Oh cation sites. This additional disorder thus leads to the γ phase,[24-26] that was refined by Pistor *et al.* during a reinvestigation of the HT PTs.[26] A few studies have considered the possibility of stabilizing γ-In_2S_3 at ambient conditions by adding a 5% of As, Sb, or Bi.[32, 33] The γ-phase of In_2S_3 is similar to the trigonal A-type phase of rare-earth sesquioxides, typical of La_2O_3; however, In atoms at the La 2d sites (z~0.25) of the La_2O_3 structure are splitted into two 2d sites of z~0.19 and 0.35 with fractional occupations in γ-In_2S_3. Noteworthy, the A-type phase of rare-earth sesquioxides was observed in In_2Se_3 at HT with a z~0.19,[34] so it is possible that the same phase is observed in γ-In_2S_3 and that problems with Rietveld refinement had yielded an additional 2d site with an abnormally high value of z (z~0.35).

HP studies in β-In_2S_3 have raised even more controversies than HT studies. The ε phase, with a corundum-like structure (S.G. *R*-3*c*, Z=6), was quenched from HP & HT studies (3.5 GPa and 800 K),[35] and this phase was also observed in Al_2S_3.[36] As regards HP studies carried out at ambient temperature, several X-ray diffraction (XRD) measurements have addressed the structural properties of the β phase under compression.[37-39] Three HP-PTs near 6.6, 11, and 35.6 GPa (the last one aided by laser heating) were reported by Lai *et al.*[37] The structure of the first two HP phases could not be determined, but the third one (hereafter named δ-In_2S_3) was identified as a defect Th_3P_4-like structure (S.G. *I*-43*d*, Z=5.33).[37] In agreement with Lai *et al.*, Yao *et al*. observed a HP-PT at 7.1 and 4.3 GPa in undoped and Ce-doped β-In_2S_3, respectively.[38] Concerning the 1st HP phase, they indexed it to a cubic structure, but no more details about the structure were given. Curiously, no HP-PT was found in a more recent HP-XRD work that studied β-In_2S_3 up to 41.3 GPa.[39] Despite this result, the same authors observed a pressure-induced metallization of In_2S_3 around 6.8 GPa in a later study;[40] a result that is in agreement with the first HP-PT seen in the two first HP-XRD studies. Finally, we must stress that the 1st HP-PT in β-In_2S_3 has been also recently evidenced by HP-Raman scattering (RS) and impedance spectroscopy measurements around 7 GPa.[41] Moreover, a semiconductor-metal PT at 41.2 GPa has been also reported.[41]

Despite the recent HP studies on β-In_2S_3, many questions are still open, being the most important ones related to the nature of the 1st and 2nd HP phases that remain unknown. On the other hand, no *ab initio* simulations of structural and vibrational properties of the β phase at HP have been conducted yet, to our knowledge, to help us to understand the obtained experimental results. Finally, neither of the already mentioned HP studies has explored if the β → α PT could be induced by pressure.

In this work, we present the results of a joint experimental and theoretical study on β-In_2S_3 under compression. HP-XRD and HP-RS measurements up to 15.0 and 21.2 GPa, respectively, are complemented with *ab initio* simulations to shed light on the above commented issues. We will show there are two HP-PTs whose onset is around

4.9 and 10.2 GPa. We will propose that the 1st HP phase has the cubic defect spinel structure (α-In_2S_3) and that the 2nd HP phase (hereafter named φ-In_2S_3) has a defect α-$NaFeO_2$-type structure. This is the first time, to our knowledge, that the defect α-$NaFeO_2$-type structure has been proposed as a post-spinel phase and the first time that it is commented on the possibility that the β → α PT could be induced by pressure. Moreover, we will show that the defect α-$NaFeO_2$-type structure bears a relation to the tetradymite-type structure, which is a typical structure of group-15 $B^{III}_2X^{VI}_3$ compounds with topological insulating properties.[42] We will also provide an experimental and theoretical characterization of the structural and vibrational properties of the three phases (β, α, and φ). For this purpose, and due to the difficulty in simulating disordered structures, like α-In_2S_3 and φ-In_2S_3, we will discuss the properties of these two phases by comparison with isostructural compounds $CdIn_2S_4$ and Na(Ag)InS_2, respectively.

Most importantly, we will finally show in this work that thiospinels (either with $B^{III}_2X^{VI}_3$ or $A^{II}B^{III}_2X^{VI}_4$ composition) undergo pressure-induced order-disorder transitions similar to those of ordered-vacancy compounds. In other words, they tend to HP phases related to the NaCl structure, typical of *AX* or ABX_2 compounds (with the same number of cations and anions) as if vacancies could be counted as additional cations. Consequently, we will show that thiospinels at HP behave more similarly to ordered-vacancy compounds than to oxospinels and propose new experiments to verify it.

2. EXPERIMENTAL AND THEORETICAL DETAILS

β-In_2S_3 powders of high purity (99.999%) used in the present study were commercially acquired from Alfa Aesar company. Additionally, α-In_2S_3 powders of high purity (99.99%) were commercially acquired from Sigma Aldrich company. Powders were characterized at ambient conditions to verify the presence of either the β or the α phase. HP measurements on β-In_2S_3 at 300 K were performed using a membrane-type diamond-anvil cell (DAC) with 400 μm diameter culet. Powder samples were placed in a 150-μm diameter hole performed in a 40 μm-thick stainless-steel gasket and pressurized by a pressure-transmitting medium (PTM), like 4:1 methanol-ethanol mixture (M-E), that remains quasi-hydrostatic up to 10 GPa.[43, 44]

Angle dispersive powder HP-XRD measurements were carried out up to 15 GPa in BL04-MSPD beamline at ALBA synchrotron using a monochromatic X-ray beam with λ = 0.4246 Å and a Rayonix MARCCD detector located at 240 mm from the sample.[45] Copper was placed inside the pressure cavity and used as the pressure sensor through copper EoS[46], and a pinhole placed before the sample position was used as a cleanup aperture for filtering out the tail of the X-ray beam, which was focused down to 20 × 20 μm^2 using Kickpatrick-Baez mirrors. Powder XRD patterns were integrated as a function of 2θ using Dioptas software in order to obtain conventional, one-dimensional, diffraction profiles[47] that were refined using GSAS-II program package.[48]

Unpolarized HP-RS measurements were carried out up to 21 GPa using a Horiba Jobin Yvon LabRAM UV HR microspectrometer equipped with a thermoelectrically cooled multichannel charge coupled device detector that allows a spectral resolution better

than 2 cm^{-1}. The Raman signal was excited with a HeNe laser (632.8 nm line) with a power of less than 10 mW and collected in backscattering geometry using an edge filter working in perpendicular configuration and cutting around 100 cm^{-1}. Raman signals down to 50 cm^{-1} or even less can eventually be detected by adjusting the angle between the edge filter and the light containing the Raman signal. The pressure was determined by the ruby luminescence method.[49] The frequencies of the Raman-active phonons were experimentally obtained by fitting Raman peaks with Voigt profiles of fixed Gaussian line width to the experimental setup resolution (1.6 cm^{-1}).[50, 51]

First-principles density-functional theory (DFT)[52] calculations at 0 K for β-In_2S_3, cubic spinel $CdIn_2S_4$, and $AgInS_2$ and $NaInS_2$ (both with α-$NaFeO_2$-type structure) were carried out with the Vienna Ab-initio Simulation Package (VASP),[53] using the projected augmented wave (PAW) scheme.[54, 55] Calculations were performed with the generalized gradient approximation (GGA) of Perdew-Burke-Ernzenhof revised for solids (PBEsol).[56] The basis set of plane waves was extended up to a cutoff 530, 600, and 530 eV for the β-In_2S_3, thiospinel $CdIn_2S_4$, and $AgInS_2$ and $NaInS_2$, respectively, in order to achieve highly converged results. For each relaxed structure, calculations were performed with the automatic k-point generation method included in the VASP package (Monkhorst-Pack scheme[57]) with Hellman-Feynman forces smaller than 0.004 eV/Å per atom and deviations of the stress tensor from the diagonal hydrostatic form smaller than 0.1 GPa.

Lattice dynamics calculations were performed at the zone center (Γ-point) of the Brillouin zone. The supercell method with the primitive cell was employed for the calculation of the dynamical matrix at the Γ-point.[53, 58] In order to obtain the phonon density of states at 0 GPa, a 2x2x2 supercell was used for β-In_2S_3 and $CdIn_2S_4$.

Structural search by theoretical means were employed to try to identify the 2nd HP crystalline structure phase of β-In_2S_3. The potential energy surface was systematically explored with the help of the minima hopping and evolutionary genetic methods. The first was employed in the multidimensional potential energy landscape of In_2S_3 with 5, 10, 15, 20, and 40 atoms in the unit cell. We have used the minima hopping method to identify the lower energy configurations at ambient pressure,[59, 60] and at least ninety symmetrically different local minima energy structures were identified for each cell size. The evolutionary genetic method was used as it is implemented in the USPEX code.[61-63] Initially, the first generation of prediction consisted of 300 structures by considering 1 to 10 formula units for fixed composition search in the unit cell. From the second generation onwards, structures were obtained by applying the 40% heredity (of each generation), 20% soft-mutation, and 20% transmutation operators. The remaining 20% of each generation was generated by using random[64] and topological generators.[65] This procedure was performed for 6 and 10 GPa pressure points, near those experimental transition observed. The structures predicted for both methods were kept according to their high symmetry, i.e., those with the least inequivalent atomic positions and a high number of symmetry operations. The study of partially occupied structures has been conducted with the Supercell program[66] to explore the different supercell configurations describing the analyzed structure. In this way, few theoretical XRD reflections and Raman modes are expected, as our HP-XRD and HP-RS measurements exhibit. For each method, each one of the selected

structures was reoptimized with VASP and symmetrized by using similar convergence criteria than in the case of the vibrational analysis. Only those structures with the smallest energies and a few XRD peaks, like the ones obtained experimentally, were considered for further analysis.

3. RESULTS AND DISCUSSION

3.1 Structural properties under high pressure

Figure 2a) shows the evolution of the XRD patterns of β-In_2S_3 upon compression and decompression (d). For the sake of clarity, we have included the Miller indices (*h k l*) of the most intense reflections of the β phase at 0.9 GPa. An example of Le Bail refinement of the β phase at 0.9 GPa is shown in **Fig. 3**. At 4.9 GPa, most reflections of β phase occur. Only the most intense peaks of the β phase, namely, (1 0 3), (1 0 9), (2 0 6), (0 0 12), (3 1 8), (2 2 12), (2 2 15) and (4 0 8) reflections remain. Above 4.9 GPa, the β phase cannot be refined anymore; therefore, we consider that this is the onset transition pressure of the 1st HP-PT. Despite the PT, the Miller indices (*h k l*) of the β phase are used above 4.9 GPa to refer to the relevant reflections from the HP phases. Above 8.2 GPa, several weak reflections disappear (**Fig. 2**). At 10.2 GPa, the (1 1 6) reflection disappears and the relative intensities between the (1 0 9) and (2 0 6) reflections changes. Therefore, we consider that a 2nd HP-PT occurs above 10.2 GPa. On decompression down to 0.6 GPa, most of the reflections that disappeared during compression emerge again, thus pointing out the reversibility of the effect exerted by the pressure on β-In_2S_3.

Analysis of the structural parameters of β-In_2S_3 under compression has been obtained by LeBail refinement (see **Fig. 4**) and compared to those provided by theoretical calculations. A rather good agreement is found between the experimental and theoretical lattice parameters *a* and *c* and their evolution with pressure (**Fig. 4a)**). In fact, there is a better agreement of theoretical calculations with the *a* lattice parameter than with the *c* lattice parameter (that is slightly overestimated). Consequently, the theoretical volumes are slightly overestimated in comparison to experimental ones (**Fig. 4b)**). To evaluate the effect of pressure on the lattice parameters *a* and *c*, we have calculated the experimental (theoretical) zero-pressure axial compressibilities, defined as $\kappa_x = -\frac{1}{x}\frac{\partial x}{\partial P}$, which are: κ_a = 5.2·10^{-3} (6.2·10^{-3}) GPa and κ_c = 6.4·10^{-3} (6.7·10^{-3}) GPa. Our results show that the theoretical and experimental values for κ_c are closer than those for κ_a, unlike the case for the lattice parameters. Additionally, it is found that the long lattice parameter *c* is more compressible than the short lattice parameter *a*. This result can be understood if we consider that the ordered vacancies are placed along a 4_1 screw axis parallel to the *c* axis.

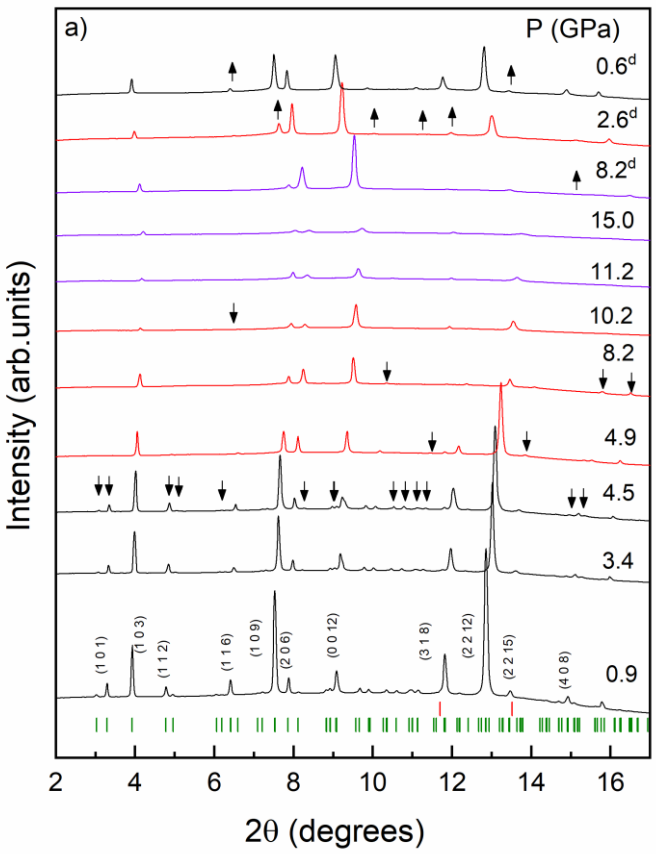

Figure 2. a) HP-XRD patterns of β-In_2S_3 on compression up to 15.0 GPa and decompression (d) down to 0.6 GPa. Labels for the most representative (h k l) indices for β-In_2S_3 are given. Green ticks represent the β-In_2S_3 reflections at the lowest pressure on upstroke. Black, red, and magenta colors represent the three β, α, and ϕ phases, respectively.

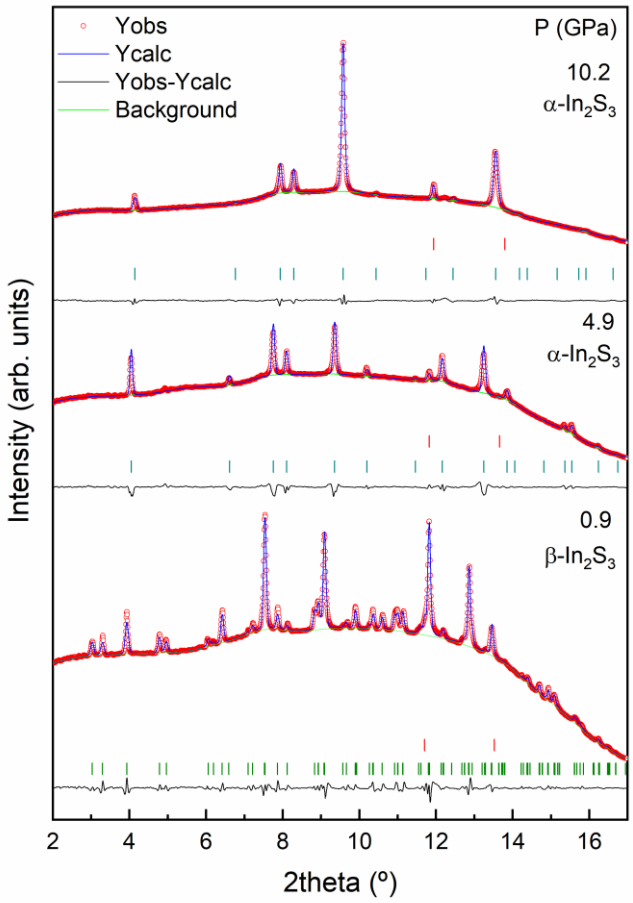

Figure 3. Le Bail refinement of selected XRD patterns of β-In_2S_3 at 0.9 GPa and of α-In_2S_3 at 4.9 and 10.2 GPa. Copper, β- and α-In_2S_3 reflections are marked with red, green and blue ticks, respectively.

To evaluate the experimental and theoretical pressure dependence of the unit-cell volume of the β phase, we have used both a 2nd and 3rd -order Birch-Murnaghan equation of state (BM2- and BM3-EoS). A good agreement between experimental and theoretical data and the corresponding BM3-EoS can be seen in **Fig. 4b)**. Our experimental and theoretical zero-pressure volume (V_0), bulk modulus (B_0), and first pressure derivative (B_0') show a good agreement, as can also be seen in **Table 1**. Our B_0 values for β-In_2S_3 are very close to that reported for In_2S_3:Ce nanoparticles,[38] slightly smaller than those reported for In_2S_3 nanoparticles[38] and for bulk In_2S_3 in **Ref. 31** and larger than those reported for bulk In_2S_3 in **Ref. 39**. Again, the use of different PTMs and their associated hydrostatic limits[43] yield different values for B_0. In particular, our B_0 values are smaller than those of works using less hydrostatic PTM,

like solid powders or silicon oil,[37, 38] and larger than those of works using equal or more hydrostatic PTM, like M-E and Ne.[39] In fact, we think that our results and those of **Ref.** [39] are not so different. The main differences between the two works stem from the pressure range used to fit the EoS. In this work, the EoS was fitted up to 4.5 GPa, while in **Ref.** [39] it was fitted up to 41.3 and 21.4 GPa, with M-E and Ne, respectively. It must be mentioned that the bulk modulus of β-In_2S_3 is similar to those of some OVCs, like α'-Ga_2S_3[67] and Ga_2Se_3,[68] and also similar to that of layered α-In_2Se_3 and β'-In_2Se_3.[69] In particular, the similar bulk modulus of an OVC, like β-In_2S_3, and of a layered material, like α-In_2Se_3, could be surprising since this last compound is a van der Waals compound that does not present vacancies in its structure; however, the gap between layers in van der Waals materials can be considered to be formed by intrinsic vacancies, as recently suggested,[70] and this justifies the similarities of both bulk moduli.

A deep analysis of the decrease of the relative volume of the different polyhedral units in β-In_2S_3, as provided by our theoretical calculations (**Fig. S1** in the Supplementary Information (SI)), shows that the small bulk modulus of β-In_2S_3 is mainly given by the compression of the polyhedral volume associated to the vacancy (Vac); i.e. the $VacS_4$ tetrahedron (centered at 4a sites). The In-based polyhedral units, InS_4 tetrahedra (centered at 8e sites) and InS_6 octahedra (centered at 8c and 16h sites), compress at a much smaller rate than the tetrahedron around the vacancy. BM2-EoS fit of polyhedral volumes yield a low bulk modulus (9.1 GPa) for the $VacS_4$ tetrahedron, which is much smaller than those for the InS_4 tetrahedron and InS_6 octahedra (8c and 16h sites), whose values are 54.8, 99.7, and 84.7 GPa, respectively. Therefore, the soft bulk modulus of β-In_2S_3 (~57 GPa) can be explained by the strong compression of the polyhedral unit around the vacancy. In fact, if one considers the polyhedral bulk moduli obtained from theoretical calculations and the multiplicity of each site in the tetragonal defect spinel structure, one can calculate a bulk modulus of ~65.5 GPa for β-In_2S_3, which is in relatively good agreement with the theoretical values for the bulk modulus obtained from the unit-cell volume (see **Table 1**).

A significant larger compression of the tetrahedron around the vacancy than of In-based polyhedra is noticed when comparing the theoretical Vac-S and In-S distances (**Fig. S2** in the SI). For the sake of completeness, we have also provided in **Fig. S3** in the SI the pressure dependence of the distortion index (D), quadratic elongation (λ), bond angle variance (σ^2), and effective coordination number (ECoN) corresponding to InS_4 and $VacS_4$ tetrahedra and both InS_6 octahedra in β-In_2S_3. Our calculations show a gradual change of all parameters with increasing pressure and, apparently, there is no abrupt change or singular value that could suggest the onset of the order-disorder PT taking place in β-In_2S_3 above 4.9 GPa.

Table 1. Experimental (exp.) and theoretical (th.) unit-cell volume at zero pressure (V_0, in Å^3), bulk modulus (B_0, in GPa), and first pressure derivative (B_0') for β-In_2S_3. PTM used, and transition pressure (TP, in GPa) are also indicated. Results of previous HP works have been added for comparison.[37-39] The volume per formula unit (V/Z, in Å^3) for β-In_2S_3 (Z=16) is shown as well.

		V_0	B_0	B_0'	V/Z	TP	PTM
β-In_2S_3	exp.[b]	1876(2)	57(4)	4.5(7)	117(1)	4.9	M-E[a]
		1875(1)	58.2(7)	4.0, fixed	117(1)		
	th.[b]	1895.0(6)	53.1(9)	4.1(4)	118(1)		
		1895.0(4)	53.5(3)	4.0, fixed	118(1)		
	exp.[c]	1880.4[d]	37.8(2)	4.4(1)	118(1)	No TP	M-E[a]
		1882(1)	39.7(2)	4.0, fixed	118(1)		
		1880.4[d]	42.8(3)	4.1(1)	118(1)	No TP	Ne
		1883(1)	42.7(2)	4.0, fixed	118(1)		
	exp.[e]	1875(3)	63(3)	4.0, fixed	117(1)	6.6	S[a]
						6.8	LiF[f]
	exp.[g]	1880.7(1)	87(4)	4.0, fixed	118(1)	7.1	S[a]
		1918.1(1)	56(4)	4.0, fixed	120(1)	4.3[h]	
	exp.[i]					6.8	No PTM
	exp.[j]					~7.2	He
						6.8	No PTM

[a] M-E: 4:1 methanol-ethanol, S: silicone oil.
[b] Present work.
[c] **Ref. [39].**
[d] Authors in **Ref. [39]** fix V_0 to 1880.4 Å^3 for the BM3-EoS for the different PTMs used**.**
[e] **Ref. [37]**.
[f] No EoS is given in **Ref. [37]**.
[g] **Ref. [38].**
[h] In_2S_3:Ce nanoparticles.
[i] **Ref. [40]**. 1st PT observed by electrical measurements.
[j] **Ref. [41]**. 1st PT observed by Raman and electrical measurements.

We will now discuss the 1st HP phase observed above 4.9 GPa. The 1st PT is characterized by the disappearance of most reflections of the tetragonal defect spinel phase and the lack of appearance of new peaks; i.e. the β phase seems to be a superstructure of the 1st HP phase. Considering the group-supergroup relation between the α and β phases of In_2S_3, we considered the α phase with cubic spinel structure as a potential candidate for the 1st HP phase of the tetragonal β phase. In fact, we have successfully performed a LeBail refinement of XRD pattern of the 1st HP phase with the α phase from 4.9 to 10.2 GPa (see **Fig. 3**). For this purpose, we have used the structural data of the α phase from Pistor *et al.*[26] Above 10.2 GPa, the α phase does not fit the experimental XRD patterns anymore.

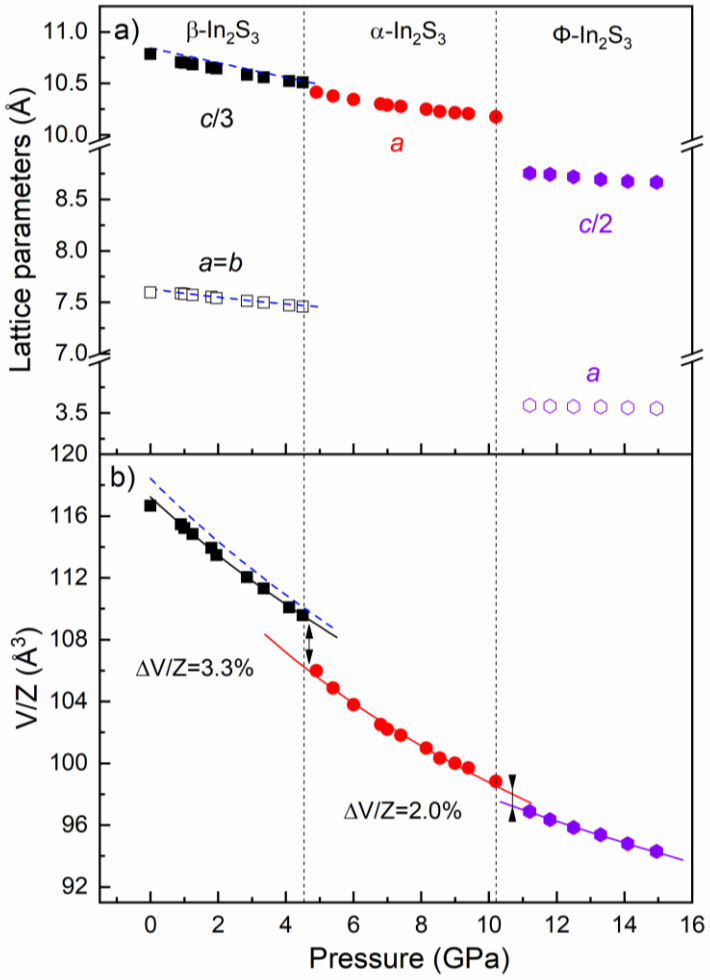

Figure 4. Pressure dependence of the lattice parameters (a) and volume per formula unit, V/Z (b), in β-, α-, and ϕ-In_2S_3. The theoretical pressure dependence of lattice parameters (dash lines) in β-In_2S_3 is plotted in a). Experimental (solid lines) and theoretical (dash lines) BM3-EoS for β-In_2S_3 are shown in b). Only experimental BM3-EoS (solid lines) are shown for α-, and φ-In_2S_3 in b).

It is interesting to mention that the cubic spinel structure has also been observed in Al_2S_3, Al_2Se_3, $CdAl_2S_4$, $HgAl_2S_4$, $CdAl_2Se_4$, and $HgAl_2Se_4$ at HP-HT conditions (around 4-7 GPa and 673-873 K).[23, 71] Therefore, we consider that we have identified the nature of 1st HP phase of β-In_2S_3 and it corresponds to the cubic spinel structure. This phase is isostructural to α-In_2S_3, observed also at HT and under varying composition.

It must be stressed that in previous HP studies of β-In_2S_3 the nature of the 1st and 2nd HP phases could not be revealed. Indeed, our assignment of the 1st HP phase to the cubic α phase agrees with the cubic symmetry found for the 1st HP phase in a previous work (the S.G. was not provided).[38] The main difference between our work and **Ref. 38** is that our HP-XRD measurements at 4.9 GPa do not show the emergence of new peaks, unlike in **Ref. 38**. In this sense, we want to comment that the XRD patterns from **Ref. 38** do not exhibit a good peak resolution, likely due to the non-uniform nanoparticle size used in that study, so the appearance of new peaks close to those of the original phase must be considered with caution. It must also be noted that the disappearance of most of the weak reflections of the β phase was also observed in **Ref. 39**, despite the fact that no PT was claimed to occur in that study.

For the sake of comparison with the β phase, we have plotted the lattice parameter *a* (**Fig. 4a)**) and the volume per formula unit, V/Z, (**Fig. 4b)**) of α-In_2S_3 as a function of pressure. We must note that Z is 8 for a typical AB_2X_4 spinel; however, we must reformulate Z in terms of B_2X_3 stoichiometry, like β-In_2S_3, to compare the V/Z of the different phases studied. For this purpose, we have to consider the Td(8a) fractional occupation of 2/3 and the multiplicity of both In and S atoms. In this way, a renormalized Z=10.67 for the cubic spinel phase of α-In_2S_3 is obtained. By looking at the pressure dependence of V/Z for the β and α phases, we have observed a relative decrease of 3.3% at the 1st PT in β-In_2S_3. Curiously, this value is similar to the volume changes reported between the low pressure (LP) and HP phases of the AIn_2S_4 thiospinels.[72] This means that this small relative volume change seems to be typical of pressure-induced order-disorder PTs in both $B^{III}{}_2X^{VI}{}_3$ and $A^{II}B^{III}{}_2X^{VI}{}_4$ thiospinels.

The *a* lattice parameter compressibility, κ_a, of the α phase ($7.9 \cdot 10^{-3}$ GPa) is larger than those of the *a* and *c* axes of the β phase. On top of that, the bulk modulus, B_0, of the α phase (obtained either with BM2- or BM3-EoS, see **Table 2**) is smaller than that of the β phase (**Table 1**). The softer pressure behaviour of the α phase, reflected in its κ_a and B_0, is justified by the fractional occupation of the Td(8a) sites in the α phase, coming from ordered Td(8e) and empty Td(4a) sites in the β phase. An estimation of the unit-cell volume fraction associated with vacancies at 0 GPa yields a 1.54 and 3.22% for the β and α phases, respectively. These values reflect the larger fraction of the unit-cell volume occupied by vacancies in the α phase than in the β phase that supports the softer pressure behavior of the α phase compared to the β-phase. In this context, the disorder of cations and vacancies in the Td(8a) sites of the defect cubic spinel phase of α-In_2S_3 also explains its smaller B_0 in comparison with the cubic spinel phase of AIn_2S_4 compounds, that do not present vacancies in their occupied atomic positions (see **Table 2**).

Table 2. Experimental (exp.) unit-cell volume at zero pressure (V_0, in Å^3), bulk modulus (B_0, in GPa), and first pressure derivative (B_0') obtained for α-In_2S_3. Experimental and and theoretical (th.) data for the low-pressure (LP) and high-pressure (HP) defect-$LiTiO_2$-type phases of the AIn_2S_4 thiospinels (*A*=Cd, Mg, Mn) are given for comparison.[72] The volume per formula unit (V/Z, in Å^3) for α-In_2S_3 (Z=10.67), as well as for the spinel (Z=8) and defect-$LiTiO_2$-type (Z=8) phases of the AIn_2S_4 thiospinels are also shown. Note that the Z value of the defect-$LiTiO_2$ structure is renormalized to that of the typical AB_2X_4 composition of spinels. PTM used, and transition pressure (TP, in GPa) are indicated.

		V_0	**B_0**	**B_0'**	**V/Z**	**TP**	**PTM**
α-In_2S_3	exp.[b]	1245(9) 1240(9)	39(3) 42(3)	4.5(8) 4.0, fixed	117(1) 116(1)	8.2	M-E[a]
$CdIn_2S_4$	LP exp.[c] LP th.[c] HP exp.[c] HP th.[c]	1274(2) 1241.45(2) 1206(6) 1174.6(8)	78(4) 79.8(2) 74(4) 71.6(4)	3.1(8) 4.65(6) 4.0, fixed 4.0, fixed	159(1) 155(1) 151(1) 147(1)	9.5 11.5	M-E[a]
$MgIn_2S_4$	LP exp.[c] LP th.[c] HP exp.[c] HP th.[c]	1227(1) 1211.9(4) 1222(6) 1124.8(6)	76.3(3) 75.4(9) 55(2) 68.8(4)	2.8(7) 4.3(3) 4.0, fixed 4.0, fixed	154(1) 152(1) 153(1) 141(1)	8.3 6.0	M-E[a]
$MnIn_2S_4$	LP exp.[c] LP th.[c] HP exp.[c] HP th.[c]	1230(1) 1200.7(5) 1187(2) 1121.0(4)	78(4) 80(2) 62(1) 70.1(3)	3.2(1) 3.9(3) 4.0, fixed 4.0, fixed	154(1) 150(1) 148(1) 140(1)	6.8 6.9	M-E[a]

[a] M-E: 4:1 methanol-ethanol, S: silicone oil.
[b] Present work.
[c] **Ref. [72].**

It must be noted that a smaller B_0 value of the 1st HP phase of the AIn_2S_4 (*A*= Cd, Mn, Mg) thiospinels, with defect $LiTiO_2$ structure, than that of the cubic spinel phase has also been observed (**Table 2**).[72] Again, this is a result of the pressure-induced order-disorder PTs. In the cubic spinel phase of AIn_2S_4 thiospinels, all cations are mainly ordered with *A* cations occupying Td(8b) sites and In cations occupying Oh(16c) sites. However, in the defect $LiTiO_2$ structure, *A* and In cations are disordered in the Oh(16c) sites, resulting in a larger compressibility than that of the cubic spinel phase.

Further support to the assignment of the 1st HP In_2S_3 phase to the α phase comes from the value of the lattice parameter *a* of the α phase extrapolated to 0 GPa: *a*= 10.758 Å (10.745 Å) from our BM3-EoS (BM2-EoS). This value compares well with the lattice parameter *a* of 10.736 Å obtained from the commercial sample powders of α-In_2S_3 at ambient pressure (see **Fig. S4a)** in the SI). These values can be nicely compared with data reported in the literature for the α phase. In fact, a value of *a*= 10.774 Å was reported many years ago at ambient conditions,[18] and a little bit longer lattice parameter *a* of 10.832 Å was refined at 749 K.[26] Moreover, the α phase was observed with a lattice parameter *a* of 10.769 and 10.758 Å in $In_{1-x}Vac_xIn_2S_4$ with In contents of 40.5 and 41.0 %, respectively.[30] As observed, these values of the lattice parameter

a for the α phase match quite well with our experimental values, thus confirming the nature of the 1st HP phase of β-In_2S_3.

As already commented, the β-α PT that is induced by HT or varying composition yields the mixing of the ordered Td(8e) and empty Td(4a) sites in the β phase within a unique disordered Td(8a) site in the α phase. Considering that 2/3 of Td positions in the β phase (the Td(8e) sites) are occupied when these sites mix with the empty Td(4a) sites, the occupation fraction in Td(8a) sites in the α phase must be 2/3. This is confirmed in the studies of HT[24-26] and it is also expected for HP since no change of composition is expected in either HT or HP studies. Unfortunately, we cannot provide the occupation fraction of Td(8a) sites in the α phase obtained at HP due to the impossibility to perform Rietveld refinements of our HP-XRD patterns. In this context, it must be noted that the α phase obtained by introducing a high In content exhibit an occupation fraction in the Td(8a) site that is higher than 2/3,[30] in opposition with what is observed at HT and is expected at HP. This reasoning allows us to predict that a slightly higher bulk modulus of the α phase should be observed in $In_{1-x}Vac_xIn_2S_4$ samples with a high content of In than in stoichiometric α-In_2S_3. In fact, this hypothesis is indirectly supported by the smaller values of the lattice parameter *a* found in $In_{1-x}Vac_xIn_2S_4$ samples with a high content of In[30] with respect to samples of almost stoichiometric α-In_2S_3,[18] if one considers the typical inverse relationship between volume and bulk modulus. Therefore, the results on $In_{1-x}Vac_xIn_2S_4$ samples give support to our assignment of the nature of the 1st HP phase in β-In_2S_3.

Now, we will focus on the 2nd HP phase observed above 10.2 GPa. First of all, we want to remember that a 2nd PT was reported above 11 GPa in **Ref. 37**. In that work, the 2nd PT was identified by the emerging of new peaks at about 2.6 and 3.0 Å of *d* spacing, but the nature of the 2nd HP phase was not identified perhaps due to the lack of an enough number of diffraction peaks and because of the weakness of the few peaks observed.[37] It must be noted that the new peaks observed in **Ref. 37** should be located around 8 and 9 degrees in our XRD patterns, near the (2 0 6) and (0 0 12) reflections of the previous β phase, respectively. Curiously, no new peaks appear near these reflections appear in our HP-XRD measurements. On the other hand, the HP-XRD patterns of **Ref. 39** show the disappearance of the (1 1 6) reflection as well as the change in the relative intensity of (1 0 9) and (2 0 6) reflections of the previous β phase, as occurs in our HP-XRD patterns (**Fig. 2** and **3**). Therefore, we can conclude that the results of **Ref. 39** provide evidence of the 2nd PT, despite the authors of **Ref. 39** said that no PTs were observed in their HP-XRD measurements.

To identify the 2nd HP phase of β-In_2S_3, several approaches have been undertaken. First, we tried with several polymorphs observed on In_2S_3 either at HP, at HT, or at HP-HT. They include the ε phase, the γ phase, and the δ phase.[37] Moreover, LP and HP phases seen in other compounds with *AX* (NaCl, CrB, LuS, TlS, CoO and NiO), ABX_2 ($LiTiO_2$, $LiFeO_2$ and $NaFeO_2$), A_2X_3 (Gd_2S_3, U_2S_3, Th_2S_3, Os_2Al_3 and In_2Se_3), ABX_3 (perovskite, post-perovskite), and AB_2X_4 (post-spinel $CaMn_2O_4$, $CaTi_2O_4$ and $CaFe_2O_4$) compositions have been tested. Further to this, we decided to use structure prediction methods to help us obtain the crystalline structure of the 2nd HP phase of β-In_2S_3. After all this challenging task, we found that the rhombohedral α-$NaFeO_2$-type (S.G. *R*-3*m*, Z=3) structure, a layered distorted variant of the NaCl-type structure[73]

observed in ABX_2 compounds,[74-78] was the only one compatible with our XRD patterns. LeBail refinements of the 2nd HP phase with a defect α-$NaFeO_2$-type structure at two pressures (11.2 and 15 GPa) are plotted in **Fig. 5**. This 2nd HP phase (φ-In_2S_3) is also a defective phase with vacancies and cations mixed at the same Wyckoff sites and has a smaller number of reflections than those in α-In_2S_3. In particular, the peak located around 6.8 degrees in α-In_2S_3 (**Fig. 3**) disappears in ϕ-In_2S_3 (**Fig. 5**). Furthermore, the notable widening of the peaks located around 8.5 and 13.8 degrees around 15 GPa (**Fig. 5**) comes from the splitting of many reflections of ϕ-In_2S_3.

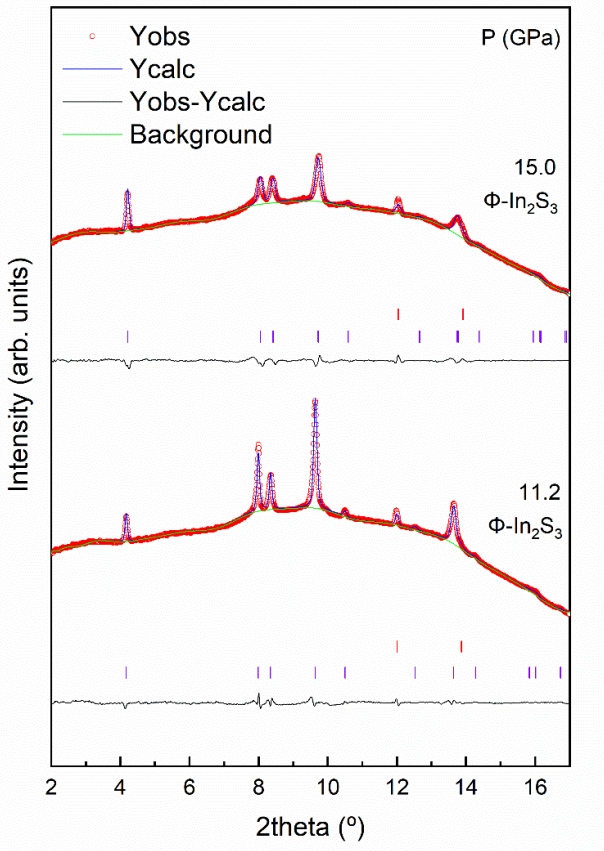

Figure 5. Le Bail refinement of selected XRD patterns of ϕ-In_2S_3 at 11.2 and 15.0 GPa. Copper and ϕ-In_2S_3 reflections are marked with red and purple ticks, respectively.

We must stress that this is the first time, to our knowledge, that a post-spinel phase with defect α-$NaFeO_2$-type structure has been proposed. Noteworthy, this phase has been obtained by chemical lithiation of spinel $LiTi_2O_4$[79] and in spinel $LiCoO_2$ at HT.[80] Additionally, the spinel structure is also found in high-energy irradiated α-$NaFeO_2$.[81] These are clear examples of the relation between the rhombohedral *R*-3*m* α-$NaFeO_2$-type structure of ABX_2 compounds and the cubic *Fd-3m* spinel structure of AB_2X_4

compounds. On top of that, the α-$NaFeO_2$-type structure has been found at ambient conditions in several $B^{III}{}_2X^{VI}{}_3$ compounds, like Sc_2S_3,[82] Ti_2S_3[83] and Zr_2Se_3.[84] These last compounds have 2 equal octahedra in 3a and 3b sites for the *B* cation and an occupation fraction of 1/3 in the 3b sites. Due to the lack of Rietveld refinements, we propose for ϕ-In_2S_3 the same occupation observed in the above mentioned $B^{III}{}_2X^{VI}{}_3$ compounds with this α-$NaFeO_2$-type structure (see **Fig. 6a)**); i.e., a full occupation of 3a sites by In atoms and a 1/3 occupation of 3b sites by In atoms. For the sake of comparison, we have included the structure of $NaInS_2$ (**Fig. 6b)**), where Na cations are in those sites where the φ-In_2S_3 has 1/3 of occupation fraction. In conclusion, we propose the defect α-$NaFeO_2$-type structure as the 2nd HP phase of ϕ-In_2S_3 at ambient temperature.

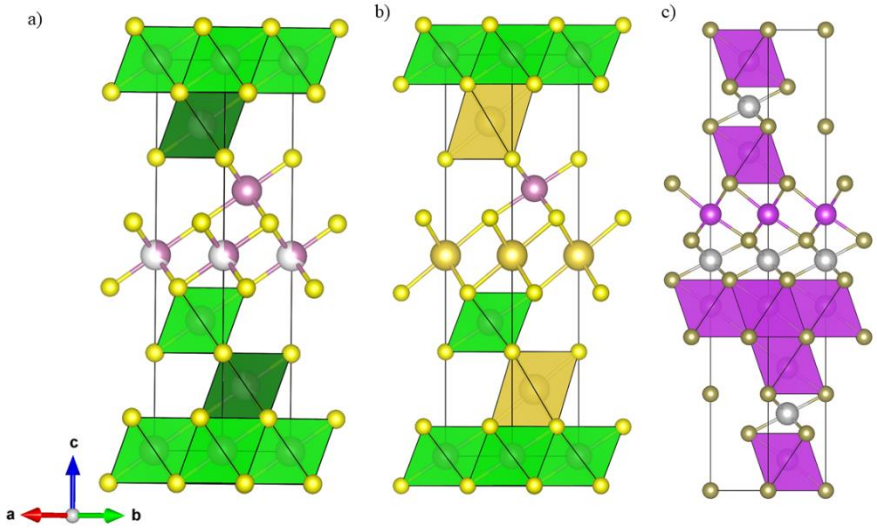

Figure 6. Comparison of ϕ-In_2S_3 a), α-$NaFeO_2$ b), and α-Bi_2Te_3 c) structures. Note that vacancies have been added at 3b sites (those between the layers) in the tetradymite structure of α-Bi_2Te_3 to highlight the similitudes the α-$NaFeO_2$-type and tetradymite-type structures.

Curiously enough, if we remove 1 of every 3 cation layers (from partially occupied 3b sites) of the defect α-$NaFeO_2$-type structure (S.G. *R*-3*m*), we can obtain the tetradymite-like structure (also S.G. *R*-3*m*) observed in many $B^{III}{}_2X^{VI}{}_3$ compounds, like Bi_2Se_3 (**Fig. 6c)**). In this way, the structural relation between the defect $NaFeO_2$-type structure and tetradymite structure is emphasized. In a recent work, it has been proposed that the array of intrinsic vacancies forming the gap between the layers in van der Waals materials, like those having a tetradymite structure, should be considered as part of the crystalline structure.[70] If we apply this rule, both structures are even more connected. In this way, it seems that for $B^{III}{}_2X^{VI}{}_3$ compounds with *B* cations in octahedral coordination, like in the NaCl-type structure, some cations that mix well with vacancies can lead to the defect α-$NaFeO_2$-type structure, like in Sc_2S_3, while other cations that do not mix well with

vacancies can lead to the tetradymite-like structure, like in Bi_2Se_3, where atoms and vacancies group into separate planes leading to quintuple layers.

For the sake of comparison with the previous phases, we have plotted the lattice parameters *a* and *c* (**Fig. 4a)**) and the volume per formula unit, V/Z, (**Fig. 4b)**) of φ-In_2S_3 as a function of pressure. Again, reformulating Z for ϕ-In_2S_3 we got Z=2 by considering the occupation fraction of 1/3 in the 3b sites and the multiplicity of both In and S atoms. Attending to the pressure dependence of V/Z for the α and φ phases, a relative volume decrease of 2.0% at the 2nd PT in β-In_2S_3 is obtained. Again, this value is similar to the volume changes reported between the LP and HP phases of the AIn_2S_4 thiospinels,[72] so this result confirms that this small relative volume change seems to be typical of pressure-induced order-disorder PTs in both $B^{III}{}_2X^{VI}{}_3$ and $A^{II}B^{III}{}_2X^{VI}{}_4$ thiospinels.

The *a* and *c* lattice parameter compressibilities, κ_a and κ_c, of the φ phase ($3.1\cdot10^{-3}$ and $5.4\cdot10^{-3}$ GPa, respectively) are smaller than those of the *a* and *c* axes of the β phase and than that of the *a* axis of the α phase. On top of that, the bulk modulus, B_0, of the ϕ phase (obtained either with BM2- or BM3-EoS, see **Table 3**) is larger than those of the β and α-phases. Note that the unit-cell volume fraction associated with vacancies in the ϕ phase is ~11.11 %; i.e. larger than those in the β and α phases, but this does not result in a softer pressure behaviour of the ϕ phase than the other two phases. The harder pressure behaviour of the ϕ phase is not justified by its fractional occupation of 1/3 in the octahedral cation 3b sites, but for the smaller compressibility of octahedra than of tetrahedra in all spinel-related structures. In addition to this, the low V/Z of the ϕ phase (109 Å^3 (Z=2)) in comparison to those of β and α phases (117.25 (Z=16) and 116.68 (Z=10.67) Å^3, respectively) support the largest incompressibility of the ϕ phase. It must be stressed that the experimental bulk modulus found for ϕ In_2S_3 is like the theoretical ones predicted for isostructural $AgInS_2$, with a similar V value, and larger than $NaInS_2$, with a larger V value (see **Table 3**). This result is in good agreement with the already mentioned inverse relation between volume and bulk modulus.

Table 3. Experimental (exp.) unit-cell volume at zero pressure (V_0, in Å^3), bulk modulus (B_0, in GPa), and first pressure derivative (B_0') obtained for ϕ-In_2S_3. Theoretical (th.) data for $NaInS_2$ and $AgInS_2$ are given for comparison. The volume per formula unit (V/Z, in Å^3) for ϕ-In_2S_3 (Z=2) and Na(Ag)InS_2 (Z=3) are shown as well.

		V_0	**B_0**	**B_0'**	**V/Z**
ϕ-In_2S_3	exp.	217(3)	78(3)	4.4(4)	109(1)
		216(3)	82(4)	4.0,fixed	108(1)
$NaInS_2$	th.	248.9(1)	51(5)	4.6(7)	83(1)
		247.8(4)	56(2)	4.0,fixed	83(2)
$AgInS_2$	th.	229.6(2)	86(2)	4.8(2)	77(1)
		229.2(3)	93(2)	4.0,fixed	76(1)

3.2 Vibrational properties under high pressure

For β-In_2S_3, containing 16 molecules in the unit cell, group theory predicts the 120 vibrational modes at the Brillouin zone center:

$$\Gamma = 9\,A_{1g} + 5\,A_{1u} + 4\,A_{2g} + 11\,A_{2u} + 9\,B_{1g} + 5\,B_{1u} + 4\,B_{2g} + 11\,B_{2u} + 17\,E_u + 14\,E_g$$

From these modes, there are 3 acoustic modes ($A_{2u} + E_u$) and 117 optic modes that correspond to 42 infrared-active modes (10 A_{2u} + 16 E_u), 50 Raman-active modes (9 A_{1g} + 9 B_{1g} + 4 B_{2g} + 14 E_g), and 25 silent modes (5 A_{1u} + 4 A_{2g} + 5 B_{1u} + 11 B_{2u}) that are all hyper-Raman-active except for the 4 A_{2g} modes. Therefore, 36 Raman-active and 26 IR-active peaks are expected since E_g modes (as well as E_u modes) are doubly degenerated. A superindex has been added to the symmetry of the vibrational modes of the different phases to classify them as a function of increasing frequency.

Fig. 7a) shows a selection of HP-RS spectra of β-In_2S_3 under compression up to 21.2 GPa and decompression (d) down to ambient pressure. The Raman modes of the β phase disappear above 4.5 GPa; i.e. at the onset of the 1st PT in good agreement with our HP-XRD measurements. When this PT occurs, the relatively narrow Raman peaks of the β phase disappear, and eight broad bands appear that are consistent with the disorder of cations and vacancies in tetrahedral sites, as expected for the α phase. Moreover, the Raman intensity of most peaks lowers noticeably (at about a 25% of the β phase's signal). For that reason, selected normalized Raman spectra from 5.6 to 21.2 GPa are shown in **Fig. 7b)**. Above 8.6 GPa, the Raman signal becomes even worse (at about a 10% of the β phase's signal), and only two broad bands can be distinguished. This marks the onset of the 2nd PT that is in good agreement with our HP-XRD measurements. Finally, upon decompression from 21.2 GPa, we observed several broad bands, as during upstroke, and the appearance of the main Raman modes of the β phase below 1.2 GPa; thus supporting the partial reversibility of the two observed PTs. This result is again in good agreement with our HP-XRD measurements.

The Raman spectrum of β-In_2S_3 at ambient conditions (see the bottom Raman spectrum of **Fig. 7a)**) is similar to that published in previous works.[30, 41, 85-87] The Raman spectrum covers a wide range (between 40 and 400 cm^{-1}) and shows similar features to those reported by Kambas *et al.*[85] Moreover, our Raman spectra at different pressures are in agreement with those already found in previous HP-RS measurements.[41] However, unlike in **Ref. 41**, we have measured a considerable frequency shift of the Raman-active modes of β-In_2S_3 (see **Fig. 8** and **Table 4**), especially for the high-frequency modes. These Raman shifts do not agree with the almost negligible Raman shifts reported in **Ref. 41** for both hydrostatic and non-hydrostatic HP-RS measurements. The experimental and theoretical pressure dependence of the frequencies corresponding to the Raman-active modes of the β phase are plotted in **Fig. 8**. The good agreement between the experimental and theoretical zero-pressure Raman frequencies and their pressure coefficients has allowed us to tentatively assign the symmetry of the 22 observed Raman-active modes of the β phase (see **Fig. 7** and **Table 4**). With the exception of the B_{1g}^2 mode, we have assigned all the predicted modes to every observed peak below 120

cm^{-1}. At higher frequencies, the assignment is more doubtful due to the large number of Raman-active modes of the β phase and the lack of clear observation of a number of them. It can be noticed that, in general, the pressure coefficient of the frequency of the Raman-active modes increases as the frequency increases (see **Table 4**). The two lowest frequencies E_g modes (near 50 cm^{-1}) show negative pressure coefficients, while the modes above 300 cm^{-1} show the highest-pressure coefficients. In particular, the E_g^{13} mode exhibits the highest theoretical pressure coefficient (10.1 $cm^{-1}GPa^{-1}$).

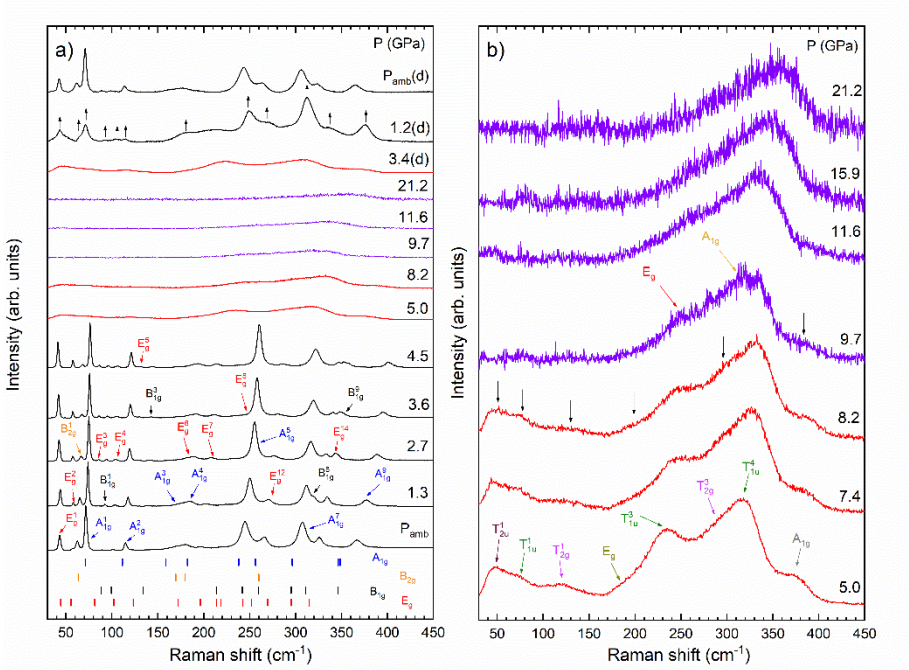

Figure 7. a) Stacked Raman spectra of β-In_2S_3 under compression up to 21.2 GPa and under decompression down to ambient pressure b) Normalized Raman spectra under compression in the range of 5.0 and 21.2 GPa, where HP phases α-In_2S_3 and ϕ-In_2S_3 are seen. Up and down arrows in both panels show the Raman peaks that disappear/emerge under both compression and decompression.

The spread of the theoretical and experimental Raman-active modes along the frequency axis and the increasing pressure coefficients of such modes with increasing frequency in β-In_2S_3 (**Fig. 8**) is similar to those observed in many OVCs, like Ga_2S_3,[67] $CdGa_2S_4$,[88] $HgGa_2S_4$,[89] $ZnGa_2Se_4$,[90] $CdGa_2Se_4$,[91] $HgGa_2Se_4$,[92] $CdAl_2S_4$,[93] and $CdIn_2Se_4$.[94] However, these OVCs exhibit phonon gaps between low-frequency modes (with negligible or negative pressure coefficients) and high-frequency modes (with positive pressure coefficients) that are not observed in β-In_2S_3. As can be observed in **Fig. S5a)** in the SI, the one-phonon density of states (PDOS) of β-In_2S_3 only has a unique narrow phonon gap below 280 cm^{-1}. The reason for the lack of a phonon gap in β-In_2S_3, unlike in other OVCs, could be

related to the existence of 4- and 6-fold coordinated In atoms in β-In_2S_3, in contrast to other OVCs, whose cations are only 4-fold coordinated. We must recall that the stretching and bending modes of InS_6 octahedra have smaller frequencies than those of InS_4 tetrahedra because of the more considerable In-S bond distances in the octahedra than in the tetrahedra. Therefore, the lower frequencies of the bending modes of the octahedra that will extend in the region below 200 cm^{-1} allow explaining the lack of the phonon gap in β-In_2S_3, unlike in tetrahedrally-coordinated OVCs. Another relevant difference between β-In_2S_3 and tetrahedrally-coordinated OVCs is the lack of the breathing mode of the vacancy in the Raman spectrum of β-In_2S_3. This mode is usually the strongest peak of the Raman spectrum in tetrahedrally-coordinated Ga-based OVCs, and it is also notably strong in $CdIn_2Se_4$ near 133 cm^{-1}.[94] Thanks to our lattice dynamics calculations and with the use of the J-ICE visualizer,[95] we have found that the breathing mode in β-In_2S_3 is the B_{2u}^9 silent mode at 296.86 cm^{-1}. The silent nature of this mode explains why the breathing mode is entirely absent in the Raman spectrum of β-In_2S_3.

Regarding the 1st PT, we must comment that the related abrupt change observed in the Raman spectrum at 5.0 GPa (**Fig. 7a)**) has also been reported at a slightly higher pressure (around 6.5 GPa) in previous HP-RS measurements with different PTM.[41] In particular, four broad Raman bands were reported between 6.5 and 10 GPa in the Raman spectra under hydrostatic (He as PTM) and non-hydrostatic conditions (no PTM).[41] Therefore, we conclude that existing HP-RS measurements confirm the existence of this 1st PT in agreement with HP-XRD measurements.

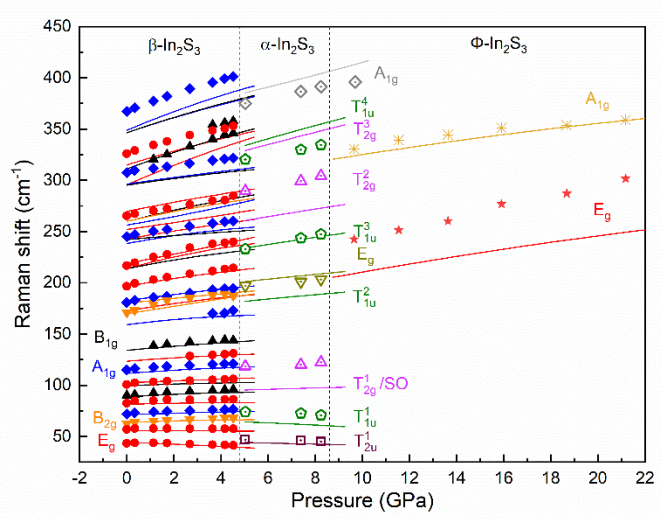

Figure 8. Pressure dependence of the experimental (symbols) Raman frequencies of β-, α-, and ϕ-In_2S_3 during compression. For comparison with experimental data of the three phases, theoretical (lines) for β-In_2S_3, $CdIn_2S_4$, and $NaInS_2$ have been plotted.

Table 4. Theoretical (th.) and experimental (exp.) Raman-active frequencies at zero pressure (ω_0, in cm^{-1}) and pressure coefficients (a_1, in $cm^{-1}\cdot GPa^{-1}$; a_2, in 10^{-2} $cm^{-1}\cdot GPa^{-2}$) in β-In_2S_3 according to fits to $\omega_0 + a_1P + a_2P^2$.

	β-In_2S3 th.			**β-In2S3 exp.**		
Mode	**ω_0**	**a_1**	**a_2**	**ω_0**	**a_1**	**a_2**
E_g^1	44.4(1)	-0.9(1)	-3(1)	44(1)	-0.3(2)	-6(4)
E_g^2	55.4(1)	-0.02(1)		58(1)	-0.06(1)	
B_{2g}^1	63.6(1)	1.0(1)	-9(1)	63(2)	2.1(3)	-20(6)
A_{1g}^1	71.2(1)	0.9(1)	-5(1)	73(2)	1.1(2)	-6(3)
E_g^3	81.5(1)	0.6(1)	-5(2)	85(3)	0.8(3)	-9(6)
B_{1g}^1	88.5(1)	1.6(1)	-14(1)	90(3)	2.0(2)	-16(4)
B_{1g}^2	99.5(1)	0.9(1)	-6(1)			
E_g^4	102.2(1)	1.1(1)	-4(2)	102(3)	1.0(2)	-3(4)
A_{1g}^2	111.6(1)	1.8(2)	-11(3)	115(2)	2.0(2)	-16(5)
E_g^5	123.4(1)	1.9(1)	-11(2)	125(3)	1.3(1)	
B_{1g}^3	134.1(1)	2.1(1)	-6(2)	135(3)	4.0(1)	-34(8)
A_{1g}^3	159.0(1)	3.0(1)	-23(1)	156(4)	3.0(2)	
B_{2g}^2	169.7(2)	3.7(2)	-2(4)			
E_g^6	172.4(1)	4.0(1)	-19(2)	171(4)	8.0(1)	-88(20)
B_{2g}^3	179.9(2)	2.6(2)	-6(4)			
A_{1g}^4	182.5(1)	3.2(1)	-10(2)	182(4)	4.0(1)	-15(10)
E_g^7	196.5(2)	4.1(2)	-15(5)	197(4)	5.0(1)	-35(10)
B_{1g}^4	213.8(2)	4.6(2)	-22(4)			
E_g^8	214.0(1)	6.3(1)	-33(3)	217(4)	8.1(4)	-64(10)
E_g^9	219.0(3)	4.3(4)	7(7)			
A_{1g}^5	238.2(3)	4.4(4)	-27(5)	245(2)	4.4(2)	-23(4)
B_{1g}^5	242.1(2)	2.1(3)	-7(5)			
E_g^{10}	242.8(2)	4.1(3)	-10(5)			
E_g^{11}	252.0(2)	3.3(2)	4(3)			
A_{1g}^6	256.3(1)	3.9(1)	13(1)			
B_{1g}^6	259.9(1)	5.8(1)	-19(2)			
B_{2g}^4	260.1(2)	5.1(3)	-18(5)			
E_g^{12}	269.7(2)	4.7(2)	-12(4)	266(2)	4.0(1)	6(20)
B_{1g}^7	295.3(2)	3.5(2)	-12(4)			
E_g^{13}	295.6(3)	10.1(4)	-28(7)			
A_{1g}^7	296.3(2)	3.4(2)	-8(3)	308(2)	3.4(3)	-7(6)
B_{1g}^8	311.1(2)	8.6(2)	-25(4)	311(3)	9.0(1)	-23(13)
E_g^{14}	315.0(4)	7.2(4)	-20(7)	326(2)	7.8(3)	-43(7)
B_{1g}^9	346.9(1)	5.9(2)		340(4)	3.9(1)	
A_{1g}^8	346.5(3)	7.8(3)	-23(6)			
A_{1g}^9	348.7(3)	9.8(3)	-33(6)	367(2)	9.1(2)	-36(3)

Regarding the 1st PT, we must comment that the related abrupt change observed in the Raman spectrum at 5.0 GPa (**Fig. 7a)**) has also been reported at a slightly higher pressure (around 6.5 GPa) in previous HP-RS measurements with different PTM.[41] In particular, four broad Raman bands were reported between 6.5 and 10 GPa in the Raman spectra under hydrostatic (He as PTM) and non-hydrostatic conditions (no PTM).[41] Therefore, we conclude that existing HP-RS

measurements confirm the existence of this 1st PT in agreement with HP-XRD measurements.

Let us now comment about the vibrational modes of the 1st HP phase. For the cubic spinel structure, one expects 42 vibrational modes at the Γ point. These modes result in 5 Raman-active (A_{1g}+ E_g + 3 T_{2g}), 4 IR-active (4 T_{1u}), and 4 silent (2 A_{2u} + 2 T_{2u}) modes, with *E* and *T* modes being doubly and triply degenerated, respectively.[96] Due to the inverse cation distribution in AIn_2S_4 thiospinels; i.e. disorder between 4-fold coordinated *A* cations and 6-fold coordinated In atoms, a partial breakdown of the Raman selection rules occurs due to the loss of translation symmetry, and IR-active and silent modes could be observed in the Raman spectrum.[97] Therefore, a total of 13 modes could be observed in the Raman spectrum of α-In_2S_3. We have measured 8 modes in the Raman spectrum of the 1st HP phase (see **Fig. 7b)**). The frequencies and pressure coefficients of the 8 modes measured and assigned to α-In_2S_3 are summarized in **Table 5**. The pressure coefficients were obtained from the experimental data fitting to the equation $\omega_0 + a_1(P - P_0)$, with P_0 = 5.0 GPa.

The fractional occupation in the Td(8a) sites of α-In_2S_3 complicates the simulation of its structural and vibrational properties. Therefore, in order to help assigning the symmetry of the experimentally observed modes of the α phase, we have tabulated in **Table 5** the theoretical and experimental[98] modes of $CdIn_2S_4$ thiospinel, as an approach to the observed modes of α-In_2S_3. That approximation is justified by the similarity of Cd and In masses and by the proximity of the molecular masses of both compounds per unit cell: 3763 and 3474 for $CdIn_2S_4$ (Z=8) and α-In_2S_3 (Z=10.66), respectively. Therefore, similar vibrational frequencies would be expected for both compounds at similar pressures. With this information, we have tentatively assigned the modes observed in the Raman spectrum obtained from the commercial sample powders of α-In_2S_3 at ambient pressure (**Fig. S4b)**) and at HP in **Fig. 7b)**. For a better comparison, the Grüneisen parameter for each vibrational mode, $\gamma = B_0 \cdot a_1/\omega_0$, is used to normalize the pressure coefficients of the modes observed in both α-In_2S_3 and $CdIn_2S_4$ (see **Table 5**). Since the value of B_0 for $CdIn_2S_4$ is almost twice that for α-In_2S_3 (see **Table 2**), γ' values for $CdIn_2S_4$ are almost twice those for α-In_2S_3 (see **Table 4**).

Table 5. Experimental (exp.) zero-pressure frequencies (ω_0, in cm^{-1}), pressure coefficients (a_1, in $cm^{-1}\cdot GPa^{-1}$; a_2, in 10^{-2} $cm^{-1}\cdot GPa^{-2}$) and Grüneisen parameters, $\gamma = B_0\cdot a_1/\omega_0$ (ω_0 at 0 GPa), of the observed modes in α-In_2S_3 as obtained from fits of Raman data to $\omega_0 + a_1(P - P_0)$, with P_0 = 5.0 GPa. Frequencies of α-In_2S_3 from commercial powders and from extrapolations of HP data are also given for comparison. Also summarized are theoretical (th.) and experimental zero-pressure frequencies, pressure coefficients, and reduced slopes of Raman-, IR- and silent-active modes in $CdIn_2S_4$. The theoretical data of $CdIn_2S_4$ have been fitted to $\omega_0 + a_1P$. To calculate γ, we have used B_0= 39 GPa for α-In_2S_3 and 79.8 GPa for $CdIn_2S_4$ and the frequencies measured at 0 GPa.

	α-In_2S_3 (exp.)[a]					**$CdIn_2S_4$ (th.)[a]**			**$CdIn_2S_4$ (exp.)[b]**		
Mode	**ω_0[c]**	**a_1**	**γ**	**ω_0[d]**	**ω_0[e]**	**ω_0**	**a_1**	**γ**	**ω_0**	**a_1**	**γ**
T_{2u}^1 (S)	48(2)	-0.5(2)	-0.4(2)	49(3)	43(1)	49.5(3)	-0.9(1)	-1.5(2)			
T_{1u}^1 (IR)	74(2)	-1.0 (1)	-0.5(2)	79(3)	70(1)	69.4(3)	-1.1(1)	-1.2(2)	70(1)	0.7(2)	0.8(3)
T_{2g}^1 (R)	119(2)[f]	1.1(2)	0.4(3)	113(1)	110(1)	92(1)	0.7(1)	0.6(1)	93(1)	0.5(2)	0.4(3)
T_{1u}^2 (IR)						169.7(2)	2.6(1)	1.0(2)			
A_{2u}^1 (S)						185.0(2)	1.6(1)	0.7(1)			
E_g (IR)	198(3)	1.9(3)	0.4(1)	187(2)	185(1)	189.1(2)	2.3(1)	1.0(1)	188(1)	2.7(2)	1.1(1)
T_{1u}^3 (IR)	236(3)	4.5(1)	0.8(1)	210(3)	217(1)	216.4(3)	3.5(4)	1.3(1)	207(1)	2.6(2)	1.0(1)
T_{2u}^2 (S)						227.7(3)	3.8(1)	1.3(1)			
T_{2g}^2 (R)						241.5(4)	3.7(1)	1.2(1)	249(1)	4.4(2)	1.4(1)
T_{2g}^3 (R)	291(3)	5(1)	0.7(2)	270(2)	264(1)	299.7(4)	6.0(1)	1.6(2)	315(1)	5(2)	1.2(1)
T_{1u}^4 (IR)	323(3)	4.4(3)	0.6(2)	298(2)	305(1)	301.2(1)	3.5(2)	1.7(1)	301(1)	3.3(2)	0.9(1)
A_{2u}^2 (S)					341(1)	354(1)	6.2(1)	1.4(1)			
A_{1g} (R)	378(3)	5(1)	0.6(2)	354(3)	370(1)	357(1)	5.8(1)	1.3(1)	360(1)[g] 367(1)[h]	6.1(2)[g] 6.1(2)[h]	1.3(1)[g] 1.3(1)[h]

[a]Present work.
[b]**Ref.** .
[c]Frequencies of α-In_2S_3 at 5.0 GPa (from data fitting).
[d]Frequencies of α-In_2S_3 at 0 GPa (extrapolated from fits to HP data).
[e]Frequencies of α-In_2S_3 at 0 GPa (experimental data from commercial α-In_2S_3).
[f]This mode can be assigned either the T_{2g}^1 symmetry or as a second order (SO) mode. Further details in the text.
[g]A_{1g} mode associated with the vibration of InS_4 tetrahedral units, according to **Ref. 98.**
[h]A_{1g} mode associated with the vibration of CdS4 tetrahedral units, according to **Ref. 98**.

According to our experimental results on α-In_2S_3 and the comparison with isostructural $CdIn_2S_4$, the bands observed in the Raman spectrum of α-In_2S_3 at ambient pressure (**Fig. S4b)**) can be explained as follows (see **Table 5**). The first band located at 43 cm^{-1} should correspond to a silent T_{2u}^1 mode that is calculated to be around 49.5 cm^{-1} in $CdIn_2S_4$. A negative value of γ is observed for this mode in α-In_2S_3 and also predicted in $CdIn_2S_4$. This T_{2u}^1 mode is neither Raman- nor IR-active and becomes Raman-active due to the cation-vacancy disorder in the T_d(8a) sites of the α phase. Concerning the T_{2u}^2 and A_{2u}^1 modes, their theoretical ω_0 do not compare well with those observed experimentally in our HP-RS measurements (**Table 5**). On top of that, they cannot be assigned properly the Raman spectra of the commercial α-In_2S_3 powders of Sigma Aldrich at ambient pressure because of the broad band between 150 and 250 cm^{-1} (**Fig. S4b)**). However, we have tentatively assigned the A_{2u}^2 mode, the highest-frequency silent mode, to the right shoulder of that peak located at about 300 cm^{-1} (**Fig. S4b)**). The band at about 70 cm^{-1} can be assigned to the IR-active T_{1u}^1 mode, with a_1 quite close to that calculated for $CdIn_2S_4$ and both with negative γ. Curiously, the experimental pressure coefficient of this mode in $CdIn_2S_4$ was found to be of opposite sign to that of calculations.[66] This soft mode was also observed in $MgIn_2S_4$,[98], while in $MnIn_2S_4$, the T_{1u}^1 mode was not observed. The T_{1u}^2 mode, not observed either in α-In_2S_3 or in $CdIn_2S_4$, should be located around 170 cm^{-1}, in accordance with our calculations for $CdIn_2S_4$. The T_{1u}^3 and T_{1u}^4 modes in α-In_2S_3 have been assigned to the broad peaks located in our Raman spectra around 217 and 305 cm^{-1} (236 and 323 cm^{-1} near 5 GPa in **Fig. 7b)**), by means of the agreement among the a_1 and ω_0 of our α-In_2S_3 (those extrapolated at 0 GPa, see **Table 5**) and both experimental and theoretical ones of the $CdIn_2S_4$. Furthermore, these T_{1u}^3 and T_{1u}^4 modes can be likely associated with the peaks observed around 237 and 306 cm^{-1} near 6.6 GPa in **Ref. 41**, but the a_1 reported in **Ref. 41** for these modes do not match with those collected in our **Table 5**. The γ values for the T_{1u}^3 mode in α-In_2S_3 and $CdIn_2S_4$ are the highest below 230 cm^{-1}. Regarding the T_{1u}^4 mode, the experimental and theoretical γ values in α-In_2S_3 and $CdIn_2S_4$, respectively, are the highest above 230 cm^{-1}.

The rest of the broad bands seen in the Raman spectra of the commercial α-In_2S_3 sample at ambient pressure and in the 1st HP phase of β-In_2S_3 are tentatively attributed to Raman-active modes of α-In_2S_3. The broad bands located around 110 and 264 cm^{-1} at ambient pressure (119 and 291 cm^{-1} near 5 GPa in **Fig. 7b**) can be assigned to the T_{2g}^1 and T_{2g}^3 modes. It must be stressed that the T_{2g}^1 could also be assigned as a second-order mode, as Ursaki *et al.* assigned for the mode observed with a zero-pressure frequency around 110 cm^{-1} in $CdIn_2S_4$.[98] On the other hand, we consider that the T_{2g}^2 mode is not observed in our Raman spectra of α-In_2S_3. This mode should be placed between 249 and 285 cm^{-1}, where the ω_0 of $CdIn_2S_4$, $MgIn_2S_4$, and $MnIn_2S_4$ thiospinels are placed for this mode.[98] On the other hand, we have assigned the broad peak located around 185 cm^{-1} at ambient pressure (198 cm^{-1} around 5 GPa in **Fig. 7b**) to the E_g mode on the basis of the close values of the experimental and theoretical a_1 and ω_0 in $CdIn_2S_4$, which are also in agreement with those experimental a_1 reported for the $MgIn_2S_4$ and $MnIn_2S_4$ thiospinels.[98] In addition, positive γ values are observed in α-In_2S_3 for this E_g mode, as well as in AIn_2S_4 thiospinels.[98] Last but not least, we have tentatively assigned the highest-frequency broad peak placed around 370 cm^{-1} at

ambient pressure (378 cm^{-1} around 5 GPa in **Fig. 7b**) to the A_{1g} mode, according to the experimental and theoretical a_1 and ω_0 in $CdIn_2S_4$. This A_{1g} mode can also be assigned to the broad band observed near 373 cm^{-1} around 7 GPa in **Ref. 41**. As was stressed by Ursaki *et al.*[98], the A_{1g} mode refers to the breathing mode (In-S symmetric stretching of InS_4); i.e. the vibration of S atoms towards the centre of the tetrahedron. This mode splits into two bands in inverse AIn_2S_4 thiospinels, associated with the S motion in AS_4 and InS_4 tetrahedra due to cation disorder. The pressure evolution of these two bands has been experimentally seen in the HP-RS measurements of AIn_2S_4 thiospinels, and this mode was found to have one of the highest values of the pressure coefficients,[98] in good agreement with our HP-RS measurements in α-In_2S_3. Similarly, the A_{1g} mode must also split in α-In_2S_3, due to the cation-vacancy disorder at Td(8a) sites, between the S motions of $VacS_4$ and InS_4. Unfortunately, we do not presently know the location of such a local vibrational mode if it exists.

A final comment can be added regarding the pressure coefficients of the β and α phases. It can be observed that the Raman modes with the smallest frequencies in both phases show negative pressure coefficients, unlike in ϕ-In_2S_3 (see **Fig. 7a)**). The negative pressure coefficients of the low-frequency modes in both phases are due to the softening of zone-edge TA phonons in tetrahedrally bonded solids that is not present in octahedrally bonded solids.[99] Some of these zone-edge phonons become Raman active due to zone folding of cubic structures in more complex structures with a smaller group symmetry, like in β-In_2S_3, or with a large number of atoms in the unit cell, like in α-In_2S_3. Therefore, the negative pressure coefficient of the lowest frequency mode in the 1st HP phase of β-In_2S_3 is a direct proof that tetrahedral coordination is still present in that phase, and thus gives support to our assignment of the 1st HP phase of β-In_2S_3 to the cubic spinel structure of α-In_2S_3 where In cations are both tetrahedrally and octahedrally coordinated as in β-In_2S_3.

Support for the identification of the 1st HP phase of β-In_2S_3 with α-In_2S_3 also comes from the matching between the Raman- and IR-active modes observed in the 1st HP phase of β-In_2S_3 and those seen in α-In_2S_3 thin films deposited on different substrates,[41-43] as well as in quenched α-In_2S_3 samples with high In contents.[30] For example, the lowest-frequency IR-active T_{1u}^1 mode has been observed weakly on cubic In_2S_3 thin films deposited on InAs substrates[100] and in quenched α-In_2S_3 samples with higher In contents.[30] The modes found in several works around 126, 240, and 266 cm^{-1} at ambient pressure can be tentatively assigned to T_{2g}^1, T_{1u}^3, and T_{2g}^2 modes (the last one not observed in our HP-RS measurements). These frequencies have been traditionally attributed to the presence of α-In_2S_3 on annealed In_2S_3 thin films deposited on glass substrates.[101, 102] A broad band observed near 166 cm^{-1} on In_2S_3 thin films[100] could be attributed to the T_{1u}^2 mode (not seen in our Raman spectra), which could also be consistent with the modes reported around 170 and 178 cm^{-1} in quenched α-In_2S_3 samples with In content of 41.0 and 41.5%, respectively.[30] In these quenched samples, the modes around 206 and 211 cm^{-1} found in samples with In content of 41.0 and 41.5%, respectively, could be related to the E_g mode at 200 cm^{-1} in our α-In_2S_3 sample at ambient pressure . Finally, the high-frequency modes T_{2g}^3, T_{1u}^4, and A_{1g} mode can be seen in In_2S_3 thin films and in quenched α-In_2S_3 samples

with a high In contents above 295 cm^{-1}.[30, 100-103] All in all, the vibrational information provided in this work for the 1st HP phase of β-In_2S_3 gives support to its α-In_2S_3 nature.

Finally, we have included the theoretical PDOS of $CdIn_2S_4$ at 0 GPa in **Fig. S5b)** in the SI, as an approach to that of α-In_2S_3, in order to compare the vibrational properties of α-In_2S_3 and β-In_2S_3. As observed, the narrow phonon gap of β-In_2S_3 located at 280 cm^{-1} (**Fig. S5a)** becomes wider in the α phase (**Fig. S5b)**). Furthermore, a second-wide phonon gap appears around 340 cm^{-1}. Curiously, the Raman spectra of the α phase under compression (**Fig. 7b)**) and that measured from the commercial powders of α-In_2S_3 (**Fig. S4b**) do not seem to show those two phonon gaps. In this context, we can speculate that perhaps the cation-vacancy disorder in Td(8a) sites in the α phase results in broad Raman bands that prevent the observation of such phonon gaps in the Raman spectrum.

As regards the 2nd HP phase of β-In_2S_3, we have already commented that above 8.2 GPa most Raman modes of the α phase disappear, and only three broad bands are observed (see **Fig. 7**). In fact, one of these modes corresponds to the A_{1g} mode of the α phase that persists up to 9.7 GPa. Therefore, only two broad bands between 200 and 350 cm^{-1} can be ascribed to the 2nd HP phase above 8.2 GPa (see **Fig. 7b)**). According to group theory, the rhombohedral α-$NaFeO_2$-type phase has 12 vibrational modes at the Γ point with irreducible representations:

$$\Gamma = 1A_{1g}(R) + 2A_{2u}(IR) + 1E_g(R) + 2E_u(IR) + 1A_{2u} + 1E_u$$

where R and IR indicate the Raman- and IR-active modes. Therefore, there are 2 Raman-active modes (E_g and A_{1g}), 4 IR-active modes ($2A_{2u}$ and $2E_u$), and 3 acoustic modes. The two Raman-active modes correspond to anion movements in the stretching and bending modes of the cation-anions bonds.[74] The frequency shifts of the two bands of φ-In_2S_3 upon compression up to 21.2 GPa are plotted in **Fig. 8**. Of these two peaks, the smallest (highest) in frequency was previously followed under pressure up to 23 (43) GPa.[41] In this respect, our HP-RS measurements agree with those already published.[41] The main difference between both HP-RS studies is that the previous work does not consider that there is a PT above 8.6 GPa, despite there are clear changes in the Raman spectra supporting this 2nd PT in β-In_2S_3.

To verify that the two observed Raman bands of the 2nd HP phase of β-In_2S_3 correspond to the *R*-3*m* structure of defect α-$NaFeO_2$, we have simulated the pressure dependence of the Raman-active frequencies of isostructural $NaInS_2$ as an approach to the observed modes of φ-In_2S_3 (see **Fig. 8** and **Table 6**). That approximation is justified by the proximity of the molecular masses of both compounds per unit cell: 620 and 656 for $NaInS_2$ (Z=3) and φ-In_2S_3 (Z=2), respectively. Therefore, similar vibrational frequencies are expected for both compounds at similar pressures. With this information, we have tentatively assigned the modes observed in the Raman spectrum of φ-In_2S_3 above 8.2 GPa in **Fig. 7b)**, whose pressure dependence of the vibrational frequencies are plotted in **Fig. 8**.

For a better comparison of φ-In_2S_3 and $NaInS_2$, the Grüneisen parameter for each vibrational mode, $\gamma = B_0 \cdot a_1 / \omega_0$, is used to normalize the pressure coefficients in both compounds (see **Table 6**). A good agreement between the extrapolated experimental

frequencies of φ-In_2S_3 at ambient pressure and the experimental[74] and theoretical frequencies of $NaInS_2$ at ambient pressure can be observed. Moreover, both compounds show similar a_1 and γ values (see **Table 6**). This result gives support to the assignment of the 2nd HP phase of β-In_2S_3 to the defect α-$NaFeO_2$-type structure. Therefore, we can conclude that our HP-RS measurements provide clear support for the existence of two pressure-induced order-disorder PTs in tetragonal β-In_2S_3 up to 20 GPa. Besides, Raman spectra of the 1st and 2nd HP phases are consistent with the cubic spinel (α-In_2S_3) and the defect α-$NaFeO_2$-type (ϕ-In_2S_3) structures, respectively, as suggested by Le Bail refinements of our HP-XRD measurements.

Table 6. Experimental (exp.) zero-pressure frequencies (ω_0, in cm^{-1}), pressure coefficients (a_1, in $cm^{-1}\cdot GPa^{-1}$; a_2, in 10^{-2} $cm^{-1}\cdot GPa^{-2}$) and Grüneisen parameters, $\gamma = B_0\cdot a_1/\omega_0$ (ω_0 at 0 GPa), of the observed modes in φ-In_2S_3 as obtained from fits of Raman data to $\omega_0 + a_1(P - P_0) + a_2(P - P_0)^2$. Also summarized are theoretical (th.) zero-pressure frequencies, pressure coefficients, and Grüneisen parameters of the Raman-active modes in $NaInS_2$ with α-$NaFeO_2$ structure. The theoretical data of $NaInS_2$ have been fitted to $\omega_0 + a_1P + a_2P^2$. To calculate γ we have used B_0= 78 GPa for ϕ-In_2S_3 and 51 GPa for $NaInS_2$.

	ϕ-In_2S_3 (exp.)					**$NaInS_2$**				
Mode	**ω_0[a]**	**a_1**	**a_2**	**γ**	**ω_0[b]**	**ω_0[c]**	**a_1[c]**	**a_{2c}**	**γ_c**	**ω_0[d]**
Eg	242(2)	5(1)	1(7)	1.6(2)	195(5)	165.1(2)	5.1(1)	-5.0(2)	1.5(1)	158
A1g	331(1)	4(1)	-14(4)	0.9(2)	279(5)	284.6(2)	4.6(1)	-5.1(2)	0.8(1)	289

[a] Frequencies of ϕ-In_2S_3 at 9.7 GPa (from data fitting).
[b] Frequencies of ϕ-In_2S_3 at 0 GPa (extrapolated from fits to HP data).
[c] Values for the $NaInS_2$ obtained from our theoretical calculations.
[d] Experimental frequencies of $NaInS_2$ at ambient conditions from **Ref. [78]**.

To finish this section, we want to stress that the defect α-$NaFeO_2$ structure bears a close relation with the defect $LiTiO_2$ structure found as a HP phase in AIn_2S_4 (*A*=Cd, Mg, Mn) thiospinels. It must be noted that two broad Raman peaks were also observed in the HP phase of AIn_2S_4 (*A*=Cd, Mg, Mn) thiospinels,[98] as it occurs in the 2nd HP phase of β-In_2S_3. In both kinds of thiospinels, a drastic decrease of the Raman signal was observed at the PT (**Fig. 5a)**). In the case of AIn_2S_4 thiospinels, a defect NaCl-type structure (typical HP phase of $A^{II}B^{III}{}_2X^{VI}{}_4$ OVCs) and later observed in $CdAl_2S_4$,[93] was first proposed as a HP phase from HP-RS measurements.[98] However, subsequent HP-XRD measurements determined that the HP phase of AIn_2S_4 (*A*=Cd, Mg, Mn) thiospinels was a defect $LiTiO_2$-type structure.[72] In this context, it must be stressed that both $LiTiO_2$ and α-$NaFeO_2$ structures are typical phases of ABX_2 compounds and that both structures derive from the NaCl-type structure, with all cations in octahedral coordination. The main difference between both structures is that in cubic $LiTiO_2$ cations are alternated in the sequence *A*-*X*-*B*-*X* along the different spatial directions, much like the NaCl structure, while in rhombohedral α-$NaFeO_2$ different types of cations and anions are grouped in different layers in a sequence *A*-*X*-*B*-*X*, thus resulting in the formation of a layered structure with atomic planes perpendicular to the *c* axis of the hexagonal unit cell. It may be speculated that the different arrangement of cations in these two structures can be related to the different size of the cations (Li and Ti have similar ionic radii, while Na and Fe have rather

different ionic radii). Following this line of reasoning, the different ionic radii of In, on one hand, and the average of the mixture of an In atom and two vacancies, on the other hand, could be responsible for the different behaviour at HP of In_2S_3 with respect to AIn_2S_4 (*A*=Cd, Mg, Mn) thiospinels.

3.3 Structural stability of β-In_2S_3 at high pressure and pressure-induced PTs

Let us now discuss the stability of β-In_2S_3 under compression based on the information provided in this and previous HP works, as summarized in **Table 1**, and the implications of the pressure-induced PTs found in β-In_2S_3.

Clearly, our measurements show two PTs up to 20 GPa for the β phase. Our first transition pressure (~4.8 GPa according to our HP-XRD and HP-RS measurements) is in agreement with that observed in In_2S_3:Ce nanoparticles[32] and smaller than those reported in In_2S_3 nanoparticles[32] and in In_2S_3 powders.[37, 40, 41] We assume that the difference in transition pressures between different works comes from the different PTM and techniques employed since in many previous HP works, rather non-hydrostatic PTMs have been used, especially considering the softness of an OVC such as β-In_2S_3.

On the other hand, results from **Ref. 39** are more controversial since no PTs were detected with different PTM, despite the fact that we consider that the two PTs were observed in **Ref. 39**. According to **Fig. 2** in **Ref. 39**, the (1 1 2) reflection disappears and the (1 1 6) decreases sharply at about 5.1 GPa with M-E (run-1), meanwhile both reflections disappear at 5.9 GPa with Ne (run-2). The same feature occurs in our HP-XRD measurements at 4.9 GPa (**Fig. 2**), thus supporting the observation of the first PT in **Ref. 39**. On the other hand, it must be stressed that in Fig. 3 of **Ref. 39**, peaks corresponding to *d spacing* values greater than 5.0 Å are not reported. Above this value, the weak (0 0 4) peak, observed at 3.03 degree at 0.9 GPa, as well as the (1 0 1) and (1 0 3) reflections can be observed in **Fig. 2a)**. In fact, the (1 0 3) peak is observed at 0.4 GPa in **Fig. 1** of **Ref. 39**, but not the (0 0 4) and (1 0 1) peaks. In this context, it is important to notice that both (0 0 4) and (1 0 1) reflections disappear at 4.9 GPa, and only the (1 0 3) reflection remains in our HP-XRD measurements at that pressure (**Fig. 2**). Besides, the disappearance of some reflections was observed in **Ref. 39** below 5.0 Å (**Figs. 3 a)** and **b)** of **Ref. 39**) for run-1 and run-2 at 5.1 and 5.9 GPa, respectively, as occurs in our HP-XRD measurements at 4.9 GPa (**Fig. 2 a)**). Noteworthy, the same authors from **Ref. 39** performed electrical measurements under HP in **Ref. 38,** where they reported a semiconductor-metal transition at 6.8 GPa by electrical measurement that is likely related to the vacancy disorder occurring in β-In_2S_3 at the first PT. In this respect, it is also noticeable that the HP-RS measurements from **Ref. 39** evidenced an abrupt change in the Raman modes at 7.2 and 6.8 GPa, with He and without PTM, respectively. Therefore, the β phase is not stable under compression between 4.8 and 6.8 GPa. In conclusion, we can confirm, on the basis of the similarities between our HP-XRD measurements and those from **Ref. 39**, that the first PT is well observed in our HP-XRD measurements and also in earlier HP works.[37, 38, 40, 41]

The existence of phase transitions in β-In_2S_3 below 20 GPa is further confirmed by our theoretical simulations of the energy vs volume and relative enthalpy vs pressure

between β-In_2S_3 and ϕ-In_2S_3 (see **Fig. S6a)** and **S6b)**, respectively, in the SI). Clearly, the simulated ϕ-In_2S_3 shows an enthalpy smaller than β-In_2S_3 above 5 GPa. This result is consistent with the α-ϕ PT observed above 8.2 GPa. The disordered ϕ-In_2S_3 could be simulated due to few possible supercells (only 7 combinations) suggested by Supercell program.[66] However, the number of possible supercells to simulate α-In_2S_3 is computationally prohibitive ($2.3 \cdot 10^{13}$), so no simulation of this phase has been performed.

We also want to comment on the reversibility of the pressure effects on β-In_2S_3. In agreement with our HP-XRD measurements at 0.6 GPa on dowstroke from 16 GPa (**Fig. 2a)**), our HP-RS measurements below 1.2 GPa on downstroke from 21 GPa also show the appearance of β-In_2S_3 (**Fig. 5a)**). The reversibility of β-In_2S_3 was already commented in a previous HP-RS work.[35] In that work, the β phase was recovered when the pressure was relaxed from 8.6 and 7.8 GPa, with He and without PTM, respectively; however, the β phase was not recovered from 43.0 GPa in both runs. This lack of reversibility of β-In_2S_3 from pressures beyond 40 GPa does not match with the reversibility observed by HP electrical measurements up to 41.6 GPa.[40] Therefore, we can conclude that the different PTMs used and the compression/decompression rates seem to provide different conditions that influence in the reversibility of the pressure-induced PTs in β-In_2S_3.

It must be stressed that the two observed PTs we have observed up to 20 GPa seem to be reversible under suitable conditions. The reversibility of pressure-induced PTs was also found in AIn_2S_4 thiospinels,[72] but not in pseudocubic $CdIn_2Se_4$.[94] The reversibility of the pressure-induced PTs of β-In_2S_3 is very interesting since α-In_2S_3 is a metastable phase at ambient conditions, which is even sold by Sigma Aldrich company, and it could be potentially retained upon decompression from pressures above 12 GPa (once the PT to the 2nd HP phase of β-In_2S_3 is completed). As already commented, the β phase was not recovered on decreasing pressure from 43.0 GPa in **Ref. 41**; however, the Raman spectrum at ambient pressure of our commercial α-In_2S_3 sample (**Fig. S4b)**) and that obtained at ambient pressure on downstroke in **Ref. 41** are rather similar. Both show a broad band between 150 and 380 cm^{-1} that has a maximum near 300 cm^{-1} and two shoulders near 200 and 350 cm^{-1}. Therefore, we think that the sample recovered from 43.0 GPa in **Ref. 41** corresponds to a very disordered or amorphous α-In_2S_3 structure. We consider that this recovered sample has disorder also at anion sites because the bands near 300 and 350 cm^{-1}, corresponding to S vibrations, are much broader in the Raman spectrum of the recovered sample in **Ref. 41** than in the Raman spectrum of commercial α-In_2S_3. Therefore, we can conclude that the pressure-induced PTs of β-In_2S_3 are reversible from 20 GPa, but are not reversible from 40 GPa. In the last case, a disordered or amorphous α phase can be recovered, which is in good agreement with the nature of the 1st HP phase of β-In_2S_3 we have reported.

Finally, we want to comment that this work has complemented previous HP works on $B^{III}{}_2X^{V}{}_3$ and $A^{II}B^{III}{}_2X^{VI}{}_4$ compounds and has found a new nexus between thiospinels and tetrahedrally-coordinated OVCs of these two families of compounds. In particular, it has been found that thiospinels undergo pressure-induced order-

disorder PTs either to the defect NaCl structure (typical of *AX* compounds and tetrahedrally-coordinated OVCs), like $CdAl_2S_4$,[93] or to defect $LiTiO_2$ and defect α-$NaFeO_2$ structures (two distorted NaCl-type structures typical of ABX_2 compounds), like thiospinel AIn_2S_4 compounds (A= Cd, Mg, and Mn)[72] and In_2S_3, respectively.

In any case, the previous statement is far from being completely proved and more studies need to be conducted. For instance, on the basis of HP-RS measurements, $ZnAl_2S_4$ thiospinel has been proposed to undergo a PT towards the $CaFe_2O_4$ structure, as many oxospinels.[104] On the other hand, an alternative sequence of pressure-induced PTs related to corundum has been recently predicted for Al_2S_3 up to 200 GPa.[105] In particular, a PT from the tetragonal defect spinel ($I4_1/amd$) to corundum (R-3c) and then to the *Pbcn* structure of In_2O_3 at HP[106] have been proposed for Al_2S_3. Therefore, this work prompts to carry out HP-XRD measurements on Al_2S_3 and spinel $ZnAl_2S_4$ to prove whether the post-spinel phase of these thiospinels is a defect NaCl-related phase, a $CaFe_2O_4$ phase, or a corundum-type phase.

4. CONCLUSIONS

We have revisited the pressure behavior of β-In_2S_3 with tetragonal defect spinel structure using HP-XRD and HP-RS measurements. Our measurements have been supported by *ab* initio calculations to evaluate the effect of pressure on the stability of this interesting OVC. As a result, we have observed two pressure-induced PTs above 5.0 and 10.5 GPa, respectively. The 1st PT is a first-order PT characterized by a 3.3% decrease of the relative volume per formula unit and corresponds to the order-disorder β-α PT. The 2nd PT is a first-order PT characterized by a 2.0% decrease of the relative volume per formula unit and corresponds to the α → φ PT. Curiously, the α phase (cubic spinel) exhibits a lower bulk modulus than the β phase due to the larger fraction of vacancies in the volume per formula unit in the α than in the β phase. Furthermore, this disorder also explains the smaller bulk modulus of α-In_2S_3 than those of isostructural AIn_2S_4 thiospinels (*A*=Cd, Mg, Mn).

After an extensive search through phases of materials with *AX*, ABX_2, B_2X_3 and AB_2X_4 composition, we have proposed that the 2nd HP phase of β-In_2S_3 (φ-In_2S_3) has the defect α-$NaFeO_2$-type structure. This structure is a derivative of the NaCl-type structure typical of ABX_2 compounds. This is the first time that this structure has been found as a post-spinel phase, to our knowledge. φ-In_2S_3 is less compressible than β- and α-In_2S_3 because it has vacancies in octahedrally coordinated positions that are less compressible than vacancies in tetrahedrally coordinated sites, as it occurs in β- and α-In_2S_3.

From the vibrational perspective, the β → α PT is characterized by an abrupt change in the Raman spectra. A decrease in the number of peaks, a considerable broadening of the peaks, and a much smaller Raman intensity were observed. On the other hand, the α-ϕ PT is characterized by a reduction in the number of broad bands from 8 to 2 and further decrease of the Raman intensity. Thanks to our lattice-dynamic calculations and their good agreement with our experimental results, we have tentatively assigned the symmetry of the experimentally observed Raman modes of the β phase. Moreover, we have assigned the symmetry of the experimentally

observed Raman modes of the α phase by comparison with the calculated Raman-, IR-, and silent-active modes of isostructural $CdIn_2S_4$ as an approach to α-In_2S_3. Similarly, we have assigned the symmetry of the experimentally observed Raman modes of the φ phase by comparing them with the calculated Raman-active modes of isostructural $NaInS_2$ as an approach to φ-In_2S_3. Moreover, our identification of the α phase as the 1st HP phase of β-In_2S_3 is supported by the comparison of the XRD and RS measurements of commercial α-In_2S_3 powder samples at ambient pressure.

As regards the reversibility of the pressure-induced PTs, both our HP-XRD and HP-RS measurements show the reversibility of the changes induced by applying pressure on β-In_2S_3 up to 21 GPa. Moreover, we have shown that previous HP measurements on β-In_2S_3 up to 40 GPa are consistent with the recovery of strongly disordered or amorphous α-In_2S_3 at ambient pressure. In summary, the present work proposes for the first time: i) that α-In_2S_3 is accessible from the stable β phase not only by HT or by varying composition, but also at HP, and that it can be recovered from HP experiments under suitable conditions, and ii) that a defect α-$NaFeO_2$-type structure can be another post-spinel phase in thiospinels.

Finally, we have shown that our present work represents an important complement to previous HP works in thiospinels. In particular, we have evidenced that many cubic group-13 thiospinels undergo pressure-induced phase transitions to defect NaCl related structures (defect $LiTiO_2$ and defect α-$NaFeO_2$), which are typical of *AX* and ABX_2 compounds (with the same number of cations and anions). Since pressure-induced PTs to the defect NaCl structure are common in tetrahedrally-coordinated OVCs, our work suggests that group-13 thiospinels with $B^{III}{}_2X^{VI}{}_3$ and $A^{II}B^{III}{}_2X^{VI}{}_4$ (with a group-2 or group-12 *A* cation) compositions show a pressure behavior closer to tetrahedrally OVCs than to oxospinels or thiospinels with transition metals. In summary, this work paves the way to better understand the behaviour under pressure of compounds with $B^{III}{}_2X^{VI}{}_3$ and $A^{II}B^{III}{}_2X^{VI}{}_4$ composition. We hope this work will stimulate HP-XRD measurements on Al_2S_3 and spinel $ZnAl_2S_4$ that will be important to validate the hypothesis here stated and get a more complete picture of pressure-induced PTs in thiospinels.

5. AUTHOR CONTRIBUTIONS

F. J. M. and O. G. conceived the project. S. G.-P., O. G. and F. J. M. planned and organized experiments. S. G.-P. analysed the data. Concerning the experimental part, HP-XRD measurements were carried out by R. V., V. P. C.-G, C. P. and F. J. M.; HP-Raman measurements by S. G.-P. Concerning the theoretical part, the total-energy and lattice dynamics DFT calculations were performed by P. R.-H. and A. M., meanwhile the minima hopping and evolutionary genetic methods for the structural search were performed by A. R., A.M. and R. A. The first manuscript draft was prepared by S. G.-P. The authors reviewed the manuscript and participated actively in the discussion of the results.

6. CONFLICTS OF INTEREST

There are no conflicts to declare.

7. ACKNOWLEDGMENTS

The authors thank the financial support from Spanish Research Agency (AEI) under projects MALTA Consolider Team network (RED2018-102612-T) and projects PID2019-106383GB-41/42/43, as well as from Generalitat Valenciana under Project PROMETEO/2018/123 (EFIMAT) and the support from the US agencies under projects DMREF-NSF 1434897, and DOE DE-SC0016176. A. M., and P. R.-H acknowledge computing time provided by Red Española de Supercomputación (RES) and MALTA-Cluster, and we also thank ALBA synchrotron light source for funded experiment 2017022088 at the MSPD-BL04 beamline. A.H.R. acknowledges the computational resources awarded by XSEDE, a project supported by National Science Foundation grant number ACI-1053575, as well as the time from the Super Computing System (Thorny Flat) at WVU, which is funded in part by the National Science Foundation (NSF) Major Research Instrumentation Program (MRI) Award #1726534, and West Virginia University. The authors also acknowledge the support from the Texas Advances Computer Center (with the Stampede2 and Bridges supercomputers). A.M. and R.A acknowledge the support from Olle Engkvists stiftelse, Sweden, Carl Tryggers Stiftelse for Vetenskaplig Forskning (CTS) and the Swedish Research Council (Grant no. VR-2016-06014 and VR-2020-04410). SNIC and HPC2N are also acknowledged for providing computing resources.

Notes

* Corresponding authors: sagalpar@doctor.upv.es (S. G. -P.) and osgohi@fis.upv.es (O. G.).

8. REFERENCES

1. N. Naghavi, S. Spiering, M. Powalla, B. Cavana and D. Lincot, *Progress in Photovoltaics: Research and Applications*, 2003, **11**, 437-443.
2. D. Hariskos, S. Spiering and M. Powalla, *Thin Solid Films*, 2005, **480**, 99-109.
3. N. Allsop, A. Schönmann, H. J. Muffler, M. Bär, M. C. Lux‐Steiner and C. H. Fischer, *Progress in Photovoltaics: Research and Applications*, 2005, **13**, 607-616.
4. S. Rasool, K. Saritha, K. R. Reddy, M. Tivanov, A. Trofimova, S. Tikoto, L. Bychto, A. Patryn, M. Maliński and V. Gremenok, *Current Applied Physics*, 2019, **19**, 108-113.
5. N. Barreau, *Solar Energy*, 2009, **83**, 363-371.
6. S.-H. Choe, T.-H. Bang, N.-O. Kim, H.-G. Kim, C.-I. Lee, M.-S. Jin, S.-K. Oh and W.-T. Kim, *Semiconductor science and technology*, 2001, **16**, 98.
7. P. Rao and S. Kumar, *Thin Solid Films*, 2012, **524**, 93-99.
8. Y. X. Chen, A. Yamamoto and T. Takeuchi, *J. Alloys Compd.*, 2017, **695**, 1631-1636.
9. Y. X. Chen, K. Kitahara and T. Takeuchi, *J. Appl. Phys.*, 2015, **118**, 245103.
10. J. Zhang, H. Wang, X. Yuan, G. Zeng, W. Tu and S. Wang, *Journal of Photochemistry and Photobiology C: Photochemistry Reviews*, 2019, **38**, 1-26.
11. L. Wang, S. K. Karuturi and L. Zan, *Applied Surface Science*, 2020, 148063.
12. K. Hara, K. Sayama and H. Arakawa, *Solar Energy Materials and Solar Cells*, 2000, **62**, 441-447.
13. N. Barreau, C. Deudon, A. Lafond, S. Gall and J. Kessler, *Solar energy materials and solar cells*, 2006, **90**, 1840-1848.
14. X. Fu, X. Wang, Z. Chen, Z. Zhang, Z. Li, D. Y. Leung, L. Wu and X. Fu, *Applied Catalysis B: Environmental*, 2010, **95**, 393-399.
15. C.-H. Ho, M.-H. Lin, Y.-P. Wang and Y.-S. Huang, *Sens. Actuators, A*, 2016, **245**, 119-126.
16. W. Huang, L. Gan, H. Yang, N. Zhou, R. Wang, W. Wu, H. Li, Y. Ma, H. Zeng and T. Zhai, *Adv. Funct. Mater.*, 2017, **27**, 1702448.
17. H. Hahn and W. Klingler, *Z. anorg. Chem.*, 1949, **260**, 97-109.
18. C. Adenis, J. Olivier-Fourcade, J.-C. Jumas and E. Philippot, *Revue de chimie minérale*, 1987, **24**, 10-21.
19. G. King, *Acta Crystallogr.*, 1962, **15**, 512-512.
20. G. Steigmann, H. Sutherland and J. Goodyear, *Acta Crystallogr.*, 1965, **19**, 967-971.
21. N. S. Rampersadh, A. M. Venter and D. G. Billing, *Phys. B*, 2004, **350**, E383-E385.
22. P. Donohue, *J. Solid State Chem.*, 1970, **2**, 6-8.
23. K.-J. Range and H.-J. Hübner, *Z. Naturforsch., B*, 1973, **28**, 353-355.
24. J. Van Landuyt, H. Hatwell and S. Amelinckx, *Mater. Res. Bull.*, 1968, **3**, 519-528.
25. R. Diehl and R. Nitsche, *J. Cryst. Growth*, 1975, **28**, 306-310.

26. P. Pistor, J. M. Merino Álvarez, M. León, M. Di Michiel, S. Schorr, R. Klenk and S. Lehmann, *Acta Crystallogr., Sect. B: Struct. Sci., Cryst. Eng. Mater.*, 2016, **72**, 410-415.
27. H. Schäfer, G. Schäfer and A. Weiss, *Z. anorg. allg. Chem.*, 1963, **325**, 77-88.
28. P. Wyżga, W. Carrillo-Cabrera, L. Akselrud, I. Veremchuk, J. Wagler, C. Hennig, A. A. Tsirlin, A. Leithe-Jasper, E. Kroke and R. Gumeniuk, *Dalton Trans.*, 2020, **49**, 15903-15913.
29. A. Lafond, X. Rocquefelte, M. Paris, C. Guillot-Deudon and V. Jouenne, *Chem. Mater.*, 2011, **23**, 5168-5176.
30. P. Wyżga, I. Veremchuk, C. Himcinschi, U. Burkhardt, W. Carrillo-Cabrera, M. Bobnar, C. Hennig, A. Leithe-Jasper, J. Kortus and R. Gumeniuk, *Dalton Trans.*, 2019, **48**, 8350-8360.
31. P. Wyżga, S. Grimm, V. Garbe, E. Zuñiga-Puelles, C. Himcinschi, I. Veremchuk, A. Leithe-Jasper and R. Gumeniuk, *J. Mater. Chem. C*, 2021, **9**, 4008-4019.
32. R. Diehl and R. Nitsche, *J. Cryst. Growth*, 1973, **20**, 38-46.
33. R. Diehl, C. D. Carpentier and R. Nitsche, *Acta Crystallogr., Sect. B: Struct. Crystallogr. Cryst. Chem.*, 1976, **32**, 1257-1260.
34. A. Likforman and M. Guittard, *Comptes Rendus des Séances de l'Académie des Sciences–Paris, Série C*, 1974, **279**, 33.
35. K. J. Range and M. Zabel, *Z. Naturforsch., B*, 1978, **33**, 463-464.
36. J. Flahaut, Contribution à l'étude du sulfure d'aluminium et des thioaluminates, University of Mason, 1952.
37. X. Lai, F. Zhu, Y. Wu, R. Huang, X. Wu, Q. Zhang, K. Yang and S. Qin, *J. Solid State Chem.*, 2014, **210**, 155-159.
38. B. Yao, H. Zhu, S. Wang, P. Wang and M. Zhang, *J. Solid State Chem.*, 2014, **210**, 150-154.
39. Y. Li, Q. Wang, Y. Gao, B. Liu, C. Gao and Y. Ma, *Mater. Res. Express*, 2017, **4**, 085902.
40. Y. Li, Y. Gao, N. Xiao, P. Ning, L. Yu, J. Zhang, P. Niu, Y. Ma and C. Gao, *AIP Advances*, 2018, **8**, 115202.
41. K. Liu, L. Dai, H. Li, H. Hu, L. Yang, C. Pu and M. Hong, *Chem. Phys.*, 2019, **524**, 63-69.
42. F. Manjón, R. Vilaplana, O. Gomis, E. Pérez‐González, D. Santamaría‐Pérez, V. Marín‐Borrás, A. Segura, J. González, P. Rodríguez‐Hernández and A. Muñoz, *phys. status solidi (b)*, 2013, **250**, 669-676.
43. S. Klotz, J. C. Chervin, P. Munsch and G. Le Marchand, *J. Phys. D: Appl. Phys.*, 2009, **42**, 075413.
44. D. Errandonea, A. Muñoz and J. Gonzalez-Platas, *J. Appl. Phys.*, 2014, **115**, 216101.
45. F. Fauth, I. Peral, C. Popescu and M. Knapp, *Powder Diffr.*, 2013, **28**, S360-S370.
46. A. Dewaele, P. Loubeyre and M. Mezouar, *Phys. Rev. B*, 2004, **70**, 094112.
47. C. Prescher and V. B. Prakapenka, *High Pressure Res.*, 2015, **35**, 223-230.
48. B. H. Toby and R. B. Von Dreele, *J. Appl. Crystallogr.*, 2013, **46**, 544-549.

49. H. K. Mao, J. A. Xu and P. M. Bell, *J. Geophys. Res.: Solid Earth*, 1986, **91**, 4673-4676.
50. A. Debernardi, C. Ulrich, M. Cardona and K. Syassen, *phys. status solidi (b)*, 2001, **223**, 213-223.
51. B. Garcia-Domene, H. Ortiz, O. Gomis, J. Sans, F. Manjón, A. Muñoz, P. Rodríguez-Hernández, S. Achary, D. Errandonea and D. Martínez-García, *J. Appl. Phys.*, 2012, **112**, 123511.
52. P. Hohenberg and W. Kohn, *Physical review*, 1964, **136**, B864-B871.
53. G. Kresse and J. Hafner, *Phys. Rev. B*, 1993, **47**, 558-561.
54. P. E. Blöchl, *Phys. Rev. B*, 1994, **50**, 17953-17979.
55. G. Kresse and D. Joubert, *Phys. Rev. B*, 1999, **59**, 1758-1775.
56. J. P. Perdew, A. Ruzsinszky, G. I. Csonka, O. A. Vydrov, G. E. Scuseria, L. A. Constantin, X. Zhou and K. Burke, *Phys. Rev. Lett.*, 2008, **100**, 136406.
57. H. J. Monkhorst and J. D. Pack, *Phys. Rev. B*, 1976, **13**, 5188.
58. Computer Code Phonon, see: http://www.computingformaterials.com/index.html).
59. M. Amsler and S. Goedecker, *J. Chem. Phys.*, 2010, **133**, 224104.
60. S. Goedecker, *J. Chem. Phys.*, 2004, **120**, 9911-9917.
61. A. R. Oganov and C. W. Glass, *J. Chem. Phys.*, 2006, **124**, 244704.
62. A. R. Oganov, A. O. Lyakhov and M. Valle, *Accounts of chemical research*, 2011, **44**, 227-237.
63. A. R. Oganov, Y. Ma, A. O. Lyakhov, M. Valle and C. Gatti, *Reviews in Mineralogy and Geochemistry*, 2010, **71**, 271-298.
64. A. O. Lyakhov, A. R. Oganov, H. T. Stokes and Q. Zhu, *Computer Physics Communications*, 2013, **184**, 1172-1182.
65. P. V. Bushlanov, V. A. Blatov and A. R. Oganov, *Computer Physics Communications*, 2019, **236**, 1-7.
66. K. Okhotnikov, T. Charpentier and S. Cadars, *J. Cheminf.*, 2016, **8**, 1-15.
67. S. Gallego-Parra, R. Vilaplana, O. Gomis, E. L. da Silva, A. Otero-de-la-Roza, P. Rodríguez-Hernández, A. Muñoz, J. González, J. Sans and V. Cuenca-Gotor, *Phys. Chem. Chem. Phys.*, 2021, **23**, 6841-6862.
68. M. Takumi, Y. Koshio and K. Nagata, *phys. status solidi (b)*, 1999, **211**, 123-129.
69. R. Vilaplana, S. G. Parra, A. Jorge-Montero, P. Rodríguez-Hernández, A. Munoz, D. Errandonea, A. Segura and F. J. Manjón, *Inorg. Mater.*, 2018, **57**, 8241-8252.
70. J. L. Da Silva, A. Walsh and H. Lee, *Phys. Rev. B*, 2008, **78**, 224111.
71. K.-J. Range, W. Becker and A. Weiss, *Z. Naturforsch., B*, 1968, **23**, 1009 - 1009.
72. D. Santamaría-Pérez, M. Amboage, F. Manjón, D. Errandonea, A. Muñoz, P. Rodríguez-Hernández, A. Mújica, S. Radescu, V. Ursaki and I. Tiginyanu, *J. Phys. Chem. C*, 2012, **116**, 14078-14087.
73. L. Gerward, J. S. Olsen and U. Benedict, *Physica B+C*, 1986, **144**, 72-78.
74. R. Hoppe, W. Lidecke and F. C. Frorath, *Z. anorg. allg. Chem.*, 1961, **309**, 49-54.

75. K.-J. Range, M. Keubler and A. Weiss, *Z. Naturforsch., B*, 1969, **24**, 1060-1061.
76. W. Schanow and K.-J. Range, *Mater. Res. Bull.*, 1983, **18**, 39-44.
77. H. Beister, S. Ves, W. Hönle, K. Syassen and G. Kühn, *Phys. Rev. B*, 1991, **43**, 9635.
78. P. Brüesch and C. Schüler, *J. Phys. Chem. Solids*, 1971, **32**, 1025-1038.
79. G. C. Mather, C. Dussarrat, J. Etourneau and A. R. West, *J. Mater. Chem.*, 2000, **10**, 2219-2230.
80. H. Porthault, R. Baddour-Hadjean, F. Le Cras, C. Bourbon and S. Franger, *Vibrational Spectroscopy*, 2012, **62**, 152-158.
81. M. M. Rahman, W.-Y. Chen, L. Mu, Z. Xu, Z. Xiao, M. Li, X.-M. Bai and F. Lin, *Nat. Commun.*, 2020, **11**, 1-13.
82. J. Dismukes and J. White, *Inorg. Mater.*, 1964, **3**, 1220-1228.
83. M. Onoda and M. Saeki, *Chem. Lett.*, 1980, **9**, 665-666.
84. F. K. McTaggart and A. Wadsley, *Aust. J. Chem.*, 1958, **11**, 445-457.
85. K. Kambas, J. Spyridelis and M. Balkanski, *phys. status solidi (b)*, 1981, **105**, 291-296.
86. P. Pistor, R. Caballero, D. Hariskos, V. Izquierdo-Roca, R. Wächter, S. Schorr and R. Klenk, *Solar Energy Materials and Solar Cells*, 2009, **93**, 148-152.
87. E. Kärber, K. Otto, A. Katerski, A. Mere and M. Krunks, *Materials Science in Semiconductor Processing*, 2014, **25**, 137-142.
88. S. Gallego-Parra, O. Gomis, R. Vilaplana, H. M. Ortiz, E. Perez-Gonzalez, R. Luna, P. Rodríguez-Hernández, A. Muñoz, V. Ursaki and I. Tiginyanu, *J. Appl. Phys.*, 2019, **125**, 115901.
89. R. Vilaplana, M. Robledillo, O. Gomis, J. A. Sans, F. J. Manjón, E. Pérez-González, P. Rodríguez-Hernández, A. Muñoz, I. M. Tiginyanu and V. V. Ursaki, *J. Appl. Phys.*, 2013, **113**, 093512.
90. R. Vilaplana, O. Gomis, E. Pérez-González, H. M. Ortiz, F. J. Manjón, P. Rodríguez-Hernández, A. Munoz, P. Alonso-Gutiérrez, M. L. Sanjuán, V. V. Ursaki and I. M. Tiginyanu, *J. Appl. Phys.*, 2013, **113**, 233501.
91. O. Gomis, R. Vilaplana, F. J. Manjón, E. Pérez-González, J. López-Solano, P. Rodríguez-Hernández, A. Muñoz, D. Errandonea, J. Ruiz-Fuertes, A. Segura, D. Santamaria-Pérez, I. M. Tiginyanu and V. Ursaki, *J. Appl. Phys.*, 2012, **111**, 013518.
92. R. Vilaplana, O. Gomis, F. J. Manjón, H. M. Ortiz, E. Pérez-González, J. López-Solano, P. Rodríguez-Hernández, A. Muñoz, D. Errandonea, V. V. Ursaki and I. M. Tiginyanu, *J. Phys. Chem. C*, 2013, **117**, 15773-15781.
93. J. A. Sans, D. Santamaría-Pérez, C. Popescu, O. Gomis, F. J. Manjón, R. Vilaplana, A. Muñoz, P. Rodríguez-Hernández, V. V. Ursaki and I. M. Tiginyanu, *J. Phys. Chem. C*, 2014, **118**, 15363-15374.
94. D. Santamaria-Perez, O. Gomis, A. L. Pereira, R. Vilaplana, C. Popescu, J. A. Sans, F. J. Manjón, P. Rodriguez-Hernandez, A. Muñoz and V. V. Ursaki, *J. Phys. Chem. C*, 2014, **118**, 26987-26999.
95. P. Canepa, R. M. Hanson, P. Ugliengo and M. Alfredsson, *J. Appl. Crystallogr.*, 2011, **44**, 225-229.

96. E. Kroumova, M. Aroyo, J. Perez-Mato, A. Kirov, C. Capillas, S. Ivantchev and H. Wondratschek, *Phase Transitions: A Multinational Journal*, 2003, **76**, 155-170.
97. H. Lutz, W. Becker, B. Müller and M. Jung, *J. Raman Spectrosc.*, 1989, **20**, 99-103.
98. V. Ursaki, F. Manjón, I. Tiginyanu and V. Tezlevan, *J. Phys.: Condens. Matter*, 2002, **14**, 6801.
99. B. Weinstein, *Phys. Rev. B*, 2021, **104**, 054105.
100. Y. Sim, J. Kim and M.-J. Seong, *J. Alloys Compd.*, 2016, **685**, 518-522.
101. H. Izadneshana and V. Gremenok, *Journal of Applied Spectroscopy*, 2014, **81**, 765-770.
102. V. F. Gremenok, K. Ramakrishna Reddy, M. S. Tivanov and A. Patryn, 2017, **93**, 89-91.
103. R. Souissi, N. Bouguila, M. Bendahan, T. Fiorido, K. Aguir, M. Kraini, C. Vázquez-Vázquez and A. Labidi, *Sens. Actuators, B*, 2020, **319**, 128280.
104. V. V. Ursaki and I. M. Tiginyanu, in *Pressure-induced phase transitions in AB_2X_4 chalcogenide compounds*, eds. F.J. Manjón, I. Tiginyanu and V. Ursaki, Springer, 2014, ch. 213-235.
105. S. Shao, W. Zhu, J. Lv, Y. Wang, Y. Chen and Y. Ma, *npj Comput. Mater.*, 2020, **6**, 1-6.
106. B. García-Domene, J. Sans, O. Gomis, F. Manjón, H. Ortiz, D. Errandonea, D. Santamaría-Pérez, D. Martínez-García, R. Vilaplana and A. Pereira, *J. Phys. Chem. C*, 2014, **118**, 20545-20552.

Supplementary Information of

Pressure-induced order-disorder transitions in β-In_2S_3: an experimental and theoretical study of structural and vibrational properties

Samuel Gallego-Parra,[1*] Óscar Gomis,[2*] Rosario Vilaplana,[2] Vanesa Paula Cuenca-Gotor,[1] Domingo Martínez-García,[3] Plácida Rodríguez-Hernández,[4] Alfonso Muñoz,[4] Aldo Romero,[5] Arnab Majumdar,[6,7] Rajeev Ahuja,[6,8] Catalin Popescu[9] and Francisco Javier Manjón[1]

[1]*Instituto de Diseño para la Fabricación y Producción Automatizada, MALTA Consolider Team, Universitat Politècnica de València, 46022 València, Spain*
[2]*Centro de Tecnologías Físicas, MALTA Consolider Team, Universitat Politècnica de València, 46022 València, Spain*
[3]*Departamento de Física Aplicada-ICMUV-MALTA Consolider Team, Universitat de València, c/Dr. Moliner 50, 46100 Burjassot (València), Spain*
[4]*Departamento de Física, Instituto de Materiales y Nanotecnología, MALTA Consolider Team, Universidad de La Laguna, 38207 San Cristóbal de La Laguna, Spain*
[5]*Physics Department, West Virginia University, Morgantown, 26505, USA*
[6]*Department of Physics and Astronomy, Box 516, Uppsala University, Uppsala, SE-75120, Sweden*
[7]*Département de Physique and Regroupement Québécois sur les Matériaux de Pointe, Université de Montréal, C. P. 6128, Succursale Centre-Ville, Montréal, Québec H3C 3J7, Canada*
[8]*Department of Physics, Indian Institute of Technology Ropar, Rupnagar 140001, Punjab, India*
[9]*ALBA-CELLS, MALTA Consolider Team, 08290 Cerdanyola del Valles (Barcelona), Catalonia, Spain*

*Corresponding authors: S. Gallego-Parra (sagalpar@doctor.upv.es), O. Gomis (osgohi@fis.upv.es)

Figure S1. Theoretical pressure dependence of the unit cell volume of β-In_2S_3 and the polyhedral volumes corresponding to the InS_4 and vacancy tetrahedra, $VacS_4$, (8e and 4a sites) and InS_6 octahedra (8c and 16h sites).

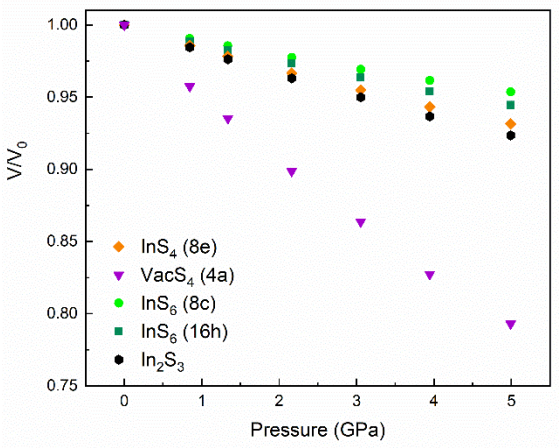

Figure S2. Theoretical pressure dependence of the interatomic distances in β-In_2S_3, corresponding to a) InS_4 and b) vacancy tetrahedra, $VacS_4$, (8e and 4a sites), c) and d) InS_6 octahedra (8c and 16h sites, respectively).

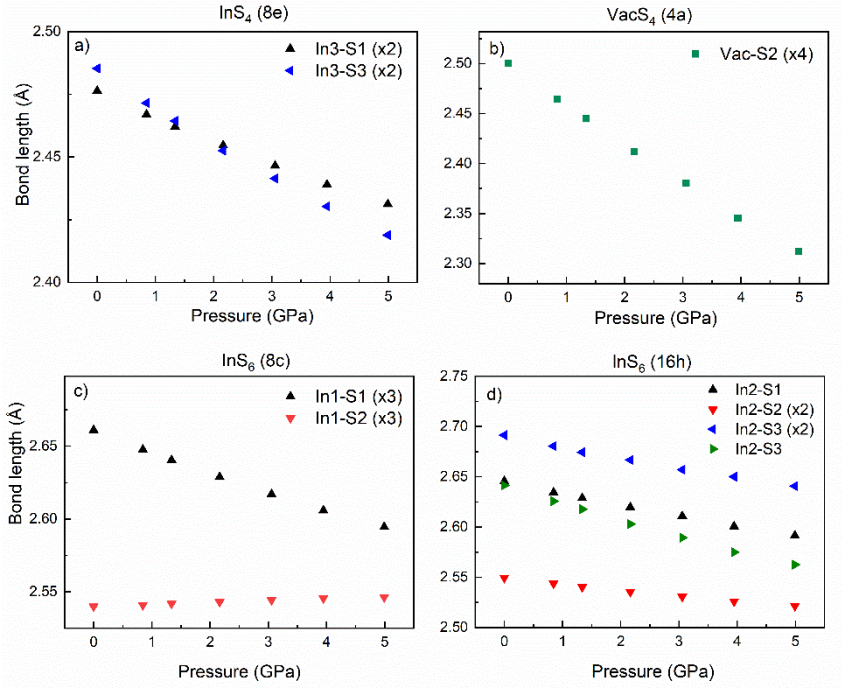

Figure S3. Theoretical pressure dependence of a) the effective coordination number (ECoN), b) bond angle variance (σ^2), c) quadratic elongation (λ) and d) distortion index (D) corresponding to InS_4 and vacancy tetrahedra, $VacS_4$, (8e and 4a sites), and InS_6 octahedra (8c and 16h sites).

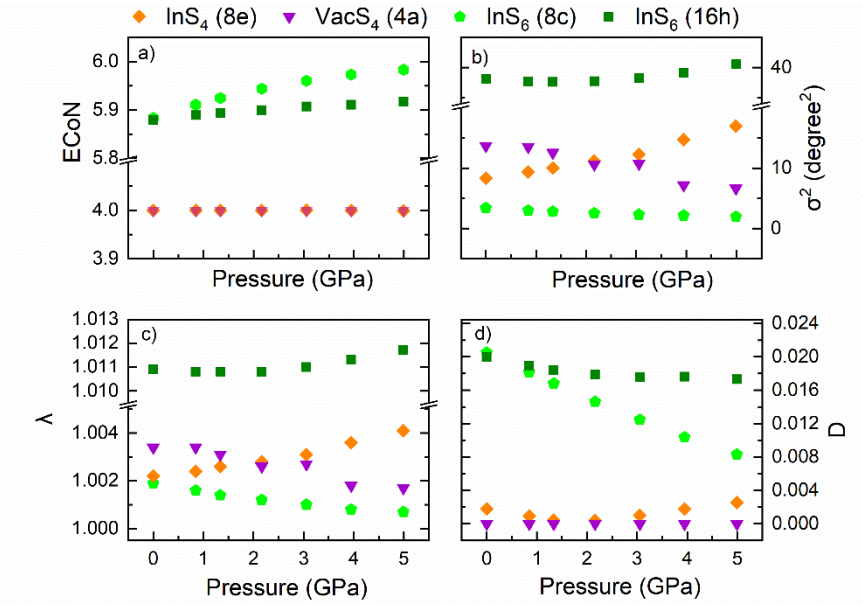

Figure S4. Commercial α-In_2S_3 powders of Sigma Aldrich at room pressure: (a) Le Bail refinement of the XRD pattern with the cubic spinel structure and (b) RS spectrum. Theoretical zero pressure frequencies of Raman-, IR-active, and silent modes of $CdIn_2S_4$ at room pressure are given by ticks.

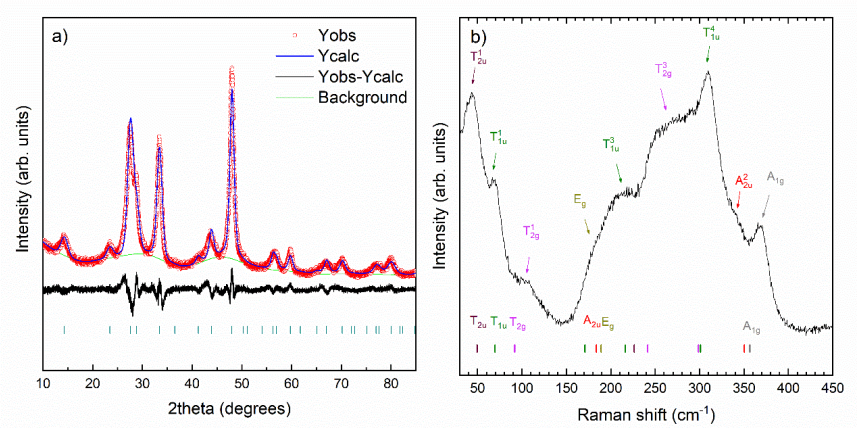

Figure S5. Theoretical one-phonon density of states of a) β-In_2S_3 and b) $CdIn_2S_4$ at room pressure.

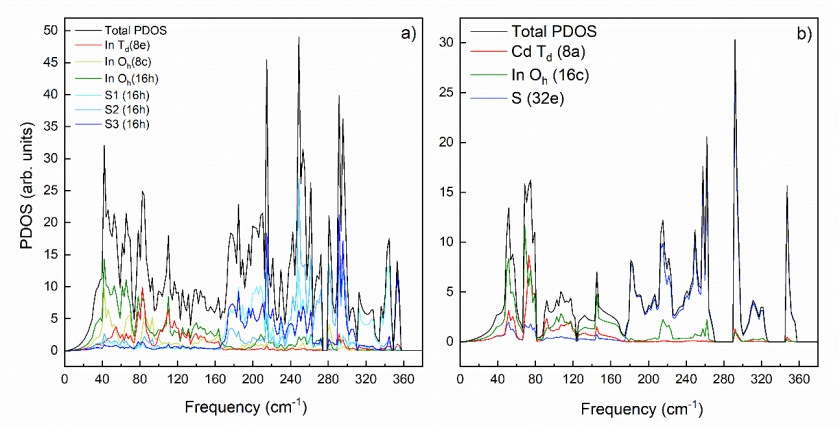

Figure S6. a) Theoretical volume dependence of the energy of β and ϕ-In_2S_3 and b) theoretical pressure dependence of the enthalpy difference between β and ϕ-In_2S_3. Enthalpy of β-In_2S_3 is taken as reference.

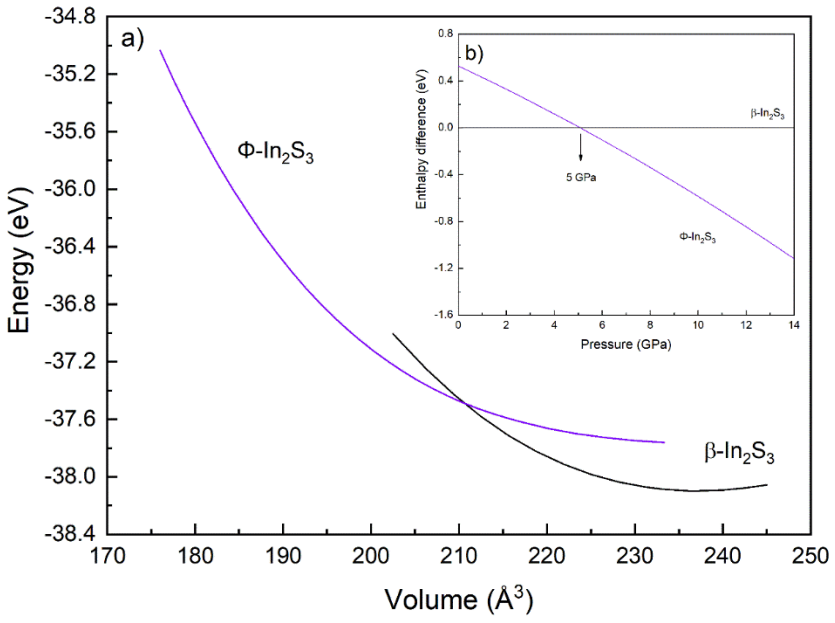

CHEMISTRY OF MATERIALS

pubs.acs.org/cm Article

High-Pressure Synthesis of β- and α-In_2Se_3-Like Structures in Ga_2S_3

Samuel Gallego-Parra,* Rosario Vilaplana,* Oscar Gomis, Plácida Rodríguez-Hernández, Alfonso Muñoz, Jesus Antonio González, Juan Angel Sans, Catalin Popescu, and Francisco Javier Manjón

Cite This: *Chem. Mater.* 2022, 34, 6068−6086 Read Online

ACCESS | Metrics & More | Article Recommendations | Supporting Information

ABSTRACT: The synthesis of polymorphs of α'-Ga_2S_3 at room temperature on compression/decompression is studied from a joint experimental and theoretical point of view to reveal the nature of their crystalline structures. The results of Raman scattering and X-ray diffraction measurements on these polymorphs have been analyzed supported by theoretical *ab initio* simulations. On compression, α'-Ga_2S_3 undergoes a phase transition above 16 GPa to β'-Ga_2S_3 with a tetradymite-like (R-3m) structure, isostructural with β-In_2Se_3. On decompression, β'-Ga_2S_3 undergoes a phase transition below 9.0 GPa to φ-Ga_2S_3, which is isostructural with α-In_2Se_3 ($R3m$). Raman signatures of symmetry breaking as well as clear structural differences between the pressure dependence of the unit-cell volume per formula unit, zero-pressure axial compressibilities, bulk modulus, and their first pressure derivative between β'-Ga_2S_3 and φ-Ga_2S_3 have allowed us to determine the $R3m$ nature of φ-Ga_2S_3. The observation of the $R3m$ phase is also supported by theoretical total energy *ab initio* simulations. This result unveils a pressure-induced paraelectric-ferroelectric R-3m-to-$R3m$ transition, like the theoretically predicted temperature-induced transition in several III−VI B_2X_3 compounds, which could find use in technological applications. Finally, φ-Ga_2S_3 undergoes a phase transition below 1.0 GPa to γ-Ga_2S_3 with a disordered zincblende (F-43m) phase, isostructural with α-Ga_2Se_3 and remains metastable at room conditions. Since the disordered zincblende phase of Ga_2X_3 chalcogenides has also been found upon decompression in AGa_2X_4 chalcogenides, we discuss the relation between the pressure-induced phase transitions of both Ga_2X_3 and AGa_2X_4 compounds.

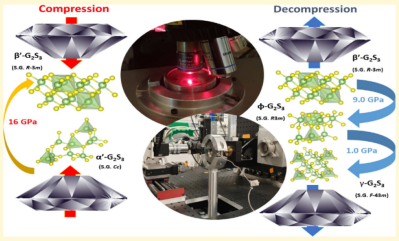

1. INTRODUCTION

Over the last years, many works have reported efforts to crystallize 2D layered structures at room conditions (RC) of the vacancy-disordered, nonlayered, and nonstoichiometric phases of Ga_2S_3 at high temperature (HT): (i) disordered zincblende (DZ)-like γ-Ga_2S_3 (cubic, space group (s.g.) F-43m, No. 216, Z = 2), at 1130−1180 K; (ii) α-Ga_2S_3 (hexagonal, s.g. $P6_1$, No. 161, Z = 6); and (iii) wurtzite-like β-Ga_2S_3 (hexagonal, s.g. $P6_3mc$, No. 186, Z = 1), both observed between 1190 and 1300 K.[1−3] To cite just a few examples, α-Ga_2S_3 has been obtained in large-size, 2D layered structures by chemical vapor deposition (CVD),[4] sulfurization,[5] and physical vapor deposition.[6,7] Additionally, 2D layers of γ-Ga_2S_3 have been grown via space-confined CVD,[8] air-spray annealing,[9] and sulfurizing epi-ready GaAs.[10] Even α'-Ga_2S_3 (monoclinic, s.g. Cc, No. 9, Z = 4 (Figure 1a), the stable polymorph at RC featuring ordered vacancies forming channels, has been obtained as 2D layered structures by gallium-based liquid metal synthesis,[11] exfoliation,[12] and pulsed-laser deposition (PLD),[13] among others. Notably, 2D layered structures with ordered vacancies (α'-Ga_2S_3) and disordered vacancies (γ, α, and β phases) allow conceiving abundant, nontoxic, and eco-friendly layers for a wide variety of applications: nano optoelectronics,[4] photonic chips,[12] electro-catalysis,[14] energy conversion and storage,[15,16] solar cells,[9] gas sensors,[11,17] laser-radiation detection,[10] and second harmonic generation (SHG).[5,8,17,18]

The above considerations also apply to other Ga-based sesquichalcogenides, like Ga_2Se_3 and Ga_2Te_3. The temperature phase diagram of Ga_2Se_3 shows at room pressure the low-temperature (LT) vacancy-ordered β-Ga_2Se_3 (monoclinic, s.g. Cc, No. 9, Z = 4, hereinafter called mono-β-Ga_2Se_3) and the DZ phase (Figure 1d) that has been obtained at LT (α-Ga_2Se_3) and at HT (γ-Ga_2Se_3).[19,20] Another phase that can be quenched depending on temperature and Ga/Se ratios is β-Ga_2Se_3 (orthorhombic, s.g. $Imm2$, No. 44, Z = 8,[21−25] hereinafter called ortho-β-Ga_2Se_3 (Figure S1) with a vacancy-ordered α-II-In_2Te_3-like structure. Mono-β-Ga_2Se_3 and ortho-β-Ga_2Se_3 differ in the short-range order, ordered zigzag vacancy lines, and (1 0 0) vacancy planes. The ortho phase has been predicted to be much less stable than the mono phase.[22,25,26] Regarding the DZ structure, the α (γ) structure of Ga_2Se_3 has been reported at LT

Received: April 18, 2022
Revised: June 6, 2022
Published: June 21, 2022

https://doi.org/10.1021/acs.chemmater.2c01169
Chem. Mater. 2022, 34, 6068−6086

High-pressure synthesis of β- and α-In_2Se_3-like structures in Ga_2S_3

Samuel Gallego-Parra[1]*, Rosario Vilaplana[2*], Oscar Gomis[2], Plácida Rodríguez-Hernández[3], Alfonso Muñoz[3], Jesus Antonio González[4], Juan Angel Sans[1], Catalin Popescu[5] and Francisco Javier Manjón[1]

[1]*Instituto de Diseño para la Fabricación y Producción Automatizada, MALTA Consolider Team, Universitat Politècnica de València, 46022 València, Spain*

[2] *Centro de Tecnologías Físicas, MALTA Consolider Team, Universitat Politècnica de València, 46022 Valencia, Spain*

[3]*Departamento de Física, Instituto de Materiales y Nanotecnología, MALTA Consolider Team, Universidad de La Laguna, 38207 San Cristóbal de La Laguna, Spain*

[4]*Ciencias de la Tierra y Fisica de la Materia Condensada, MALTA Consolider Team, Universidad de Cantabria, 39005, Santander, Spain*

[5]*ALBA-CELLS, MALTA Consolider Team, 08290 Cerdanyola del Valles (Barcelona), Spain*

*Corresponding authors: S. Gallego-Parra (sagalpar@doctor.upv.es), R. Vilaplana (rovilap@fis.upv.es)

ABSTRACT

The synthesis of polymorphs of α'-Ga_2S_3 at room temperature on compression/decompression is studied from a joint experimental and theoretical point of view to reveal the nature of their crystalline structures. The results of Raman scattering and X-ray diffraction measurements on these polymorphs have been analyzed supported by theoretical *ab initio* simulations. On compression, α'-Ga_2S_3 undergoes a phase transition above 16 GPa to β'-Ga_2S_3 with tetradymite-like (*R*-3*m*) structure, isostructural with β-In_2Se_3. On decompression, β'-Ga_2S_3 undergoes a phase transition below 9.0 GPa to φ-Ga_2S_3, which is isostructural with α-In_2Se_3 (*R*3*m*). Raman signatures of symmetry breaking as well as clear structural differences between the pressure dependence of the unit-cell volume per formula unit, zero-pressure axial compressibilities, bulk modulus and their first pressure derivative between β'-Ga_2S_3 and φ-Ga_2S_3 have allowed us to determine the *R*3*m* nature of φ-Ga_2S_3. The observation of the R3m phase is also supported by theoretical total energy *ab initio* simulations. This result unveils a pressure-induced paraelectric-ferroelectric *R*-3*m*-to-*R*3*m* transition, like the theoretically predicted temperature-induced transition in several III-VI B_2X_3 compounds, that could find use in technological applications. Finally, φ-Ga_2S_3 undergoes a phase transition below 1.0 GPa to γ-Ga_2S_3 with a disordered zincblende (*F*-43*m*) phase, isostructural with α-Ga_2Se_3 and remains metastable at room conditions. Since the disordered zincblende phase of Ga_2X_3 chalcogenides has also been found upon decompression in AGa_2X_4 chalcogenides, we discuss the relation between the pressure-induced phase transitions of both Ga_2X_3 and AGa_2X_4 compounds.

1. INTRODUCTION

Over the last years, many works have reported efforts to crystallize 2D layered structures at room conditions (RC) of the vacancy-disordered, non-layered, and non-stoichiometric phases of Ga_2S_3 at high temperature (HT): i) disordered zincblende (DZ)-like γ-Ga_2S_3 (cubic, space group (s.g.) F-43*m*, No. 216, Z=2), at 1130-1180 K; ii) α-Ga_2S_3 (hexagonal, s.g. $P6_1$, No. 161, Z=6); and iii) wurtzite-like β-Ga_2S_3 (hexagonal, s.g. $P6_3mc$, No. 186, Z=1), both observed between 1190 and 1300 K. [1-3] To cite just a few examples, α-Ga_2S_3 has been obtained in large-size, 2D layered structures by chemical vapor deposition (CVD),[4] sulfurization,[5] and physical vapor deposition.[6, 7] Additionally, 2D layers of γ-Ga_2S_3 have been grown via space-confined CVD,[8] air-spray annealing,[9] and sulfurizing epi-ready GaAs.[10] Even α'-Ga_2S_3 (monoclinic, s.g. *Cc*, No. 9, Z=4 (**Fig. 1a)**), the stable polymorph at RC featuring ordered vacancies forming channels, has been obtained as 2D layered structures by gallium-based liquid metal synthesis,[11] exfoliation,[12] and pulsed-laser deposition (PLD),[13] among others. Notably, 2D layered structures with ordered vacancies (α'-Ga_2S_3) and disordered vacancies (γ, α, and β phases) allow conceiving abundant, non-toxic, and eco-friendly layers for a wide variety of applications: nano optoelectronics,[4] photonic chips,[12] electrocatalysis,[14] energy conversion and storage,[15, 16] solar cells,[9] gas sensors,[11, 17] laser-radiation detection,[10] and second harmonic generation (SHG).[5, 8, 17, 18]

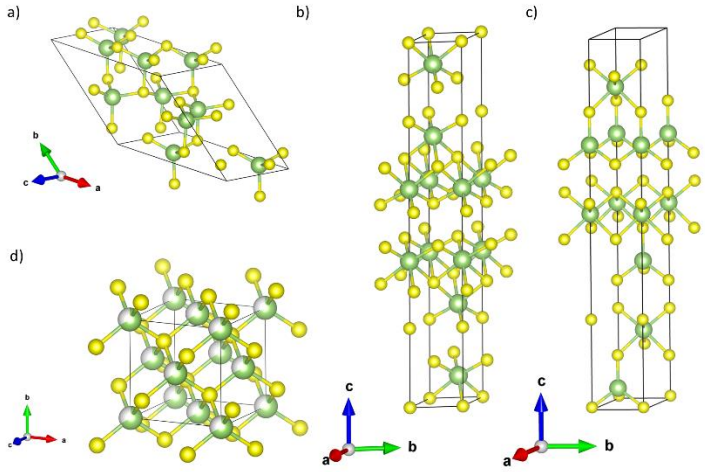

Figure 1. Representation of the structures of Ga_2X_3 compounds involved in this work. a) monoclinic α'-Ga_2S_3 (s.g. *Cc*, isostructural to mono-β-Ga_2Se_3 and mono-α-Ga_2Te_3), b) rhombohedral β'-Ga_2S_3 (s.g. *R*-3*m*, isostructural to β-In_2Se_3), c) rhombohedral φ-Ga_2S_3 (*R*3*m*, isostructural to α-In_2Se_3), and d) DZ γ-Ga_2S_3 (s.g. *F*-43*m*, isostructural to α-Ga_2Se_3 and β-Ga_2Te_3). Cations and anions are depicted as yellow and green spheres, respectively.

The above considerations also apply to other Ga-based sesquichalcogenides, like Ga_2Se_3 and Ga_2Te_3. The temperature phase diagram of Ga_2Se_3 shows at room pressure

the low-temperature (LT) vacancy-ordered β-Ga_2Se_3 (monoclinic, s.g. *Cc*, No. 9, Z=4, hereinafter called mono-β-Ga_2Se_3) and the DZ phase (**Fig. 1d)**) that has been obtained at LT (α-Ga_2Se_3) and at HT (γ-Ga_2Se_3).[19, 20] Another phase that can be quenched depending on temperature and Ga/Se ratios is β-Ga_2Se_3 (orthorhombic, s.g. *Imm*2, No. 44, Z=8,[21-25] hereinafter called ortho-β-Ga_2Se_3 (**Fig. S1**)) with vacancy-ordered α-II-In_2Te_3-like structure. Mono-β-Ga_2Se_3 and ortho-β-Ga_2Se_3 differ in the short-range order, ordered zig-zag vacancy lines, and (1 0 0) vacancy planes. The ortho phase has been predicted to be much less stable than the mono phase.[22, 25, 26] Regarding the DZ structure, the α (γ) structure of Ga_2Se_3 has been reported at LT (HT) with a lattice parameter of 5.4222 (5.463 Å).[26, 27] This result suggests that both phases are the same one, being the lattice parameter affected by thermal expansion. On the other hand, the temperature phase diagram of Ga_2Te_3 only shows β-Ga_2Te_3 with DZ structure.[28-30] However, α-Ga_2Te_3 (hereinafter, ortho-α-Ga_2Te_3) with vacancy-ordered α-II-In_2Te_3-like structure has been crystallized by varying Ga/Te ratios at HT.[31, 32]

Similarly to defective Ga_2S_3 phases, the defective non-layered phases of Ga_2Se_3 and Ga_2Te_3 have also been grown in 2D forms: mono-β-Ga_2Se_3 by chemical close-spaced vapour transport,[33, 34] low-pressure (LP) CVD[35] and sol-gel method;[36] α-Ga_2Se_3 by molecular beam epitaxy (MBE),[37, 38] thermal evaporation,[39] and heteroepitaxial growth;[40] and β-Ga_2Te_3 by LP CVD,[35, 41] direct synthesis,[42] and PLD.[43] These phases have been used in a number of applications, like in high-performance thermoelectric devices,[41, 44, 45] phase change memories,[35, 43, 46] radiation detectors,[25, 39] light emitters, [47, 48] solar-energy devices,[33, 47, 49] SHG,[50] and photocatalytic water splitting (PWS) systems.[51]

In an attempt to find additional structures in III-VI B_2X_3 (*B*=Al,Ga,In; *X*=S,Se,Te) sesquichalcogenides, recent theoretical works have conducted density functional theory (DFT) and molecular dynamics simulations to evaluate the stability and properties of non-centrosymmetric α-In_2Se_3 (hexagonal, s.g. *R*3*m*, No. 160, Z=3, **Fig. 1c**) and centrosymmetric β-In_2Se_3 (hexagonal, s.g. *R*-3*m*, No. 166, Z=3, **Fig. 1b**). This latter phase is isostructural with tetradymite-like V-VI sesquichalcogenides, Bi_2Se_3, Sb_2Te_3, and Bi_2Te_3, which are topological insulators at RC.[52] In this context, it is known that α-In_2Se_3 is stable at room temperature (RT)[53] and it undergoes a phase transition (PT) to β-In_2Se_3 at HT.[54-56] Curiously, the α-β PT sequence in In_2Se_3 differs at high pressure (HP) because of the presence of an intermediate β'-In_2Se_3 (monoclinic, s.g. *C*2/*m*, No. 12, Z=3) phase.[57, 58] Importantly, ferroelectricity in out-of-plane (OP) and in-plane (IP) polarizations was predicted for the *R*3*m* phase.[59] The optimal lattice parameters, electronic band structures, and dynamic stability of α- and β-In_2Se_3 as well as in their isostructural III-VI sesquichalcogenides were also reported. It was commented that the α-In_2Se_3-like structure in these sesquichalcogenides was dynamically stable at RC, unlike the β-In_2Se_3-like structure. Therefore, α-In_2Se_3-like sesquichalcogenides were proposed as 2D ferroelectric materials. Another theoretical work of single- and few-layer α-In_2Se_3-like B_2X_3 (*B*=Ga,In; *X*=S,Se) sesquichalcogenides[60] predicted that these layered structures are energetically and mechanically stable, with strong OP and IP ferroelectricity, SHG coefficients, and piezoelectricity. Most extensively, band structures, OP and IP ferroelectricity, as well as analysis of the optical absorption spectrum with quantum and energy efficiencies

of ultraviolet, visible, and infrared light absorption, were tabulated in α-In_2Se_3-like sesquichalcogenides to examine the solar-to-hydrogen efficiencies for PWS.[61] All of them were predicted to exhibit an efficiency above 10% and the best of these compounds, In_2Te_3, promises a much higher efficiency above the theoretical efficiency limit (32.1%). Later, molecular dynamics simulations studied the temperature-induced ferroelectric-paraelectric PT associated to the α-β PT in III-VI sesquichalcogenides[62] and spontaneous OP and IP ferroelectricity was found in the α-In_2Se_3-like structure of these compounds at RC. Moreover, the temperatures of the α-β PT were predicted to follow the sequence Al_2X_3 > Ga_2X_3 > In_2X_3. Another theoretical work revised and improved the band gaps of III-VI sesquichalcogenides using DFT+U+V simulations.[63] Finally, recent molecular dynamics simulations of both the α-β and β-α PTs in III-VI sesquichalcogenides[64] predicted that the ferroelectric-paraelectric, α-β PT is fast at HT and assisted by an IP shear phonon mode, while the β-α PT is hindered by an entropy barrier due to a pseudo-centrosymmetric β phase. In summary, theoretical studies have shown a strong interest in the *R*3*m* structure of III-VI B_2X_3 sesquichalcogenides for their interesting potential applications.

In this context, the properties of α-In_2Se_3-like (*R3m*) Ga_2S_3 has drawn particular attention because several theoretical works suggest that it could form heterojunctions with Ga_2X_2Y (*X*=S, Se, *Y*=Se, Te) Janus monolayers, whose band gap and energy levels can be tuned by switching electric dipoles.[65-68] Therefore, 2D band-gap-tuneable III-VI sesquichalcogenides will stimulate future works devoted to ultrathin 2D photodetection, SHG, piezoelectric devices, emerging quantum applications, PWS, catalytic applications, gas sensors, ultrafast and ultrathin data storage, thermal imaging, energy harvesting, 2D heterojunctions, photovoltaics, and high mobility field-effect transistors.[60, 62, 64-67]

In Ga_2X_3 (*X*=S, Se, Te) sesquichalcogenides, it has been shown that neither α-In_2Se_3-like nor β-In_2Se_3-like structures can be attained at HT or by varying Ga/*X* ratios. However, there is a controversy regarding whether these phases could be observed in these compounds at HP. X-ray diffraction (XRD) measurements under compression showed a PT to β-In_2Se_3-like (*R*-3*m*) Ga_2S_3 (hereinafter, β'-Ga_2S_3) around 16 GPa, being the PT assisted by laser heating (LH).[69] However, a PT was found at similar pressures at RT in a study of the structural and vibrational properties of α'-Ga_2S_3 at HP; i.e. without the need of LH.[70] Similarly, Raman scattering (RS) measurements at RT observed a PT at 11.3 (17.2 GPa) with (and without) He as pressure-transmitting medium (PTM).[71] In addition, this last work reported two new phases observed in Ga_2S_3 under decompression below 8.0 and 3.0 GPa, both under hydrostatic and non-hydrostatic conditions, but their structures were neither provided nor suggested. Regarding the HP works focused on Ga_2Se_3 and Ga_2Te_3, both DZ-like α-Ga_2Se_3 and mono-β-Ga_2Se_3 undergo a reversible HP-PT to a disordered rocksalt (DR) structure above 16 GPa.[72-74] No HP studies of ortho-β-Ga_2Se_3 have been conducted to our knowledge. On the other hand, DZ-like β-Ga_2Te_3 was found to undergo a PT to the β-In_2Se_3 structure (hereinafter, β'-Ga_2Te_3) above 5 GPa.[75] The reversibility of this PT has not been verified since it has been suggested from resistance measurements at HP. All in all, it can be concluded that there is no report about the observation of the α-In_2Se_3 (*R*3*m*) structure in Ga_2X_3 sesquichalcogenides either at HT or at HP, to our

knowledge. Moreover, it is clear that β'-Ga_2S_3 and β'-Ga_2Te_3, isostructural to β-In_2Se_3 (*R*-3*m*), have been only obtained at HP. Noteworthy, a recent work has synthesized β'-Ga_2Te_3 via nanotectonic compression in bulk glassy Ga-Te alloys from a supercooled liquid after PLD;[46] therefore, this result opens the door to the synthesis of β'-Ga_2S_3 as a metastable phase at RC.

In this work, we report HP-RS and HP-XRD measurements up to 23.7 and 21.1 GPa, respectively, on α'-Ga_2S_3 in both under compression and decompression to study the nature and behavior of its HP phases. The structural and vibrational properties of the HP phases of α'-Ga_2S_3 are jointly analyzed by comparing experimental and theoretical methods. In this way, we address several controversial points from previous works: 1) whether the HP phase of α'-Ga_2S_3 observed at RT[70, 71] is the β' phase observed at HP aided by LH;[68] i.e. whether there is need of thermal energy[69] to promote the α'-to-β'-Ga_2S_3 HP-PT around 16 GPa; 2) the nature of the soft mode (SM) reported on the RS spectra of β'-Ga_2S_3,[71] which is not a first-order mode expected in the tetradymite-like *R*-3*m* structure on the basis of the RS spectra of several tetradymite-like sesquichalcogenides;[52, 57] and 3) the nature of the two unknown phases observed upon decompression at 8.0 and 3.0 GPa in previously reported HP-RS measurements.[71]

Regarding the first controversial point, we will show that the α'-to-β'-Ga_2S_3 HP-PT is verified at RT; therefore, it does not require additional thermal energy to occur. As regards the second point, we will show that the SM of the *R*-3*m* phase can be explained as a second-order Raman mode coming from the A_{1g}^1-E_g^1 combination. Finally, the answer to the third point is the most important contribution of this work. We will show that the 1st phase observed on decompression from β'-Ga_2S_3, hereinafter φ-Ga_2S_3, has the α-In_2Se_3-like structure (s.g. *R*3*m*). The existence of the α-In_2Se_3-like structure in a Ga-based sesquichalcogenide is here experimentally reported for the first time to our knowledge. More importantly, this result implies the existence of a pressure-induced paraelectric-ferroelectric β'-φ phase transition, similar to the predicted temperature-induced ferroelectric-paraelectric α-β-In_2Se_3-like PT in all III-VI sesquichalcogenides,[62, 64] thus connecting PTs either at HP or at HT in these compounds. This result opens new possibilities for Ga_2S_3 to design cheap, non-toxic, non-rare-earth, and abundant-element-based devices for SHG, PWS, ferroelectric, pyroelectric, and piezoelectric applications. Moreover, it will guide further works devoted on other III-VI sesquichalcogenides to synthetize α- and β-In_2Se_3-like structures not only at HP but also at RC via existing or emerging 2D materials synthesis methods[9, 15, 16, 66, 76-78] or by PLD as β'-Ga_2Te_3 was recently obtained.[46] Finally, we will propose that the 2nd phase observed on decompression shows a DZ structure and therefore is identified with the γ-Ga_2S_3 phase observed at HT. Since the DZ-like phase has been already observed on the downstroke in ternary ordered-vacancy compounds (OVCs), like AGa_2X_4 compounds (*A*=Zn,Cd,Hg; *X*=S,Se), with original defective chalcopyrite (DC) and defect stannite (DS),[79, 80] we have reformulated the PT sequence of these ternary OVCs at HP.[81] In this way, we propose a new PT diagram of OVCs at HP that include the family of binary Ga_2X_3 compounds and establish that the presence of vacancies and their pressure-induced disorder connects both the LP and HP phases in both families of compounds. Therefore, this

work allows us to understand the behaviour of III-VI sesquichalcogenides at HP as well as their relation to ternary OVCs at HP.

2. EXPERIMENTAL DETAILS

α'-Ga_2S_3 and α-In_2Se_3 powders were obtained from Alfa Aesar suplier, with high purity (99.99%). For both HP-RS and HP-XRD measurements, α'-Ga_2S_3 powders were placed in a 150-μm-diameter hole made in an Inconel gasket. A membrane-type diamond-anvil cell (DAC) with a 400-μm-diameter diamond culet was employed. A 4:1 methanol-ethanol (M-E) mixture and silicon oil (S) were used as PTM in HP-RS measurements, while M-E was used in HP-XRD measurements.

Unpolarized HP-RS measurements on α'-Ga_2S_3 at RT up to 23.7 (run-1) and 27.6 (run-2) GPa with M-E as a PTM as well as RS measurement of α-In_2Se_3 at RC were collected with a LabRAM HR UV Raman microspectrometer, equipped with a thermoelectrically cooled CCD camera, with a spectral resolution better than 2 cm^{-1}. Unpolarized HP-RS measurements on α'-Ga_2S_3 at RT up to 60.0 (run-3) and 29.2 (run-4) GPa with S as a PTM were collected with a T64000 Horiba Raman microspectrometer, equipped with a nitrogen cooled CCD camera, with a spectral resolution better than 2 cm^{-1}. Excitation of all RS signals was performed using the He:Ne line (632.8 nm) with a power below 1 mW. The ruby luminescence method was used to determine the pressure in all HP-RS mesurements [82]. Raman peaks have been fitted to Voigt profiles with the Gaussian linewidth fixed to the experimental setup resolution (1.6 cm^{-1}).[83]

Angle-dispersive powder HP-XRD measurements on α'-Ga_2S_3 at RT up to 21.1 GPa were performed at the BL04-MSPD beamline of ALBA synchrotron, employing a monochromatic X-ray beam with $\lambda = 0.4246$ Å focused to 20×20 μm^2 (full width half-maximum).[84] The pressure calibration inside the hole was determine using the equation of state (EoS) of copper.[85] The X-ray beam was focused by Kirkpartrick-Baez mirrors and images were collected using a Rayonix SX165 CCD detector and located at 240 mm from the sample. The two-dimensional diffraction images integrated into one-dimensional profiles of intensity versus 2θ and the calibration using standard LaB_6 were performed with Python-based Dioptas software.[86] Le Bail method was employed in our refinements with GSAS-II software.[87]

3. THEORETICAL DETAILS

Density functional theory (DFT)[88] calculations of β'- and φ-Ga_2S_3 have been carried out with the Vienna Ab-initio Simulation Package (VASP).[89] The projected augmented wave (PAW) potentials[90, 91] have been employed to describe valence electrons of Ga ($4s^2 3d^{10} 4p^1$) and S ($3s^2 3p^4$) atoms, considering the full nodal character of the all-electron charge density in the core region but with an affordable basis-set. A plane-wave kinetic-energy cutoff of 380 eV was defined for both β'- and φ-Ga_2S_3 to achieve highly converged results. The exchange-correlation energy was described with the generalized gradient approximation (GGA) of Perdew-Burke-Ernzenhof revised for solids (PBEsol).[92] In order to take into account the weak van der Waals interactions, we also achieve simulations with the PBE functional[93] including the Grimme-D3 dispersion correction.[94] Calculations were performed with dense special

k-meshes of 10x10x10 for β'- Ga_2S_3 and 6x6x6 for φ-Ga_2S_3, primitive cells. The simulations provide a data set of volumes, energies, and pressures (from the stress tensor), by fully optimizing the cell parameters and the atomic positions of the structures at selected volumes. For the optimized structures, the Hellmann-Feynman forces were below 0.006 eV/Å per atom and the deviations of the stress tensor from the diagonal hydrostatic form were smaller than 0.1 GPa.

Lattice-dynamic calculations were performed at the zone center (Γ-point) of the Brillouin zone for Ga_2S_3 employing the direct force-constant approach.[89, 95] The transversal optical (TO) modes of β'-Ga_2S_3 and both TO and longitudinal (LO) modes of φ-Ga_2S_3 where analysed, using a 2x2x2 supercell in order to include the non-analytical corrections due to the long-range interaction of the electric field.

Additional simulations have been carried out for several phases of Ga_2Se_3 and Ga_2Te_3, employing the unit cell, with PAW pseudopotentials and the GGA-PBEsol approximation, as for Ga_2S_3. The plane-wave kinetic-energy cutoff was 400 eV. In the case of the mono-β-, ortho-β-, β'-, and φ-Ga_2Se_3, dense special k-meshes of 4x4x2, 8x6x2, 9x9x2, and 9x9x2, respectively, were used. Finally, for the simulations of mono-α-, ortho-α-, β'-, and φ-Ga_2Te_3, isostructural with the above mentioned Ga_2Se_3 structures, the special k-meshes were 4x4x2, 8x6x2, 9x9x2, and 9x9x2.

4. RESULTS

4.1 Vibrational study under compression and decompression

4.1.1 Compression

As has been commented in section 2, four runs of HP-RS measurements have been performed on α'-Ga_2S_3 at RT. For simplicity, we show in **Fig. 2** only the upstroke and downstroke of run 1. HP-RS spectra on the upstroke of runs 2, 3, and 4 can be seen in panels a), b), and c), respectively, of **Fig. S2** in the Supporting Information (SI). In **Fig. 2**, we observe the continuous disappearance of the most intense mode (A'(6)) of the LP phase α'-Ga_2S_3 that can be observed up to 17.0 GPa. Such mode corresponds to the breathing mode, the vibrations of S atoms towards the centre of the channels that are characteristic of this ordered-vacancy compound (OVC).[70] We refer the reader to **Ref. 70** for further information about the pressure dependence of the Raman-active modes of α'-Ga_2S_3.

In **Fig. 2**, new Raman modes coming from the HP phase of α'-Ga_2S_3 start appearing at 14.6 GPa and are all observed around 80, 140, 220, 380, and 390 cm^{-1} at 15.8 GPa. The same changes in the RS spectra are also observed in runs 2, 3, and 4 at 16.1, 17.7, and 14.8 GPa, respectively (**Fig. S2**). The selected RS spectra of the HP phase of α'-Ga_2S_3 on upstroke between 15.8 and 23.7 GPa (**Fig. 2a**) resemble those already reported (both with and without He as a PTM).[71] Note that we have observed a low-frequency mode around 80 cm^{-1} that previous HP-RS measurements (made above 100 cm^{-1}) did not report. Despite this drawback, Yang *et al.*[71] assumed the s.g. *R*-3*m* for this HP phase; i.e. they identified it with the β'-Ga_2S_3 observed in previous HP-XRD measurements.[69]

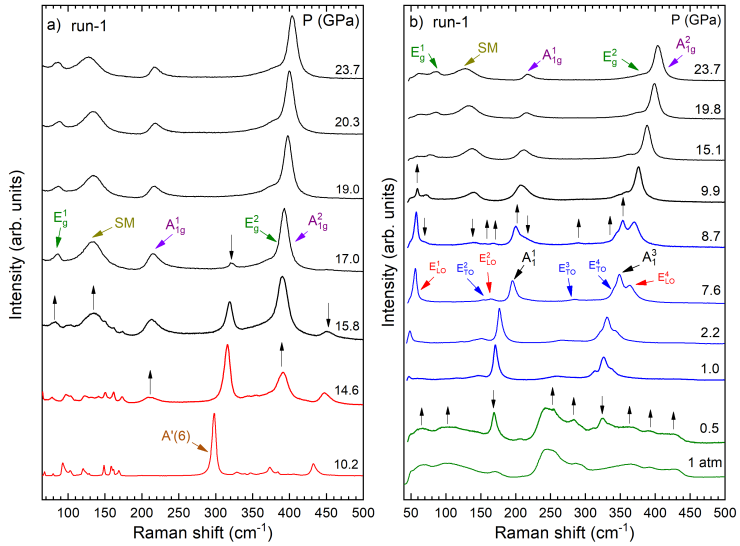

Figure 2. Selected normalised Raman spectra of α'-Ga_2S_3 (run-1) on upstroke a) and downstroke b). Down and up arrows indicate the disappearance/emerging of peaks under both compression and decompression. Red, black, blue, and green colours represent the α', β', φ, and γ phases, respectively**.** For the sake of clarity, only the most intense Raman mode, the A'(6), of α'-Ga_2S_3 is marked in panel a). The reader is referred to our previous work (**Ref. 70**) for further information about the pressure dependence of the Raman-active modes of α'-Ga_2S_3. All the observed Raman-active modes have been labelled in β'-Ga_2S_3 and φ-Ga_2S_3. The soft mode in β'-Ga_2S_3 is labelled as the SM mode.

To verify whether the modes of the HP phase of α'-Ga_2S_3 can be explained with the s.g. *R*-3*m*, we have calculated the theoretical pressure dependence of the Raman frequencies in β'-Ga_2S_3. According to group theory, 15 modes are predicted for the centrosymmetric *R*-3*m* phase, 3 acoustic ($A_{2u} + E_u$) and the remaining 12 optical ($2E_g(R) + 2A_{1g}(R) + 2E_u(IR) + 2A_{2u}(IR)$) modes are either Raman-active (*R*) or Infrared-active (*IR*). In this work, a superindex has been added to each mode in increasing frequency to distinguish among them. The theoretical Raman-active frequencies are plotted together with the experimental ones of the four runs in **Fig. 3a**. Moreover, theoretical and experimental zero-pressure frequencies and their pressure coefficients are summarized in **Table 1**. The nice comparison of the theoretical and experimental zero-pressure frequencies and pressure coefficients has allowed us to identify in the HP phase of α'-Ga_2S_3 all the four first-order Raman-active modes (E_g^1, A_{1g}^1, E_g^2, and A_{1g}^2) characteristic of the s.g. *R*-3*m* (see **Fig. 2a)** and **Fig. 3a)**). Therefore, we have verified that β'-Ga_2S_3 is the HP phase of α'-Ga_2S_3 and that it can be obtained at RT without LH. Further details of the structural properties of β'-Ga_2S_3 upon compression will be given in the next section.

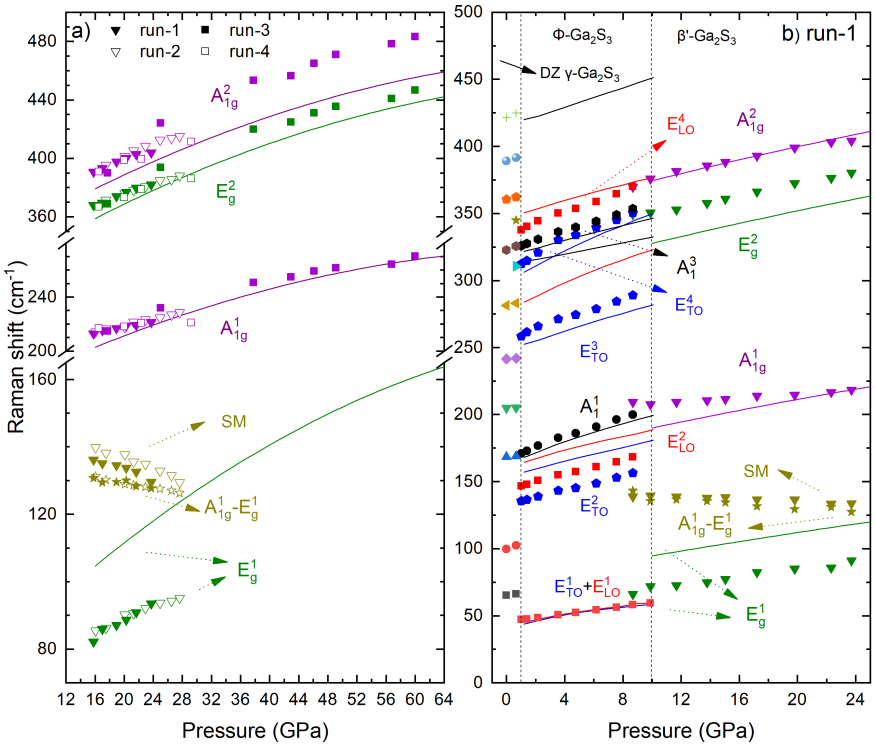

Figure 3. Experimental (symbols) and theoretical (solid lines) pressure dependence of Raman frequencies of a) β'-Ga_2S_3 on upstroke (all runs) and b) β', φ, and γ phases on downstroke (run-1). Dotted vertical lines in panel b) indicate the phase transition pressures on downstroke. Both in panel a) and b), the experimental frequency of the $A_{1g}^1(\Gamma)$–E_g^1 (Γ) difference mode is labeled with hollow star symbols to compare with the SM mode. Black, blue, and red solid lines refer to the theoretical pressure dependence of the frequencies of the A_1, E_{TO}, and E_{LO} modes of φ-Ga_2S_3 in panel b), respectively. The reader is referred to **Ref. 70** for further information about pressure dependence of the Raman frequencies of α'-Ga_2S_3.

Additional support to our assignment has been obtained from the comparison of the HP-RS spectra of β'-Ga_2S_3 and that of β-In_2Se_3 from **Ref. 57** at 19.0 and 12.7 GPa, respectively (**Fig. 4a)**). Both RS spectra show a relatively good agreement if we consider the different masses of Ga, In, S, and Se. The main difference between the RS spectra of β'-Ga_2S_3 and β-In_2Se_3 is the appearance of an extra mode in β'-Ga_2S_3 located at around 140 cm^{-1}. This mode, called the SM band, was also observed in previous HP-RS measurements[71] but no explanation for this mode was reported despite this peak does not appear in the RS spectra of binary sesquichalcogenides with tetradymite-like structure.[52, 57]

Table 1. Theoretical and experimental frequencies (cm^{-1}), pressure coefficients a_1 (in cm^{-1}/GPa) and a_2 (in 10^{-2} cm^{-1}/GPa^2) of the Raman-active modes of β'-Ga_2S_3 (from run-1 to 4) and φ-Ga_2S_3 (only for run-1). Pressure dependence of the mode frequencies has been fitted to $\omega_i = \omega_{io} + a_1(P - P_0) + a_2P(P - P_0)^2$, where P_0 is the transition pressure. Theoretical P_0 for the β' and φ phases are fixed to 16 GPa and 1 GPa, respectively. Experimental P_0 are indicated at the table foot.

β'-Ga_2S_3	**Theoretical**			**Experimental**			**φ-Ga_2S_3**	**Theoretical**			**Experimental**		
Mode	**ω_0**	**a_1**	**a2**	**ω_0**	**a_1**	**a_2**	**Mode**	**ω_0**	**a_1**	**a_2**	**ω_0**	**a_1**	**a_2**
E_g^1	105.3(2)	1.7(2)	-0.96(4)	84(1)[a]	1.5(3)[a]	-3.2(4)[a]	E_{TO}^1	42.6(4)	2.9(1)	-11.2(1)			
							E_{LO}^1	44.0(3)	2.7(1)	-10.2(1)	47(1)	1.7(2)	-3.5(3)
SM				138(2)[a]	-0.4(2)[a]	-6(2)[a]	E_{TO}^2	155.7(3)	3.2(1)	-5.0(1)	136(2)	2.6(3)	1.1(4)
							E_{LO}^2	163.2(3)	3.5(1)	-7.2(1)	147(2)	3.0(2)	-3.0(3)
A_{1g}^1-E_g^1	98.2(2)	0.4(1)	-0.48(2)	129(1)[a]	-0.2(2)[a]	-0.5(2)[a]	A_1^1	166.5(3)	4.6(1)	-10.6(1)	171(1)	4.3(3)	-9.0(1)
A_{1g}^1	203.3(2)	2.1(2)	-1.48(1)	214(3)[a]	1.3(3)[a]	-3.6(4)[a]	E_{TO}^3	251.3(1)	3.8(1)	-4.6(1)	260(3)	4.0(1)	-9.0(1)
				214(1)[b]	1.6(1)[b]	-2.8(4)[b]	E_{LO}^3	282.1(3)	5.8(1)	-13.0(1)			
							E_{TO}^4	304.2(3)	6.3(1)	-13.0(1)	313(2)	6.8(4)	-25.7(4)
E_g^2	343.6(3)	2.4(1)	-1.49(1)	366(6)[a]	2.2(3)[a]	-4(3)[a]	A_1^2	314.0(1)	1.9(3)	1.4(1)			
				366(1)[b]	2.7(4)[b]	-4.4(2)[b]	A_1^3	320.9(1)	3.1(4)	-2.6(1)	326(1)	3.7(3)	-3.0(4)
A_{1g}^2	390 (1)	2.5(1)	-1.6(3)	390(3)[a]	3.0(4)[a]	-11.3(3)[a]	E_{LO}^4	349.5(2)	3.5(1)	-5.2(1)	338(1)	4.2(5)	-2(1)
				389(3)[b]	3.4(4)[b]	-5.2(4)[b]	A_1^4	419.3(2)	3.3(1)	1.9(1)			

* M-E: methanol-ethanol, S: silicon oil, P_0: transition pressure.

[a] average parameters between run-1 and run-2 (M-E, run-1 P_0 = 15.8 and 1 GPa for β' and φ phases, respectively, and run-2 P_0 = 15.8 GPa for β'-Ga_2S_3).

[b] average parameters between run-3 and run-4 (S, run-3 P_0 = 17.7 GPa and run-4 P_0 = 14.8 GPa for β'-Ga_2S_3).

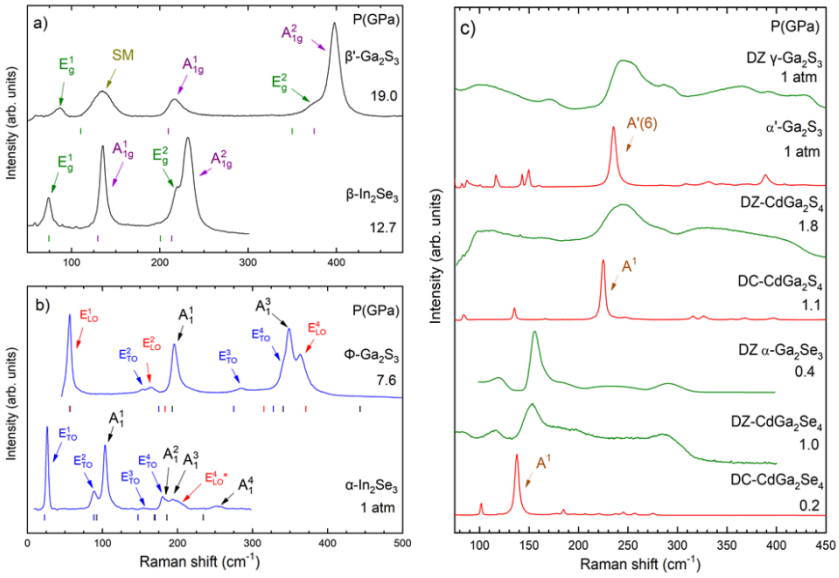

Figure 4. Comparative RS spectra at selected pressures of: a) β'-Ga_2S_3 and β-In_2Se_3 (from **Ref. 57**) with s.g. *R*-3*m*, b) φ-Ga_2S_3 and α-In_2Se_3 (at 1 atm) with s.g. *R*3*m*, and c) DZ γ-Ga_2S_3 and α'-Ga_2S_3 (from Ref. [70]), DZ and DC-$CdGa_2S_4$ (from **Ref. 79**), DZ α-Ga_2Se_3 (from **Ref. 74**) and DZ and DC-$CdGa_2Se_4$ (from **Ref. 80**). Vertical ticks represent the theoretical frequencies at the selected pressures of the different phases showed on a) and b) panels.

Curiously, the SM mode of β'-Ga_2S_3 shows a redshift with increasing pressure (see **Figs. 2a)**, **Fig. 3a)** and **Fig. S2)**) that does not agree with the blueshift shown by the four first-order Raman-active modes typical of the tetradymite-like III-VI and V-VI sesquichalcogenides.[52, 57] In fact, the SM of β'-Ga_2S_3 is not compatible with either Raman-active modes of E_g or A_{1g} symmetries or with IR-active modes of E_u or A_{2u} symmetries, according to our simulations. Instead, we propose that the SM mode is a second-order Raman-active mode related to A_{1g}^1-E_g^1 difference combination along the Brillouin zone (see **Table 1**). This hypothesis is supported by the comparison of the experimental frequencies and pressure coefficients of the SM mode and the $A_{1g}^1(\Gamma)$-$E_g^1(\Gamma)$ combination (see **Fig. 3a) and b)**). The slight frequency shift between the experimental $A_{1g}^1(\Gamma)$-$E_g^1(\Gamma)$ combination and the experimental SM mode is likely caused by the participation of phonons of the A_{1g}^1 and E_g^1 branches outside the Γ point. On the other hand, the theoretical $A_{1g}^1(\Gamma)$-$E_g^1(\Gamma)$ combination shows a larger deviation from the experimental $A_{1g}^1(\Gamma)$-$E_g^1(\Gamma)$ combination because of the large overestimation of the theoretical E_g^1 mode frequency with respect the experimental one in our PBEsol calculations. In this sense, it is known that PBEsol calculations tend to overestimate the frequency of the lowest-frequency (interlayer) vibrational modes in vdW layered materials that are related to shear vibrations between neighbour layers due to the underestimation of the c lattice parameter.[96, 97] However, we must note that the large

overestimation of the E_g^1 mode frequency in β'-Ga_2S_3 is also found in calculations using the PBE-D3 functional (**Fig. S3**), which additionally underestimates the frequencies of E_g^2 and A_{1g}^2 modes (**Fig. S3**) in a larger extent than calculations using the PBEsol functional.

In regards the origin of the SM mode in β'-Ga_2S_3, we can speculate that it is likely due to the existence of a considerable structural defect. Such defects are likely due to the reconstructive nature of the HP-PT, especially between a layered and a non-layered phase,[98] as it is the case of the α' (*Cc)* and β'(*R-3m*) phase in Ga_2S_3. Since the SM mode could be related to defects present in layered β'-Ga_2S_3, we may wonder whether the α'-to-β' PT would require an extra energy (thermal energy) contribution to overcome the energy barrier between both phases and relax the pressure gradient inside the hole, as Lai *et al.* suggested from their HP study where β'-Ga_2S_3 was obtained after applying LH.[69] In this context, our HP-RS measurements (with M-E and S as PTMs) and those reported by Yang *et al*. (with He and without PTM)[71] suggest that the α'-to-β' HP-PT occurs at RT without the need of LH. Note that Yang *et al*., who performed HP experiments without PTM;[71] i.e. under more non-hydrostatic conditions than using LiF plates as Lai *et al*. used in its HP-XRD measurements,[69] reproduced the α'-to-β' PT with a coexistence of both phases between 17.2 and 19.3 GPa. Therefore, α'-Ga_2S_3 turns into β'-Ga_2S_3 at HP without the need of LH between 11.3 and 19.3 GPa depending on the hydrostatic conditions. However, it must be commented that an energy contribution via LH could favour the α'-to-β' PT, thus providing a phase with lower structural defects. In this context, it remains to be seen whether the SM appears in such synthesis conditions.

To shed light on the dynamic stability of β'-Ga_2S_3 at HP and the possible effect of temperature on the α'-to-β' HP-PT, we have calculated the phonon dispersion curves of β'-Ga_2S_3 at 17.6 and 18.6 GPa (**Fig. S4a)** and **b)**). We observe an imaginary phonon at the high symmetry point T at 17.6 GPa (**Fig. S4a)**). This result is different to that reported in **Ref. 64** (**Fig. S11d)**), which show imaginary phonons at all high symmetry paths, as it has been observed in the β-In_2Se_3 at RC.[62, 64] Pressure dynamically stabilizes the *R*-3*m* structure in Ga_2S_3 since at 18.6 GPa (**Fig. S4b)**) no imaginary phonons appear. Since experimentally the *R*-3*m* phase appears from 12 GPa on at RT depending on the hydrostatic conditions as exemplified in this work and in **Refs. 69, 71**, our lattice dynamics calculations at 0K suggest that temperature also plays a role in stabilizing this phase at RT at smaller pressures than theoretically predicted to be stable. Therefore, we conclude that the *R*-3*m* phase is reached in Ga_2S_3 at RT and HP in the same way as the *R*-3*m* phase is found in In_2Se_3 at RT and HP.[99]

4.1.2. Decompression

On decompression from above 20 GPa, we have observed that all RS spectra correspond to α'-Ga_2S_3 down to 10 GPa (see **Fig. 2b)**) and there is a good agreement between the pressure dependence of the experimental and theoretical Raman frequencies in the whole pressure range (**Fig. 3b)**). Several changes in the RS spectrum can be observed below 10 GPa (see **Fig. 2b)**). A new peak arises in the left side of the E_g^1 mode at 9.9 GPa, thus suggesting a 1st PT (from α'-Ga_2S_3 to φ-Ga_2S_3) on decompression. Between 8.7 and 7.6 GPa, the E_g^1, A_{1g}^1, and SM modes of β'-Ga_2S_3

disappear and more small peaks emerge between 180 and 300 cm^{-1}. Additionally, strong modes appear in the right and left side of A_{1g}^1 and A_{1g}^2 modes, respectively. The new Raman modes of φ-Ga_2S_3 are observed on downstroke between 9.9 and 1.0 GPa. At 0.5 GPa, a few broad peaks between 50 and 425 cm^{-1} emerge in the RS spectrum, thus suggesting a 2nd PT (from φ-Ga_2S_3 to γ-Ga_2S_3) on decompression. The broad Raman peaks remain at ambient pressure, which points out the non-reversibility of the PTs of the original phase (α'-Ga_2S_3) at HP. All these changes are quite in agreement with earlier HP-RS measurements,[71] at least with the onset of the 1st PT on decompression. Regarding the 2nd PT on decompression, Yang *et al*. observed the phase transition from φ-Ga_2S_3 to another phase (we will assume it is also γ-Ga_2S_3) below 3 GPa, but no Raman peaks both with He and without PTM, were reported for γ-Ga_2S_3.

As already commented, Yang *et al.* could not suggest any s.g. for both φ-Ga_2S_3 and γ-Ga_2S_3.[71] In this context, we have explored the literature on III-VI sesquichalcogenides to find potential candidates for φ-Ga_2S_3 and γ-Ga_2S_3. Both s.g. *R*3*m* and *R*-3*m* have been already observed in α- and β-In_2Se_3, respectively, and have been theoretically predicted in other III-VI sesquichalcogenides.[59, 60, 62, 64] Moreover, the α-In_2Se_3-like structure in these compounds has been predicted to be dynamically stable at RC, unlike β-In_2Se_3-like structure.[59, 62, 64] On top of that, both are layered phases, the *R*3*m* structure has 6 and 4-fold coordinated cations, while the *R*-3*m* structure features only 6-fold coordinated cations. This decrease in the cation coordination from the former to the latter structure stands the *R*3*m* phase as the candidate at LP on downstroke from the *R*-3*m* phase. Consequently, in view of these antecedents, we have explored the α-In_2Se_3-like structure as a potential candidate for φ-Ga_2S_3.

According to group theory and considering the LO-TO splitting of the polar *E* modes in the non-centrosymmetric *R*3*m* structure, there are 15 normal modes of vibration at Γ, whose mechanical decomposition is: 3 acoustic ($A_1 + E_{TO} + E_{LO}$) modes and 12 optical ($4A_1(R, IR) + 4E_{TO}(R, IR) + 4E_{LO}(R, IR)$) modes. We have calculated the theoretical pressure dependence of the Raman frequencies in Ga_2S_3 with *R*3*m* structure and plotted them in **Fig. 3b** together with those experimentally observed in φ-Ga_2S_3. In addition, we have tabulated the experimental pressure coefficients and zero-pressure frequencies of φ-Ga_2S_3 and those theoretically predicted for Ga_2S_3 with *R*3*m* structure in **Table 1**. The good agreement between the experimental and the calculated zero-pressure frequencies and pressure coefficients suggests that φ-Ga_2S_3 could have the *R*3*m* structure. In this scenario, we have tentatively identified 8 of the 12 predicted Raman-active modes (see **Fig. 2b)** and **Fig. 3b)**). At 1 GPa, they are the E^1 ($E_{TO}^1 + E_{LO}^1$) mode at 47 cm^{-1}; the E_{TO}^2, E_{LO}^2, and A_1^1 modes between 135 and 175 cm^{-1},the E_{TO}^3 mode at 260 cm^{-1}, and the E_{TO}^4, A_1^3, and E_{LO}^4 modes in the range between 275 and 350 cm^{-1}. We have not observed either the E_{LO}^3 mode (predicted around 282 cm^{-1}), the A_1^2 mode (predicted around 314 cm^{-1}), or the highest-frequency A_1^4 mode (predicted around 419 cm^{-1}). Curiously, this mode was observed by Yang *et al*. around 450 cm^{-1} (see **Fig. 2b)** and **3b)** of **Ref. 71**), what gives additional support to our assignment.

Further support to our assignment has been obtained from the comparison of the HP-RS spectra of φ-Ga_2S_3 at 7.6 GPa with that of α-In_2Se_3 at RC (**Fig. 4b)**). As observed, both RS spectra are rather similar and are dominated by a narrow and strong E^1 mode (this mode was not reported for α-In_2Se_3 in a previous work[57] because of the edge filter cutoff in previous RS measurements). As observed, there is a nice agreement of experimental frequencies with theoretical frequencies (vertical ticks in **Fig. 4b)**). Note that vertical ticks of φ-Ga_2S_3 correspond to both calculated TO and LO counterparts of the E modes, while vertical ticks of α-In_2Se_3 correspond only to the theoretical A_1 and E_{TO} mode frequencies, since the LO counterpart of the polar E modes was not calculated in **Ref. 57**. Apart from the highest-intensity lowest-frequency E^1 mode, both RS spectra also show a rather strong A_1^1 mode and a complex band with at least the E_{TO}^4, A_1^3 and E_{LO}^4 modes. The main difference between both RS spectra is that E_{TO}^2 and E_{LO}^2 modes are observed at close frequencies in φ-Ga_2S_3, while they are quite apart in α-In_2Se_3.[57] Additionally, the highest-frequency A_1^4 mode found in α-In_2Se_3 and observed by Yang *et al*. in φ-Ga_2S_3[71] could not be seen in our HP-RS measurements, as already commented.

To verify if φ-Ga_2S_3 (*R*3*m*) is dynamically stable at RC, as suggested by **Refs. 59** and **68**, we have calculated the phonon dispersion curves of φ-Ga_2S_3 at 15 GPa (**Fig. S4c)**). It is observed that φ-Ga_2S_3 (*R*3*m*) is dynamically stable at that pressure. This result agrees with the experimental pressure value of the β'-to-φ PT on decompression and the pressure range in which the φ-Ga_2S_3 is experimentally observed, according to this work and Yang *et al*.[71] In summary, we can conclude that our RS measurements and those of Yang *et al*. for φ-Ga_2S_3 are consistent with the experimental RS spectra of α-In_2Se_3 and consistent with the calculated Raman-active modes of the *R*3*m* phase in Ga_2S_3. Therefore, we consider that φ-Ga_2S_3 has the α-In_2Se_3-like structure. In the next section, we will confirm the α-In_2Se_3-like structure of φ-Ga_2S_3 with HP-XRD measurements and discuss the behaviour of the structural properties of this new phase at HP.

Regarding the 2nd phase observed on decompression, we only could measure two RS spectra, at 0.5 GPa and 1 atm (see bottom RS spectra in **Fig. 2b)**). Both RS spectra are dominated by broad bands, being the strongest one located around 250 cm^{-1}. The lack of narrow peaks suggest that this phase has a strong disorder corresponding either to amorphous α'-Ga_2S_3 nor to another disordered phase, as γ-Ga_2S_3. Since amorphous α'-Ga_2S_3 should show a RS spectrum that resembles the one-phonon density of states of crystalline α'-Ga_2S_3, we have compared the RS spectra of the recovered sample (γ-Ga_2S_3) near RC in **Fig. 2b** with the one-phonon density of states of α'-Ga_2S_3 (see **Fig. S20** in **Ref. 70**) in order to verify whether the recovered sample could correspond to amorphous α'-Ga_2S_3. It can be observed that broad Raman bands in the RS spectrum of decompressed Ga_2S_3 are observed in the regions where bands of the one-phonon density of states are expected. However, we cannot explain the strongest Raman band near 250 cm^{-1} of decompressed Ga_2S_3 with the one-phonon density of states of crystalline α'-Ga_2S_3. Therefore, we conclude that it is not likely that the recovered sample corresponds to amorphous α'-Ga_2S_3.

On the other hand, it is well known that γ-Ga_2S_3 is a HT phase with DZ structure that is isostructural with α-Ga_2Se_3 and β-Ga_2Te_3[19, 20, 28-30] and that in the case of Ga_2Se_3

this DZ phase has also been observed at LT (α-Ga_2Se_3). Additionally, DZ structures have been obtained in several decompressed ternary AGa_2X_4 (*A*=Zn,Cd,Hg; *X*=S,Se) OVCs.[79, 80] To investigate whether γ-Ga_2S_3 might have a DZ structure, we have plotted in **Fig. 4c)** the RS spectra of DZ γ- and α'-Ga_2S_3, DZ- and DC-$CdGa_2S_4$, DZ α-Ga_2Se_3, and DZ- and DC-$CdGa_2Se_4$. As can be observed, the RS spectrum of γ-Ga_2S_3 is very similar to that of DZ-$CdGa_2S_4$ with a broad and intense band near 250 cm^{-1}. Note also the similarities between the strongest Raman modes of ordered phases, like α'-Ga_2S_3[70] and DC-$CdGa_2S_4$[79] at 0.5 and 1.1 GPa, respectively, in **Fig. 4c)**. On the other hand, there is a notable difference between the RS spectra of ordered (red spectra) and disordered phases (green spectra) in all plotted compounds. The same comments done for the RS spectra of ordered and disordered phases of Ga_2S_3 are also valid for Ga_2Se_3 (see the comparison of DZ α-Ga_2Se_3,[74] DZ- and DC-$CdGa_2Se_4$[80] at 0.4, 1.0, and 1.2 GPa, respectively). In particular, the RS spectra of DZ α-Ga_2Se_3 is very similar to that of DZ-$CdGa_2Se_4$. Both compounds show a strong band located ca. 150 cm^{-1} (**Fig. 4c)**). It must be stressed that the only difference between DZ-Ga_2X_3 and DZ-AGa_2X_4 compounds concerns to the cation Wyckoff sites. In DZ-Ga_2X_3, the cation Wyckoff site is occupied by a mixture of Ga atoms and vacancies, while in DZ-AGa_2X_4 is occupied by a mixture of *A* and Ga atoms and vacancies.

The strongest peaks located at 250 and 150 cm^{-1} in DZ-$CdGa_2S_4$ and DZ-$CdGa_2Se_4$ (band 4 reported for both compounds from **Refs. 79** and **80**, respectively) were attributed to the highest-frequency and highest-intensity A^1 modes of DC-$CdGa_2S_4$ and DC-$CdGa_2Se_4$, which represent the breathing mode; i.e. the vibration of anions against the vacancies. This mode is similar to the A'(6) of the α'-Ga_2S_3, where S atoms vibrate toward the center of the channels. Instead, such strongest peaks in the RS spectra of these DZ phases correspond to an optical mode related to the vacancies and it has no counterpart in binary zincblende *AX* compounds (with no vacancies in the structure), as was discussed in **Refs. 79** and **80**. Therefore, on the light of the similitudes here commented, we conclude that decompressed Ga_2S_3 likely has the same DZ structure as γ-Ga_2S_3. Future XRD measurements are needed to verify it; however, in the next section we will discuss the XRD patterns of the recovered samples reported by Yang *et al.*[71] that provide arguments to support the DZ structure of decompressed Ga_2S_3 at RC.

4.2 Structural study under compression and decompression

4.2.1 Compression

Figure 5 shows normalized XRD patterns at selected pressures both on upstroke and downstroke. As we have previously mentioned, in this work we focus on the pressure behaviour of the HP phases of α'-Ga_2S_3, concretely, in β'-Ga_2S_3 and φ-Ga_2S_3 that are obtained under compression and decompression, respectively. Therefore, only a couple of XRD patterns of α'-Ga_2S_3 are shown at 14.0 and 16.1 GPa in **Fig. 5**. We refer the reader to **Ref. 70** for details about the structural pressure dependence of α'-Ga_2S_3 up to the PT to β'-Ga_2S_3. As commented in our previous work,[70] our HP-XRD patterns show Cu reflections that at certain pressures are even stronger than reflections of the HP phases observed both on compression and decompression; consequently, we have only been able to perform Le Bail refinements (see **Fig. 6**).

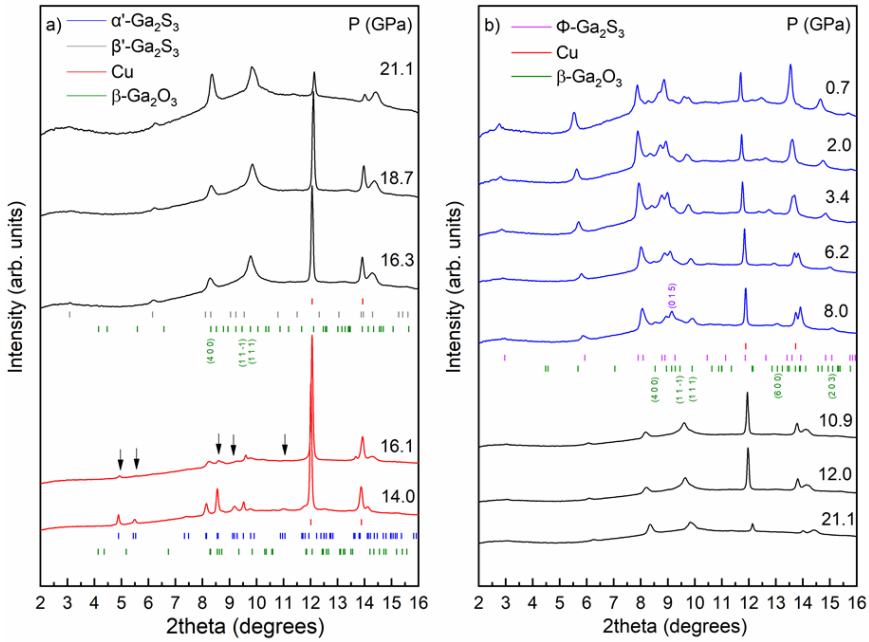

Figure 5. Selected normalized HP-XRD patterns of α'-Ga_2S_3 on upstroke a) and downstroke b). Down arrows indicate the disappearance of several peaks of α'-Ga_2S_3 on upstroke. XRD patterns in red, black, and blue colors correspond to α'-Ga_2S_3, β'-Ga_2S_3, and φ-Ga_2S_3, respectively. Blue, grey, purple, green, and red vertical ticks mark the α'-Ga_2S_3, β'-Ga_2S_3, φ-Ga_2S_3, β-Ga_2O_3 and copper Bragg reflections, respectively. The reader is referred to **Ref. 70** for further information about the pressure dependence of the structure of α'-Ga_2S_3 and the presence of β-Ga_2O_3 identified as an impurity contained in the commercial sample. Several relevant reflections from β-Ga_2O_3 and φ-Ga_2S_3 are indicated.

Before analyzing the phases of Ga_2S_3 it must be mentioned that our HP-XRD measurements have detected the presence of an impurity in the commercial α'-Ga_2S_3 powders, as Lai *et al*. already did.[69] The presence of this impurity has not been observed in our HP-RS measurements due to the small quantity in the original sample and the more local character of RS measurements than of XRD measurements. HT-RS spectra and Le Bail refinements of XRD patterns in **Ref. 70** allowed us to identify this impurity as β-Ga_2O_3 (monoclinic, s.g. *C*2/*m*, No. 12). One can notice that, even though β-Ga_2O_3 is present in a small quantity (0.01% according to the product specifications from Alfa Aesar), the most intense peak at 9.8 degrees observed in our HP-XRD patterns belongs to this impurity. This intense peak is mainly composed of 2 reflections, the (1 1 -1) and (1 1 1) labelled in **Fig. 5a)**. In particular, the (1 1 1) reflection shows the highest structure factor among all the reflections of β-Ga_2O_3, thus explaining the high intensity of this peak. Other relevant reflection to remark is the (4 0 0), which makes broader that peak of β'-Ga_2S_3 located at about 8.5 degrees (**Figs.**

5a) and **6b)**). Therefore, vertical ticks as well as such abovementioned reflections indicating the presence of this impurity are provided in **Figs. 5** and **6**.

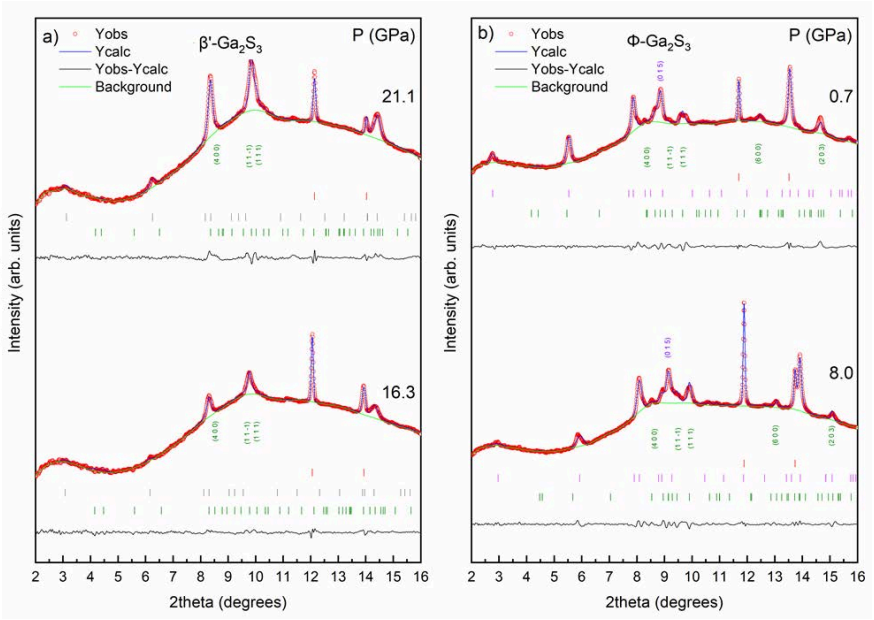

Figure 6. Selected normalized HP-XRD patterns of a) β'-Ga_2S_3 on upstroke and b) φ-Ga_2S_3 on downstroke. Gray, purple, green, and red vertical ticks mark the β'-Ga_2S_3, φ-Ga_2S_3, β-Ga_2O_3, and copper Bragg reflections. Several relevant reflections from β-Ga_2O_3 and φ-Ga_2S_3 are indicated.

On upstroke, we can observe remarkable changes in the XRD patterns (**Fig. 5a)**) between 16.1 and 16.3 GPa. Most of the α'-Ga_2S_3 peaks present at 16.1 GPa disappear at 16.3 GPa and new ones emerge with smaller intensity than those of Cu (at about 12 and 14 degrees). The new peaks of the HP phase with relevant intensity are located at about 3.1, 6.2, 8.2, 9.8 and 14.3 degrees at 16.3 GPa (see **Fig. 5a)** and **Fig. 6a)**). Apart from the peaks of Cu and β-Ga_2O_3 (near 9.5 degrees), the new peaks of the XRD patterns from 16.3 GPa to 21.1 GPa have been successfully refined via Le Bail method with the s.g. *R*-3*m* of β'-Ga_2S_3 (**Fig. 5a** and **6a)**), thus supporting the results previously obtained by HP-RS measurements. Note that peaks at 8.2 and 14.3 degrees are overlapped reflections from both β'-Ga_2S_3 and β-Ga_2O_3. At 21.1 GPa, the maximum pressure achieved, the peaks of β'-Ga_2S_3 are clearly more intense than at 16.3 GPa (**Fig. 5a)** and **Fig. 6a)**) with the peak of β'-Ga_2S_3 located near 8.4 degrees being of similar intensity as that of β-Ga_2O_3.

It is important to stress that our HP-XRD measurements between 16.3 and 21.1 GPa at RT agree with earlier HP-XRD measurements at RT.[69] Lai *et al*. also used the same commercial α'-Ga_2S_3 powders and also reported the most intense peak around 0.4 $Å^{-1}$ (corresponding to our 9.5 degrees) at 21 GPa at RT; i.e. prior to applying LH.

However, since they could not identify the nature of the impurity, they could not refine the XRD pattern at RT with the β-In_2Se_3-like structure. Only the use of LH helped them to observe the β-In_2Se_3-like structure at 17.2 GPa in run-2, via improved crystallization, reducing possible internal, micro, and long-range internal stresses or anisotropic strains.[100] As a result, they improved the XRD signal of this structure, even making visible the two lowest reflections at about 0.14 and 0.26 $Å^{-1}$ (in our HP-XRD patterns at about 3.1 and 6.2 degrees (**Fig. 5a)** and **6a)**), and masking the signal of the impurity β-Ga_2O_3. All in all, our HP-XRD and HP-RS measurements, as well as previous HP-XRD and HP-RS measurements,[69] have clearly proved the feasibility of promoting the α'-to-β'-Ga_2S_3 PT at RT, with LH allowing to improve the XRD signal of the β-In_2Se_3-like structure in Ga_2S_3 under compression.

4.2.2 Decompression

On downstroke, XRD peaks from β'-Ga_2S_3 and the impurity, β-Ga_2O_3, increase their intensity down to 8 GPa (**Fig. 5b)**). On top of that, new peaks emerge from both phases, whose Miller indices (hkl) have been included. However, changes occur below 8 GPa. If we try to refine XRD patterns from 8 to 0.7 GPa via Le Bail method either with the s.g. *R*-3*m* or with the *R*3*m*, we find a relatively good fit, but there is a discontinuity in the volume around 8 GPa. This means that, even though the impossibility of discerning the s.g. *R*-3*m* and *R*3*m* by powder XRD measurements, they can be distinguished by the volume discontinuity and the different pressure behavior below and above 8 GPa as we will discuss in the next subsection. For that reason, we have refined XRD patterns from 8 to 0.7 GPa with the s.g. *R*3*m* structure of α-In_2Se_3 (see **Fig. 6b)**). Such refinements are consistent with the considerations made in section 4.1 regarding lattice dynamical experiments and calculations. The overall increase of the peak intensities, the emergence of new peaks, both from β-Ga_2O_3 and β'-Ga_2S_3, and thinner peaks from 8 GPa can be justified by the more hydrostatic conditions that allows the M-E, which does not guarantee such conditions above 10.5 GPa because of its glass transition.[101, 102] The (4 0 0), (1 1 1), (1 1 -1), (6 0 0) and (2 0 3) reflections of β-Ga_2O_3, marked in **Fig. 5b)** and **6b)** are similar to those found in the XRD measurements of α'- Ga_2S_3 in **Fig. 2** of **Ref. 70** at about 8.3, 9.1, 9.6, 12.3 and 14.5 degrees, respectively, at 0.1 GPa.

At this point, we want to mention that a nice way to distinguish between centrosymmetric and non-centrosymmetric structures is by means of RS measurements, especially when analyzed together with lattice dynamics calculations.[103] Usually, non-centrosymmetric structures lead to a larger number of Raman-active modes than centrosymmetric structures, as has been shown for the *R*3*m* and *R*-3m phases of Ga_2S_3 in the previous section and in In_2Se_3.[57] Even for the identification of the α-In_2Se_3 (*R*3*m*) at RC, several works have carried out RS measurements to identify it from its centrosymmetric *R*-3*m* and other phases.[57, 104-107] Further support to the existence of both *R*-3*m* and *R*3*m* phases in Ga_2S_3 is given by PBEsol total energy calculations of α'-Ga_2S_3 (*Cc*), φ-Ga_2S_3 (*R*3*m*), and β'-Ga_2S_3 (*R*-3*m*) in **Fig. S5a)**. It is shown that β'-Ga_2S_3 is energetically favourable above 9.5 GPa, while φ-Ga_2S_3 is energetically favourable between α'-Ga_2S_3 and β'-Ga_2S_3; i.e. between 5.2 and 9.5 GPa (**Fig. S5b)**). On top of that, our theoretical phonon dispersion

curves of β'-Ga_2S_3 (*R*-3*m*) (**Fig. S4a)**) show that this phase is not dynamically stable for pressures below 17.6 GPa. On the contrary, φ-Ga_2S_3 (*R*3*m*) is energetically stable below 9.5 GPa and it is dynamic stable even at 15 GPa (**Fig. S4c)**) and, according to the previous theoretical works, is dynamically stable even at RC,[59, 68] unlike β'-Ga_2S_3.[64] Consequently, we conclude that our combined HP-XRD and RS measurements supported by theoretical calculations have allowed us to confirm the *R*-3*m* and *R*3*m* nature of both β'-Ga_2S_3 and φ-Ga_2S_3, respectively.

Now the question is why the φ phase is not observed on upstroke from the α' phase. The answer is that there is likely a kinetic energy barrier between the two phases that cannot be overcome without extra energy and when this extra energy is obtained at higher pressure, there is another phase (in our case, β') that it is energetically more competitive. The existence of this kinetic energy barrier between the α' and φ phases on upstroke is the minimum energy that we need to apply to the α' phase to move atoms in the direction of the φ phase, breaking bonds of the α' phase to favour the formation of new bonds in the φ phase. This kinetic energy barrier is the same that avoids the transition from the φ phase to the α' phase on downstroke, giving support to the transition from the φ phase to the DZ phase on downstroke. Note that we have not included the DZ phase in **Fig. S5** because of the fractional occupation of cation positions in this phase makes difficult to simulate this structure. However, we consider that the DZ phase must be a metastable structure competitive in energy with the α' phase since this phase has been also observed in Ga_2Se_3 and Ga_2Te_3 at RC.[19, 20, 28-30]

Regarding the 2nd PT on downstroke, we have tentatively attributed to the DZ structure of γ-Ga_2S_3 by considering the similarity of our RS measurements and those of DZ-$CdGa_2S_4$ and also the similarity of the RS spectra of DZ γ-Ga_2Se_3 and DZ-$CdGa_2Se_4$ (**Fig. 4c)**). As it was previously commented, we could not measure XRD patterns below 0.7 GPa, therefore we do not have XRD data to identify the structure of γ-Ga_2S_3. However, we want to comment on the XRD results obtained Yang *et al*. on α'-Ga_2S_3 since they showed XRD patterns of the recovered samples (**Fig. 8** of **Ref. [71]**). Unfortunately, Yang *et al*. did not provide any information about the PTM used in one of their runs, the type of gasket used, and the X-ray wavelength employed for the XRD measurements, so we cannot discuss their patterns in quantitative terms. In qualitative terms, however, we can conclude that **Fig. 8** of **Ref. 71** undoubtedly shows that the recovered XRD pattern does not match with the original α'-Ga_2S_3. Moreover, we can tentatively identify the peaks located at around 0.26 and 0.27 $Å^{-1}$ with the (1 1 1) and (2 0 0) reflections of DZ-type structure, as can be seen in the recovered DZ-$CdGa_2Se_4$ in **Ref. 108**. The rest of the peaks do not match with other reflections of the DZ structure, and they could be related with high-intense β-Ga_2O_3 or PTM reflections instead.

Additional support to the observation of the DZ phase in decompressed Ga_2S_3 comes from the fact that both β'-Ga_2S_3 and φ-Ga_2S_3 show vacancies in the structure, so an order-disorder PT can occur on downstroke. In this context, we must note that b'-Ga_2S_3 is a distorted rocksalt phase with 6-fold coordinated cation that has a plane of vacancies forming the interlayer space.[99, 109] Similarly, φ-Ga_2S_3 has cations with 6-

fold and 4-fold coordination and also has the same plane of vacancies at the interlayer space. Therefore, a PT to the DZ phase on downstroke in α'-Ga_2S_3 is highly possible in its way to attain a 4-fold cation coordination at RC if no thermal energy is added to the system. Note that the original *Cc* structure of α'-Ga_2S_3 is an ordered phase with vacancies located on well-defined channels that could be difficult to obtain at RC on downstroke without additional thermal energy. This can be seen as a the presence of an energy barrier between the α' and φ phases already discussed. In summary, we conclude that the recovered phase on downstroke is likely γ-Ga_2S_3 with a DZ structure; however, further XRD measurements should be carried out to verify the DZ nature of the recovered phase from the structural point of view.

4.2.3 Pressure dependence of lattice parameters and volume of β'- and φ-Ga_2S_3

Let us now analyze the pressure dependence of the structural parameters of both β'-Ga_2S_3 and φ-Ga_2S_3. **Fig. 7a** shows the experimental and theoretical PBEsol and PBE-D3 pressure dependence of the lattice parameters of β'-Ga_2S_3 and φ-Ga_2S_3. Additionally, experimental and theoretical LDA data sets of β'-Ga_2S_3 from Lai *et al.* [69] are included. As regards β'-Ga_2S_3, our experimental *a* and *c* values are slightly larger than those reported by Lai *et al.* This difference likely stems from the different PTM used or to the LH employed by Lai *et al*. to assist the α'-to-β' PT. Theoretical PBE-D3 calculations predict *c* values closer to those experimental ones than PBEsol and LDA calculations. On the other hand, the three theoretical calculations predict similar values for the lattice parameter *a*, with a tendency of LDA > PBE-D3 > PBEsol. Concerning φ-Ga_2S_3, our theoretical PBE-D3 calculations predict the experimental *c* values perfectly and also the a values are better predicted with PBE-D3 calculations than with PBEsol calculations. One can notice that the experimental and theoretical *a* values of β'-Ga_2S_3 and φ-Ga_2S_3 have an almost linear pressure dependence along the whole range of pressures. On the other hand, the experimental *c* values of both phases show a more non-linear pressure dependence because both β'-Ga_2S_3 and φ-Ga_2S_3 are layered phases whose interlayer space have a big compression at LP and a much smaller compression at HP as a consequence of the hardening of the interlayer vdW bonds at HP.

Table 2 gathers the zero-pressure axial compresibilities, defined as $\kappa_x = -\frac{1}{x}\frac{\partial x}{\partial P}$, of both a and c axes for β'-Ga_2S_3 and φ-Ga_2S_3. As expected from any 2D material, the *c* axis (OP direction) is more compressible that the *a* (and *b*) axis (IP directions). For β'-Ga_2S_3, our experimental values for K_a are quite close to theoretical PBEsol and PBE-D3 calculations and much smaller than the experimental and theoretical LDA values of Lai *et al.*[69] In contrast, our experimental K_c value is similar to the theoretical PBEsol one, smaller (almost half) than that predicted by PBE-D3 calculations, and much smaller than the experimental and theoretical LDA values of Lai et al. Taking into account all experimental and theoretical data available (including extrapolated theoretical LDA and experimental data sets reported by Lai *et al.*[69] and included in **Table 2**), we can see that both the values of K_a and K_c follow the same tendency: LDA[69] > experimental[69] > PBE-D3 > PBEsol > experimental (ours). In fact, our experimental and theoretical K_a and K_c values are much smaller (around three times) than those obtained by Lai *et al*. and also, much smaller than those from their

theoretical LDA calculations. On the other hand, the experimental values of K_a and K_c for β-In_2Se_3 from **Ref. 57** (see **Table 2**) are similar although slightly smaller than those obtained by us for β'-Ga_2S_3. This result shows the consistency of our values for β'-Ga_2S_3 and indicate that the *R*-3*m* phase in In_2Se_3 exhibits a larger compressibility than in Ga_2S_3.

Table 2. Experimental (exp.) and theoretical PBEsol and PBE-D3 (th.) zero-pressure axial compressibilities (K_a and K_c, in 10^{-3} GPa^{-1}), zero-pressure unit-cell volume (V_0, in $Å^3$), bulk modulus (B_0, in GPa) and bulk modulus first pressure derivative (B_0') for β'- and φ-Ga_2S_3. Results of β'-Ga_2S_3, β- and α-In_2Se_3 from previous HP works have been added for comparison.

		K_a	K_c	V_0	B_0	B_0'
β'-Ga_2S_3	exp.[a]	2.5(1)	8.0(1)	297(1)	66(2)	5.4(2)
				295(1)	74(3)	4 (fixed)
	PBEsol[a]	3.5(1)	9.5(1)	269(1)	64(1)	4.9(2)
				266(1)	76(1)	4 (fixed)
	PBE-D3[a]	3.3(1)	14.6(1)	276(1)	59(1)	4.9
				272(1)	71(1)	4 (fixed)
	exp.[b]	7.2(1)	18.2(1)	270(1)	91(3)	4 (fixed)
	LDA[b]	11.3(1)	31.1(1)	264(1)	75(2)	3.9(3)
				264(3)	74(1)	4 (fixed)
β-In_2Se_3	exp.[c]	1.6(1)	6.8(1)	375(2)	60(6)	4 (fixed)
	exp.[d]			370	66	4 (fixed)
	PBE[c]	3.2(1)	5.1(1)	382(1)	50(1)	4.7(2)
				375(1)	61(1)	4 (fixed)
φ-Ga_2S_3	exp.[a]	3.9(1)	12.0(1)	313(1)	41(2)	8.2(1)
				311(1)	53(2)	4 (fixed)
	PBEsol[a]	3.9(1)	16.0(1)	297(1)	33(1)	9.9(1)
				294(1)	51(1)	4 (fixed)
	PBE-D3[a]	4.2(1)	23.1(1)	303(1)	36(1)	8.1(1)
				302(1)	46(1)	4 (fixed)
α-In_2Se_3	exp.[c]			401(1)	40(2)	4 (fixed)
	exp.[d]			407.9	31	4 (fixed)
	PBE[c]	6.1(1)	20(1)	436(1)	23(1)	3.3(1)
				434(1)	26(2)	4 (fixed)

[a] Present work, [b] **Ref. 69**, [c] **Ref. 57**, [d] **Ref. 58**.

Regarding φ-Ga_2S_3, the experimental and theoretical PBEsol K_a and K_c values are in good agreement. However, theoretical PBE-D3 calculations predict a K_c value higher than those of theoretical PBEsol calculations and experiments. Comparison of experimental Ka and Kc values of φ-Ga_2S_3 with experimental values for a-In_2Se_3 is not possible because only a few XRD measurements were obtained in a few pressures in **Ref. 57** and it is not possible to obtain such parameters. However, theoretical PBE calculations for a-In_2Se_3 from **Ref. 57** yield values of Ka and Kc of similar magnitude as those calculated in φ-Ga_2S_3 (see **Table 2**). Additionally, theoretical PBE calculations for a-In_2Se_3 also yield K_a and K_c values that are higher than those for β-In_2Se_3. This is also found in Ga_2S_3 that shows K_a and K_c values in φ-Ga_2S_3 that are 60% larger than those in β'-Ga_2S_3. These results agree with what it is expected for a *R*3*m* phase, with 6- and 4-fold coordinated cations, in contrasting with *R*-3*m* phase,

with only 6-fold coordinated cations. Therefore, the existence of the β'-to-φ PT on downstroke is consistent with the large differences found between the zero-pressure axial compressibilities of both phases, both experimentally and theoretically.

Figure 7. Pressure dependence of a) lattice parameters and b) volume per formula unit, V/Z (b), in α'-Ga_2S_3, β'-Ga_2S_3, and φ-Ga_2S_3. Full and open symbols represent experimental data under compression and decompression, respectively. Theoretical PBEsol (dashed lines) and PBE-D3 (dash dot lines) pressure dependence of lattice parameters in β' and φ phases is plotted in a). Experimental (solid lines) and theoretical (dashed lines) BM3-EoS for the α', β'and φ phases are shown in b). Theoretical PBEsol and experimental ΔV/Z observed in the α'-β' and β'-φ phase transitions are indicated in dark green and magenta, respectively. For the sake of comparison, the experimental (black squared plus symbols) and theoretical (LDA, dot lines) pressure dependence of the lattice parameters of the β' phase from **Ref. 69** are included in panel a), while theoretical (LDA, dot lines) BM3-EoS from the β' phase from **Ref. 69** is included in panel b).

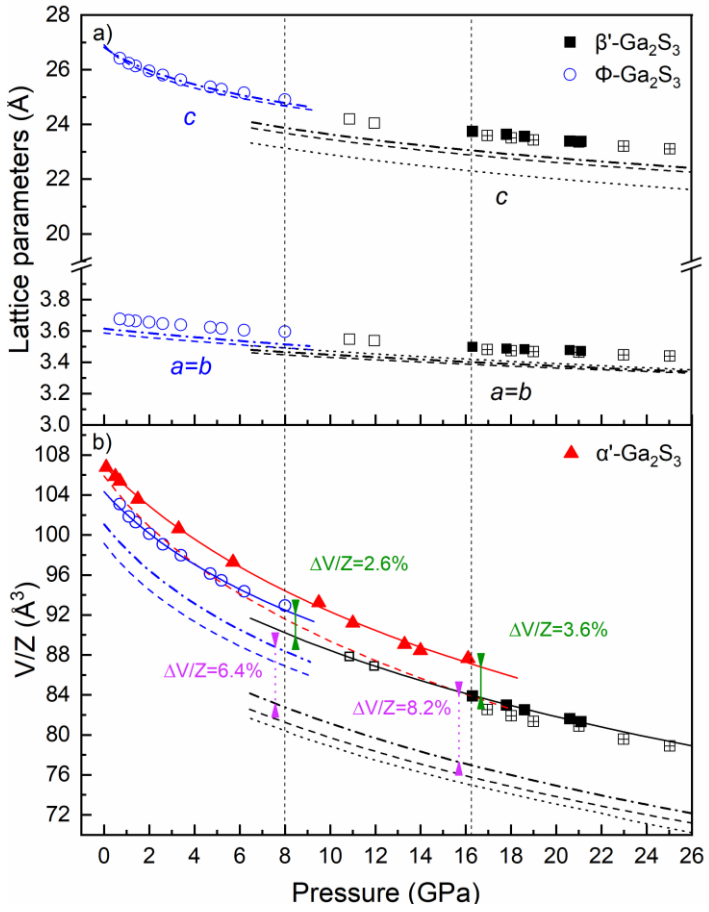

As already mentioned, strong evidence of the existence of the β'-to-φ PT on downsstroke also arise from the relative volume change at the PT pressure. **Fig. 7b)** shows the experimental and theoretical PBEsol pressure dependence of the unit-cell volume per formula unit, V/Z, in α'-Ga_2S_3, β'-Ga_2S_3, and φ-Ga_2S_3. In addition, the theoretical PBE-D3 pressure dependence of V/Z is also included for β'- and φ-Ga_2S_3. All data in **Fig. 7b)** have been fitted to a third-order Birch-Murnaghan equation of state (BM3-EoS), whose values of zero-pressure volume, V_0, bulk modulus, B_0, and its pressure derivative, B_0', are summarized in **Table 2**. Also the experimental pressure dependence of V/Z, the BM2-EoS, and the theoretical LDA BM2-EoS and BM3-EoS obtained for β'-Ga_2S_3 by Lai *et al.*[69] are included in both **Fig. 7b** and **Table 2** for comparison. Concerning the α'-to-β' PT, we have observed a 3.6% decrease of the experimental relative change of the unit-cell volume per formula unit, $\Delta V/Z$. Our PBE-D3 (PBEsol) calculations predict a $\Delta V/Z$ decrease of 8.2% (9.8%); i.e. more than two times the experimental one. These results compare with the experimental and theoretical LDA $\Delta V/Z$ around 11% reported by Lai *et al.* [69]. The experimental $\Delta V/Z$ reported by Lai *et al.* is three times larger than ours, which can be explained not only for a PTM (LiF plates) that is less hydrostatic than ours (M-E), but also because of the use of LH. On the other hand, their theoretical LDA $\Delta V/Z$ is a 34% larger than ours. That makes sense if we consider than theoretical LDA calculations for β'-Ga_2S_3 predict a much smaller volume than our calculations for β'-Ga_2S_3. On downstroke, the β'-to-φ PT shows an experimental $\Delta V/Z$ increase of 2.6% that compares with the theoretical PBE-D3 (PBEsol) values of 6.4% (7.1%). Therefore, our calculations predict $\Delta V/Z$ for both a'-to-β' and β'-to-φ PTs that are at least two times larger than experimentally measured.

Let us analyse now the pressure behavior of the experimental and theoretical unit-cell volume of β'-Ga_2S_3 and φ-Ga_2S_3. As already commented, **Table 2** summarizes the values of V_0, B_0, and B_0' of our experimental and theoretical (PBEsol and PBE-D3) data for β'-Ga_2S_3 and φ-Ga_2S_3, as obtained from fits to a BM3-EoS or to a BM2-EoS (B_0' fixed to 4). Also experimental and theoretical LDA data for β'-Ga_2S_3 from **Ref. 69** are analyzed. It can be observed that for β'-Ga_2S_3 there is a good agreement between our experimental values for B_0 and B_0' and theoretical (LDA, PBEsol, and PBE-D3) values. This means that our experimental pressure behavior of the unit-cell volume is well accounted for by calculations, despite the disagreement in the absolute value of V_0 (only theoretical PBE-D3 calculations yield a V_0 closer to the experimental value). It is well known that LDA and PBEsol calculations usually yield understimated V_0 values for layered vdW materials and much better agreement is obtained with PBE-D3 calculations that include vdW interactions. In this context, we must stress that experimental V_0 for β'-Ga_2S_3 is difficult to obtain since experimental values are extrapolated from above 8 GPa to 0 GPa always with considerable uncertainty. On the other hand, the experimental B_0 of Lai *et al.* is considerably larger than calculations, thus showing a larger incompressibility of β'-Ga_2S_3 compared to our experiments. This result can be understood if we consider that Lai *et al.* made a fit over a very small range of pressures (17 to 25 GPa)) while we have used a much larger range of pressures for the fit (11 to 23 GPa), in addition to their no so hydrostatic PTM (LiF plates) and the LH employed. Finally, we have to note that the experimental and theoretical B_0 values obtained in this work for the *R*-3*m* phase of Ga_2S_3 are of the

same order as those obtained for the *R*-3*m* phase of In_2Se_3,[57] what give us confidence about our present results.

Concerning φ-Ga_2S_3, there is a nice agreement between the experimental and theoretical (PBEsol and PBE-D3) values of V_0, B_0, and B_0'. It can be observed that φ-Ga_2S_3 is more compressible than β'-Ga_2S_3, as expected for the lower atomic coordination of the former phase. Additionally, the experimental and theoretical B_0 values obtained in this work for the *R*3*m* phase of Ga_2S_3 are of the same order as those obtained for the *R*3*m* phase of In_2Se_3,[57] what again give us confidence about our present results.

In summary, we can conclude that the analysis of the structural parameters of φ-Ga_2S_3 and β'-Ga_2S_3 has allowed us to clearly distinguish between the respective *R*3*m* and *R*-3*m* phases. Note that the pressure dependence of their lattice parameters *a* and *c* and volume, more specifically, the zero-pressure axial compressibilities (K_a and K_c), as well as the bulk modulus, B_0, and its pressure derivative, B_0', of the two phases are clearly different, as it is already confirmed by our theoretical calculations. Moreover, RS scattering measurements are clearly different in both phases and the observed Raman-active modes in both phases are consistent with *R*3*m* and *R*-3*m* phases of φ-Ga_2S_3 and β'-Ga_2S_3, respectively. Additionally, HP electrical conductivity measurements carried out by Yang *et al*.[71] show relevant changes below 9 GPa, which is another significant indicator of the β'-to-φ PT.

4.3 Mechanism of the *R-3m*-to-*R3m* phase transition in B_2X_3 (B=Ga, In; *X*=S, Se, Te) compounds

Now we are going to describe the PT mechanism between the R-3m and R3m structures in B_2X_3 (B=Ga, In; *X*=S, Se, Te) compounds. For that purpose, we are going to focus on the *R*-3*m*-to-*R*3*m* PT in Ga_2S_3 (see **Fig. 8**). On one hand, the centrosymmetric R-3m tetradymite-like structure of β'-Ga_2S_3 is a layered structure composed of quintuple layers and presents a 3-fold rotoinversion axis with only one independent Ga atom, Ga1, and two independent S atoms, S1 (internal anion of the layer) and S2 (external anion of the layer). In this way, the quintuple layers stacked along the *c* axis are formed by alternate S2-Ga1-S1-Ga1-S2 atoms (**Fig. 8a)**). In this structure, Ga1 cation is 6-fold coordinated, the internal S1 anion is also 6-fold coordinated, and the external S2 anion is threefold coordinated. On the other hand, the non-centrosymmetric *R*3*m* structure of φ-Ga_2S_3 is also a layered structure composed of quintuple layers and presents a 3-fold axis with two independent Ga atoms, Ga1 and Ga2, and three independent S atoms, S1, S2, and S3. In this way, the quintuple layers along the *c* axis are formed by S1-Ga1-S2-Ga2-S3 atoms. In this structure, Ga1 is 6-fold coordinated, Ga2 is 4-fold coordinated, the internal S2 anion is 4-fold coordinated and the external S1 and S3 anions are threefold coordinated (**Fig. 8b)**).

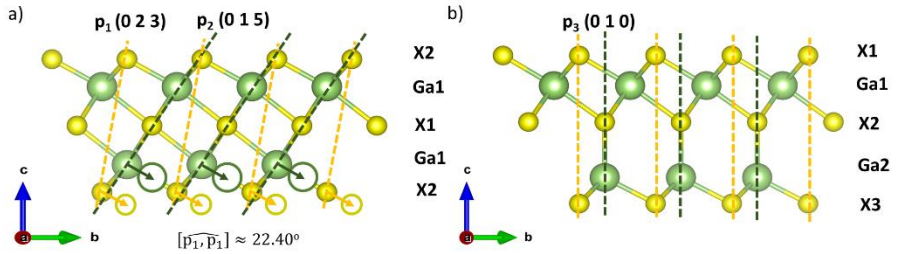

Figure 8. Side view parallel to the *a* axis of a) paraelectric, centrosymmetric β'-Ga_2X_3 and b) ferroelectric, non-centrosymmetric φ-Ga_2X_3 phases. (0 2 3) and (0 1 5) planes based on *X*2-*X*2 and Ga1-*X*1 atoms, respectively, of β'-Ga_2X_3 phases transform into (0 1 0) planes in φ-Ga_2X_3 phases. (0 2 3) and (0 1 5) planes are secant, with an angle of 22.40°, become parallel (0 1 0) planes.

To describe the mechanism of the *R*-3*m*-to-*R*3*m* PT in **Fig. 8**, we draw lines along the (0 2 3) planes (planes p_1) in the *R*-3*m* structure that contain S2 atoms from the top and the bottom of the layers (**Fig. 8a)**). We also draw lines along the (0 1 5) planes (planes p_2) that contain the sequence S2-Ga1-S1-Ga1-S2. These two families of planes intersect at the S2 atoms and form an angle of ca. 22.4 degrees above 9 GPa. At the PT below 9 GPa, there is a gliding of the Ga1 and S2 atoms in these two planes along the (1 1 -1) direction of the *R-3m* phase, as it is illustrated in **Fig. 8a)**. This gliding can be seen as the rotation of the p_1 and p_2 planes in β'-Ga_2S_3 (**Fig. 8a)**) in the anti-clockwise direction, yielding parallel (0 1 0) planes (plane p_3) in φ-Ga_2S_3 (**Fig. 8b)**). This gliding leads to the disappearance of the 3-fold rotoinversion axis of the R-3m phase giving rise a 3-fold axis and to two Ga and three S atom types in the *R*3*m* phase (**Fig. 8b)**). The gliding also leads to the breaking of the half of Ga1-S1 bonds in β'-Ga_2S_3, yielding the change from 6-to-4 fold coordination of the Ga atoms that are now Ga2 atoms in φ-Ga_2S_3 (**Fig. 8b)**). As a result of this gliding there is a jump in the lattice parameter *c*, without a jump in the lattice parameter *a* (**Fig. 7a)**). In this context, we must note that the jump in the *c* value occurs despite bonds in tetrahedra are shorter than octahedra because one of the Ga-S bonds in φ-Ga_2S_3 is parallel to the *c* axis.

At this point, we want to comment on the reverse PT; i.e. from the *R*3*m* to the *R*-3*m* phase on increasing pressure. This HP-PT would be driven by a gliding of Ga2 and S3 atoms in the *R*3*m* phase along the (111) direction of the hexagonal lattice of the *R*3*m* structure. In this way, both 4-fold-coordinated cations and anions become 6-fold-coordinated in the *R*-3*m* phase. However, this simple step seems not to occur in In_2Se_3 because of the appearance of an intermediate β'(*C*2/*m*) phase under increasing pressure.[57]

Now we want to comment on the role of temperature as a driving force to promote the *R*3*m*-to-*R*-3*m* PT (or vice versa). This HT-PT was studied in B_2X_3 compounds by means of molecular dynamics calculations (**Fig. 4** and **Fig. S4)** in **Ref. 62**). Their results agree totally with our PT mechanism proposed on decompression. The *R*3*m*-to-*R*-3*m* HT-PT is driven by the gliding of *B*2 and *X*3 layers in *R*3*m*, becoming *B*1 and *X*2 layers in *R*-3*m*. This is the reverse direction that we propose in our **Fig. 8** for the *R*-3*m*-to-*R*3*m* PT on decompression. Additionally, the molecular dynamics simulations corroborated the mechanism of the *R*3*m*-to-*R*-3*m* PT at HT

experimentally observed in α-In_2Se_3.[55, 56, 110] In a more recent work,[64] the feasibility of *R*3*m*-to-*R*-3*m* PT at HT was evaluated again via molecular dynamics calculations. For the opposite PT (*R*-3*m*-to-*R*3*m*), they revealed a Mexican-hat potential energy surface (a general feature of these B_2X_3 compounds), which acts as an entropy barrier that hampers such PT on decreasing temperature. To overcome such entropy barrier, the application of an OP electric field was proposed. However, upon decompression we have observed in our results, in agreement with those reported by Yang *et al*.,[71] that β'-Ga_2S_3 turns into φ-Ga_2S_3 just decreasing pressure, without the need to apply external fields or LH. We think that molecular dynamics calculations are needed to study the *R*3*m*-to-*R*-3*m* HP-PT in all B_2X_3 sesquichalcogenides, which complement the already performed molecular dynamics simulations of this PT at HT.[62, 64] Those calculations will allow to verify the barriers between these phases at different pressures.

4.4 Relation between the HP phases of Ga_2X_3 (*X*=S, Se, Te) and AGa_2X_4 (*X*=S, Se) compounds

It has been previously commented that β'-Ga_2Te_3 (R-3m) was observed above 5 GPa from β-Ga_2Te_3 (DZ).[75] However, there is still no experimental evidence of β'-Ga_2Se_3 (*R*-3*m*) neither at RC nor at HP. At this point, we have wondered if the *R*3*m* and the *R*-3*m* phases are energetically competitive in Ga_2Se_3 and Ga_2Te_3. To answer this question we have performed DFT PBEsol calculations of several phases in both compounds (see **Figs. S6** and **S7**). We have named β' and φ, the corresponding *R*-3*m* and *R*3*m* phases in Ga_2Se_3 and Ga_2Te_3. As already commented, we have not included either the DZ or DR phases of both compounds because the fractional occupation of cation positions in both phases makes difficult to simulate these structures.

Fig. S6a) evidences that only mono-β-Ga_2Se_3 and β'-Ga_2Se_3 are energetically more favourable than ortho-β-Ga_2Se_3 and φ-Ga_2Se_3. Taking mono-β-Ga_2Se_3 and ortho-β-Ga_2Se_3 as references, β'-Ga_2Se_3 (*R*-3*m*) is predicted to occur above 6.8 (**Fig. S6b)**) and 5.8 GPa (**Fig. S6c)**), respectively, while φ-Ga_2Se_3 (*R*3*m*) is not expected to occur in this sesquichalcogenide. In this context, it is known that DZ α-Ga_2Se_3 and mono-β-Ga_2Se_3 undergo a PT to DR-Ga_2Se_3 above 14 GPa,[72-74] being the DZ-to-DR PT reversible. Concerning the ortho-β-Ga_2Se_3 there are no HP studies, therefore further HP works are required to unveil the possibility that the *R*-3*m* phase could be obtained at HP in Ga_2Se_3.

Regarding Ga_2Te_3, **Fig. S7a)** shows that φ-Ga_2Te_3 (*R*3*m*) is energetically favourable between mono-α-Ga_2Te_3 and ortho-α-Ga_2Te_3 and β'-Ga_2Te_3 (*R*-3*m*), as it occurs in Ga_2S_3. Again, taking mono-α-Ga_2Te_3 and ortho-α-Ga_2Te_3 as references, φ-Ga_2Te_3 is predicted between 11.2 and 11.6 GPa and between 7.2 and 11.6 GPa (**Fig. S7b)** and **Fig. S7c)**), respectively, while β'-Ga_2Te_3 is predicted above 11.6 GPa. At HP only α-Ga_2Te_3 with DZ structure has been studied and β'-Ga_2Te_3 has been obtained above 5 GPa, thus giving support to our calculations.[75] Moreover, HP-electrical measurements have suggested the reversibility of the α-to-β'-Ga_2Te_3 HP-PT.[111] Therefore, future HP works devoted to both mono-α-Ga_2Te_3 and ortho-α-Ga_2Te_3 are needed to explore whether both β' (*R*-3*m*) and φ (*R*3*m*) phases can be attained at HP. If such β'-to-φ PT

is observed in Ga_2Te_3, the PT mechanism could be that explained in the previous section.

The theoretical calculations mentioned in the previous paragraphs and the experiments performed in the three Ga_2X_3 sesquichalcogenides mentioned in the introduction section show that phases at RC, at HT, and at HP are related in these compounds. In particular, they exhibit DZ phases (γ-Ga_2S_3, α-Ga_2Se_3, and β-Ga_2Te_3) or a wurtzite-like superstructure (monoclinic α'-Ga_2S_3, β-Ga_2Se_3, α-Ga_2Te_3, and orthorrombic β-Ga_2Se_3 and α-Ga_2Te_3) at RC or at HT.[23] The difference between them is that the former are disordered phases featuring cation-vacancy mixing at cation positions and the latter exhibit ordered vacancies forming channels. Additionally, these compounds show either the DR (in Ga_2Se_3) or *R*-3*m* (in Ga_2S_3 and Ga_2Te_3) phases at HP (being the *R*3*m* phase, observed in this work for the first time in Ga_2S_3, also energetically competitive in Ga_2Te_3). Considering that the *R*-3*m* phase is a distortion of the rocksalt structure, we can stablish that all Ga_2X_3 sesquichalcogenides share a common NaCl-like phase at HP. Both DR and *R*-3*m* phases differ in the way that vacancies are located. In the DR phase, the 6-fold coordinated cations are mixed with vacancies at cations sites. In contrast, in the β' phase, the 6-fold coordinated cations are ordered and vacancies form planes (interlayer space). Since both Ga_2S_3 and Ga_2Te_3 show the *R*-3*m* phase at HP, we can speculate that the observation of either the DR or *R-3m* phases is not related to the anion size but perhaps to the crystalline structure of the original phase being compressed. In this context, more works of the different polymorphs of these chalcogenides at HP are needed to verify this hypothesis.

What happens when pressure is totally released can be considered another common point of Ga_2X_3 sesquichalcogenides. These compounds usually exhibit a tetrahedral coordination in the original structure at RC and this coordination is again recovered on downstroke despite the PTs at HP could not be reversible; i.e. do not return to the original phase. In this context, it is expected that all Ga_2X_3 phases at LP tend to exhibit the DZ phase with 4-fold coordinated cations mixed with vacancies in the same crystallographic site.

It must be noted that the DZ-to-DR HP-PT is usually reversible since both the initial and final structures are already fully disordered. This has been observed in DZ α-Ga_2Se_3 that transforms into the DR phase (*Fm*-3*m*) on compression.[72, 74] Curiously, DZ α-Ga_2Te_3 turns into β'-Ga_2Te_3 (*R*-3*m*) on compression,[75] and it has been suggested on the basis of resistivity studies at HP that this PT is reversible [111]. In this context, further HP experiments must be conducted in these compounds and especially in DZ-Ga_2S_3 to see if it will undergo a PT to β'-Ga_2S_3 or to the DR phase on compression. We initially expect that DZ-Ga_2S_3 undergoes a reversible PT to the DR phase at HP, as occurs in Ga_2Se_3[72, 74] and also in $CdGa_2S_4$[79] and $CdGa_2Se_4$.[80]

Now, we will review the phases of AGa_2X_4 (*X*=S, Se) OVCs at LP and HP to see the relation between binary and ternary Ga-based chalcogenides. It is well known that AB_2X_4 (*A*=Zn,Cd,Hg; *B*=Al,Ga,In; *X*=S,Se,Te) chalcogenides usually crystallize in DC (*A*=Cd, Hg) and DS (*A*=Zn) phases that are tetrahedrally-coordinated structures derived from the zincblende structure of *AX* compounds. On compression, cations and

vacancies in both DC or DS phases exhibit a pressure-induced cation-vacancy disorder process. This corresponds to an order-disorder PT leading to intermediate partially disordered DS phases prior to undergo a total cation-vacancy disorder process at higher pressures when they undergo a PT to the DR phase.[81, 108, 112] Once the pressure is released, they cannot recover their original DC and DS phases. Instead, a DZ phase is obtained. Moreover, it has been shown that a reversible DZ-to-DR HP-PT is observed in these chalcogenides.[79, 80, 113-115] All this information regarding the pressure-induced order-disorder PTs in ternary OVCs was mapped by Meenakshi *et al.* [81] after taking into consideration the temperature-induced order-disorder PTs in OVCs [116]. Latter, Manjón *et al.* revised and discuss all the possible order-disorder PTs between the DC and the DZ structure in order to classify the degree of disorder in these compounds.[117]

Even though ternary AGa$_2X_4$ and binary Ga$_2X_3$ compounds do not share the same LP phases, all of them can be derived from the tetrahedrally-coordinated zincblende and wurtzite structures and include a second cation and vacancies (AGa$_2X_4$) or just vacancies (Ga$_2X_3$) in cation positions. Therefore, it is clear from the above considerations that both families of Ga-based chalcogenides (Ga$_2X_3$ and AGa$_2X_4$) are OVCs that share common DZ and DR structures at LP and HP, respectively, and that phases can be obtained on compression and decompression. Therefore, considering the information already mentioned we have reformulated the Meenakshi's scheme of HP-PTs in AGa$_2X_4$ compounds to include the experimental and theoretical predicted phase transitions on Ga$_2X_3$ sesquichalcogenides. In this way, we show that Ga$_2X_3$ sesquichalcogenides can also be considered as binary OVCs not only from the point of view of the behavior at HT but also at HP (**Fig. 9**).

One difference between both families of Ga$_2X_3$ and AGa$_2X_4$ chalcogenides shown in **Fig. 9** is that in ternary Ga-based OVCs all HP-PTs are order-disorder PTs, e.g. the DC-to-DR PT. However, most binary Ga-based OVCs show HP-PTs characterized by a relocation of the vacancies rather than a mixture of cations and vacancies (the exception seems to be β-Ga$_2$Se$_3$ that undergoes a PT to the DR phase). In this case, the interlayer space in φ-Ga$_2$S$_3$ and β '-Ga$_2$S$_3$ can be considered as planes of vacancies, as recently suggested.[99, 109] Another difference between both families of chalcogenides is that ternary AGa$_2X_4$ chalcogenides only exhibit DR phases at HP (the R-3m phase has never been found). This difference can be explained because in binary Ga$_2X_3$ compounds, the lack of a second cation allows to obtain either the DR phase (Ga$_2$Se$_3$) or the β' phase (Ga$_2$S$_3$ and Ga$_2$Te$_3$) on compression.

In short, the HP relations emphasized in **Fig. 9** point out that, despite the different stoichiometry of Ga$_2X_3$ and AGa$_2X_4$ compounds and how vacancies are placed in their structures at RC, leading to somewhat different tetrahedrally-coordinated structures, they finally end up sharing an octahedrally-coordinated DR phase at HP as well as a tetrahedrally-coordinated DZ phase on decompression. It is important to emphasized that our newly proposed scheme of pressure-induced phase transitions in Ga-based OVCs include different paths to explore: i) the β'-φ phase transition in Ga$_2$Te$_3$, ii) the obtention of β'-Ga$_2$Se$_3$, and iii) the pressure-induced phase transitions in DZ-Ga$_2$S$_3$.

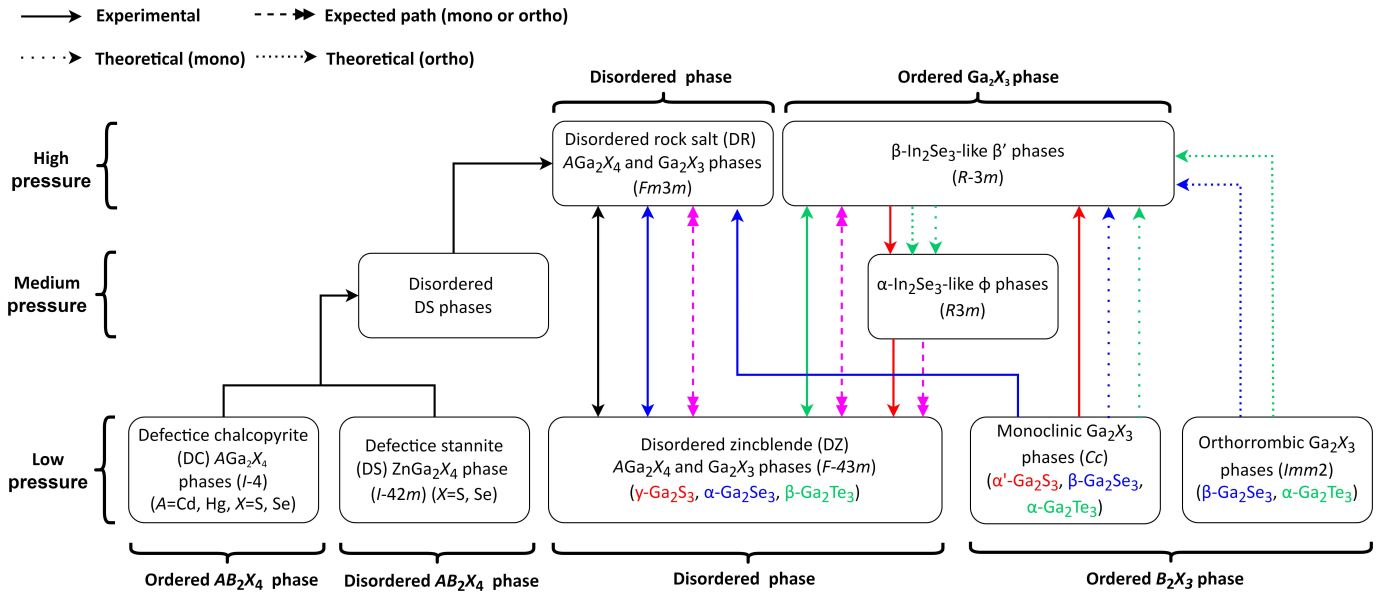

Figure 9. Schematic representation of the behavior of Ga_2X_3 (X=S,Se,Te) and AGa_2X_4 (X=S, Se) chalcogenides at high pressure. Black solid arrows concern to those phase transitions related to the AGa_2X_4 compounds experimentally observed. Red, blue, and green solid arrows show the same for Ga_2S_3, Ga_2Se_3, and Ga_2Te_3, respectively. Blue and green dot arrows refer to that theoretical predicted phase transitions for Ga_2Se_3 and Ga_2Te_3, starting from their monoclinic (*Cc*) phases. The same concerns for blue and green short dot arrows but from their orthorrombic (*Imm*2) phases. Pink dash double arrows indicate that phase transitions expected from both monoclinic and orthorrombic phases, from Ga_2S_3, Ga_2Se_3, and Ga_2Te_3.

5. CONCLUSIONS

In this work, we have reported HP-RS and HP-XRD measurements on α'-Ga_2S_3 (s.g. *Cc*) and DFT simulations of different phases on Ga_2S_3, Ga_2Se_3, and Ga_2Te_3 to identify and analyse the behavior of the HP phases of α'-Ga_2S_3 observed upon compression and decompression. We have demonstrated that the pressure-induced phase transition from α'-Ga_2S_3 to β'-Ga_2S_3 (s.g. *R-3m*, isostructural with β-In_2Se_3) occurs ca. 16.0 GPa and does not require LH to occur, although additional thermal energy could ease the phase transition. The identification of all the Raman-active modes observed above 16 GPa confirms the *R-3m* nature of β'-Ga_2S_3. Moreover, we have shown that the SM observed in β'-Ga_2S_3 comes from the A_{1g}^1-E_g^1 combination and we have provided a hypothesis for its observation that would require to perform HP-RS measurements at HT. On decompression, we have shown that below 9.0 GPa a new phase (φ-Ga_2S_3) with s.g. *R3m* (isostructural with α-In_2Se_3) is attained, and their Raman-active modes have been reported. The experimental and theoretical pressure dependence of the vibrational modes and structural parameters (unit-cell volume per formula unit, zero-pressure axial compressibilities, bulk modulus and their first pressure derivative) have allowed us to identify the nature of φ-Ga_2S_3. This *R-3m*-to-*R3m* phase transition is also supported by the lower energy of the *R3m* phase than the *R-3m* structure at low pressures as evidenced by theoretical *ab initio* simulations.

According to the literature, this is the first time that a *R3m* phase has been synthesised in Ga-based sesquichalcogenides. What is more, this implies a pressure-induced paraelectric-ferroelectric β'-φ phase transition that is similar to the temperature-induced ferroelectric-paraelectric phase transition from α-In_2Se_3-like structure to β-In_2Se_3-like structure predicted in III-VI sesquichalcogenides. Moreover, we have proposed a mechanism to explain the *R-3m*-to-*R3m* phase transition on downstroke for Ga_2S_3 that could also be valid for other III-VI sesquichalcogenides.

On the other hand, a new phase has been observed in Ga_2S_3 on downstroke below 1.0 GPa (γ-Ga_2S_3) that remains metastable at RC. We have tentatively proposed that this phase has a DZ structure (a structure also observed at HT); however, this must be still confirmed by detailed XRD measurements. We have also proposed that γ-Ga_2S_3 is expected to show a phase transition at HP to the DR structure, as it occurs for a-Ga_2Se_3 and DZ-$CdGa_2S_4$. In this context, we have studied the different phase transitions of Ga_2S_3, Ga_2Se_3, and Ga_2Te_3 either at HT or at HP. On the light of the similarities of the HT and HP phase transitions in Ga_2X_3 chalcogenides and AGa_2X_4 chalcogenides, we have reformulated the pressure-behaviour scheme for AGa_2X_4 compounds by including the Ga_2X_3 chalcogenides as another kind of OVCs. In this scheme, both families share the DR phase at HP and the decompressed DZ structure either at LP or at HT, regardless the different stoichiometries and starting structures. These shared phases can only be understood if we consider the presence of ordered vacancies in the crystalline structure of both families at room conditions.

Finally, it must be stressed that our results open new possibilities for the Ga_2S_3 system to design cheap, non-toxic, non-rare-earth, and abundant-element-based devices for SHG, PWS, ferroelectric, pyroelectric, and piezoelectric applications. Moreover, it could guide future works devoted to synthetize of α- and β-In_2Se_3-like structures in

other III-VI B_2X_3 (B=Al, Ga, In; X=S, Se, Te) chalcogenides via compression/decompression, via existing or emerging 2D materials synthesis methods, or even by PLD, as it has been recently demonstrated in β'-Ga_2Te_3.

6. ACKNOWLEDGEMENTS

This publication is part of the project MALTA Consolider Team network (RED2018-102612-T), financed by MINECO/AEI/ 10.13039/501100003329; by I+D+i projects PID2019-106383GB-42/43, FIS2017-83295-P, and PGC2018-097520-A-100 financed by MCIN/AEI/10.13039/501100011033; by project PROMETEO/2018/123 (EFIMAT), financed by Generalitat Valenciana. J.A.S. acknowledges the Ramon y Cajal fellowship (RYC-2015-17482) for financial support. A.M. and P.R.-H. acknowledge computing time provided by Red Española de Supercomputación (RES) and MALTA-Cluster. We also thank ALBA synchrotron light source for funded experiment 2017022088 at the MSPD-BL04 beamline.

7. REFERENCES

1. M. Pardo, M. Guittard, A. Chilouet and A. Tomas, *J. Solid State Chem.*, 1993, **102**, 423-433.
2. A. Tomas, M. Guymont, M. Pardo, M. Guittard and J. Flahaut, *phys. status solidi (a)*, 1988, **107**, 775-784.
3. M. Guymont, A. Tomas, M. Pardo and M. Guittard, *phys. status solidi (a)*, 1989, **113**, K5-K7.
4. Y. Zheng, X. Tang, W. Wang, L. Jin and G. Li, *Adv. Funct. Mater.*, 2021, **31**, 2008307.
5. C. Jastrzebski, D. J. Jastrzebski, V. Kozak, K. Pietak, M. Wierzbicki and W. Gebicki, *Materials Science in Semiconductor Processing*, 2019, **94**, 80-85.
6. J. Kim, W. Park, J.-H. Lee and M.-J. Seong, *Nanotechnol.*, 2019, **30**, 384001.
7. S. Al Garni and A. Qasrawi, *J. Electron. Mater.*, 2017, **46**, 4848-4856.
8. N. Zhou, L. Gan, R. Yang, F. Wang, L. Li, Y. Chen, D. Li and T. Zhai, *ACS Nano*, 2019, **13**, 6297-6307.
9. G. Murtaza, S. Alderhami, Y. T. Alharbi, U. Zulfiqar, M. Hossin, A. M. Alanazi, L. Almanqur, E. U. Onche, S. P. Venkateswaran and D. Lewis, *ACS Appl. Energy Mater.*, 2020, **3**, 1952-1961.
10. H. Liu, K. A. Antwi, N. Yakovlev, H. Tan, L. Ong, S. Chua and D. Chi, *ACS Appl. Mater. Interfaces*, 2014, **6**, 3501-3507.
11. M. M. Alsaif, N. Pillai, S. Kuriakose, S. Walia, A. Jannat, K. Xu, T. Alkathiri, M. Mohiuddin, T. Daeneke and K. Kalantar-Zadeh, *ACS Appl. Nano Mater.*, 2019, **2**, 4665-4672.
12. K. Xu, B. Y. Zhang, Y. Hu, M. W. Khan, R. Ou, Q. Ma, C. Shangguan, B. J. Murdoch, W. Chen and X. Wen, *J. Mater. Chem. C*, 2021, **9**, 3115-3121.
13. K. Eriguchi, C. Biaou, S. Das, K. M. Yu, J. Wu and O. D. Dubon, *AIP Advances*, 2020, **10**, 105215.
14. S. Chandrasekaran, D. Ma, Y. Ge, L. Deng, C. Bowen, J. Roscow, Y. Zhang, Z. Lin, R. Misra and J. Li, *Nano Energy*, 2020, **77**, 105080.
15. N. Zhou, R. Yang and T. Zhai, *Materials Today Nano*, 2019, **8**, 100051.

16. F. Wang, Z. Wang, T. A. Shifa, Y. Wen, F. Wang, X. Zhan, Q. Wang, K. Xu, Y. Huang and L. Yin, *Adv. Funct. Mater.*, 2017, **27**, 1603254.
17. S. Alharbi and A. Qasrawi, *Plasmonics*, 2017, **12**, 1045-1049.
18. 2017.
19. F. Zheng, J. Shen, Y. Liu, W. Kim, M. Chu, M. Ider, X. Bao and T. Anderson, *Calphad*, 2008, **32**, 432-438.
20. M. Kerkhoff and V. Leute, *J. Alloys Compd.*, 2004, **381**, 124-129.
21. J. Woolley, B. Pamplin and P. Holmes, *J. Less-Common Met.*, 1959, **1**, 362-376.
22. G.-Y. Huang, N. Abdul-Jabbar and B. Wirth, *J. Phys.: Condens. Matter*, 2013, **25**, 225503.
23. E. Finkman, J. Tauc, R. Kershaw and A. Wold, *Phys. Rev. B*, 1975, **11**, 3785-3794.
24. D. Weitze and V. Leute, *J. Alloys Compd.*, 1996, **236**, 229-235.
25. G.-Y. Huang, N. Abdul-Jabbar and B. Wirth, *Acta Mater.*, 2014, **71**, 349-369.
26. Z. Dai and F. Ohuchi, *Appl. Phys. Lett.*, 1998, **73**, 966-968.
27. R. Ollitrault-Fichet, J. Rivet and J. Flahaut, *J. Solid State Chem.*, 1980, **33**, 49-61.
28. Y. Liu, Z. Dou, M. Enoki, Y. Oyama and H. Ohtani, *Calphad*, 2020, **71**, 102206.
29. J. Antonopoulos, T. Karakostas, G. Bleris and N. Economou, *J. Mater. Sci.*, 1981, **16**, 733-738.
30. M. Guymont, A. Tomas and M. Guittard, *Philos. Mag. A*, 1992, **66**, 133-139.
31. C. Chou, J. Hutchison, D. Cherns, M. J. Casanove, J. Steeds, R. Vincent, B. Lunn and D. Ashenford, *J. Appl. Phys.*, 1993, **74**, 6566-6570.
32. P. Newman and J. Cundall, *Nature*, 1963, **200**, 876-876.
33. M. Rusu, S. Wiesner, S. Lindner, E. Strub, J. Röhrich, R. Würz, W. Fritsch, W. Bohne, T. Schedel-Niedrig and M. C. Lux-Steiner, *J. Phys.: Condens. Matter*, 2003, **15**, 8185-8193.
34. K. Ueno, S. Tokuchi, K. Saiki and A. Koma, *J. Cryst. Growth*, 2002, **237**, 1610-1614.
35. K. George, C. H. de Groot, C. Gurnani, A. L. Hector, R. Huang, M. Jura, W. Levason and G. Reid, *Chem. Mater.*, 2013, **25**, 1829-1836.
36. I. H. Mutlu, M. Z. Zarbaliyev and F. Aslan, *Journal of sol-gel science technology*, 2009, **50**, 271-274.
37. N. Kojima, C. Morales, Y. Ohshita and M. Yamaguchi, *Ga_2Se_3 and $(InGa)_2Se_3$ as novel buffer layers in the GaAs on Si system* in *9th Int. Conf. on Concentrator Photovoltaic Systems. AIP Conference Proceedings*, 2013.
38. B. Li, Y. Xia, W. Ho and M. Xie, *J. Cryst. Growth*, 2017, **459**, 76-80.
39. M. Isik and N. Gasanly, *Vacuum*, 2020, **179**, 109501.
40. E. Yitamben, T. Lovejoy, D. Paul, J. Callaghan, F. Ohuchi and M. Olmstead, *Phys. Rev. B*, 2009, **80**, 075314.
41. P.-Y. Su, S. Banerjee, R. Dahal and I. B. Bhat, *Electronic Materials Letters*, 2016, **12**, 82-86.

42. A. Kolobov, P. Fons, M. Krbal, K. Mitrofanov, J. Tominaga and T. Uruga, *Phys. Rev. B*, 2017, **95**, 054114.
43. H. Zhu, J. Yin, Y. Xia and Z. Liu, *Appl. Phys. Lett.*, 2010, **97**, 083504.
44. R. Al-Orainy, A. Nagat, S. Hussein and A. Ebnalwaled, *Int. Res. J. Eng. Technol.*, 2015, **2**, 816.
45. H.-C. Chang, M.-H. Chiang, T.-C. Tsai, T.-H. Chen, W.-T. Whang and C.-H. Chen, *Nanoscale*, 2014, **6**, 14280-14288.
46. A. Tverjanovich, M. Khomenko, C. J. Benmore, S. Bereznev, A. Sokolov, D. Fontanari, A. Kiselev, A. Lotin and E. Bychkov, *J. Mater. Chem. C*, 2021, **9**, 17019-17032.
47. C.-H. Ho, *ACS Omega*, 2020, **5**, 18527-18534.
48. Y. Hu, J. Wang, J. Lai, X. Zheng, H. Ji, H. Liu and Z. Jin, *Mater. Lett.*, 2016, **170**, 151-155.
49. R. Valeev, V. Kriventsov and N. Mezentsev, *Bull. Russ. Acad. Sci.: Phys.*, 2013, **77**, 1154-1156.
50. S. P. Guo, X. Cheng, Z. D. Sun, Y. Chi, B. W. Liu, X. M. Jiang, S. F. Li, H. G. Xue, S. Deng and V. Duppel, *Angewandte Chemie International Edition*, 2019, **131**, 8171-8175.
51. H. Jin, H. Zhang, J. Li, T. Wang, L. Wan, H. Guo and Y. Wei, *The journal of physical chemistry letters*, 2019, **10**, 5211-5218.
52. F. Manjón, R. Vilaplana, O. Gomis, E. Pérez‐González, D. Santamaría‐Pérez, V. Marín‐Borrás, A. Segura, J. González, P. Rodríguez‐Hernández and A. Muñoz, *phys. status solidi (b)*, 2013, **250**, 669-676.
53. S. Popović, A. Tonejc, B. Gržeta-Plenković, B. Čelustka and R. Trojko, *J. Appl. Crystallogr.*, 1979, **12**, 416-420.
54. J. Ye, S. Soeda, Y. Nakamura and O. Nittono, *Jpn. J. Appl. Phys.*, 1998, **37**, 4264-4271.
55. K. Osamura, Y. Murakami and Y. Tomiie, *J. Phys. Soc. Jpn.*, 1966, **21**, 1848-1848.
56. G. Han, Z. G. Chen, J. Drennan and J. Zou, *Small*, 2014, **10**, 2747-2765.
57. R. Vilaplana, S. G. Parra, A. Jorge-Montero, P. Rodríguez-Hernández, A. Munoz, D. Errandonea, A. Segura and F. J. Manjón, *Inorg. Mater.*, 2018, **57**, 8241-8252.
58. J. Zhao and L. Yang, *J. Phys. Chem. C*, 2014, **118**, 5445-5452.
59. W. Ding, J. Zhu, Z. Wang, Y. Gao, D. Xiao, Y. Gu, Z. Zhang and W. Zhu, *Nat. Commun.*, 2017, **8**, 14956.
60. L. Hu and X. Huang, *RSC Adv.*, 2017, **7**, 55034-55043.
61. C.-F. Fu, J. Sun, Q. Luo, X. Li, W. Hu and J. Yang, *Nano Lett.*, 2018, **18**, 6312-6317.
62. J. Liu and S. Pantelides, *2D Mater.*, 2019, **6**, 025001.
63. J. Huang, S.-H. Lee, Y.-W. Son, A. Supka and S. Liu, *Phys. Rev. B*, 2020, **102**, 165157.
64. Y.-T. Huang, N.-K. Chen, Z.-Z. Li, X.-B. Li, X.-P. Wang, Q.-D. Chen, H.-B. Sun and S. Zhang, *Appl. Phys. Rev.*, 2021, **8**, 031413.
65. L. Hu and D. Wei, *J. Phys. Chem. C*, 2018, **122**, 27795-27802.

66. H. Cai, Y. Gu, Y.-C. Lin, Y. Yu, D. B. Geohegan and K. Xiao, *Appl. Phys. Rev.*, 2019, **6**, 041312.
67. J. Shang, X. Tang and L. Kou, *Wiley Interdisciplinary Reviews: Computational Molecular Science*, 2021, **11**, e1496.
68. N. N. Hieu, H. V. Phuc, A. Kartamyshev and T. V. Vu, *Phys. Rev. B*, 2022, **105**, 075402.
69. X. Lai, F. Zhu, S. Qin, D. Chen, Y. Li, K. Yang and X. Wu, *J. Appl. Phys.*, 2014, **116**, 193507.
70. S. Gallego-Parra, R. Vilaplana, O. Gomis, E. L. da Silva, A. Otero-de-la-Roza, P. Rodríguez-Hernández, A. Muñoz, J. González, J. Sans and V. Cuenca-Gotor, *Phys. Chem. Chem. Phys.*, 2021, **23**, 6841-6862.
71. L. Yang, J. Jiang, L. Dai, H. Hu, M. Hong, X. Zhang, H. Li and P. Liu, *J. Mater. Chem. C*, 2021, **9**, 2912-2918.
72. M. Takumi, A. Hirata, T. Ueda, Y. Koshio, H. Nishimura and K. Nagata, *Phys. Status Solidi*, 2001, **223**, 423-426.
73. M. Takumi, Y. Koshio and K. Nagata, *phys. status solidi (b)*, 1999, **211**, 123-129.
74. M. Hong, L. Dai, H. Hu and X. Zhang, *Crystals* 2021, **11**, 746.
75. N. Serebryanaya, *Powder Diffr.*, 1992, **7**, 99-102.
76. Z. Lu, G. P. Neupane, G. Jia, H. Zhao, D. Qi, Y. Du, Y. Lu and Z. Yin, *Adv. Funct. Mater.*, 2020, **30**, 2001127.
77. P. Tao, S. Yao, F. Liu, B. Wang, F. Huang and M. Wang, *J. Mater. Chem. A*, 2019, **7**, 23512-23536.
78. H. Yuan, H. Wang and Y. Cui, *Accounts of chemical research*, 2015, **48**, 81-90.
79. S. Gallego-Parra, O. Gomis, R. Vilaplana, H. M. Ortiz, E. Perez-Gonzalez, R. Luna, P. Rodríguez-Hernández, A. Muñoz, V. Ursaki and I. Tiginyanu, *J. Appl. Phys.*, 2019, **125**, 115901.
80. O. Gomis, R. Vilaplana, F. J. Manjón, E. Pérez-González, J. López-Solano, P. Rodríguez-Hernández, A. Muñoz, D. Errandonea, J. Ruiz-Fuertes, A. Segura, D. Santamaria-Pérez, I. M. Tiginyanu and V. Ursaki, *J. Appl. Phys.*, 2012, **111**, 013518.
81. S. Meenakshi, V. Vijyakumar, B. K. Godwal, A. Eifler, I. Orgzall, S. Tkachev and H. D. Hochheimer, *J. Phys. Chem. Solids*, 2006, **67**, 1660-1667.
82. H. K. Mao, J. A. Xu and P. M. Bell, *J. Geophys. Res.: Solid Earth*, 1986, **91**, 4673-4676.
83. A. Debernardi, C. Ulrich, M. Cardona and K. Syassen, *phys. status solidi (b)*, 2001, **223**, 213-223.
84. F. Fauth, I. Peral, C. Popescu and M. Knapp, *Powder Diffr.*, 2013, **28**, S360-S370.
85. A. Dewaele, P. Loubeyre and M. Mezouar, *Phys. Rev. B*, 2004, **70**, 094112.
86. C. Prescher and V. B. Prakapenka, *High Pressure Res.*, 2015, **35**, 223-230.
87. B. H. Toby and R. B. Von Dreele, *J. Appl. Crystallogr.*, 2013, **46**, 544-549.
88. P. Hohenberg and W. Kohn, *Physical review*, 1964, **136**, B864-B871.
89. G. Kresse and J. Hafner, *Phys. Rev. B*, 1993, **47**, 558-561.
90. P. E. Blöchl, *Phys. Rev. B*, 1994, **50**, 17953-17979.

91. G. Kresse and D. Joubert, *Phys. Rev. B*, 1999, **59**, 1758-1775.
92. J. P. Perdew, A. Ruzsinszky, G. I. Csonka, O. A. Vydrov, G. E. Scuseria, L. A. Constantin, X. Zhou and K. Burke, *Phys. Rev. Lett.*, 2008, **100**, 136406.
93. J. P. Perdew, K. Burke and M. Ernzerhof, *Phys. Rev. Lett.*, 1996, **77**, 3865-3868.
94. S. Grimme, J. Antony, S. Ehrlich and H. J. T. J. o. c. p. Krieg, *Journal of Chemical Physics*, 2010, **132**, 154104.
95. Computer Code Phonon, see: http://www.computingformaterials.com/index.html).
96. J. Sans, F. Manjón, A. Pereira, R. Vilaplana, O. Gomis, A. Segura, A. Muñoz, P. Rodríguez-Hernández, C. Popescu and C. Drasar, *Phys. Rev. B*, 2016, **93**, 024110.
97. J. A. Sans, R. Vilaplana, E. L. da Silva, C. Popescu, V. P. Cuenca-Gotor, A. n. Andrada-Chacón, J. Sánchez-Benitez, O. Gomis, A. L. Pereira and P. Rodríguez-Hernández, *Inorg. Mater.*, 2020.
98. F. Manjón, D. Errandonea, A. Segura, J. Chervin and V. Muñoz, *High Pressure Res.*, 2002, **22**, 261-266.
99. S. Gallego-Parra, Ó. Gomis, R. Vilaplana, V. P. Cuenca-Gotor, D. Martínez-García, P. Rodríguez-Hernández, A. Muñoz, A. Romero, A. Majumdar and R. Ahuja, *Phys. Chem. Chem. Phys.*, 2021, **23**, 23625-23642.
100. T. Ungár, G. Tichy, J. Gubicza and R. Hellmig, *Powder Diffr.*, 2005, **20**, 366-375.
101. S. Klotz, J. C. Chervin, P. Munsch and G. Le Marchand, *J. Phys. D: Appl. Phys.*, 2009, **42**, 075413.
102. R. J. Angel, M. Bujak, J. Zhao, G. D. Gatta and S. D. J. J. o. A. C. Jacobsen, 2007, **40**, 26-32.
103. F. J. Manjón, J. Á. Sans, P. Rodríguez-Hernández and A. Muñoz, 2021, **11**, 1283.
104. R. Lewandowska, R. Bacewicz, J. Filipowicz and W. Paszkowicz, *Mater. Res. Bull.*, 2001, **36**, 2577-2583.
105. J. Weszka, P. Daniel, A. Burian, A. Burian and A. Nguyen, *J. Non-Cryst. Solids*, 2000, **265**, 98-104.
106. N. Balakrishnan, E. D. Steer, E. F. Smith, Z. R. Kudrynskyi, Z. D. Kovalyuk, L. Eaves, A. Patanè and P. H. Beton, *2D Mater.*, 2018, **5**, 035026.
107. L. Liu, J. Dong, J. Huang, A. Nie, K. Zhai, J. Xiang, B. Wang, F. Wen, C. Mu and Z. Zhao, *Chem. Mater.*, 2019, **31**, 10143-10149.
108. A. Grzechnik, V. V. Ursaki, K. Syassen, I. Loa, I. M. Tiginyanu and M. Hanfland, *J. Solid State Chem.*, 2001, **160**, 205-211.
109. J. L. Da Silva, A. Walsh and H. Lee, *Phys. Rev. B*, 2008, **78**, 224111.
110. X. Tao and Y. Gu, *Nano Lett.*, 2013, **13**, 3501-3505.
111. D. Bose, S. Sen, D. Joshi and S. Vaidya, *Mater. Lett.*, 1982, **1**, 61-63.
112. S. Meenakshi, V. Vijayakumar, A. Eifler, H. J. J. o. P. Hochheimer and C. o. Solids, *J. Phys. Chem. Solids*, 2010, **71**, 832-835.
113. R. Vilaplana, M. Robledillo, O. Gomis, J. A. Sans, F. J. Manjón, E. Pérez-González, P. Rodríguez-Hernández, A. Muñoz, I. M. Tiginyanu and V. V. Ursaki, *J. Appl. Phys.*, 2013, **113**, 093512.

114. R. Vilaplana, O. Gomis, F. J. Manjón, H. M. Ortiz, E. Pérez-González, J. López-Solano, P. Rodríguez-Hernández, A. Muñoz, D. Errandonea, V. V. Ursaki and I. M. Tiginyanu, *J. Phys. Chem. C*, 2013, **117**, 15773-15781.
115. R. Vilaplana, O. Gomis, E. Pérez-González, H. M. Ortiz, F. J. Manjón, P. Rodríguez-Hernández, A. Munoz, P. Alonso-Gutiérrez, M. L. Sanjuán, V. V. Ursaki and I. M. Tiginyanu, *J. Appl. Phys.*, 2013, **113**, 233501.
116. J. E. Bernard and A. Zunger, *Phys. Rev. B*, 1988, **37**, 6835-6856.
117. F. J. Manjón, O. Gomis, R. Vilaplana, J. A. Sans and H. M. Ortiz, *phys. status solidi (b)*, 2013, **250**, 1496-1504.

Supplementary Information of

High-pressure synthesis of β- and α-In_2Se_3-like structures in Ga_2S_3

Samuel Gallego-Parra[1]*, Rosario Vilaplana[2*], Oscar Gomis[2], Plácida Rodríguez-Hernández[3], Alfonso Muñoz[3], Jesus Antonio González[4], Juan Angel Sans[1], Catalin Popescu[5] and Francisco Javier Manjón[1]

[1]*Instituto de Diseño para la Fabricación y Producción Automatizada, MALTA Consolider Team, Universitat Politècnica de València, 46022 València, Spain*

[2] *Centro de Tecnologías Físicas, MALTA Consolider Team, Universitat Politècnica de València, 46022 Valencia, Spain*

[3]*Departamento de Física, Instituto de Materiales y Nanotecnología, MALTA Consolider Team, Universidad de La Laguna, 38207 San Cristóbal de La Laguna, Spain*

[4]*Ciencias de la Tierra y Fisica de la Materia Condensada, MALTA Consolider Team, Universidad de Cantabria, 39005, Santander, Spain*

[5]*ALBA-CELLS, MALTA Consolider Team, 08290 Cerdanyola del Valles (Barcelona), Spain*

*Corresponding authors: S. Gallego-Parra (sagalpar@doctor.upv.es), R. Vilaplana (rovilap@fis.upv.es)

Figure S1. Crystal structure of ortho- β-Ga_2Se_3 and α-Ga_2Te_3 (orthorhombic, S.G. *Imm*2, No. 44, Z=8). Cations and anions are depicted as yellow and green spheres, respectively.

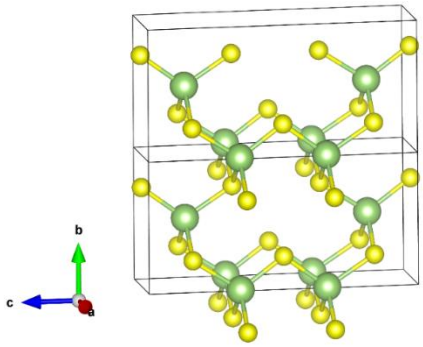

Figure S2. Selected normalized Raman spectra of α'-Ga_2S_3 under compression from a) run-2, b) run-3 and c) run-4. Red and black colors represent spectra of α'-Ga_2S_3 and β'-Ga_2S_3, respectively. For the sake of clarity, only the most intense Raman mode, the A'(6), of α'-Ga_2S_3 is marked. Down and up black arrows indicate emerging or disappearing peaks under compression. In β'-Ga_2S_3, the soft mode (with negative pressure coefficient) is labeled as the SM mode. The reader is referred to our previous work (**Ref. 1**) for further information about pressure dependence of the Raman modes of α'-Ga_2S_3. In runs 3 and 4, rotational N_2 and O_2 modes below 150 cm^{-1} appear above 14.0 and 13.1 GPa, respectively.

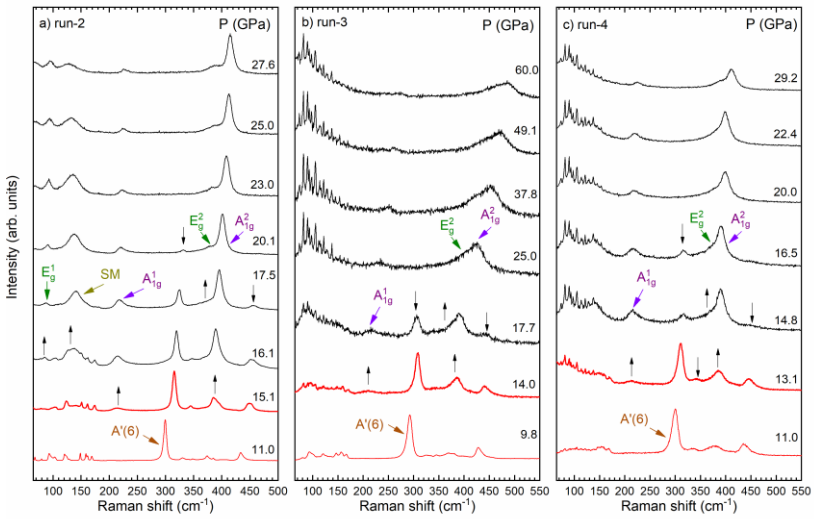

* M-E: methanol-ethanol, S: silicon oil.
[a] run-2, M-E, [b] run-3, S, [c] run-4, S.

Figure S3. Experimental (symbols) and theoretical (solid lines) PBE-D3 pressure dependence of the Raman frequencies of β'-Ga_2S_3 on upstroke (all runs). The experimental A_{1g}^1-E_g^1 frequency is labeled with hollow star symbols to compare with the SM mode.

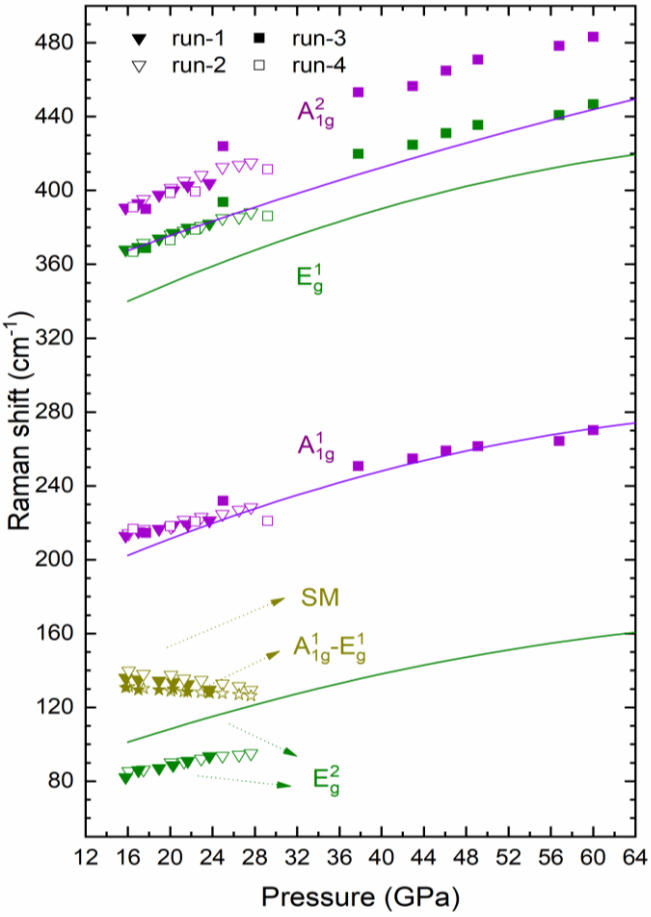

Figure S4. Theoretical phonon dispersion curves of β'-Ga_2S_3 at a) 17.9 and b) 18.6 GPa and c) φ-Ga_2S_3 at 15 GPa.

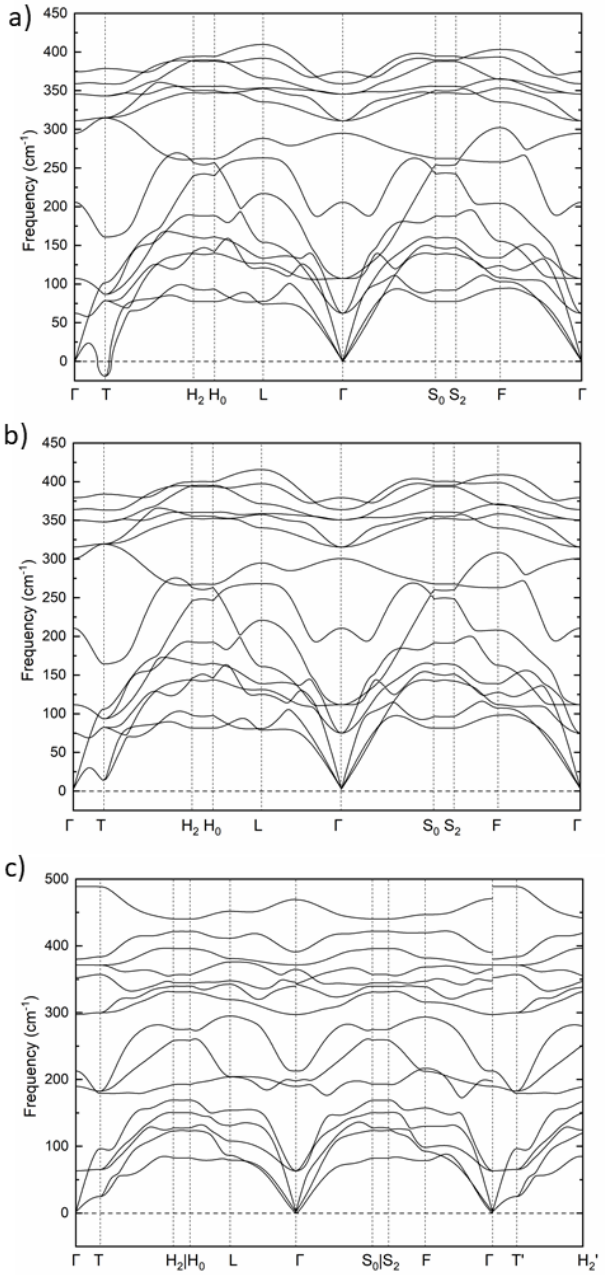

Figure S5. a) Theoretical volume dependence of the total energy of α'-, β'-, and φ-Ga_2S_3 and b) theoretical pressure dependence of the enthalpy difference between α'-, β'-, and φ-Ga_2S_3. Enthalpy of α'-Ga_2S_3 is taken as reference.

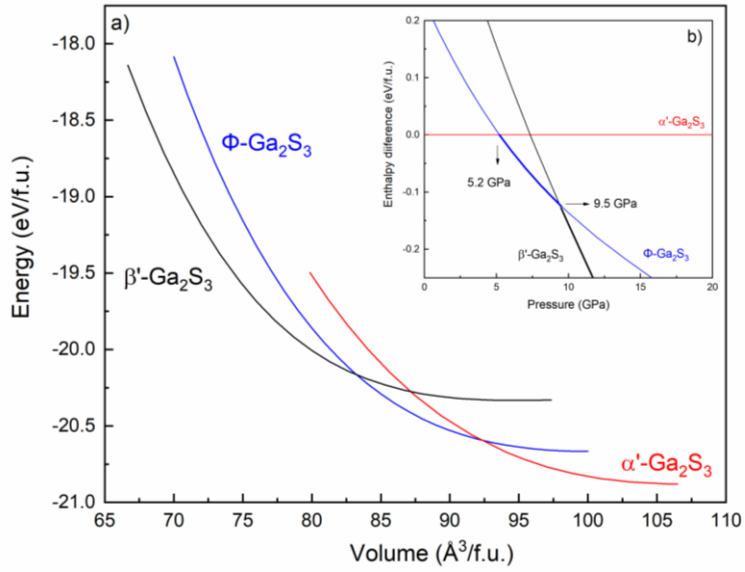

Figure S6. a) Theoretical volume dependence of the total energy of mono-β-, ortho-β-, β'-, and φ-Ga_2Se_3. b) Theoretical pressure dependence of the enthalpy difference between mono-β-, β'-, and φ-Ga_2Se_3, taking the former as a reference, and c) between ortho-β-, β'-, and φ-Ga_2Se_3, taking the former as a reference.

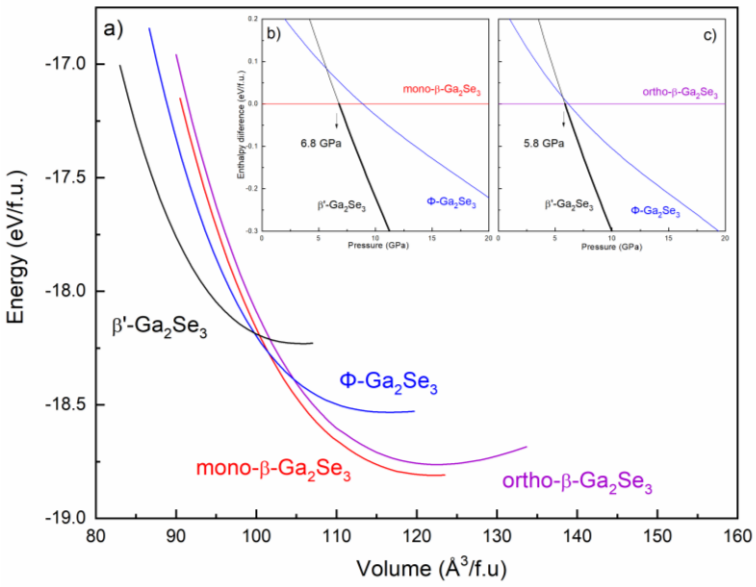

Figure S7. a) Theoretical volume dependence of the energy of mono-α-, ortho-α-, β'-, and φ-Ga_2Te_3. b) Theoretical pressure dependence of the enthalpy difference between mono-α-', β'-, and φ-Ga_2Te_3, taking the former as a reference, and c) between ortho-α-, β-', and φ-Ga_2Te_3, taking the former as a reference.

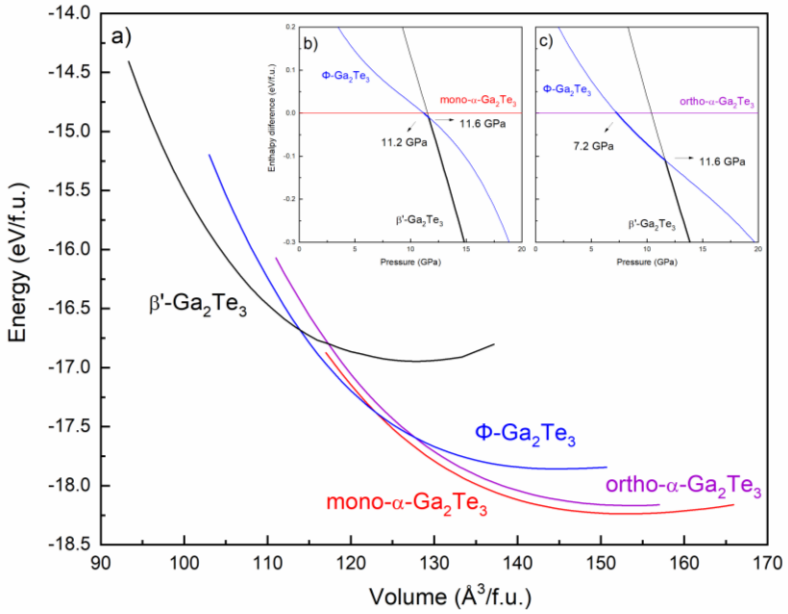

References

1. S. Gallego-Parra, R. Vilaplana, O. Gomis, E. L. da Silva, A. Otero-de-la-Roza, P. Rodríguez-Hernández, A. Muñoz, J. González, J. Sans and V. Cuenca-Gotor, *Phys. Chem. Chem. Phys.*, 2021, **23**, 6841-6862.

Chapter 3
Discussion

For sake of simplification, throughout this chapter, **Refs. 1, 2, 3,** and **4** will refer to the published articles reported in sections **2.1**, **2.2**, **2.3** and **2.4** respectively. An additional section will be added for the references cited in this chapter. In this way, the reader does not require to consult such references in **Chapter 2**.

3.1. Experimental and theoretical studies on α-In_2Se_3 at high pressure

Before commenting our work, we have to mention that the pressure effects were evaluated not only in α-In_2Se_3 (S.G. *R*3*m*) in **Refs. 5, 6,** and **7**, but also in γ-In_2Se_3 (S.G. $P6_1$) in **Ref. 8**. In this latter work, authors studied powder and nanowire samples and observed a γ → β (S.G. *R*-3*m*) PT between 2.8-3.2 GPa and 3.2-3.7 GPa, respectively. The XRD patterns at 3.1 and 3.8 GPa, for powder and nanowire samples, respectively, show the characteristic (003), (006), and (105) reflections peaks of tetradymite-like β-In_2Se_3 (Fig. 2 and 4 of **Ref. 8**). However, additional data regarding the pressure dependence of volume, EoS, and XRD patterns of β-In_2Se_3 above such pressures were not provided. Regarding the HP behaviour of α-In_2Se_3, there were many controversial points in the previous HP works. First, **Refs. 5** and **6** concluded that the α→β PT occurred at about 0.8 GPa, without any intermediate phase, at the sight of their XRD measurements. However, according to XRD measurements, three PTs in total, following a sequence: α → β' → β → defective Th_3P_4-like structure, at 0.8, 5.0 and 32.1 GPa, respectively, were reported in **Ref. 7**. In that work, HP-RS measurements from 1.2 to 26.9 GPa were also reported (**Fig. S4** of **Ref. 7**). Unfortunately, the authors could not measure several RS spectra of the low-pressure phase α-In_2Se_3 due to small range of pressures measured before the PT to ~~the~~ β'-In_2Se_3. Another fact to remark about that work is the softening of a Raman mode located at around 230 cm^{-1} at 1.2 GPa that was observed up to 26.9 GPa. It is noteworthy the increase of the intensity of this mode abruptly above 5.2 GPa. At this pressure, a change in the trend of such soft mode was observed, which was associated to the β'→ β PT, as observed in HP-XRD measurements. It must be stressed that a soft mode has not been theoretically predicted nor experimentally found in HP-RS measurements in other tetradymite-like (S.G. *R*-3*m*) compounds, such as α-Sb_2Te_3, α-Bi_2Se_3, and α-Bi_2Te_3.[9]

In view of these points, we decided to revisit the different pressure-induced PTs on α-In_2Se_3, in addition to study the pressure dependence of its vibrational properties and evaluate the presence of the soft mode in the RS. For this reason, we performed HP-XRD and HP-RS measurements, supported with computational simulations (total-energy and lattice-dynamics calculations). Our HP-XRD measurements up to 20.2 GPa confirmed the sequence α → β'→ β, as was published in **Ref. 7**. Both α and β' phases are easily distinguished by their characteristic XRD patterns (**Fig. 2** of **Ref. 1**). Above 1.2 GPa, the β' phase can be indexed, whereas it was not clear at which pressure the β'→ β PT happened. According to **Ref. 7**, the β'→ β PT was determined at 5 GPa by the merging of two peaks in the XRD patterns. However, this merging is progressive, from 2.5 to 7.2 GPa, in view of **Fig. S2** of **Ref. 7** or even in our HP-XRD measurements (**Fig. S1** of **Ref. 1**), so we cannot taxatively conclude at which pressure the PT occurs in this pressure range. Instead, we found a peak in our XRD patterns whose disappearance at 12.7 GPa points out the β'→ β PT. This peak is located at around 15.4 degrees at 11.9 GPa (inset of **Fig. 2** of **Ref. 1**), indexed in the β' phase

but not with β phase, and disappears at 12.7 GPa, allowing to index the β phase with better R-values than before such pressure. In our work (**Ref. 1**), further support to this β'→ β PT above 10 GPa is given by our HP-RS and computational simulations.

According to the pressure dependence of the experimental and theoretical volumes of the different phases involved (**Fig. 3** of **Ref. 1**), the α → β' PT is of 1st order character since it implies a relative volume change $\Delta V/V = 6\%$. However, the small relative volume change of the β' → β PT ($\Delta V/V = 1\%$), within the incertitude of the experimental estimation, could be a 2nd order PT. Despite our disagreement in determining the pressure of the β → β' PT in comparison to **Ref. 7**, our $\Delta V/V$ obtained for both PTs are similar to those published in such work, thus confirming the nature of the two PTs. When it comes to structural properties derived from the EoS, more specifically the bulk moduli from the BM2-EoS, we realise that those published for α and β' phases in Ref. 7 are notably underestimated with respect to our values (**Table 2** of **Ref. 1**). However, the bulk moduli calculated from our results and those published from **Ref. 7** for both phases follow the same sequence B_0 (β) > B_0 (β') > B_0 (α). The underestimation of the bulk moduli is mainly due a bad fit of experimental data due to the use of volume values corresponding to high enough pressures in which phase coexistence has been found. To avoid this fit distortion, we just fitted data from smaller pressure ranges, in which phase coexistence can be ruled out.

After our work was published, another work reporting HP-XRD and HP-RS measurements in β'-In_2Se_3 was released in 2020.[10] In that work, silicon oil was used as a PTM and original β'-In_2Se_3 samples (with SeO_2 impurity) were compressed. In that work, HP-XRD measurements (**Fig. 1** of **Ref. 10**) suggested a β' phase observed above 1.1 GPa with β' → β PT occurring at 11.5 GPa, by the disappearance of the same peak that we observed at 15.4 degrees at 12.7 GPa (at 22 degrees at 11.5 GPa, see inset of **Fig. 1** of **Ref. 10**). However, the presence of peaks from SeO_2 impurity and the many broad peaks above 22 degrees in the XRD patterns do not make easy to discern properly the β' → β PT. Their $\Delta V/V$ associated to the β' → β PT is 1.6%, quite like our value, supporting the 2nd order character of this PT. On the other hand, their bulk moduli from BM2-EoS are 40.5 GPa and 73.8 GPa, for β' and β phases, respectively. Whereas the former is between those from **Ref. 7** and our value, the latter is much higher than those from **Ref. 7** and our value. We consider that the larger value of the bulk modulus of the β phase occurring above 10 GPa is probably due to the non-hydrostatic conditions of the PTM used in **Ref. 10** above than pressure. It must be mentioned that the results from **Ref. 10** must be taken with caution since in that work very few information is provided about the sample and DAC used.

Regarding the HP-RS measurements carried out up to 18.5 GPa (Fig. 4 of **Ref. 1**), our first motivation was twofold: firstly, to study the pressure evolution of the vibrational modes of α-In_2Se_3, which was not performed in **Ref. 7**, and secondly, to ascertain the presence of the soft mode reported in the same work. For the first reason, we loaded the DAC with an initial pressure below that of α → β' PT. As can be seen in **Fig. 4** of **Ref. 1**, we just could obtain one RS spectrum of α-In_2Se_3 inside the DAC at 0.9 GPa, in addition to that measured at RC. Both RS spectra resemble quite well to those previously published at RC.[11-13] Despite we only had two RS spectra, we obtained a good agreement between the experimental and theoretical frequencies (**Table 4** and

Fig. 5 of **Ref. 1**), allowing us to assign the symmetry of each mode observed. In this sense, this is the first time that the pressure dependence of the vibrational properties of α-In_2Se_3 have been studied, both experimentally and theoretically.

Before discussing the β' → β PT from the vibrational point of view, we can observe the lack of the soft mode in our RS spectra (**Figs. 4** and **5** of **Ref. 1**). Without a doubt whatsoever, the soft mode published in **Ref. 7** came from Se clusters, from the thermal degradation of the sample under a high laser power employed (20 mW of laser power used in **Ref. 7**, unlike our less than 1 mW used in our HP-RS measurements, modulated by filters). The reader can compare the softening mode observed in the RS spectra, from **Fig. S4** of **Ref. 7**, with those observed in the RS spectra of amorphous Se samples at HP.[14-16] Going back to the β' → β PT, the A_g^4 mode of the β' phase emerges at 0.9 GPa, in coexistence with the α phase (**Fig. 4** of **Ref. 1**). As it happened with the α phase, we could assign the symmetry of each observed mode for both β' and β phases (**Table 5** and **6** of **Ref. 1**). The mode pairs A_g^2 and E_g^1, and A_g^4 and A_{1g}^2 from β' and β phases are almost indistinguishable experimentally. However, the fact that the E_g^1 and A_{1g}^2 (from the β phase) clearly have different pressure coefficients in comparison to those from A_g^1 and B_g^2 (from the β' phase), linked to the disappearance of B_g^1 and A_g^3 of the β' phase, support experimentally the onset of the β' → β PT between 10-12 GPa. The theoretical trends of these modes from both β' and β phases support this PT between 10-12 GPa as well (**Fig. 5** of **Ref. 1**). Another experimental support to this PT is the pressure dependence of the FWHM of the A_g^2 of β' phase (**Fig. 6** of **Ref. 1**), which is stabilized between 10-12 GPa because this A_g^2 becomes the A_{1g}^1 of the β phase. It must be noted that the similar trend of A_g^2 and E_g^1 modes from β' and β phases, respectively, and the disappearance of the A_g^3 mode of the former phase were also observed in the HP-RS measurements of the later work published (**Ref. 10**).

Even the theoretical frequencies of most of IR modes for both phases exhibit great similarities (**Fig. S6** of **Ref. 1**), but different pressure dependence in the pressure range of 10-12 GPa, as has been stressed for the Raman modes. However, the lowest-frequency IR modes of the β' phase, the A_u^1 and B_u^1 modes, increase their frequencies sharply from negative to positive values. Above 10 GPa, these IR modes of the β' phase intersect with the lowest-frequency IR mode of the β phase, the A_u^1 mode, giving further theoretical support to the β' → β PT from the vibrational point of view. We measured the RS spectra of In_2Se_3 under decompression from 18.5 GPa down to room pressure (**Fig. S4** of **Ref. 1**). From those measurements we conclude that the β' → β PT is reversible, unlike the α → β' PT, as can be seen in **Fig. S5** of **Ref. 1**. In view of this figure, we tentatively concluded that the recovered sample at RC is likely to be an amorphous or disordered α phase, although the RS spectrum of the recovered sample does not resemble to that of the amorphous α phase previously published.[11, 17-21] Another possibility, not considered in our published work, is that the recovered phase could correspond to a mixture of another amorphous phase, such as γ-In_2Se_3, whose most intense mode is around 150 cm^{-1} followed by a weaker mode at about 250 cm^{-1},[13, 22-24] and β'-In_2Se_3, whose main peaks are at about 100 and 200 cm^{-1}. One can observe that the RS spectrum of the recovered sample (**Fig. S5** of **Ref. 1**) exhibits broad peaks around the above mentioned frequencies. Moreover, the γ-In_2Se_3 can be

grown at RC, as was stressed in **Chapter 1**. On the other hand, when it comes to β'-In_2Se_3, the last work published about the HP behaviour β'-In_2Se_3 showed the recovery of this phase after reaching 20.2 GPa (see **Fig. 4** of **Ref. 10**). Therefore, the above features suggest the observation of a mixture of both γ and β' phases at RC is feasible on downstroke. Moreover, this result could be reasonable if we consider that the α- β' PT is accompanied by a $\Delta V/V = 6\%$, which can be a remarkable rearrangement to come back to α-In_2Se_3. Instead, a mixed of amorphous β'+ γ phases could be obtained after releasing pressure. Nevertheless, such hypothesis should be check in future works.

To give further support to the PTs observed experimentally, we employed VESTA software[25] to plot the relaxed structures of the different phases of In_2Se_3 obtained from VASP and get their bond lengths and effective coordination number. The α phase has two inequivalent In atoms, with tetrahedral and octahedral coordination. Conversely, β' and β phases only exhibit octahedral coordination, for the former distorted octahedra, for the latter undistorted. On the other hand, the α phase is composed of Se tetrahedra, whereas both β' and β phases are composed of Se octahedra (**Fig. 7** of **Ref. 1**). According to **Fig. 8** of **Ref. 1**, we observe a clear discontinuity in the bond lengths associated to the α → β' PT, pointing out its 1st order character. As regards the β' → β PT, the bond lengths of octahedra (two In-centered and one Se-centered) of the β' phase become equal above 10 GPa, matching with the bong lengths of the β phase at such pressure. At the same time, the effective coordination number of Se-centered octahedra of the β' phase becomes exactly 6, as those octahedra from β phase (**Figure 12** of **Ref. 1**). This progressive symmetrization of bond lengths and regularization of octahedra as pressure increases gives further support to the 2nd order character of the β' → β PT.

3.2. Structural, vibrational and electronic properties of α′-Ga_2S_3 under compression

As was stressed in **Chapter 1**, all the structures of B_2X_3 sesquichalcogenides have vacancies in their different structures, both at RC or at HT/HP. What it was not mentioned is that, due to the presence of vacancies, anions are three-fold coordinated and have a single LEP. Vacancies and their associated anion LEPs are displayed in helixes, layers, or in disordered in cation sites. However, this situation is different for just one structure among all showed in **Chapter 1**; i.e. S.G. *Cc* (**Fig. 1d)**). This phase is one of the phases of Ga_2S_3 and Ga_2Se_3 at RC, the α' and mono-β phase, respectively. In this structure, vacancies are arranged in straight lines forming empty channels. In such arrangement, there are two types of anions: three and two-fold coordinated, with single and double LEPs (see **Fig. 1** of **Ref. 2**). Lewis dot diagrams suggest that tetrahedrally-coordinated Ga cations must have a dative bond from one of the S anions. While the behaviour of cationic LEPs at HP has been extensively studied in the last decade, especially in oxides and chalcogenides with group 14 and 15 cations,[26-29] the behaviour of anionic LEPs at HP is far from being understood.

Before our work was published, only two works addressed the behaviour of α'-Ga_2S_3 at HP, the former with XRD and XANES measurements,[30] the latter with RS and electrical measurements,[31] both supported by computational simulations. Both works

observed PTs under increasing/decreasing pressure, among other remarkable features; however, the effect of pressure on the channels of the crystalline structure and on the single and double LEPs that fill such channels, was not carefully studied. Since α'-Ga_2S_3 stands out as an ideal compound to study how these LEPs behave under HP. For this reason, we performed HP-XRD, HP-RS, and HT-RS measurements supported by computational simulations, to evaluate the pressure dependence of structural and vibrational properties as well as the anharmonic vibrational properties. As another theoretical support, we employed the quantum theory of atoms in molecules (QTAIM) and electron localization function (ELF) analysis to characterize the chemical bonds involved and the role played by the LEPs at HP. Finally, we studied the electronic band structure by computational simulations. In this section, we will comment on the changes observed in the *Cc* structure of α'-Ga_2S_3 at HP. Any detail concerning the PTs observed at HP in the earlier works and its associated changes will be discussed in section **3.4**.

Because of the similar pressure dependence of both lattice parameters and volume of α'-Ga_2S_3 between our both experimental and theoretical data sets with those published in **Ref. 30** (**Fig. 3** of **Ref. 2**), we used these data sets to have a comparative view of EoS, axial compressibilites, principal axes (ev_i) and their compressibilities (λ_i). Bulk moduli from BM3-EoS of α'-Ga_2S_3 were collected in **Table 1** of **Ref. 2**, which experimental value are in agreement, even with that from mono-β-Ga_2Se_3. LDA calculations predict a harder B_o than those obtained from GGA-PBEsol. Unlike LDA calculations of **Ref. 30**, our GGA-PBEsol calculated pressure derivatives (B_o') is higher than 4, as often happens in other compounds with LEPs located in channels.[26, 32] According to normalized stress (F_E) vs finite stress (f_E) (**Fig. S2** of **Ref. 2**), both our experimental data sets and our GGA-PBEsol calculations are better fixed with BM3-EoS than BM2-EoS. Axial compressibilities of our data and that from **Ref. 30** show that the lattice parameter *c* is the less compressible axis, both experimentally and theoretically. However, to obtain reliable axial compressibilities in a monoclinic system with non-orthogonal crystallographic axes, a study of the isothermal compressibility tensor is required to obtain ev_i and their λ_i (**Table 3** of **Ref. 2**). In this occasion, PASCAL software was employed.[33] Directions given by ev_1 and ev_2 vectors, which imply the cross sections of the channels (**Table 3** of **Ref. 2**), are responsible for a total compression between 70-80%. Therefore, channels mainly govern the overall compression of α'-Ga_2S_3. This is also appreciated in the theoretical large value of B_0 of both GaS_4 tetrahedra and the small value of B_0 of α'-Ga_2S_3, which unveils the high compressibility of the empty channels of the crystalline structure.

Regarding the HP-RS measurements, the RS spectra can be divided into two regions: the low- and high-frequency regions below and above 200 cm^{-1}, respectively (**Fig. 6** of **Ref. 2**). Group theory predicts 54 vibrational modes for α'-Ga_2S_3, considering the TO and LO counterparts. Tentative symmetry assignment of the observed Raman-active modes was made thanks to lattice-dynamic calculations (see **Fig. 7** and **Table S1** of **Ref. 2**). Among all of these modes, the breathing mode labelled as *A'*(6) is related with the symmetric stretching vibration of S anions around the channels. It is relevant to remark that this breathing mode is observed in OVCs with AGa_2S_4 stoichiometry, with vacancies displayed in a helix way.[34-36] From the HP-RS

measurements from **Ref. 31**, we can only properly discern the *A'*(6) because the lack of symmetry assignment and pressure coefficients of the observed modes. Regarding the pressure coefficients, the *A'*(6) mode exhibits the highest value, as happens with the breathing mode in mono-β-Ga_2Se_3[37] and OVCs with *A*Ga_2S_4 stoichiometry.[34-36]

The anharmonic properties were evaluated from the joint analysis of HP-RS and HT-RS measurements. This analysis yielded a complete description of the cubic and quartic contributions to each observed mode. In particular, the *A'*(6) mode shows the highest |A/B| ratio (A(B) = cubic(quartic) contribution, see **Table S2** of **Ref. 2**), which means that the vibrations of the S anions around vacancies are dominated by the cubic contribution. Since the *A'*(6) mode does not overlap with other Raman-active modes, we could measure the temperature dependence of its FWHM and determine that cubic contribution governs at LT whereas quartic contribution governs at HT.

Now we turn to the topological analysis of the charge density ($\rho(r)$) of α'-Ga_2S_3 under HP via QTAIM.[38] **Fig. S24** of **Ref. 2** shows the pressure dependence of atomic volumes of the Ga and S basins, in addition to their Bader atomic charges (Q_i) and charge transfers (CT_i). The higher atomic volumes of S basins come from the more diffuse distribution of $\rho(r)$ than Ga basins. Among the different S basins, the S3 anion reflects the highest atomic volume due to the presence of the double LEP. Since basin properties are additive, we can evaluate the total unit-cell volume and bulk modulus considering the contribution of both cationic and anionic basins. In this sense, S basins represent a 75% of the overall unit-cell volume, reinforcing their dominance in the crystal compressibility. If we consider the respective B_0 of each atomic basin, S basins have the smaller values, standing out the S3 basin with the smallest value. These small values of B_0 denote, again, the relevance of the high compressibility of the single and double LEPs to give account for the pressure behaviour of α'-Ga_2S_3. Both Q_i and CT_i for all basins show the polar nature of the different chemical bonds involved, decreasing the ionicity under HP. For a more specific analysis of the chemical bonds, one must evaluate the topological properties of the bond critical points (BCPs), whose distribution in the unit cell can be consulted in **Fig. S25** of **Ref. 2**. The topological properties studied under increasing pressure were $\rho(r)$, its laplacian ($\nabla^2\rho(r)$), and the ratios H_b/ρ_b, G_b/ρ_b and $|V_b|/G_b$, where H_b, G_b and V_b are the total, kinetic and potential local densities, respectively (**Fig. 10** and **11** of **Ref. 2**).

By means of these properties we have catalogued the Ga-S bonds as polar bonds (small ρ_b, positive $\nabla^2\rho_b$, $H_b/\rho_b < 0$, $G_b/\rho_b > 0$ and $1 < |V_b|/G_b < 2$) and the S-S interactions as having a vdW character (smaller ρ_b than Ga-S BCPs, positive $\nabla^2\rho_b$, $H_b/\rho_b > 0$, $G_b/\rho_b > 0$ and $|V_b|/G_b < 1$). Within the Ga-S bonds, we proposed Ga1-S1* and Ga2-S2* bonds to have a dative character for their smallest ρ_b, intermediate positive $\nabla^2\rho_b$, highest H_b/ρ_b, smaller G_b/ρ_b and $|V_b|/G_b$, in addition to other features observed (highest bond lengths, bonds located almost along the direction with the minimum compressibility and different compressibilities, compared to those from the rest of the Ga-S bonds). We tried to identify such dative bonds with the 1D-ELF profiles, but we could not discern them among the rest of the bonds (**Fig. S26** of **Ref. 2**). Under increasing pressure, the topological properties of Ga-S bonds are within the range of polar bonds, although Ga1(2)-S3 bonds have a

larger covalent character because their largest $|H_b/\rho_b|$ ratios. The nature of S-S interactions and how they change with increasing pressure is rather surprising. Below 10 GPa they maintain a vdW character, but above such pressure $H_b/\rho_b > 0$ change to 1 and $|V_b|/G_b < 1$ change to 0. This is explained by an increment of the charge concentration along the channels, induced by the decrease of S-S distances. This change in the charge can be seen in the decreasing LEP volume (**Fig. 12** of **Ref. 2**) and the increasing angle formed by the double LEPs (**Fig. 13** of **Ref. 2**) as increasing pressure. Such increase of charge concentration could be the onset of the PT observed in the two previous works and ours (**Ref. 4**). We must stress that the evaluated ratios H_b/ρ_b, G_b/ρ_b and $|V_b|/G_b$ allow to go into much more detail in the characterization of chemical bonds, more than just using $\rho(r)$ and $\nabla^2\rho(r)$, because such ratios can be compared with other systems.[39-45]

Regarding the electronic properties under HP, there were many controversial points in the theoretical pressure dependence of the band gap of α'-Ga_2S_3. According to Ref. 30, the band gap decreases at HP, unlike the increasing band gap at HP reported in Ref. 31. These results do not match with the nonlinear theoretical pressure dependence of the band gap, which decreases above 7.5 GPa, in the isostructural mono-β-Ga_2Se_3 (**Ref. 46**). Such nonlinear behaviour was reported in other OVCs with AGa_2X_4 stoichiometry. Both in mono-β-Ga_2Se_3 and these other OVCs was showed that this nonlinear behaviour in the band gap was rooted in their vacancies and in the anionic LEPs accommodated in them.[46] Therefore, in view of these earlier results, we examined the theoretical electronic band structure of α'-Ga_2S_3 under HP. In contrast to **Refs. 30** and **31**, we employed the complex *k* path taken from the Seek-path tool[47, 48] to explore the electronic band structures and partial DOS (PDOS) under increasing pressure (**Fig. 14, S28** and **S29** of **Ref. 2**). **Fig. 15a)** of the same work depicted the pressure dependence of theoretical band gap, direct and indirect. Our calculations showed an increase of the direct band gap at LP, a direct-to-indirect band gap crossover at around 5.5 GPa, and a decrease of the direct band gap at around 7 GPa; i.e. at almost the same pressure at which the onset of the decrease of the band gap is observed in mono-β-Ga_2Se_3.[46] Therefore, our results for the electronic band structure of α'-Ga_2S_3 at HP are consistent with those published for isostructural Ga_2Se_3. Our results mainly differ from those published in **Refs. 30** and **31** because both use a simple *k* path proposed by Materials Project Database,[49] in addition to the use of LDA functional in the former ref. and GGA-PBEsol in the latter. In **Fig. 15b)** of **Ref. 2** we can see the evolution of the lowest three conduction band minima (CBM) and the 1st valence band maximum (VBM) at Γ point, together with the CBM at the V_2' point, under increasing pressure. Among these bands, the 1st VB is the most sensitive under HP, which is reasonable considering that this band is mainly occupied by both single and double LEPs. The strong increase of the energy of the 1st VB with pressure can be explained by the strong increase of the repulsion among LEPs as channels are compressed. The changes showed before at 5.5 and 7 GPa are explained with the different crossovers that occur among the 1st CBs, at Γ and V_2' points, and the 2nd CB at Γ point, coming from their relative pressure coefficients, as is seen in **Fig. 15b** of **Ref. 2**. The study of these electronic properties under HP of α'-Ga_2S_3 show its nonlinear behaviour, as was published for other OVCs earlier.[46]

3.3. Pressure-induced order–disorder transitions in β-In_2S_3: an experimental and theoretical study of structural and vibrational properties

Unlike the well-known HT phases of In_2S_3 reported in the literature, the HP behaviour of β-In_2S_3 at room temperature have raised many controversial results in recently published HP works. In the first work published, three PTs were observed, at about 6.6, 11, and 35.6 GPa (the last one assisted by laser heating). The nature of the two first phases could not be resolved, in contrast to that observed at 35.6 GPa, which was attributed to a defect Th_3P_4-like structure (S.G. *I*-43*d*) called δ-In_2S_3.[50] After this work, another HP work evaluated the effects of the pressure on β-In_2S_3 with Ce doping.[51] In undoped and Ce-doped β-In_2S_3 nanoparticles, the 1st PT was observed at 7.1 and 4.3 GPa, respectively. In this case, it was claimed that a cubic structure could be indexed to the XRD patterns measured of this HP phase. However, further details about such proposed cubic structure were not given. Conversely, a more recent HP-XRD study concluded that no pressure-induced PT occurs in β-In_2S_3 up to 41.3 GPa.[52] Surprisingly, the same authors observed a metallization on β-In_2S_3 at about 6.8 GPa in a later work,[53] in agreement with the first two earlier publications. The last work devoted to the HP behaviour of β-In_2S_3 published both HP-RS and impedance spectroscopy measurements, evidencing the 1st PT around 7 GPa.[54] Excepting the **Ref. 52**, all these works agree in the 1st PT observed. At this point, many gaps were unsolved. First, the nature of the 1st and 2nd HP phases. Secondly, the reversibility of these pressure-induced PTs. Thirdly, it was not known if the cubic defect spinel structure, α-In_2S_3, attainable at HT and at RC by playing with stoichiometry, could be obtained at HP. To shed light on these points, we carried out HP-XRD and HP-RS measurements supported by computational simulations to re-examine the pressure behaviour of β-In_2S_3.

According to **Fig. 2** of **Ref. 3**, the onset of the 1st PT is shown at 4.9 GPa, where only the most intense peaks of β phase remain. At higher pressures, incremental changes were seen in the XRD patterns. More precisely, many weak peaks vanished above 8.2 GPa and, additionally, at 10.2 GPa the relative intensities change, suggesting the existence of a 2nd PT. In view of the earlier works, we first focused on the behaviour of the crystalline structure of β-In_2S_3 at HP. We determined the B_0 values with both BM2 and BM3-EoS and compared them with the values previously published, taking into account the different types of PTMs used (see **Table 1** of **Ref. 3**). Despite we use methanol-ethanol (M-E) as PTM, as in **Ref. 52**, a clear comparison of the values of the two works could not be done because authors of **Ref. 52** claimed not to observe any PT and consequently used a very large pressure range to fit the EoS. As regards the 1st HP phase seen at 4.9 GPa and considering the group-supergroup relation between β and α phases, we consider the α phase as a candidate for this 1st HP phase. In view of **Fig. 3** of **Ref. 3**, we succeeded in refining this phase, which could be properly indexed above 10.2 GPa. This phase was observed in other OVCs, as Al_2S_3, Al_2Se_3, $CdAl_2S_4$, $HgAl_2S_4$, $CdAl_2Se_4$ and $HgAl_2Se_4$ at HP-HT conditions (around 4-7 GPa and 673-873 K).[55, 56] As it occurs in In_2S_3 at HT or at RC by varying composition, pressure produces a mixing of ordered vacancies and In cations in β-In_2S_3, from Td(8e) and Td(4a) sites, respectively. As a consequence, a PT to α-In_2S_3 occurs in which both vacancies and In cations are located in disordered Td(8a) sites. To

compare the pressure dependence of the V/Z of β and α phases, we renormalized the formula unit, Z, to consider the disordered vacancies in the α phase, yielding $Z = 10.67$. In view of **Fig. 4** of **Ref. 3**, the β-α PT is accompanied by a $\Delta V/V = 3.3\%$; a value that is quite close to those observed in the pressure-induced PTs of $A In_2S_4$ thiospinels.[57] The B_0 of the α phase (**Table 2** of **Ref. 3**) is lower than that of the β phase. This can be explained by attending to the unit-cell volume fraction of vacancies (estimated at 0 GPa) of β and α phases, 1.54 and 3.22%, respectively. This decrease of B_0 also occurs between the LP and HP (defect $LiTiO_2$ structure) phases of $A In_2S_4$ thiospinels (**Table 2** of **Ref. 3**), but in this case the disorder is seen between *A* and In cations in Oh(16c) sites, unlike in α-In_2S_3, where the disorder is located in Td(8a) sites.

Regarding the 2nd HP phase, many approaches were explored from seeking possible candidates with different stoichiometries (*AX*, A_2X_3, ABX_3 and AB_2X_4) to be employed by structure prediction methods. Finally, we found a defect α-$NaFeO_2$-type (S.G. *R*-3*m*) structure, hereinafter φ-In_2S_3, which is a layered distorted NaCl-type structure, and that is observed in ABX_2 compounds. **Fig. 5** of **Ref. 3** depicts Le Bail refinements of this structure at two pressures and **Fig. 6** evidences the similarities between ϕ-In_2S_3, defect α-$NaFeO_2$, and tetradymite-type structures. To our knowledge, it is the first time that the α-$NaFeO_2$-type structure has been proposed as a post-spinel phase (in this case for a cubic defect spinel structure in In_2S_3). Moreover, this defect α-$NaFeO_2$-type structure has been observed in other B_2X_3 sesquichalcogenides, like Ti_2S_3[58], Sc_2S_3,[59] and Zr_2Se_3,[60] at RC with fractional occupation of 1/3 in octahedral 3b cation sites. Again, we normalized Z of ϕ-In_2S_3 ($Z = 2$) to compare its pressure dependence of V/Z with the β and α phases (**Fig. 4** of **Ref. 3**). The α-φ PT has a low relative volume change ($\Delta V/V = 2.0\%$), similar to that observed between the LP and HP phases of the $A In_2S_4$ thiospinels.[57] The value of B_0 in the φ phase is higher than those from β and α phases (**Table 3** of **Ref. 3**), despite its larger unit-cell volume fraction associated with vacancies (≈11%). In this case, the higher value of B_0 for the φ phase comes from the smaller compressibility of the octahedra than tetrahedra in spinel-like structures. Other reason is the lower V/Z of the φ phase (109 $Å^3$) in relation to those of β (117.25 $Å^3$) and α (116.68 $Å^3$) phases. This inverse relation between bulk modulus and volume can be checked if one compares the value of B_0 in φ-In_2S_3 with those of isostructural indium sulfides, such as $AgInS_2$ and $NaInS_2$ (**Table 3** of **Ref. 3**). The former exhibits a similar B_0 (similar V_0), while the later has a smaller B_0 (larger V_0).

Now we evaluate the effect of pressure on β-In_2S_3 by means of HP-RS measurements up to 21.1 GPa (see **Fig. 7a)** of **Ref. 3**). RS spectra change drastically above 5 GPa, where α phase appears as we showed in our HP-XRD measurements and in agreement with **Ref. 54**. Above 8.6 GPa the Raman signal worsens (~10% of β-In_2S_3 signal), and two broad bands at high frequencies can be only discerned; thus pointing out the onset of the 2nd PT. As regards β-In_2S_3, our lattice-dynamic simulations allowed us to tentatively assign the symmetry of the 22 observed modes (**Table 4** of **Ref. 3**) from the 36 modes predicted by group theory. Among all modes, we must stress the vibrational mode corresponding to S anions moving toward the centre of vacancies located in Td(4a) sites (**Fig. 1** of **Ref. 3**). Unlike the Raman-active breathing mode α'-

Ga_2S_3, the breathing mode in β-In_2S_3 is a silent mode, the B_{2u}^9 (296.86 cm^{-1}), which was found with the J-ICE visualizer.[61] Lattice-dynamic calculations on α-In_2S_3 are quite complex because of the fractional occupation in Td(8a) sites. Then to assign the symmetry of the observed modes of α-In_2S_3, we calculated the theoretical frequencies at several pressures of those modes of $CdIn_2S_4$ thiospinel, together with those experimentally measured in **Ref. 57**. This approach is justified not only for the ordered cations in $CdIn_2S_4$, but also because its molecular mass per unit cell is quite close to that of α-In_2S_3, 3763 and 3474, respectively. **Table 4** of **Ref. 3** shows the tentative symmetry assignment done for the 8 observed Raman-active modes from the 13 modes expected according to group theory. As an additional support to claim for the observation of α-In_2S_3 at HP, we tabulated the Grüneisen parameter, γ, together with those experimental modes observed in commercial α-In_2S_3 powder (see both XRD and RS measurements of this sample in **Fig. S4** of **Ref. 3**). Regarding the φ phase observed above 8.7 GPa, only two broad bands are observed. In the same manner as we did for the α phase, we performed lattice-dynamic simulations to calculate the theoretical pressure dependence of $NaInS_2$, isostructural with φ-In_2S_3 and both with similar molecular masses per unit cell (620 and 656, respectively), and again we tabulated γ's values. **Table 6** of **Ref. 3** shows a good symmetry assignment, in terms of pressure coefficients and γ's values.

To complement our HP-XRD and HP-RS results and give further support to the observation of the φ phase at HP, we calculated the volume and pressure dependence of the energy and the relative enthalpy of β and φ phases (**Fig. S6a)** and **S6b)** of **Ref. 3**, respectively). Due to the fractional occupation in octahedral 3b cation sites of φ phase, we used Supercell program[62] to explore all possible supercells. For the φ phase, we found only 7 supercells, so we could simulate them and get an average value. The calculation could not be done for the α phase because of the unmanageable number of supercells to calculate ($2.3 \cdot 10^{13}$). A lower relative enthalpy was found for the φ phase above 5 GPa with respect to the β phase. This value was in agreement with the experimental α-φ PT observed above 8.2 GPa.

Other point to check was the reversibility of the two PTs characterized along this work. After relaxing pressure, β-In_2S_3 can be recovered, according to the XRD pattern at 0.6 GPa, where β-In_2S_3 is partially obtained (**Fig. 1** of **Ref. 3**), and the RS spectrum at ambient pressure, where β-In_2S_3 is fully obtained (**Fig. 7** of **Ref. 3**). This reversibility was also seen in AIn_2S_4 thiospinels,[57] unlike pseudocubic $CdIn_2Se_4$.[63] Lastly, we want to stress that these results complemented previous HP works on B_2X_3 and AB_2X_4 compounds, yielding a nexus between thiospinels and tetrahedrally-coordinated OVCs. In particular, thiospinels can undergo a pressure-induced order-disorder PT to a defect NaCl structure, such as $CdAl_2S_4$,[64] to a defect $LiTiO_2$ structure, such as thiospinel AIn_2S_4 compounds (A= Cd, Mg, and Mn)[57], or to a defect α-$NaFeO_2$ structure, as has been evidenced for In_2S_3 in this work.

3.4. High-Pressure Synthesis of β- and α-In_2Se_3-like Structures in Ga_2S_3

In this last work, we analyzed the pressure-induced PTs transitions on α'-Ga_2S_3 observed in earlier works, concretely in **Refs. 30** and **31**. In **Ref. 30** a tetradymite-like phase (S.G. *R*-3*m*, hereinafter β'-Ga_2S_3) was observed above 16 GPa and assisted by

laser heating (LH). The RS measurements of **Ref. 31** evidenced such α'→ β' PT at 11.3 and 17.2 GPa, under hydrostatic and no hydrostatic conditions, respectively, but without LH. Curiously enough, HP-RS measurements of **Ref. 31** observed a soft mode (SM) in β'- Ga_2S_3 that does not agree with previous HP-RS measurements of many tetradymite-like sesquichalcogenides.[1, 9] Unlike in **Ref. 30**, authors of **Ref. 31** followed the RS spectra under decreasing pressure and found two new phases below 8.0 and 3.0 GPa; however, further explanations about their structure were not given. To address the different controversies regarding the need of LH to promote the α'→ β' PT, the origin of the SM observed in β' phase, and the nature of the two phases seen under decompression in **Ref. 31**, we performed HP-RS and HP-XRD measurements on α'-Ga_2S_3 with the support of computational simulations.

To evaluate the effect of the PTM, we carried out four runs of HP-RS measurements. Run-1 with methanol-ethanol (M-E), both upstroke (up to 23.7 GPa) and downstroke, is depicted in **Fig. 2** of **Ref. 4**. Run-2, with M-E, and runs 3 and 4, with silicon oil (S) are shown in **Fig. S2a)**, **S2b)** and **S2c)**, and **Fig 3a)** of **Ref. 4**, respectively. In view of all these runs, we could see that the α'→ β' PT is observed at around 16 GPa when M-E is used and at 17.6 and 14.8 GPa when S is used. We could clearly confirm that LH is not required to promote such a PT. Despite that in **Ref. 31** was claimed the appearance of β' phase at around 16 GPa, the only support to this was the indexation of such phase by XRD measurements published by the first work (**Ref. 30**). In our case, to identify the β' phase, we additionally performed lattice-dynamic calculations to obtain the theoretical pressure dependence of the modes of this phase. We observed a good agreement between experimental and theoretical frequencies and their pressure coefficients what confirms the S.G. *R*-3*m* of β'-Ga_2S_3. The tetradymite nature of β'-Ga_2S_3 is also supported by the comparison of the RS spectra of isostructural β'-Ga_2S_3 and β-In_2Se_3 (**Fig. 4a)** of **Ref. 4**). The frequency range of both RS spectra differs because of the different masses of these compounds, but they show a good qualitative resemblance. The only difference comes from the broad band in β'-Ga_2S_3 at about 140 cm^{-1}; i.e. the SM. We proposed that the SM in β'-Ga_2S_3 is a second-order mode, in particular the difference between A_{1g}^1 and E_g^1 modes along the whole Brillouin zone. The reason for this explanation is the good agreement between the experimental frequency and pressure coefficient of the SM mode and the theoretical frequency and pressure coefficient of the A_{1g}^1-E_g^1 difference at the Γ point of the Brilloin zone shown in **Table 1** of **Ref. 4**. The difference between the frequencies of the two features mainly comes from the overestimated theoretical frequencies of the E_g^1 mode, both with PBEsol and PBE-D3 (**Fig. S3** of **Ref. 4**). To complement the appearance of β'-Ga_2S_3 above 16 GPa, we tabulated the phonon dispersion at 17.6 and 18.6 GPa (**Fig. S4a)** and **S4b)** of **Ref. 4**). The instability observed at the high symmetry point T at 17.6 GPa vanishes at 18.6 GPa, supporting that pressure stabilizes the *R*-3*m* phase on Ga_2S_3 above this last pressure that is in good agreement with the onset of the PT to this phase above 16 GPa.

During the downstroke we can visualize that different changes occur in **Fig. 2b)** of **Ref. 4**. The RS spectra show changes below 8.7 and 0.5 GPa that are consistent with the two PTs previously reported in **Ref. 31**. As it was mentioned, the nature of these two phases, hereinafter φ and γ phases, was completely unknown. At this point, we

examined the literature concerning B_2X_3 sesquichalcogenides. Surprisingly, along the last decades several theoretical works have addressed the stability of both S.G. *R*-3*m* and *R*3*m* phases at HT in the whole family of B_2X_3 sesquichalcogenides.[65-68] According to those theoretical works, the S.G. *R*3*m* happens to be dynamically stable at RC in these compounds. However, to stabilize the S.G. *R*-3*m*, HT is required. On the other hand, both phases differ in the cation coordination, 6 and 4-fold coordination in S.G. *R*3*m* and only 6-fold coordination in S.G. *R*-3*m*. The results of such theoretical works, together with the decrease of cation coordination when going from the *R*-3*m* and *R*3*m*, suggested that the S.G. *R*3*m* could be a candidate for one of the two phases found on downstroke in the Ga_2S_3 system. For this reason, we performed lattice-dynamics calculations of the *R*3*m* structure in Ga_2S_3 (see theoretical frequencies and pressure coefficients of the *R*3*m* phase in **Fig 3a)** and **Table 1** of **Ref. 4**). Both pressure coefficients and zero-pressure frequencies of φ-Ga_2S_3 and those theoretical assuming the S.G. *R*3*m* agree very nicely, thus suggesting that φ-Ga_2S_3 has S.G. *R*3*m*. As we did with β'-Ga_2S_3, we compared the RS spectra of φ-Ga_2S_3 and the isostructural α-In_2Se_3 (**Fig. 4b)** of **Ref. 4**). We could clearly see the great similarities between both RS spectra, not only in the number of modes observed, but also in their relative intensities. Again, we calculated the phonon dispersion curve of φ-Ga_2S_3 to check the dynamical stability, in this occasion at 15 GPa (**Fig. S4c)** of **Ref. 4**), which does not exhibit any instability. Since the previous theoretical calculations confirmed the dynamical stability at RC, we can assume the stability of φ-Ga_2S_3 from 15 to 0 GPa. Therefore, from the vibrational point of view, φ-Ga_2S_3 has α-In_2Se_3-like structure with S.G. *R*3*m*. We will confirm this structurally from our HP-XRD measurements.

Regarding γ-Ga_2S_3, observed below 0.5 GPa on downstroke, it exhibits several broad bands that suggest the presence of a strong disorder. However, it could not correspond to disordered α'-Ga_2S_3 because a broad and strong mode observed at about 250 cm^{-1} does not match with the one-phonon density of state of ordered α'-Ga_2S_3 (**Fig. S20** of **Ref. 2**). On the other hand, the RS spectrum of γ-Ga_2S_3 is very similar to those from recovered samples of several AGa_2X_4 (*A*=Zn,Cd,Hg; *X*=S,Se) OVCs[35, 69], as well as to the RS spectrum of α-Ga_2Se_3, the LP phase of Ga_2Se_3 (**Fig. 4c)** of **Ref. 4**). α-Ga_2Se_3 and all the recovered samples from the above-mentioned AGa_2X_4 OVCs present a disordered zincblende (DZ) structure with 4-fold coordinated cations that is consistent with the 4-fold coordination of Ga in many compounds at room conditions. On the light of the similarities seen in the RS spectra of these compounds with γ-Ga_2S_3, we concluded that γ-Ga_2S_3 likely has the DZ structure. However, this should be checked in future HP-XRD works.

In order to evaluate the PTs observed in upstroke and downstroke, we will focus on the HP-XRD measurements of α'-Ga_2S_3 up to 21.1 GPa (**Fig. 5** of **Ref. 4**). **Fig. 5a)** indicates the onset of the α'→ β' PT at 16.3 GPa without LH (see LeBail refinements of β'-Ga_2S_3 in **Fig. 6a)** of **Ref. 4**). This result means that this PT occurs without the need of LH, although using LH could help to crystallize the β'-Ga_2S_3 at HP and improve the quality of the XRD signal. As regards the downstroke, peak intensities of the β phase increase and many new peaks can be distinguished below 8 GPa (**Fig. 5b)** of **Ref. 4**). Good LeBail refinements of φ-Ga_2S_3 can be obtained with S.G. *R*3*m* (see **Fig. 6b)** of **Ref. 4**), but also with S.G. *R*-3*m* since both phases cannot be discerned by

powder XRD measurements. However, we realized that when one tries to refine with with S.G. *R*-3*m* along all XRD patterns on downstroke, a discontinuity in the volume is observed around 8 GPa (**Fig. 7b)** of **Ref. 4**). This feature and the change of RS spectra at the same pressure (Raman measurements can distinguish between both phases) suggest a phase transition from S.G. *R*-3*m* to S.G. *R*3*m* on downstroke in Ga_2S_3. The β'→ φ PT has an experimental and theoretical ΔV/V of 2.6 and 6.4%, respectively. In addition to evaluate the EoS of β' and φ-Ga_2S_3, we gathered those parameters from β and α-In_2Se_3 for the sake of comparison (**Table 2** of **Ref. 4**). In terms of bulk moduli, we can stablish the following sequence: B_0 (β'-Ga_2S_3) ≈ B_0 (β-In_2Se_3) > B_0 (φ-Ga_2S_3) ≈ B_0 (α-In_2Se_3). As happened with In_2Se_3, the *R*-3*m* phase in Ga_2S_3 exhibits a higher B_0 than that of the *R*3*m* phase. Finally, the experimental and theoretical bulk moduli of β'-Ga_2S_3 and its isostructural β-In_2Se_3 (S.G. *R*-3*m*) are of the same order. The same occurs between φ-Ga_2S_3 and its isostructural α-In_2Se_3 (S.G. *R*3*m*), giving further support to the β'→ φ PT in the Ga_2S_3 system.

As it was mentioned, several theoretical works studied both *R*3*m* and *R*-3*m* phases in the B_2X_3 sesquichalcogenide family at HT, with particular interest in the mechanism behind the *R*3*m*-to-*R*-3*m* PT (or vice versa). For this reason, we studied and proposed the mechanism *R*-3*m*-to-*R*3*m* (β'→ φ) PT in Ga_2S_3 on downstroke (**Fig. 8** of **Ref. 4**). We realise that the rotation of (0 2 3) and (0 1 5) planes of β'-Ga_2S_3 in the anti-clockwise direction give rise to (0 1 0) planes of φ-Ga_2S_3, therefore showing the mechanism behind the *R*-3*m*-to-*R*3*m* PT under decreasing pressure, below 9 GPa for the β'→ φ PT in Ga_2S_3. Curiously, the *R*-3*m*-to-*R*3*m* PT under decreasing temperature was theoretically found to be hampered by an entropy barrier and it was proposed that out-of-plane polarization could help to overcome such an entropy barrier.[66] However, we observed that from the *R*-3*m* phase just decreasing pressure the *R*3*m* phase is attainable. More computational simulations are required to study the *R*3*m*-to-*R*-3*m* at HT and under increasing/decreasing pressure in all these compounds.

In this context, we wondered if the phases found in Ga_2S_3 at HP could be also found in Ga_2Se_3 and Ga_2Te_3. In particular, if the S.G *R*3*m* (φ phase) and *R*-3*m* (β' phase) could be energetically competitive in Ga_2Se_3 and Ga_2Te_3 at HP (**Fig. S5** of **Ref. 4**). Taking as a reference the mono-β-(S.G. *Cc*) and ortho-β-Ga_2Se_3 (S.G. *Imm*2), which are ordered phases unlike the DZ-α-Ga_2Se_3, we theoretically predicted that β'-Ga_2Se_3 could be attained in Ga_2Se_3 and Ga_2Te_3 above 6.8 and 5.8 GPa, respectively (**Fig. S6b)** and **S6c)** of **Ref. 4**). In contrast, the *R3m* phase is not energetically favourable in these two compounds at any pressure range. Regarding the mono-β- and DZ-α-Ga_2Se_3, both phases are reported to undergo a reversible PT from the DZ structure to a disordered rocksalt (DR) phase above 14 GPa;[37, 70, 71] however, no HP work on ortho-β-Ga_2Se_3 has been repoprted to our knowledge. As regards Ga_2Te_3, we took mono-α (S.G. *Cc*) and ortho-α (S.G. *Imm*2) phases as references (**Fig. S7b)** and **S7c)** of **Ref. 4**) and found that φ-Ga_2Te_3 with *R3m* structure is energetically favorable starting from both phases, between 11.2 and 11.6 GPa from the former, and between 7.2 and 11.6 GPa from the latter. Above 11.6 GPa, β'-Ga_2Te_3 with *R3m* structure becomes the most favorable phase for both starting phases. This is consistent with the experimental observation of β'-Ga_2Te_3 above 5 GPa from DZ-α-Ga_2Te_3.[72]

Our last aim in this work was to relate Ga_2X_3 and AGa_2X_4 chalcogenides (these latter known to be OVCs). More specifically their LP and HP phases, characterized by how vacancies are relocated under increasing/decreasing pressure (**Fig. 9** of **Ref. 4**). In the binary Ga_2X_3 compounds, HP-PTs rearrange the vacancies to form planes in β' and φ phases, except for β-Ga_2Se_3 that undergoes a PT to the DR phase, with vacancies and cations fully disordered at cation sites. In contrast, in ternary AGa_2X_4 compounds all the HP-PTs are order-disorder PTs, with disorder at cation sites either of both *A* and Ga cations or of *A* and Ga cations with vacancies. Despite these differences, both families tend to octahedrally-coordinated (DR or β') phases with increasing pressure and to tetrahedrally-coordinated DZ phases on decompression due to the irreversibility of pressure-induced order-disorder PTs without additional energy. With this reformulated scheme, we suggested Ga_2X_3 compounds to be considered as OVCs and proposed different paths to explore binary Ga-based compounds under increasing/decreasing pressure, as the possibility of a β'-φ PT in Ga_2Te_3, the obtention of β'-Ga_2Se_3, and the possible pressure-induced PTs starting from DZ-γ-Ga_2S_3.

3.5. References

1. R. Vilaplana, S. G. Parra, A. Jorge-Montero, P. Rodríguez-Hernández, A. Munoz, D. Errandonea, A. Segura and F. J. Manjón, *Inorg. Mater.*, 2018, **57**, 8241-8252.
2. S. Gallego-Parra, R. Vilaplana, O. Gomis, E. L. da Silva, A. Otero-de-la-Roza, P. Rodríguez-Hernández, A. Muñoz, J. González, J. Sans and V. Cuenca-Gotor, *Phys. Chem. Chem. Phys.*, 2021, **23**, 6841-6862.
3. S. Gallego-Parra, Ó. Gomis, R. Vilaplana, V. P. Cuenca-Gotor, D. Martínez-García, P. Rodríguez-Hernández, A. Muñoz, A. Romero, A. Majumdar and R. Ahuja, *Phys. Chem. Chem. Phys.*, 2021, **23**, 23625-23642.
4. S. Gallego-Parra, R. Vilaplana, O. Gomis, P. Rodríguez-Hernández, A. Muñoz, J. A. González, J. A. Sans, C. Popescu and F. J. Manjón, *Chem. Mater.*, 2022, **34**, 6068-6086.
5. A. M. Rasmussen, S. T. Teklemichael, E. Mafi, Y. Gu and M. D. McCluskey, *Appl. Phys. Lett.*, 2013, **102**, 062105.
6. F. Ke, C. Liu, Y. Gao, J. Zhang, D. Tan, Y. Han, Y. Ma, J. Shu, W. Yang and B. Chen, *Appl. Phys. Lett.*, 2014, **104**, 212102.
7. J. Zhao and L. Yang, *J. Phys. Chem. C*, 2014, **118**, 5445-5452.
8. A. M. Rasmussen, E. Mafi, W. Zhu, Y. Gu and M. D. McCluskey, *High Pressure Res.*, 2016, **36**, 549-556.
9. F. Manjón, R. Vilaplana, O. Gomis, E. Pérez-González, D. Santamaría-Pérez, V. Marín-Borrás, A. Segura, J. González, P. Rodríguez-Hernández and A. Muñoz, *phys. status solidi (b)*, 2013, **250**, 669-676.
10. J. Liang, H. Jin, J. Zhang and X. Chen, *Structural Evolution of β'-In2Se3 under Pressure*, in *J. Phys.: Conf. Ser.*, 2020.
11. J. Weszka, P. Daniel, A. Burian, A. Burian and A. Nguyen, *J. Non-Cryst. Solids*, 2000, **265**, 98-104.
12. R. Lewandowska, R. Bacewicz, J. Filipowicz and W. Paszkowicz, *Mater. Res. Bull.*, 2001, **36**, 2577-2583.

13. N. Balakrishnan, E. D. Steer, E. F. Smith, Z. R. Kudrynskyi, Z. D. Kovalyuk, L. Eaves, A. Patanè and P. H. Beton, *2D Mater.*, 2018, **5**, 035026.
14. Z. He, Z. Wang, H. Zhu, X. Liu, J. Peng and S. Hong, *Appl. Phys. Lett.*, 2014, **105**, 011901.
15. A. Bandyopadhyay and L. Ming, *Phys. Rev. B*, 1996, **54**, 12049.
16. K. Yang, Q. Cui, Y. Hou, B. Liu, Q. Zhou, J. Hu, H.-K. Mao and G. Zou, *J. Phys.: Condens. Matter*, 2007, **19**, 425220.
17. X. Tao and Y. Gu, *Nano Lett.*, 2013, **13**, 3501-3505.
18. D. Wu, A. J. Pak, Y. Liu, Y. Zhou, X. Wu, Y. Zhu, M. Lin, Y. Han, Y. Ren and H. Peng, *Nano Lett.*, 2015, **15**, 8136-8140.
19. C.-H. Ho, Y.-C. Chen and C.-C. Pan, *J. Appl. Phys.*, 2014, **115**, 033501.
20. S. Mukherjee, D. Dutta, P. K. Mohapatra, L. Dezanashvili, A. Ismach and E. Koren, *ACS nano*, 2020, **14**, 17543-17553.
21. L. Tang, C. Teng, Y. Luo, U. Khan, H. Pan, Z. Cai, Y. Zhao, B. Liu and H.-M. Cheng, *Res.*, 2019, **2019**.
22. R. Rashid, F. C.-C. Ling, S.-P. Wang, K. Xiao, X. Cui, Q. Rao and D.-K. Ki, *J. Alloys Compd.*, 2021, **870**, 159344.
23. C. d. Groot and J. Moodera, *J. Appl. Phys.*, 2001, **89**, 4336-4340.
24. S. Li, Y. Yan, Q. Deng, Z. Yu, Y. Zhang, Y. Jiang, X. Song, H. Zhao, J. Su and J. Li, *J. Alloys Compd.*, 2020, **845**, 156270.
25. K. Momma and F. Izumi, *J. Appl. Crystallogr.*, 2011, **44**, 1272-1276.
26. A. L. Pereira, J. A. Sans, R. Vilaplana, O. Gomis, F. Manjón, P. Rodriguez-Hernandez, A. Muñoz, C. Popescu and A. Beltrán, *J. Phys. Chem. C*, 2014, **118**, 23189-23201.
27. V. P. Cuenca-Gotor, J. Á. Sans, O. Gomis, A. Mújica, S. Radescu, A. Munoj, P. Rodriguez-Hernadez, E. L. Da Silva, C. Popescu, J. Ibañez, R. Vilaplana and F. J. Manjon, *Phys. Chem. Chem. Phys.*, 2020.
28. I. Efthimiopoulos, J. Kemichick, X. Zhou, S. V. Khare, D. Ikuta and Y. Wang, *J. Phys. Chem. A*, 2014, **118**, 1713-1720.
29. M. Xu, S. Jakobs, R. Mazzarello, J.-Y. Cho, Z. Yang, H. Hollermann, D. Shang, X. Miao, Z. Yu and L. Wang, *J. Phys. Chem. C*, 2017, **121**, 25447-25454.
30. X. Lai, F. Zhu, S. Qin, D. Chen, Y. Li, K. Yang and X. Wu, *J. Appl. Phys.*, 2014, **116**, 193507.
31. L. Yang, J. Jiang, L. Dai, H. Hu, M. Hong, X. Zhang, H. Li and P. Liu, *J. Mater. Chem. C*, 2021, **9**, 2912-2918.
32. J. A. Sans, R. Vilaplana, E. L. da Silva, C. Popescu, V. P. Cuenca-Gotor, A. n. Andrada-Chacón, J. Sánchez-Benitez, O. Gomis, A. L. Pereira and P. Rodríguez-Hernández, *Inorg. Mater.*, 2020.
33. M. J. Cliffe and A. L. Goodwin, *J. Appl. Crystallogr.*, 2012, **45**, 1321-1329.
34. V. V. Ursaki, I. I. Burlakov, I. M. Tiginyanu, Y. S. Raptis, E. Anastassakis and A. Anedda, *Phys. Rev. B*, 1999, **59**, 257.
35. S. Gallego-Parra, O. Gomis, R. Vilaplana, H. M. Ortiz, E. Perez-Gonzalez, R. Luna, P. Rodríguez-Hernández, A. Muñoz, V. Ursaki and I. Tiginyanu, *J. Appl. Phys.*, 2019, **125**, 115901.

36. R. Vilaplana, M. Robledillo, O. Gomis, J. A. Sans, F. J. Manjón, E. Pérez-González, P. Rodríguez-Hernández, A. Muñoz, I. M. Tiginyanu and V. V. Ursaki, *J. Appl. Phys.*, 2013, **113**, 093512.
37. M. Hong, L. Dai, H. Hu and X. Zhang, *Crystals* 2021, **11**, 746.
38. R. Bader, *A Quantum Theory*, *Clarendon*, Oxford, 1990.
39. J. Zhang, L. Song, M. Sist, K. Tolborg and B. B. Iversen, *Nat. Commun.*, 2018, **9**, 4716.
40. R. Bianchi, G. Gervasio and D. Marabello, *Inorg. Mater.*, 2000, **39**, 2360-2366.
41. H. Yang, P. Boulet and M.-C. Record, *J. Solid State Chem.*, 2020, **286**, 121266.
42. R. F. Bader and H. Essén, *J. Chem. Phys.*, 1984, **80**, 1943-1960.
43. E. Espinosa, I. Alkorta, J. Elguero and E. Molins, *J. Chem. Phys.*, 2002, **117**, 5529-5542.
44. C. Gatti, *Z. Kristallogr. Cryst. Mater.*, 2005, **220**, 399-457.
45. T. Lankau and C. H. Yu, *J. Phys. Chem. A*, 2020, **124**, 3795-3804.
46. F. J. Manjón, O. Gomis, P. Rodríguez-Hernández, E. Pérez-González, A. Muñoz, D. Errandonea, J. Ruiz-Fuertes, A. Segura, M. Fuentes-Cabrera, I. M. Tiginyanu and V. Ursaki, *Phys. Rev. B*, 2010, **81**, 195201.
47. Y. Hinuma, G. Pizzi, Y. Kumagai, F. Oba and I. Tanaka, *Comput. Mater. Sci.*, 2017, **128**, 140-184.
48. A. Togo and I. Tanaka, *arXiv preprint arXiv:1808.01590*, 2018.
49. A. Jain, S. P. Ong, G. Hautier, W. Chen, W. D. Richards, S. Dacek, S. Cholia, D. Gunter, D. Skinner and G. Ceder, *Apl Materials*, 2013, **1**, 011002.
50. X. Lai, F. Zhu, Y. Wu, R. Huang, X. Wu, Q. Zhang, K. Yang and S. Qin, *J. Solid State Chem.*, 2014, **210**, 155-159.
51. B. Yao, H. Zhu, S. Wang, P. Wang and M. Zhang, *J. Solid State Chem.*, 2014, **210**, 150-154.
52. Y. Li, Q. Wang, Y. Gao, B. Liu, C. Gao and Y. Ma, *Mater. Res. Express*, 2017, **4**, 085902.
53. Y. Li, Y. Gao, N. Xiao, P. Ning, L. Yu, J. Zhang, P. Niu, Y. Ma and C. Gao, *AIP Advances*, 2018, **8**, 115202.
54. K. Liu, L. Dai, H. Li, H. Hu, L. Yang, C. Pu and M. Hong, *Chem. Phys.*, 2019, **524**, 63-69.
55. K.-J. Range and H.-J. Hübner, *Z. Naturforsch., B*, 1973, **28**, 353-355.
56. K.-J. Range, W. Becker and A. Weiss, *Z. Naturforsch., B*, 1968, **23**, 1009 - 1009.
57. D. Santamaría-Pérez, M. Amboage, F. Manjón, D. Errandonea, A. Muñoz, P. Rodríguez-Hernández, A. Mújica, S. Radescu, V. Ursaki and I. Tiginyanu, *J. Phys. Chem. C*, 2012, **116**, 14078-14087.
58. M. Onoda and M. Saeki, *Chem. Lett.*, 1980, **9**, 665-666.
59. J. Dismukes and J. White, *Inorg. Mater.*, 1964, **3**, 1220-1228.
60. F. K. McTaggart and A. Wadsley, *Aust. J. Chem.*, 1958, **11**, 445-457.
61. P. Canepa, R. M. Hanson, P. Ugliengo and M. Alfredsson, *J. Appl. Crystallogr.*, 2011, **44**, 225-229.
62. K. Okhotnikov, T. Charpentier and S. Cadars, *J. Cheminf.*, 2016, **8**, 1-15.

63. D. Santamaria-Perez, O. Gomis, A. L. Pereira, R. Vilaplana, C. Popescu, J. A. Sans, F. J. Manjón, P. Rodriguez-Hernandez, A. Muñoz and V. V. Ursaki, *J. Phys. Chem. C*, 2014, **118**, 26987-26999.
64. J. A. Sans, D. Santamaría-Pérez, C. Popescu, O. Gomis, F. J. Manjón, R. Vilaplana, A. Muñoz, P. Rodríguez-Hernández, V. V. Ursaki and I. M. Tiginyanu, *J. Phys. Chem. C*, 2014, **118**, 15363-15374.
65. J. Liu and S. Pantelides, *2D Mater.*, 2019, **6**, 025001.
66. Y.-T. Huang, N.-K. Chen, Z.-Z. Li, X.-B. Li, X.-P. Wang, Q.-D. Chen, H.-B. Sun and S. Zhang, *Appl. Phys. Rev.*, 2021, **8**, 031413.
67. W. Ding, J. Zhu, Z. Wang, Y. Gao, D. Xiao, Y. Gu, Z. Zhang and W. Zhu, *Nat. Commun.*, 2017, **8**, 14956.
68. L. Hu and X. Huang, *RSC Adv.*, 2017, **7**, 55034-55043.
69. O. Gomis, R. Vilaplana, F. J. Manjón, E. Pérez-González, J. López-Solano, P. Rodríguez-Hernández, A. Muñoz, D. Errandonea, J. Ruiz-Fuertes, A. Segura, D. Santamaria-Pérez, I. M. Tiginyanu and V. Ursaki, *J. Appl. Phys.*, 2012, **111**, 013518.
70. M. Takumi, Y. Koshio and K. Nagata, *phys. status solidi (b)*, 1999, **211**, 123-129.
71. M. Takumi, A. Hirata, T. Ueda, Y. Koshio, H. Nishimura and K. Nagata, *Phys. Status Solidi*, 2001, **223**, 423-426.
72. N. Serebryanaya, *Powder Diffr.*, 1992, **7**, 99-102.

Chapter 4
Conclusions

With the four published works included in this PhD thesis, we have deepened in the pressure behavior of In_2Se_3, In_2S_3, and Ga_2S_3, which were previously but for which many points remained unclear.

More precisely, in our 1st HP work about In_2Se_3, we shed light on the nature of the α(R) phase, with S.G. *R*3*m*, and confirm the pressure-induced α → β' → β PTs. Regarding the β' → β PT, we highlighted the different pressures reported for such PT, mainly due to its second-order character. Our HP-XRD and HP-RS measurements and our computational simulations allowed us to stablish the β' → β PT about 10-12 GPa. The FWHM of the A_g^2 mode of the β´ phase stabilizes between 10-12 GPa and the regularization of 6-fold coordinated Se anions on β', determined theoretically, above 10 GPa support this gradual β' → β PT. Moreover, with our RS results supported with lattice-dynamic calculations we properly made the symmetry assignment of the Raman-active modes of the three metioned phases, which were not published before. Finally, other works have taken advantage of our results to identify these three phases, thus the high number of citations since this first work was published.

As regards our 2nd HP work, we explored the pressure behaviour of single and double LEPs, from S1(2) and S3 anions, respectively, located in the channels of α'-Ga_2S_3. We showed that the maximum and intermediate compressibilities compromised the cross-sections of the channels and its compressibility rules the overall behaviour of the unit cell. Combined HP-RS and HT-RS measurements allowed to study the anharmonic properties of the Raman modes of α'-Ga_2S_3, standing the *A'*(6) mode, the breathing mode, with the highest anharmonicity at HP and cubic anharmonic contribution at HT.

Due to the presence of these single and double LEPs, we employed QTAIM method via Critic2 software to evaluate the different properties related to the Ga and S basins, in addition to study the character of the chemical bonds involved in α'-Ga_2S_3. In this way, we determined that the almost overall compressibility of the unit cell lies with that of S basin volume, which contains the volume associated to the channels. From the chemical bond classification and the effect of pressure, we found that the vdW character observed in the channels abruptly changes above 10 GPa, because of the higher charge concentration along such channels. In terms of bond lengths, their diffferent compressibilities, and the topological properties considered, we proposed Ga1-S1* and Ga2-S2* bonds as dative bonds. In addition to the change of the vdW character of channels at HP, the ELF visualization allowed us to see the decrease of the single and double LEP volume with increasing pressure and, furthermore, the associated angle of the double LEPs increase to compensate the channel shrinking. Such sharpen changes may anticipate the PTs observed at about 16 GPa. Other relevant point of this work is the use of the topological properties (basin volume and charge, charge transfer, ρ_b, $\nabla^2\rho_b$ and the H_b/ρ_b, G_b/ρ_b and $|V_b|/G_b$ ratios) to study the chemical interactions within this system. With mayor emphasis, we want to stress the above-mentioned ratios, which enables a systematic comparison with other systems, not only at RC but also at HP, as has been showed in this work.

Due to the earlier HP works devoted on the electronic properties of OVCs as AGa_2S_4 and the isostructural β-Ga_2Se_3, we analysed the pressure dependence of the band gap

and the different valence and conduction bands of α'-Ga_2S_3. As was published earlier for other OVCs, α'-Ga_2S_3 exhibited a direct-to-indirect band gap crossover around 5.5 GPa, before the nonlinear pressure behaviour of the direct band gap at about 7.5 GPa. This nonlinear pressure behaviour is mainly rooted in the dominance of the double LEPs in the topmost valence band and their HP dependence.

Moving again to an In-based In_2X_3 compound and its different pressure-induced PTs, we revisited in our 3rd HP work the influence of pressure on β-In_2S_3 due to the clear discordances reported in earlier published works. We observed two PTs, at about 5.0 and 10.5 GPa, respectively. The 1st PTs gives rise to a α-In_2S_3, a defective cubic spinel which has been found at HT and also at RC by varying composition. This α phase owns a bulk modulus smaller than that observed in the β phase, as happens between the LP and HP phases of AIn_2S_4 thiospinels (*A*=Cd, Mg, Mn). The 2nd HP phase seen, the φ phase, has the defect α-$NaFeO_2$-type structure, which has been proposed for the first time as a post-spinel phase. This φ phase exhibits the highest bulk modulus in comparison to the previous phases because the disordered cations are octahedrally coordinated. As regards the RS measurements, because of the disordered cations in α and φ phases, we used lattice-dynamic calculations to calculate the pressure dependence of those modes from $CdIn_2S_4$ and $NaInS_2$, both ordered phases and isostructural of our observed disordered phases. In this way, we were able to do the symmetry assignment of the Raman-active modes observed in both α and φ phases. Both our HP-XRD and HP-RS measurements showed that the PTs observed were completely reversible. Lastly, we expect that this work concerning the pressure-induced PTs on β-In_2S_3 is useful to complement earlier HP works on thiospinels and promote future studies on other B_2X_3 and AB_2X_4 compounds, like Al_2S_3 and spinel $ZnAl_2S_4$, to evaluate if the defect α-$NaFeO_2$-like structure could be proposed as their HP phase.

In our last HP work, we studied the pressure-induced PTs of α'-Ga_2S_3, both under compression and decompression, with were based on our previously published results. Both our HP-RS and HP-XRD measurements supported that the α' phase underwent a PT to the β phase (s.g. *R-3m*, isostructural with β-In_2Se_3) at 16 GPa and without the need of LH. We identified the symmetry of the modes observed in this β phase and proposed that the SM could come from A_{1g}^1-E_g^1 difference. Despite not using LH, we propose that its use could help to crystallize the β phase and eliminate the SM. Under decreasing pressure, we observed φ-Ga_2S_3 (s.g. *R3m*, isostructural with α-In_2Se_3) below 9 GPa. This could be possible by the symmetry assignment thanks to our lattice-dynamic calculations joint to its pressure dependent structural properties, as axial compressibilities and bulk modulus. Regarding the 2nd phase observed under decreasing pressure below 1 GPa, we identified it with the DZ structure, whose RS spectrum is quite similar to those from recovered samples of AGa_2S_4 under HP and to that from the DZ-α-Ga_2Se_3 at RC.

The finding of this φ phase implies a pressure-induced ferroelectric β'-φ PT under decreasing pressure in Ga_2S_3. Additionally, this φ phase with S.G. *R3m* in Ga_2S_3 is the first time that has been synthetized. Because of previous several theoretical works predicted both *R3m* and *R-3m* phases in these B_2X_3 sesquichalcogenides, we evaluated

by computational simulations if such phases could be attained in Ga_2Se_3 and Ga_2Te_3 under increasing/decreasing pressure. Both *R3m* and *R-3m* phases could be synthetized in Ga_2Te_3, whereas only *R-3m* phase could be obtained in Ga_2Se_3. With these results, we reformulated the pressure-behaviour scheme for AGa_2X_4 compounds considering the Ga_2X_3 sesquichalcogenides as part of the family of OVCs. Both families show similar LP and HP phases, regardless the different stoichiometries and starting structures. We hope that this scheme serves as a landscape for future HP works. Finally, the synthesis of α- and β-In_2Se_3-like in Ga_2S_3 will boost its exploitation to design cheap, non-toxic and abundant-element-based devices, in addition to seek such phases in the rest of B_2X_3 sesquichalcogenides under different extreme conditions.

Regarding future HP works, we must mention the lack of experimental HP works in Al_2X_3 (X=S, Se, Te). In view of the predicted phases to occur in Ga_2Se_3 and Ga_2Te_3 under increasing/decreasing pressure, we hope further efforts in such sesquichalcogenides to crystallize their ordered monoclinic and orthorhombic phases and evaluate how pressure triggers different PTs.